ABSTRACT

Title of Dissertation: BRAIN ENDOTHELIAL BARRIER, METABOLIC, AND TRANSPORT DYSFUNCTION IN NIEMANN-PICK DISEASE TYPE C: MECHANISMS AND THERAPEUTIC STRATEGIES

Bilal Moiz, Doctor of Philosophy, 2024

Dissertation Directed By: Dr. Alisa Clyne
Professor
Fischell Department of Bioengineering
Brain and Behavior Institute
Robert E. Fischell Institute for Biomedical Devices

Brain microvascular endothelial cells (BMECs) form the blood-brain barrier, which protects the brain from neurotoxic elements and simultaneously transports glucose and other vital nutrients into the brain. Neurovascular dysfunction is implicated in pathogenesis of neurodegenerative diseases such as Alzheimer's disease and Parkinson's disease; however, little is known about how neurovascular changes contribute to rare inherited neurogenetic disorders such as Niemann-Pick Disease (NP-C). NP-C is caused by mutations in the intracellular cholesterol trafficking proteins NPC1 and NPC2, which leads to endolysosomal cholesterol accumulation and membrane cholesterol depletion. Clinical manifestations vary by age and genetic factors but include neurological symptoms such as developmental delay, cognitive impairment, ataxia, and seizures. Current clinical management strategies are challenged by diagnostic difficulties and poor therapeutic efficacy. Hydroxypropyl-beta-cyclodextrin (HPβCD), an agent

believed to release accumulated cholesterol, has shown promising clinical results; however, its efficacy is limited due to poor brain penetration.

The major objective of this thesis was to determine how NPC1-deficiency impacts BMEC barrier function, metabolism, and nanoparticle uptake. I found that NPC1 deficiency diminishes barrier integrity in BMECs by disrupting claudin-5 and occludin morphology. Using isotope labeling, mass spectrometry, and computational flux analysis, I also observed that NPC1 inhibition leads to systemic metabolic changes, including increased glycolytic flux, elevated activity in peripheral glycolytic pathways, and reduced mitochondrial respiration. HPβCD treatment attenuated barrier function changes and partially restored BMEC metabolic phenotype. Finally, I found that isoproprylacrylamide (NIPAA-m) nanogels loaded with HPβCD were transported across NPC1-deficient BMECs, suggesting their potential for HPβCD delivery to the brain.

This thesis demonstrates a unique, integrated computational-translational approach that unveils the role of BMEC in NP-C pathology, possibly leading to improved therapeutic strategies. In addition, this thesis improves our understanding of how variants in cholesterol metabolism and trafficking, as well as in proteins such as NPC1, which has been implicated in Alzheimer's, diabetes, obesity, and atherosclerosis, contribute to brain endothelial dysfunction.

BRAIN ENDOTHELIAL BARRIER, METABOLIC, AND TRANSPORT DYSFUNCTION IN NIEMANN-PICK DISEASE TYPE C: MECHANISMS AND THERAPEUTIC STRATEGIES

by

Bilal Abdul Moiz

Dissertation submitted to the Faculty of the Graduate School of the
University of Maryland, College Park in partial fulfillment
of the requirements for the degree of
Doctor of Philosophy
2024

Advisory Committee:
Dr. Alisa Moss Clyne, Chair
Dr. Ganesh Sriram, Dean's Representative
Dr. Helim Aranda-Espinoza, MD-PhD Committee Representative
Dr. Tao Lowe
Dr. Kimberly Stroka

Dedication

This work is dedicated to my family, especially Maaria, Osama, and Moosa, who inspired and motivated me to pursue biomedical research.

Acknowledgements

I am forever grateful to everyone who has supported me and guided me during this journey. Without the help of all these people, none of this would be possible.

A huge thank you to Dr. Alisa Clyne who has mentored me for the past 4.5 years. Without her, none of this would be possible. I am extremely grateful for her open-mindedness and encouragement of my research endeavors, allowing my creativity to flourish, while ensuring I stay on track to meet all the milestones. Thank you for meeting with me regularly, for reaching out whenever things went south and helping me overcome all the roadblocks. I honestly could not have asked for a better mentor and experience during my PhD. I can honestly say that my PhD has been one of the best phases of my life and you've provided me with lessons that I can take forward, not just in science, but life as a whole.

I would also like to acknowledge my thesis committee for providing their expertise and a willingness to collaborate to help facilitate my ideas and projects forward.

A huge shout out to all my lab mates. Thanks for creating a fun and collaborative lab environment. A special shout out to Callie, who started at the same time with me. During our time together, we've worked on quite a few collaborative projects and I look forward to continuing to do so when we start VKLab West™. Also, without you and the expertise you brought to the lab, I'm not sure if I would have ever been able to get the brain endothelial cell cultures up and running. Another special shout out to Gurneet who started not long after me. Throughout the years, I've had a blast from the random anime conversations, gym sessions, and ramen meet ups. And thank you to the rest of my lab mates – Marzy, Lauren, Michael, and everyone else who makes it a joy to work in the Vascular Kinetics lab.

I also cannot go without thanking all the wonderful undergrads who have worked besides me over the past few years. Vivi, Andrew, Matt, Ani, Sara, Anthony, Tristan, Angela, and Arielle. It's been a joy to work with you and act as your graduate mentor. I've thoroughly enjoyed seeing you all navigate through research and move forward with your career and personal goals.

Finally, I would like to thank my family and friends who have been there for me day and out throughout the entire journey. A big thank you to my parents and siblings for driving and inspiring me each and every day. And of course, a big thank you needs to go out to my amazing and beautiful wife, Hiba. Without her endless love, patience, and support none of this would be possible.

Table of Contents

Chapter 1 – Background and Significance

1.1. Clinical Significance

Niemann-Pick disease type C1 (NP-C) is a rare autosomal recessive disorder with an incidence of 1:90,000 live births. NP-C is caused by mutations in *NPC1* (95% of cases) or *NPC2*, which regulate cholesterol efflux from the lysosome [1,2]. Clinically, patients present with a mixture of neurological and visceral (pulmonary dysfunction, hepatosplenomegaly) symptoms. The disease is heterogeneous, as clinical presentation and severity vary among patients due to genetic background, age of onset, sex, and environmental factors; however, nearly all patients present with neurological manifestations [3]. In the classical form (60-70% of cases), patients present with childhood onset of neurodegeneration, which can manifest as cerebellar ataxia, loss of motor skills, intellectual disability, and seizures [4]. Patients with this form of the disease typically only live to 10-25 years of age [3]. An adult-onset form of the disease has also been reported in recent literature [5]. In this form, patients live relatively normal lives early on due to slow disease progression but eventually present with psychiatric and/or neurological abnormalities (Figure 1.1) [6]. In all cases, patients suffer from progressive neurodegeneration that is ultimately fatal, usually due to aspiration pneumonia incurred by dysphagia (loss of swallowing) [7].

On a cellular level, NP-C is characterized by endolysosomal cholesterol and glycosphingolipid accumulation, as well as cholesterol depletion from the plasma membrane, endoplasmic reticulum, and golgi apparatus [8–11] (Figure 1.2). Both endogenously synthesized and exogenously acquired cholesterol are eventually trafficked to the lysosome [12,13]. In the lysosome, luminal protein NPC2 first binds to free, unesterified cholesterol and transfers it to the transmembrane protein NPC1, which then facilitates cholesterol transport to the *trans*-Golgi network, plasma membrane, and endoplasmic reticulum [14,15]. Absence of cholesterol in the endoplasmic reticulum activates the cholesterol biosynthetic transcription factors sterol regulatory element-binding protein 1 and 2 (SREBP1/2). This results in a catastrophic feedback loop, as compensatory cholesterol continues to get trapped in the lysosome (Figure 2).

Currently, NP-C treatment options remain limited and there is no cure. Initial strategies used cholesterol-lowering agents, which reduced hepatic and plasma cholesterol with no effect on neurodegeneration [16,17]. Miglustat, which targets glucosylceramide synthase, is FDA-approved for treatment of Gaucher's disease but has been used off-label for NP-C. Miglustat is blood-brain barrier (BBB) penetrant and slows neurodegeneration; however, it does not improve visceral symptoms or effectively halt neurological decline and can lead to gastrointestinal side effects that hinder patient adherence [18,19]. Other therapies, such as histone deacetylase inhibitors (HDACi), may also correct cholesterol metabolism, lipid trafficking, and accumulation in NPC1 patient fibroblasts. However, HDACi delivery via intraperitoneal injection in missense murine models did not extend lifespan, likely due to poor BBB penetration [20].

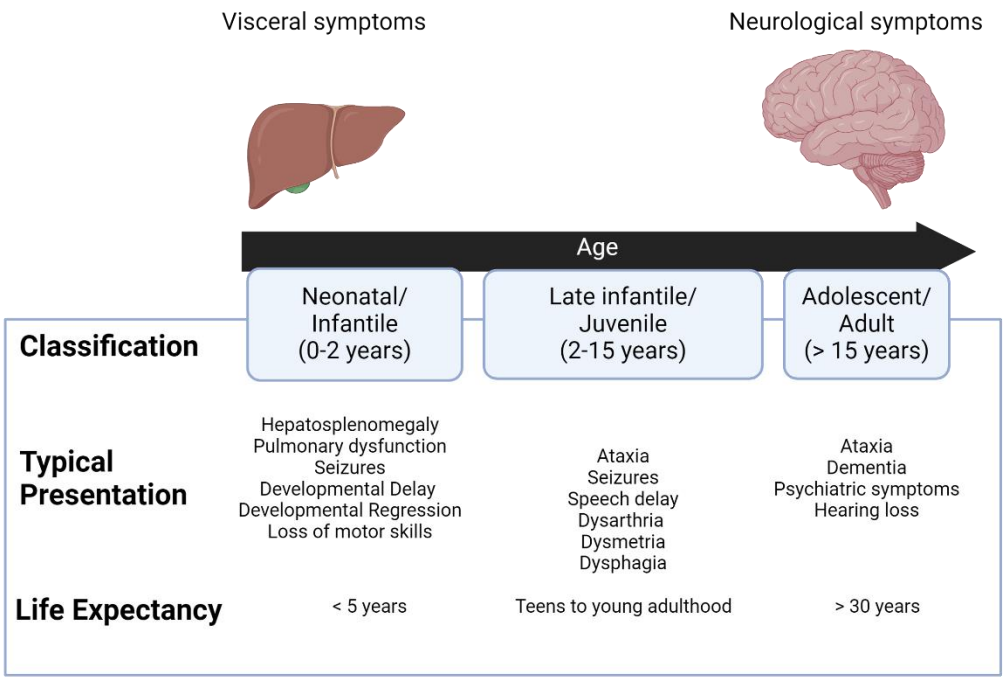

Figure 1.1. Niemann Pick Disease Type C (NP-C) has a heterogeneous presentation that varies with age of onset. There is significant phenotypic variation in NP-C with a greater incidence of visceral symptoms in earlier onset forms. All forms show neurological manifestations and progressive neurodegeneration. Figure adapted from [6].

2-hydroxypropyl-β-cyclodextrin (HPβCD), which mechanistically releases cholesterol from NPC1-deficient cells into the cytosol and organelles, can treat both neurological and visceral aspects of the disease [16,21,22]. Recent HPβCD studies report increased lifespan in NPC1 deficient feline and murine models and slowed human disease progression in Phase II/III human clinical trials [16,23,24]. However, HPβCD cannot effectively cross the BBB and must be administered intrathecally to treat neurological manifestations [23,25]. In addition, intrathecal delivery avoids the pulmonary toxicity induced by systemic administration. When administered intrathecally on a monthly basis, HPβCD appeared to reduce neuronal damage and slow disease progression. All patients reported hearing loss as an adverse effect, which may have been due to the high HPβCD concentrations used. Recently, a novel HPβCD formulation developed by Cyclo Therapeutics was reported to have some capability of crossing BBB when delivered intravenously, as evidenced by detection of low levels of HPβCD in cerebrospinal fluid (CSF) as well as changes in key CSF biomarkers such as tau protein and 24(S)-hydroxycholesterol [26]. However, hearing loss was once again reported as an adverse effect, especially at high HPβCD concentrations. Although HPβCD shows promise, improved dosing, targeting, and delivery strategies must be examined, as the high concentrations and frequent administration required to get the drug across the BBB may lead to the reported adverse effects [16].

Although NP-C is rare, improving my understanding of NP-C can elucidate underlying mechanisms and potential therapeutic strategies for more common neurodegenerative diseases. NP-C has also been colloquially referred to as “Childhood Alzheimer’s Disease” [10], as it shares many biochemical and pathological similarities with Alzheimer’s Disease (AD). AD risk factors and biomarkers, such as APOE ε4, Aβ40 and Aβ42, are associated with NP-C, while intracellular cholesterol accumulation and decreased membrane cholesterol increase Aβ accumulation into amyloid plaques and potentially increase AD risk [10,27]. Furthermore, variations in *NPC1* and *NPC2* have both been found to be associated with sporadic late-onset AD [10]. There are also several other diseases characterized by disturbed cholesterol metabolism, including Antley-Bixier Syndrome (< 50 cases), lathosterolosis (4 cases), desmosterolosis (3 cases), and Smith-Lemli-Opitz syndrome (1:50,000 live births) [11,28]. Improved understanding and knowledge of NP-C may also benefit clinical outcomes for these diseases. Furthering my understanding

of NP-C is also important for peripheral diseases, since NPC1 mutations are associated with obesity, coronary heart disease, and type 2 diabetes [14,29,30].

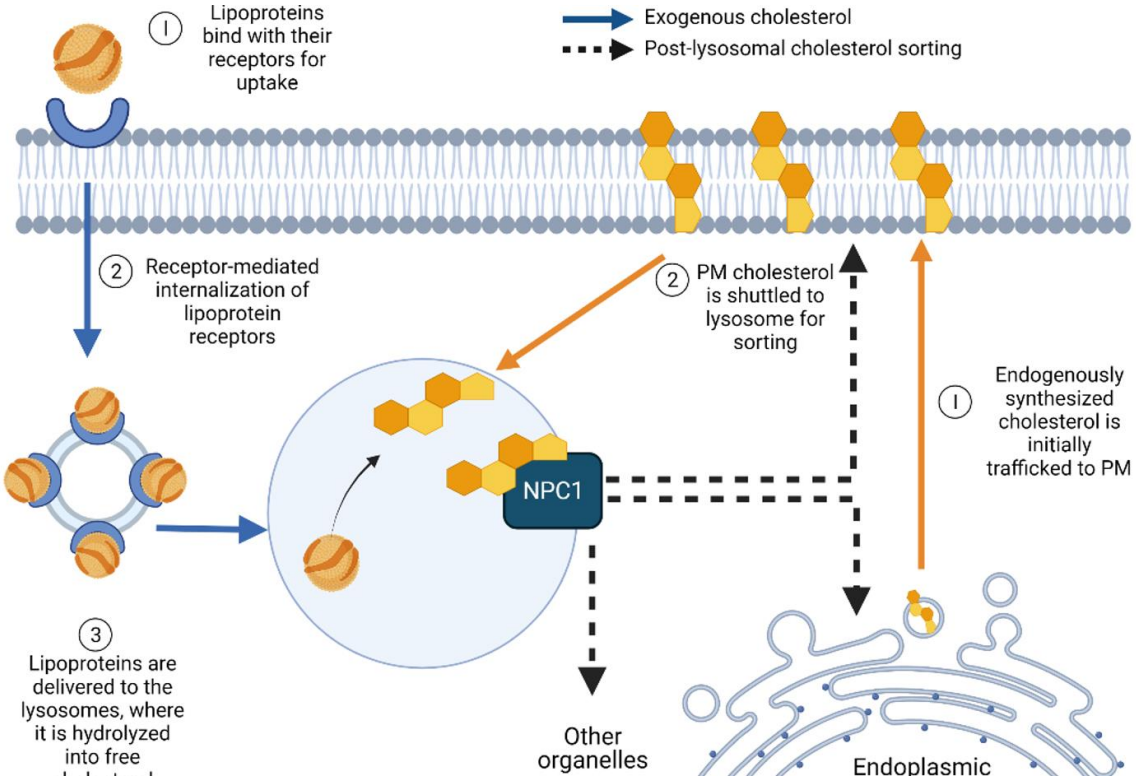

Figure 1.2. Endogenous and exogeneous cholesterol routes. The final steps of endogenous cholesterol synthesis take place in the endoplasmic reticulum, after which it is shuttled out to the plasma membrane (PM). Within 8 hours, PM-cholesterol is shuttled to the lysosome to be sorted and distributed to other cellular organelles, including back to the PM. Exogeneous cholesterol is bound to lipoprotein particles and internalized into the lysosome, where the bound cholesterol is hydrolyzed to free cholesterol. NPC1 deficiency traps both endogenous and exogeneous cholesterol in the lysosome, leading to lysosomal cholesterol accumulation and membrane cholesterol deficiency.

1.2. Blood-Brain Barrier (BBB) and Tight Junction proteins

The blood-brain barrier (BBB) is formed by brain microvascular endothelial cells (BMECs) that selectively traffic molecules between the blood and central nervous system. These endothelial cells are distinct from peripheral endothelial cells and are relatively impermeable, owing to the presence of tight junction proteins that limit paracellular transport. Instead, BMECs have highly specialized transporters that result in transcellular movement of only a limited array of substrates. BMECs play an important role in maintaining brain homeostasis by transporting nutrients such as glucose into the brain, controlling efflux

of compounds from the brain, regulating blood flow in response to the energetic needs of parenchymal brain cells, and protecting the brain parenchyma from exogenous neurotoxins and inflammatory elements [31].

The unique barrier properties of BMECs are mediated by tight junction (TJ) and adherens junction (AJ) proteins that link neighboring cells together, effectively sealing paracellular gaps (Figure 1.3). Key TJ proteins include claudins, occludin, and zonula occludens (ZO). The TJs are localized to the apical side of BMECs, where they form a complex that binds to the actin cytoskeleton. When forming cell-cell junctions, TJs will dimerize with their corresponding partner on neighboring cells. As a result, the paracellular permeability of the BBB is very low, only allowing small, typically nonpolar solutes with a molecular weight < 400 daltons to pass through [32].

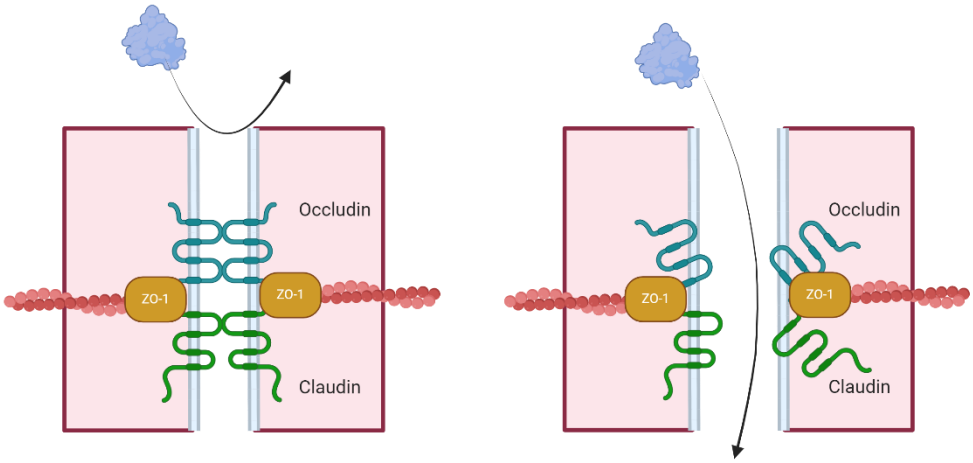

Figure 1.3. Tight junctions seal paracellular gaps and protect the brain from neurotoxic and inflammatory factors. The blood-brain barrier (BBB) is formed by tight junction (TJ) proteins such as occludin and claudin which bind to their counter parts on adjacent cells. These proteins also interface with the adaptor zonula occluden (ZO) proteins. ZO proteins essentially act as linkers that connect the TJ complex to the actin skeleton. The connection between TJs on adjacent cells seals off paracellular gaps, forming an impermeable barrier that prevents neurotoxic and inflammatory elements from entering the brain. However, when TJs are disrupted, these factors can enter the brain and cause inflammation or neuronal damage.

Claudin proteins, of which the most well-characterized is claudin-5, are noted as the “key structural” TJ proteins. Claudin-5 (CLDN5) is the most highly expressed tight junction protein, as it is expressed at levels > 100 times higher than other TJ proteins. This expression level has been observed in multiple

animal models, suggesting its role in the BBB is important enough to be evolutionarily conserved [33]. Claudins are dynamically regulated as they dimerize in both intra- and transcellular configurations and continuously break and reseal to transiently allow small solutes to diffuse across the barrier [32]. CLDN5 is particularly important in regulating BBB permeability of small molecules < 800 daltons. Mouse CLDN5 knockouts showed increased penetration of smaller MW tracers but no change to permeability of microperoxidase (1.9 kDa) or 10 kDa dextran [34]. CLDN5-knockout mice also died within 10 hours of birth, suggesting that CLDN5 is essential for survival. In addition, modification of claudin-5 with a palmitate residue (a process known as palmitoylation) is essential for its functionality. Palmitoylation allows claudin-5 to localize to cholesterol-rich lipid rafts in the plasma membrane, where it then achieves functional configuration [35]. Disruption to this process may impede claudin-5 dimerization and subsequently decrease barrier integrity.

Occludin, a 65 kDa tetraspan protein, is also required to maintain barrier integrity. In contrast to claudin-5, occludin appears to regulate BBB permeability to larger molecules up to 3 kDa. This was evidenced by a double siRNA knockout of claudin-5 and occludin in mice, which had increased penetration of 3 kDa but not 10 kDa tracer molecules [36]. Interestingly, occludin knockout mice had morphologically intact epithelial tight junctions and no gross phenotypic abnormalities at birth, but they showed several histological abnormalities such as inflammation and hyperplasia of gastric epithelial cells and brain calcification [37]. Several *in vitro* studies demonstrated that decreasing occludin can increase BBB permeability and alter actin organization [38]. Occludin-deficient mice also show increased infarction volume, BBB dysfunction, and decreased neurological function as compared to wild type mice. Following stroke, they showed greater leakage of Evans blue dye, as well as lower claudin-5 and ZO-1 expression compared to wild type mice, suggesting that occludin deficiency exacerbates BBB dysfunction following stroke [39].

Unlike occludin and claudins, which are integral membrane proteins localized on the plasma membrane, proteins in the ZO family are located intracellularly. ZO proteins do not directly connect adjacent cells but instead act as linkers that anchor TJs to the actin cytoskeleton within the cytoplasm. Specifically, ZO proteins are members of the membrane-associated guanylate kinase-like homologues

(MAGUKs), which are characterized by several PDZ binding domains and one guanylate kinase-like (GUK) domain, that often connect multiple membrane proteins at cytoplasmic surfaces [40]. The presence of these domains allows ZO-1 and ZO-2 form a multicellular complex in which they bind to claudins through the PDZ domain and occludin through the GUK domain. Interestingly, while ZO-1 is crucial to assemble claudins and occludin [41], the reverse does not hold true as ZO-1 is still capable of forming tight junction complexes in occludin-deficient cells [42]. Knockout of ZO-1, the most well characterized ZO protein in BMECs, obliterates tight junction formation in epithelial cells. ZO-1-null mice also fail to survive past embryonic stage and exhibit significant defects in vascular development, further highlighting the importance of this protein [43].

TJ dysfunction has been implicated in several neurological diseases that demonstrate BBB breakdown and dysfunction, such as AD, Parkinson's disease, Huntington's disease, amyotrophic lateral sclerosis (ALS), multiple sclerosis, and stroke [44,45]. In AD, neuroimaging studies showed increased gadolinium permeability in earlier preclinical and early AD stages, while post-mortem studies demonstrated diminished TJ protein expression along with increased infiltration of blood-derived proteins and inflammatory cells into the brain. Similar neuropathological findings have also been noted in Parkinson's disease and ALS [44]. In patients with temporal lobe epilepsy, loss of TJ proteins and increased protein leakage was observed in hippocampal sections of the brain. Interestingly, BBB dysfunction was found to positively correlate with seizure frequency [44,46]. Psychiatric conditions also show evidence of BBB breakdown. For example, claudin-5 is reduced in the hippocampus of patients with major depression or schizophrenia [47].

Despite the plethora of evidence implicating BBB dysfunction and breakdown in neurodegeneration, there is currently little known about the BBB in lysosomal storage diseases and inherited disorders of metabolism such as NP-C. Most research on altered cholesterol metabolism and neurovascular function centered on high serum cholesterol and its role in common neurodegenerative diseases [48,49]. Hypercholesterolemia leads to BBB tight junction disruption and increased permeability [50,51], inflammation [52] and oxidative stress [53]. Studies on cholesterol depletion in endothelial cells demonstrated decreased membrane fluidity and cell death in bovine pulmonary endothelial cells [54] and

increased rat BBB permeability [55,56]; however, studies on low cholesterol effects are limited. Studying the BBB in the context of these disorders may improve my understanding of how the BBB may contribute to neurodegeneration and also offer insight into the role of specific genes in BBB function.

1.3. BMEC support brain metabolism

BMECs play a critical role in supporting brain metabolism by precisely regulating cerebral blood flow and by selectively transporting essential nutrients such as glucose across the BBB. These cells are uniquely positioned to dictate metabolite availability for other brain cells and just as importantly, remove toxic metabolic byproducts produced by parenchymal cells. Nutrient regulation is a dynamic process in which BMECs respond to cues from other cell types to fulfill the brain's energetic needs. In this section, I explore how brain endothelial cells supply and dynamically respond to the metabolic needs of other brain cells by managing blood flow and nutrient transport.

1.3.1. Nutrient transport

BMEC are responsible for transporting nutrients from the circulation into the brain. Due to the relative impermeability of the BBB, these nutrients must first be selectively taken up by BMECs and then secreted basolaterally for use by brain parenchymal cells. Therefore, BMEC nutrient transporter expression, regulation, and localization dictates parenchymal nutrient availability.

1.3.1.1. Glucose

Glucose is the primary energy source in the brain, and therefore its transport has been extensively characterized [57]. Glucose cannot diffuse across the BBB and must enter the brain through BMEC glucose transporters. Glucose transport is regulated so that cerebral glucose levels only reach 20% of blood glucose levels, which is just sufficient for neuronal demand [58]. This tight glucose regulation is hypothesized to balance the reliance of the brain on glucose for energy while simultaneously preventing potential neurotoxic glucose [58]. Glucose transported across the BBB is either released into the CSF or diffuses into the gap junctions of astrocytes that are in contact with BMEC.

The most prominent BMEC glucose transporter is GLUT1, a sodium-independent glucose transporter. GLUT1 is found at much higher levels in BMECs than in peripheral endothelial cells [59]. The importance

of GLUT1 in cerebral glucose transport was shown by the fact that no glucose was found in the cerebrospinal fluid (CSF) of patients with GLUT1 deficiency syndrome [60]. Approximately 12% of BMEC GLUT1 is on the apical (blood-facing) cell membrane, while 48% of BMEC GLUT1 is on the basolateral cell membrane, and the remaining 40% of BMEC GLUT1 resides in the cytosol [61]. BMEC have other glucose transporters such as GLUT3 and GLUT4, as well as sodium-dependent glucose transporters such as SGLT1; however, these are less important for glucose transport [62]. For example, haploinsufficient GLUT3 mice had normal glucose uptake [63]. Glucose movement across all of these glucose transporters occurs through facilitated diffusion due to the glucose concentration gradient across BMEC [64].

GLUT1 is regulated by other cell types and secondary factors. Rat BMECs increased GLUT1 expression following treatment with conditioned-media from astrocytes cultured in glucose-deprived conditions [65]. Hypoxia inducible factor 1α (HIF-1α), a master transcriptional regulator of the cellular hypoxic response, may modulate GLUT1 levels. Endothelial-specific HIF-1α KO mice had reduced cerebral brain glucose uptake, as evidenced by a lower cerebral:blood glucose ratio. Additionally, HIF-1α-deficient endothelial cells showed reduced glucose uptake *in vitro*, which was rescued through forced GLUT1 expression [66].

Reduced BMEC glucose transport can lead to cerebral glucose hypometabolism, which is associated with neurodegeneration and has even been proposed to be a driver of neuropathology [67,68]. A murine endothelial GLUT1 knockout triggered severe neuroinflammation and reduced brain-derived neurotrophic factor. This effect was exaggerated when the GLUT1 knockout was induced neonatally. Furthermore, murine GLUT1 haploinsufficiency reduced extracellular brain glucose by 90% and also reduced brain-derived neurotropic factor (BDNF), which is essential for neuronal survival and growth [69]. Indeed, in another study endothelial-specific GLUT1-KO mice had reduced neuronal density and widespread brain inflammation [70]. Therefore, dysregulated BMEC glucose transport can have devastating effects for the brain.

1.3.1.2. Lactate

Lactate may also be an essential fuel source in the brain, specifically by exchanging fuel between cerebral cells with different glycolytic and oxidative metabolic rates (Bergersen, 2015; Brooks, 2009). At rest, BMEC transport lactate out of the brain; however, when blood lactate levels increase, BMEC transport lactate from the blood into the brain (Rasmussen et al., 2010). Lactate is transported across the BBB by monocarboxylate transporter 1 (MCT1), a medium-high affinity isoform which is equally localized to the apical cell membrane, basolateral cell membrane, and cytosol (Bergersen, 2007; Froberg et al., 2001; Gerhart et al., 1997). Lactate transport across BMEC via MCT1 depends on the lactate and pH gradients (Dienel, 2012).

Lactate may be a crucial nutrient for pericytes, which wrap around cerebral blood vessels and share a basement membrane with BMEC. BMEC-specific GLUT1 deletion decreased CSF lactate as well as reduced pericyte coverage due to increased apoptotic pericyte cell death. Pericytes cultured *in vitro* were incubated with the glycolytic inhibitor iodoacetic acid to minimize their own basal lactate production and then co-cultured with GLUT1-knockout or control BMECs. Pericytes cultured with GLUT1-KO BMECs had markedly reduced lactate, indicating that decreased BMEC lactate production also decreased pericyte lactate. Administration of exogeneous lactate to BMEC-specific GLUT1 null mice rescued pericyte coverage, showing the importance of this endothelial-derived metabolite for pericyte function (H. Lee et al., 2022).

In contrast, lactate may be cytotoxic for neurons. Phosphatase and tensin homolog (PTEN) upregulates the lactate transporter MCT1 in BMEC. Mice with PTEN-deficient BMEC showed increase brain lactate concentration, which was caused by decreased MCT1 and significantly lower lactate efflux. Lactate accumulation impaired neurogenesis and cognitive function in mice, which was attenuated by restoring MCT1 in BMEC (Wang et al., 2019). Thus, BMEC may need to carefully regulate lactate transport to feed pericytes while maintaining neuron viability.

1.3.1.3. Amino acids

BMEC maintain the concentration of most amino acids tenfold lower in the brain than in the plasma, with the exception of glutamine which is present in a similar concentration in the brain and plasma. Amino

acid transport across the BBB is regulated by ten amino acid transporter systems, including some that are facilitative Na+ independent transporters and some that are Na+ dependent. L amino acid transporter 1 (LAT1) transports large, neutral amino acids such as leucine and phenylalanine into the cell in exchange for intracellular glutamine. LAT1 is highly expressed in BMEC, where it is found in a 2:1 ratio in the apical and basolateral cell membranes (Asano et al., 2007; Duelli et al., 2000; Sánchez del Pino et al., 1995; Yanagida et al., 2001). Cationic amino acid transporter 1 (CAT1) is responsible for arginine transport from the blood into the brain (Stoll et al., 1993).

Apical facilitative Na+ independent transporters control glutamate efflux from brain to blood, as well as glutamine and cysteine transport from blood to brain. Glutamine is the most abundant amino acid in both blood and CSF and is a precursor for both the excitatory neurotransmitter glutamate and the inhibitory neurotransmitter γ-aminobutyric acid (GABA). Since LAT1 inhibition did not inhibit glutamine transport into the brain, it is thought that there exists another glutamine facilitative transporter (system n). Glutamate is transported out of the brain by a Na+-indpendent transporter on the basolateral BMEC membrane and a facilitative carrier on the apical BMEC cell membrane (system X_C^-) (R. Hawkins & Viña, 2016; W.-J. Lee et al., 1998). Indeed, this transporter exchanges extracellular cystine for intracellular glutamate. In addition, five Na+-dependent amino acid transporter systems couple amino acid transport out of the brain with Na+ import into the brain. The Na+ gradient is then maintained by a Na+ pump at the endothelial basolateral membrane.

Disruption of amino acid transport across the BBB has neurological consequences. A LAT1 mutation was recently identified as a rare cause of autism spectrum disorders (Tărlungeanu et al., 2016). While an endothelial-specific LAT1 knockout model has not yet been examined, systemic LAT1 deletion causes embryonic lethality in mice (Ohgaki et al., 2017). LAT1 mRNA decreased in mouse BMEC following lipopolysaccharide (LPS) administration, suggesting that inflammation may downregulate BMEC amino acid transport (Wittmann et al., 2015). By ablating LAT1 in the cerebral cortex, Knaus *et al* showed that deficiency of large neutral endogenous amino acids shortly after birth changed cortical neuron lipid metabolism, excitability, and survival (Knaus et al., 2023). Together, these studies highlight a need to further investigate BMEC LAT1, especially in the context of neurodegeneration.

1.3.1.4. Fatty acids

Lipids constitute nearly 50% of the brain's dry weight (Svennerholm et al., 1997); however, the brain has a limited capacity to synthesize fatty acids and must instead import them from circulation. Lipids enter the circulation through dietary absorption, through production in the liver, or through release from adipose tissue. Due to their hydrophobic nature, lipids must bind to soluble proteins such as albumin or be integrated into lipoprotein complexes to remain in circulation. Lipoproteins have a hydrophilic outer shell and an internal core composed of cholesterol and triglycerides, which are formed of three fatty acids and glycerol. Lipids form a major part of brain cell membranes, and two key fatty acids, arachidonic acid and docosahexaenoic acid (DHA), play extensive roles in neuroprotection, brain development, synaptogenesis, and neural differentiation (Sambra et al., 2021).

Free fatty acids (FFAs) can passively diffuse across the BMEC membrane even though they are at low concentration close to the endothelium (7.5 nM) (Mitchell et al., 2011; Murphy, 2017). First, the fatty acids dissociate from their carrier proteins through hydrolysis by membrane-associated lipases. The FFAs then adsorb to the endothelium and flip from the outer plasma membrane to the cytosolic plasma membrane. However, the flippase activity that facilitates FFA movement across the membrane is thermodynamically unfavorable, and fatty acid translocase (FAT, CD36) or fatty acid transport proteins (FATP) are needed to make FFA transport into BMEC possible (Mitchell et al., 2011). Once inside the cell, FFAs are ferried through the cytoplasm by fatty acid binding proteins (FABP). For example, FABP5 binds to and carries DHA across BMEC (Pan et al., 2015). Once the FFAs reach the basolateral BMEC plasma membrane, they flip across to diffuse to other cerebral cells (Murphy, 2017). FFA transport rate depends on several factors, including the fatty acid/albumin dissociation rate as well as the fatty acid size and lipophilicity. Longer chain fatty acids are less lipophilic and therefore typically have decreased transport (Mitchell et al., 2011).

Lipid can also be moved across BMEC by clathrin dependent and caveolae mediated transcytosis. Low-density lipoprotein (LDL) is taken up by BMEC via clathrin dependent transcytosis after binding to the LDL receptor (LDLR) or LDLR-related protein 1 (LRP1). LDL particles are then directed to the lysosome, where they are degraded and released as cholesterol and fatty acids. LDL can also be taken

up via LDLR in caveolae, which is thought to transfer LDL without its degradation (Dehouck et al., 1997). Interestingly, while BMEC internalize LDL, they do not transport the cholesterol into the brain (Kakava et al., 2022).

Finally, lipids can be transported into the brain via transport proteins. FFAs can be incorporated into lysophosphatidylcholine (lysoPC), which is then transported across the plasma membrane by monocarboxylic acid transporters (MCTs) or FATPs. LysoPC can also be transported by Mfsd2a, specifically lysoPC that contains DHA (Lacombe et al., 2018). Mfsd2a appears to be involved in maintaining DHA levels in BMEC and in other brain cells, and therefore Mfsd2a loss inhibited BBB function and caused neuronal loss, cognitive deficits, and microcephaly (Ben-Zvi 2014, Andreone 2017; Nguyen 2014, Zhou 2019, Razmara 2020, Wong and Silver 20202; Alakbarzade et al., 2015).

Alterations in lipid transport across BMEC may play a role in aging and disease. Indeed, the brain loses 42% of its phospholipids and 47% of its cholesterol as humans age from 20 and 100 years (Svennerholm et al., 1997). Cerebral DHA transport was studied in mice with the human apolipoprotein 4 (APOE4) allele, a main genetic risk factor for late onset AD. The DHA uptake rate was 24% lower in APOE4 mice (Vandal et al., 2014). Similarly, in the 3x-TG mouse model of AD, DHA cerebral transport was 25% lower (Calon, 2011).

1.3.2. BMEC metabolism impacts BBB integrity and cerebral function

1.3.2.1. Glucose

Both *in vitro* and *in vivo* evidence suggest that glucose transport via GLUT1 plays an important role in BBB function. Barrier integrity was characterized in induced pluripotent stem cell derived BMECs (iPSC-BMECs) with GLUT1 knocked out via CRISPR-Cas9 *in vitro*. GLUT1 KO decreased iPSC-BMEC transendothelial electrical resistance (TEER) compared to control; however, no tight junction morphology differences were observed [71]. Likewise, glucose deprivation diminished iPSC-BMEC barrier integrity. The barrier loss was maintained even following supplementation with ketone bodies, which are used by the brain during glucose deprivation [72]. *In vivo,* GLUT1 KO zebra fish had decreased BMEC tight junction proteins and increased barrier permeability [73]. Global GLUT1 haploinsufficiency reduced tight junction proteins and increased endogenous plasma protein leakage in the brain of 2-week-old mice. In

mice overexpressing amyloid β-peptide, a transgenic Alzheimer's disease model, endothelial-specific GLUT1 KO initiated BBB breakdown [59]. However, endothelial-specific GLUT1-KO mice (1-week old) did not show differences in BBB integrity, specifically in terms of brain water content, Evans Blue or gadolinium permeability, or tight junction morphology [70]. The differences in *in vivo* BBB integrity with GLUT1 KO may be age dependent, as a later study found no permeability changes in 5-day endothelial-GLUT1-KO mice but found increased permeability in 10-day old mice [74].

High glucose, which is studied to understand the neurological effects of diabetes, has also been shown to impair BBB function. In primary human BMECs, exposure to high glucose (25 mM D-glucose) media increased BMEC permeability to 150 kDa dextran, reduced TEER, and decreased tight junction protein expression. These changes were not observed with osmotically-controlled media. High glucose decreased AMPK activation, and increasing AMPK attenuated barrier changes in high glucose [75]. In mouse BMECs, high glucose upregulated HIF-1α, increased permeability, and decreased tight junction proteins. These changes were blunted with a HIF-1α inhibitor [76]. Methylglyoxal, a reactive carbonyl species that is a precursor to advanced glycation end products that are damaging in diabetes, also led to BMEC barrier dysfunction. This reduced TEER was exacerbated by high glucose or reduction in the antioxidant glutathione but abrogated by addition of the antioxidant N-acetyl cysteine [77]. Thus oxidative stress may be an important BBB regulator.

Glucose metabolism is critical for angiogenesis [78,79]. Cerebral angiogenesis is particularly important during early development. Endothelial-specific GLUT-1 deletion in 1-3 day old mice decreased BMEC proliferation, the number of tip cells, and blood vessel length [80]. In another study, endothelial-specific GLUT1 haploinsufficiency induced in two-day old mice led to later reduced brain CSF, sparser capillary density, and fewer tip cells compared to age-matched controls [69].

1.3.2.2. Glutamate

Glutamate, which is derived primarily from uptake of the amino acid glutamine, acts as both a metabolite intermediate that feeds the TCA cycle and as a vital neurotransmitter in the brain. Glutamate concentration usually ranges from 50-100 μM in the plasma and 0.5-2 μM in extracellular fluids [81]. The cerebral glutamate concentration is tightly regulated by bidirectional glutamate transporters on BMEC,

including SLC1A1, SLC1A2, SLC1A3, and SLC1A6. BMEC can also bind glutamate to ionotropic receptors such as N-methyl-D-aspartate (NMDA) receptors that regulate ion flux and membrane potentials [82,83] and metabotropic glutamate receptors such as metabotropic glutamate receptor 5 (mGluR5) that initiate intracellular signaling cascades through second messengers [84].

High cerebral extracellular glutamate concentrations cause excitotoxicity resulting in cell death. Glutamate binding to NMDA receptors induces calcium influx into immortalized human BMEC [85]. As cytosolic calcium rises, calcium entry into mitochondria also increases thereby elevating mitochondrial membrane potential. This increased mitochondrial potential drives increased flux through oxidative phosphorylation, a byproduct of which is increased reactive oxygen species (ROS) production leading to oxidative stress and cell death [86]. Though there are few studies to validate this mechanism in human primary BMEC, glutamate concentrations as low as 250 μM decreased transgenic rat BMEC viability, likely as a result of excitotoxicity and downstream oxidative stress [87]. In mouse hippocampal neurons, cellular oxygen consumption, a measure of mitochondrial metabolism, increased following 24-hours of treatment with 4 mM glutamate [88]. In these same cells, tetramethylrhodamine (TMRM) staining indicated that 4 mM extracellular glutamate hyperpolarized the mitochondrial membrane which in turn elevated ROS production [88].

In mouse BMEC, glutamate-induced increases in intracellular calcium can also increase nitric oxide production (Zuccolo et al., 2019). However, this is likely because glutamate treatment reduces eNOS RNA and increases iNOS RNA [87]. While eNOS is generally considered vasoprotective and produces nitric oxide to initiate vasodilation, iNOS produces large bursts of nitric oxide in oxidative environments. Through this mechanism, iNOS leads to ROS production and downstream inflammation and apoptosis.

BMEC must precisely regulate glutamate concentration to maintain the BBB and protect neurons in the surrounding brain tissue. 30 minutes of exposure to 1 mM extracellular glutamate, which is much higher than the physiological concentration, increased *in vivo* rat BBB permeability by almost 20% [90]. In immortalized cerebral endothelial cells, 1 mM glutamate and 1 mM NMDA both significantly decreased barrier function, as shown by lower TEER. The barrier loss was inhibited by MK-801, an NMDA receptor

antagonist [83]. These studies indicate that glutamate decreases BMEC barrier function through an NMDA receptor-mediated mechanism.

1.3.2.3. Fatty Acids

Disturbances in fatty acid metabolism have been linked to neurodegenerative diseases [91,92]. Fatty acids are taken up by BMEC and can then be fated for metabolism or stored as cytosolic lipid droplets [93]. The fatty acid metabolism pathway depends on the fatty acid length. Very long chain fatty acids (VLCFA, carbons >= 22) are metabolized via β oxidation in the peroxisome, while shorter chain fatty acids are first converted into acyl-CoA in the cytosol and then transported into the mitochondria for β oxidation [94].

While fatty acid metabolism is thought to provide only a small portion of endothelial ATP production, fatty acids support other critical endothelial cell functions such as nucleotide synthesis, post-translational protein modifications, signal transduction pathway activation, and gene regulation [95]. Quiescent peripheral endothelial cells, including cells exposed to physiological shear stress, had higher expression of carnitine-palmitoyl transferase (CPT1A), which controls mitochondrial fatty acid import and is the rate limiting step of fatty acid oxidation. Quiescent endothelial cells also had higher fatty acid oxidation than proliferating endothelial cells. Fatty acid oxidation was dispensable for energy production and biomass synthesis but was critical for redox homeostasis. CPT1A inhibition or knockout dramatically increased endothelial ROS, which then led to endothelial dysfunction and increased leukocyte adhesion and permeability through VE-cadherin disruption [96,97]. Cellular supplementation with acetate, which is metabolized into the fatty acid downstream product acetyl-CoA, decreased ROS in CPT1A-knockdown peripheral endothelial cells and reduced leukocyte infiltration into the lungs [97].

While few studies address fatty acid oxidation in BMECs specifically, current evidence suggests an important role for fatty acid oxidation in maintaining barrier function. Fatty acid metabolism byproducts and intermediates can directly mediate BMEC function. Palmitoylation, the covalent attachment of fatty acids to protein cysteine residues, is particularly important for claudin-5, a key tight junction protein. Palmitoylated claudin-5 translocated to cholesterol-rich lipid rafts, where it dimerized and restricted paracellular permeability to enhance BBB function [35,98].

While fatty acid oxidation may be essential for BBB maintenance, high serum lipids can damage the BBB. BMECs exposed to elevated postprandial triglyceride-rich lipoproteins, a risk factor for vascular dementia, had elevated ROS and increased expression of the stress-responsive protein ATF3 [99]. A follow up study showed that triglyceride-rich lipoprotein treatment increased mitochondrial oxidative stress and protein leakage, but this effect could be reduced by CPT1A1 siRNA knockdown [100].

1.4. The BBB as a challenge for neurotherapeutics

1.4.1. Uptake at the blood-brain barrier

Treatment of neurological disorders is significantly hindered by BBB impermeability, with almost 100% of large molecule and 98% of small molecule drug candidates unable to cross the BBB [101]. This poor penetrance necessitates drug concentrations or more invasive delivery strategies, both which can lead to adverse effects. The initial challenge involves effectively delivering therapeutic molecule across the BBB into the brain. However, even if this is successful, efficacy can be blunted by processes that occur once the drug is in the brain. Efflux transporter activity that removes drugs from the brain and pumps them back into the blood, enzymatic degradation in the brain, and poor targeting to target parenchymal cells are further challenges that need to be addressed for effective drug delivery [102].

Effective drug delivery therefore requires careful delivery vehicle design to overcome these obstacles and still provide a therapeutic dose once the drug is in the brain. Numerous non-invasive BBB drug delivery vehicles have been explored, including viral vectors, nanoparticles, and chimeric proteins [103]. Of these, nanoparticles (NPs) offer the most control since their shape, size, functional groups, and charge can be modified to enhance targeted delivery and cargo [104]. These NP properties have been exploited to design nanoparticles that target uptake pathways in brain endothelium.

The brain endothelium exhibits several uptake and internalization pathways that can exploited for drug delivery. These include facilitative transporters used primarily for passive uptake of nutrients across a concentration gradient, which were discussed previously in the section on nutrient transporters. Numerous NP platforms target the GLUT1 transporters that are highly expressed on brain endothelial

surfaces by functionalizing particles with GLUT1-targeting ligands such as mannose [105,106] or 2-deoxy-2-glucose [107].

In contrast to the facilitative pathways are the endocytic uptake pathways, which involve energy expenditure and can be divided into three phases: uptake and internalization, sorting, and exocytosis [108]. Three major routes of endocytic uptake have been identified in BMECs: clathrin-mediated endocytosis, caveolin-mediated endocytosis, and micropinocytosis [109]. The most commonly exploited for BBB drug delivery is clathrin-mediated endocytosis (CME), a process in which clathrin proteins coat the internal leaflet of the plasma membrane, leading to inward budding of the plasma membrane and eventual vesicle internalization [110,111]. CME is a major route of uptake into and across brain endothelium, since BMEC have limited ability to take up solutes via macropinocytosis and caveolin-mediated endocytosis [112]. Thus, many brain drug delivery strategies functionalize agents with ligands to target highly expressed clathrin-mediated endocytic receptors in BMECs, for example by adding ApoE peptides to target LDL receptors (LDLr) or transferrin ligand to target transferrin receptor (TfR) [113–117].

While micropinocytosis and caveolin-mediated endocytosis are downregulated in BMECs compared to other endothelial cell types, they are not completely absent. Caveolin is downregulated in BMECs by Mfsd2a, which transports lipids that inhibit this pathway. Caveolin has been shown to drive increased permeability in Mfsd2a-KO mice but its role in normal physiological states remains unclear [108,118]. Macropinocytosis is a non-specific process in which membrane protusions form and collapse inward, engulfing any extracellular particles inside the inward budding vesicle. BMECs have been shown to take up pathogens, microvesicles, and platelets via micropinocytosis [119].

Although targeting major uptake pathways such as clathrin-mediated endocytosis and facilitative transport has shown some degree of success, it is crucial to account for pathological conditions that can further complicate therapeutic delivery by altering these innate transport mechanisms that are exploited by nanoparticles. For example, many of the drugs manufactured for enzyme replacement therapy exploit clathrin-mediated endocytosis M6P receptor to target recombinant enzymes to the lysosome [120]. This pathway was shown to be defective in macrophages with mutations modeling acid sphingomyelinase (ASM) deficient form of Niemann-Pick disease type A (NP-A) [121]. All three major endocytic pathways

have been shown to be perturbed in different lysosomal storage diseases [122]. In Alzheimer's disease, there is significant downregulation of PICALM, a critical protein in clathrin-mediated endocytosis [123,124].

Interestingly, disease states do not always downregulate uptake and transcytosis pathways, but may still lead to favorable transport of specific pathways . A recent study showed that ASM actually increased expression of intracellular adhesion molecular-1 in BMECs and increased transcytosis of anti-ICAM nanocarriers. The anti-ICAM nanocarriers, which target the clathrin- and caveolin-independent CAM-uptake pathway, appeared to be more favorable for delivery than other formulations targeting the clathrin-mediated endocytic marker transferrin receptor (TfR) and caveolin endocytic marker plasmalemma vesicle-associated protein (PV1). In this case, expression of all three receptors increased in the disease state, but ICAM-1 showed much higher expression than the other two receptors. In another study comparing endocytic pathways in patient-derived fibroblasts from four lysosomal storage disorders (NP-C, NP-A, Fabry disease, and Gaucher disease), clathrin-dependent endocytosis was downregulated in all four diseases, while macropinocytosis was actually upregulated in NP-C [122].

1.4.2. Nanogels in CNS drug delivery

To address the challenge of site-specific delivery of therapeutic across the BBB, multiple nanoscale agents have been deployed, including polymeric nanoparticles, liposomes, dendrimers, and more. However, many of these agents have been limited by poor stability, burst release of cargo, cytotoxicity, and poor biocompatibility. A nanocarrier that can non-invasively enter the BBB following circulation must be amendable to targeting, effectively cross the BBB, and maintain controlled release to only delivery the cargo once in the brain. For this reason, nanogels, which are essentially nanoscale hydrogels composed of crosslinking polymer networks, are excellent candidates to facilitate targeted delivery of therapeutic cargo across the BBB. Nanogels are primarily defined by their use for controlled release and swelling, but also offer tunability, high stability, large drug payload capacity, and excellent biodegradability and safety profile [125,126]

Nanogels are synthesized similarly to hydrogels but instead from polymers less than 200 nm. They can be specifically synthesized to respond to specific changes in temperature, pH, ionic environments ,

and even ultrasound or magnetic stimuli [125]. Poly(N-isopropylacrylamide) (NIPAA-m) nanogels are the most widely used and studied nanogel systems, owing to the ease of their synthesis and unique thermoresponsive properties [127]. Specially, nanogels are designed to have a lower critical solution temperature (LCST) that optimizes their stability *in vivo*. The LCST is the temperature at which nanogels transition from solution to gel. When in solution at a temperature below LCST, water molecules align with internal hydrophilic amide moieties in the nanogel, causing them to swell or dissolve into solution [128,129]. Conversely, at higher temperatures, water is expelled from the nanogel interior, causing them to gelate. When designed to maintain gelation at physiological temperatures, nanogels therefore maintain extreme stability *in vivo*. Degradation of these gels can be controlled by incorporating a hydrolytically degradable cross-linker that links the PNIPAA-m polymers. These crosslinkers can be specified to response to specific stimuli, thus resulting a highly controlled drug release platform.

1.5. Experimental and computational methods

1.5.1 In vitro models: iPSC-derived BMECS vs. primary BMECS

Currently, *in vitro* human BBB models can be created with either human primary BMEC (hpBMEC), human immortalized BMEC (hCMEC/D3), or human induced pluripotent stem cell-derived BMEC-like cells (iPSC-BMEC) [130–132]. hCMEC/D3 have low barrier function and tight junction protein expression but offer a renewable source of cells due to their immortalized nature. However, immortalization can also lead to phenotypic differences that do not adequately model BMEC phenotype. hpBMECs are sourced from human brain tissue and can more accurately model *in vivo* BMECs. Long-term usage of these cells is complicated by their poor availability and high cost, as well as alterations in phenotype with increasing passage number.

In contrast, iPSC-BMECs) are renewable and have superior barrier function (2000-8000 ohms) compared to hpBMECs and hCMEC/D3 cells (~200 ohms). In addition, iPSCs are amenable to gene editing and can also be derived from patient cells, allowing them to be used to model genetic diseases [133]. However, recent evidence suggests that hiBMEC may retain an epithelial-like transcriptomic profile, reducing their relevancy to *in vivo* physiology [134,135]. my recent work also showed that while these cells are satisfactory for modeling glucose metabolism [136], they do not recapitulate other metabolic features

observed in hpBMECs, such as glutamate efflux. When I examined systemic differences between iPSC-BMECs and hpBMEC metabolism, I found that iPSC-BMECs only secrete trace amounts of glutamate. Instead, iPSC-BMECs directed more glutamate flux into glutathione, aspartate, and alpha-ketoglutarate. They also showed metabolic inflammatory markers, specifically in leukotriene and eicasanoid metabolism, suggesting elevated inflammation in baseline conditions. Furthermore, these cells also showed evidence of kynurenine metabolic reactions which were not present in hpBMECS. Kynurenine plays essential roles epithelial cells and this may therefore suggest iPSC-BMECs model an epithelial-like metabolic phenotype [137].

While these challenges require careful consideration when studying BMEC metabolism, iPSC-BMECs still offer a superior barrier function model. Additionally, recent work confirmed that iPSC-BMEC have receptor-mediated transcytosis (RMT), which is essential for transport of large solutes across the BBB. In this study, functional transport assays for transferrin, a ligand of RMT, showed that iPSC-BMECs are a preferable model for transport compared to immortalized BMECs [138]. This conclusion stemmed from the finding that iPSC-BMECs significantly limit paracellular permeability of RMT tracers due to their high barrier fidelity while still maintaining transcellular uptake and transport of these compounds, similar to what is seen *in vivo*.

1.5.2. Modeling NP-C and cholesterol depletion

Multiple agents can be used to chemically modify cholesterol distribution and trafficking *in vitro*. One of the most prominent classes of cholesterol modifying agents are the cyclodextrins, which are a family of cyclic, water-soluble oligosaccharides with an outer hydrophilic surface and inner hydrophobic core. There are multiple cyclodextrin derivatives, manufactured to control water solubility, stability, and interactions [139]. Methyl-β cyclodextrin (MβCD) is commonly used to acutely deplete cholesterol. MβCD can form a 2:1 complex with cholesterol, and this favorable interaction passively sequesters cholesterol away from the plasma membrane and into the hydrophobic cavity, leading to membrane cholesterol depletion [140]. In contrast, the NP-C drug HPβCD is typically internalized into the endolysosome, where it then transports cholesterol into the cytosol [16]. However, to achieve this specific function, it must be

carefully dosed. High doses can cause cholesterol depletion (similar to MβCD) as well as lysosomal exocytosis [141,142].

The amphipathic compound 3-b-[2-(diethylamino)ethoxy]androst5-en-17-one, otherwise known as U18666A, is a versatile tool to investigate changes in cholesterol trafficking and biosynthesis. U18666A can inhibit cholesterol efflux by blocking the NPC1 protein, possibly by altering the lysosomal membrane domain [143]. However, at higher concentrations, U18666A can also alter cholesterol synthesis due to its ability to inhibit the cholesterol biosynthetic enzymes 7-Dehydrocholesterol reductase 24 (DHCR24) and oxidosqualene cyclase (OSC) [144]. U18666A and other OSC inhibitors can be cataractogenic and have historically been deployed to induce cataracts in animal models. An examination of U18666A on rat lens suggested that the amphipathic nature of U18666A and its structural similarities to cholesterol allows it to intercalate in cellular membranes of the rat eye lens, where it increases membrane rigidity and can disrupt function of membrane-bound proteins [144]. While this may be a lens cell specific response, it still remains crucial to carefully dose U18666A and scrutinize the resulting cell phenotype to ensure it mimics NP-C cholesterol distribution without major off-target effects [143].

Genetic knockout models can potentially better recapitulate the NP-C phenotype. The use of knockout models has become increasingly prevalent in NP-C studies, especially with the growing popularity of induced pluripotent stem cell (iPSC) lines that offer a stable, renewable source of NPC1-null cells. iPSCs are generated from somatic cells, typically dermal fibroblasts, although it is also possible to derive them in a less invasive manner from hematopoietic stem cells or kidney epithelial cells excreted in urine. Once collected, somatic cells are reprogrammed through forced expression of the “Yamanaka” factors (Oct3/4, Klf4, Sox2, and c-Myc), which eventually directs a portion of them towards a pluripotent stem cell phenotype. From there, the reprogrammed cells can be isolated and directed into multiple cell lineages, including brain cells such as neurons, pericytes, astrocytes, and BMECs [145–147].

Genetic knockout models of NP-C can be sourced from two different methods. Somatic cells can be isolated from NP-C patients and converted to iPSCs [148]. Alternatively, gene editing of wild-type cells can eliminate NPC1 expression. In either case, genome engineering through as CRISPR-Cas9 is typically necessary, as even patient cells may need to be corrected to generate isogenic controls for comparisons.

Alternatively, multiple iPSC lines from both wild-type and afflicted patients can be used for experiments, but this is often costly and labor intensive. In prior studies, iPSCs were used to generate NPC1-deficient models of neurons [149] and astrocytes [148].

1.5.3. Barrier function

1.5.3.1. Modeling the BMEC barrier

The BMEC barrier is primarily modeled with microfluidic devices and Transwell inserts. Microfluidic devices typically consist of tubular channels in a polymeric material. The channels are then lined with BMECs and connected to a perfusion device to mimic blood flow through a brain vessel. In Transwell insert experiments, BMECs are cultured as a monolayer on a semiporous membrane which separates a well into an apical ("brain") and basolateral ("blood") side. In both types of models, other cell types, such as neurons and astrocytes, can be loaded in adjacent microfluidic channels or one Transwell compartment to represent cell-cell interactions in the brain. Alternative approaches such as organoids and spheroids, in which multiple cell types are cultured together to generate a 3D environment with close cell-cell interactions, do not offer options to measure permeability or junction morphology [150,151].

Microfluidic devices recreate a more relevant 3D environment than Transwell inserts and enabling shear stress studies. However, manufacturing microfluidic devices requires advanced engineering capabilities. Commercial options are costly compared to Transwells. Additionally, a lower number of cells can be cultured in microchannels which greatly limits their use for protein, RNA, and mass spectrometry assays [151,152]. Transwell models are simplified, as they lack features such as flow-induced shear stress. However, their simple structure enabled them to be used to rapidly assess barrier integrity using trans-endothelial electrical resistance (TEER), permeability assays, and tight junction imaging [153,154].

In this thesis, I solely used Transwell inserts to model the BMEC barrier because they allowed me to assay permeability, image tight junctions, quantify gene and protein expression, and analyzed metabolites by mass spectrometry while being cost effective and requiring minimal engineering design. I also solely used BMECs in the model, as other cells would complicate my experimental design and interpretation, particularly for metabolic assays.

1.5.3.2. Transendothelial Electrical Resistance

Transendothelial electrical resistance (TEER) offers a non-destructive and repeatable method to measure barrier integrity in cell cultures. TEER measurements are typically performed by placing electrodes on both sides of a porous membrane (such as a Transwell insert). The electrodes apply an alternating current (AC) voltage signal, and the voltage difference is used to calculate the resistance of the cell layer. The resistance is also be measured in a membrane that does not contain any cells. This resistance is then subtracted from the resistance measured in experimental samples to calculate the true cell monolayer resistance. The resistance is also corrected to the cell layer surface area, as electrical resistance is inversely proportional to area. The rationale for this is that a larger area can increase the number of paracellular routes that an electrical current can pass through. Therefore, resistance readings in a larger Transwell surface underestimate the true resistance. The final TEER measurement after these corrections reflects the paracellular ionic conductance of the cell barrier [155,156].

TEER can be used to measure barrier function over time with minimal disruption to the cells. However, there are confounding variables that can distort TEER data interpretation, including electrode position, temperature, cell density, and media composition. Furthermore, ionic conductance may not reflect cell monolayer permeability to larger molecules. In some situations, the cell monolayer may be sufficiently altered to modulate ion permeability, and hence change TEER, but not enough to impact large solute permeability [155,156].

1.5.3.3. Permeability Tracers

Permeability tracers can be used to examine size-selective changes in barrier integrity. Permeability tracers vary in size, from low molecular weight solutes such as sodium fluorescein (376 Da) to larger dextrans which can be upwards of 100 kDa. These tracers are typically not transported through the cells and can therefore only pass through the paracellular route. In a permeability tracer assay, a solution of fluorescent tracer molecules is loaded into the apical compartment of a Transwell insert. At specified time intervals, the media in the basolateral comportment is sampled. The media sample fluorescence is then quantified with a fluorescent plate reader. After correcting for background signal, the measurements are then used to calculate the clearance volume. The clearance volume is interpreted as the theoretical

volume from which the substance would be completely eliminated. For example, in a highly permeable barrier, a larger volume would be emptied of the solute compared to a less permeable barrier within the same time frame. The relationship between clearance and time can be used to calculate the linear slope. The slope is then normalized to the slope of the cell-free membrane, inverted, and normalized to area to calculate the permeability coefficient. The permeability coefficient can then be compared among different conditions.

1.5.4. Metabolic assays and analysis

1.5.4.1. YSI

The YSI Bioanalyzer uses enzyme sensor technology to quantify metabolites in media samples. For this assay, media samples are collected into 96-well plates, placed into the YSI Bioanalyzer, and queued for readings. Each sample is drawn and passed into an enzyme probe that contains a three-layer membrane: an outer, sample facing polycarbonate membrane; an internal membrane with an immortalized oxidase enzyme; and finally a cellulose acetate membrane situated close to platinum anode. The outer polycarbonate membrane interfaces with the buffer into which the sample is injected. As the sample diffuses from the outer compartment into the central membrane, it reacts with the immobilized oxidase enzyme to produce hydrogen peroxide, which is then itself oxidized once it reaches the acetate membrane. The second oxidation step produces a steady flow of electrons that is linearly proportional to the substrate concentration. The measured current can therefore be used to calculate the substrate concentration once the system has been properly calibrated. The YSI Bioanalyzer used for this dissertation has modules to measure L-Lactate, D-Glucose, L-Glutamine, and L-Glutamate. All data showing uptake or secretion of these metabolites were acquired using the YSI bioanalyzer.

1.5.4.2. Seahorse XF analyzer

Seahorse Extracellular Flux (XF) assays can be used to continuously monitor extracellular acidification rate (ECAR) and oxygen consumption rate (OCR) in real time, allowing us to observe immediate metabolic responses. In this assay, cells are seeded onto specialized 96-well plates and then prepared for analysis. Prior to the assay, the cells are degassed to allow CO_2 diffusion from the cells and

medium to maintain optimal pH levels for the assay. Additionally, the top cartridge, which contains four drug loading ports for each well, is prepared.

The Seahorse instrument uses two fluorophores that are quenched with either oxygen or pH to measure these components in the cell media during the assay. For the Seahorse Mito Stress Test (Chapter 3), the cartridge was prepared to inject oligomycin, carbonyl cyanide-4 (trifluoromethoxy) phenylhydrazone (FCCP), and rotenone/antimycin A. Oligomycin inhibits ATP synthase/Complex V in the mitochondrial electron transport chain, which immediately decreases cellular ATP production and linked oxygen respiration. The difference in OCR before and after oligomycin treatment is quantified as the ATP-linked respiration. Afterwards, cells are injected with FCCP, which uncouples oxygen respiration from mitochondria, obliterates the mitochondrial proton gradient, and disrupts mitochondrial potential. FCCP causes the cells to achieve maximal respiration, which then allows quantification of the maximal respiration capacity. Finally, the cells are treated with rotenone and antimycin A, which target mitochondrial Complex I and Complex III, respectively. This shuts down all mitochondrial respiration, allowing calculation of any nonmitochondrial respiration.

1.5.4.3. Isotope Labeling Experiments

A detailed analysis of cellular metabolism is essential for a complete understanding of cellular function in health and disease. Most cell metabolism studies focus on experimentally measured metabolite concentrations. However, metabolite concentrations can change for varied reasons (e.g., increased upstream vs. decreased downstream reaction rates) [157]. Alternatively, metabolite concentrations could remain unchanged despite changes in flux (e.g., if upstream and downstream fluxes change by exactly the same amount). Therefore, I gain limited information from metabolite concentrations alone.

Metabolic fluxes, defined as the metabolic reaction rate (moles/time), provide much more information than metabolite concentration alone. The fluxome indicates the traffic of carbon and other elements among metabolites and therefore provides information on both metabolite concentrations and reaction rates. Since the reaction rates depend on upstream and downstream enzyme expression and activation,

the fluxome integrates the cellular metabolome with the transcriptome, proteome, and regulome to offer a dynamic, comprehensive representation of the cell metabolic state [158,159].

Metabolic fluxes include extracellular fluxes (transport reactions that cross the cell membrane) and intracellular fluxes. While extracellular fluxes can be directly measured by tracking metabolite concentrations in the culture medium, intracellular fluxes cannot be measured directly and must be inferred from their effect on the incorporation pattern of an isotopically labeled nutrient substrate (e.g., ^{13}C-glucose) [160] into a biological system (e.g., cell, animal). Metabolic reactions convert the supplied labeled carbon sources to intermediate metabolites and secreted products, whose labeling state (isotopomers) depend on the reaction fluxes and the carbon atom rearrangements [161].

While a metabolite with *n* carbon atoms can have up to 2^n isotopomers, only a subset of this gamut of isotopomers can be measured, depending on the analytical tool used. Traditional MS or single-quadrupole MS provides labeling information in the form of mass distribution vectors (MDVs), which can range from completely unlabeled metabolites with zero labeled carbons [M+0] to fully labeled metabolites with all labeled carbons [M+n], where n is the number of carbons in the metabolite [160]. These MDVs describe each isotopomer's fractional enrichment (isotopomer abundance normalized to the sum of all isotopomers). The range of isotopomers increases with analytical tools that provide atomic position specific information such as NMR and tandem or triple-quadrupole mass spectrometry (MS/MS). Ideally, a combination of multiple analytical techniques could provide a comprehensive measurement of isotopomers, a demonstrated recently [162]

These metabolite labeling patterns can be classified as either isotopologues or isotopomers. Isotopologues differ in mass due to the number of labeled atoms while isotopomers differ in both mass and position. Therefore, an isotopologue can have multiple isotopomers with the same mass but with different positions. While a metabolite with *n* carbon atoms can have up to 2^n isotopomers, only a subset of this gamut of isotopomers can be measured, depending on the analytical tool used. Traditional MS or single-quadrupole MS provides labeling information only on isotopologues, as they cannot distinguish positional differences in isotopomers with the same mass. The range of measurable isotopomers

increases with analytical tools that provide atomic position specific information such as NMR and tandem or triple-quadrupole mass spectrometry (MS/MS) [162].

Isotopomer information is typically described in the form of mass distribution vectors (MDVs), which describe each isotopomer's fractional enrichment (isotopomer abundance normalized to the sum of all isotopomers). MDV isotopomers can range from completely unlabeled isotopomers with zero labeled carbons [M+0] to fully labeled metabolites with all labeled carbons [M+*n*], where *n* is the number of carbons in the metabolite [160,162].

Labeled tracer nutrients should be strategically chosen to maximize information for the experimental objective. In general, there are three important tracer nutrient parameters to consider when choosing a labeling scheme: the specific labeled tracer nutrients used in the study, their relative abundance (e.g., the proportion of the metabolic substrate that the labeled tracer nutrient constitutes), and tracer mixes/parallelization.

The tracer nutrient and which atom positions in the tracer nutrient are labeled determines the MDV labeling pattern. While uniformly labeled tracer nutrients provide information on major metabolic pathways, tracer nutrients with a specific number and location of labeled atoms can elucidate specific pathways. For example, the first carbon of glucose-6-phosphate is lost as carbon dioxide (CO_2) at the branch point from glycolysis to the pentose phosphate pathway (PPP). [1,2-^{13}C] glucose is ideal for measuring this branch point, as glucose produces M+2 lactate when it is metabolized through glycolysis and M+1 lactate as it is metabolized through the PPP [163] (Figure 1.4). In contrast, uniformly labeled glucose is metabolized into M+3 lactate in both scenarios and thus cannot be used to distinguish flux between these two pathways. Detailed tables explaining which tracers are ideal for each metabolic pathway are found elsewhere [157].

1.5.4.4. Mass spectrometry and MDV Quantification

The three principal techniques to experimentally measure MDVs are liquid chromatography coupled to mass spectrometry (LC-MS), gas chromatography coupled to mass spectrometry (GC-MS), and nuclear magnetic resonance (NMR) [76]. Mass spectrometric methods ionize molecules, separate them by the mass-to-charge ratio (m/z), and measure them with a detector. Mass spectrometers are typically

paired with chromatographic methods to further resolve spectra and separate isomers, compounds with identical molecular formulas and m/z ratios but different structures [75,77]. In contrast, NMR applies strong magnetic fields and radio frequency pulses to atoms, causing their nuclei to spin and emit energy upon relaxation. This energy is measured in the NMR spectrum, which can be used to identify and quantify metabolites. Generally, mass spectrometry is more sensitive and allows detection of sparsely abundant isotopomers but lacks the specific structural information provided in NMR.

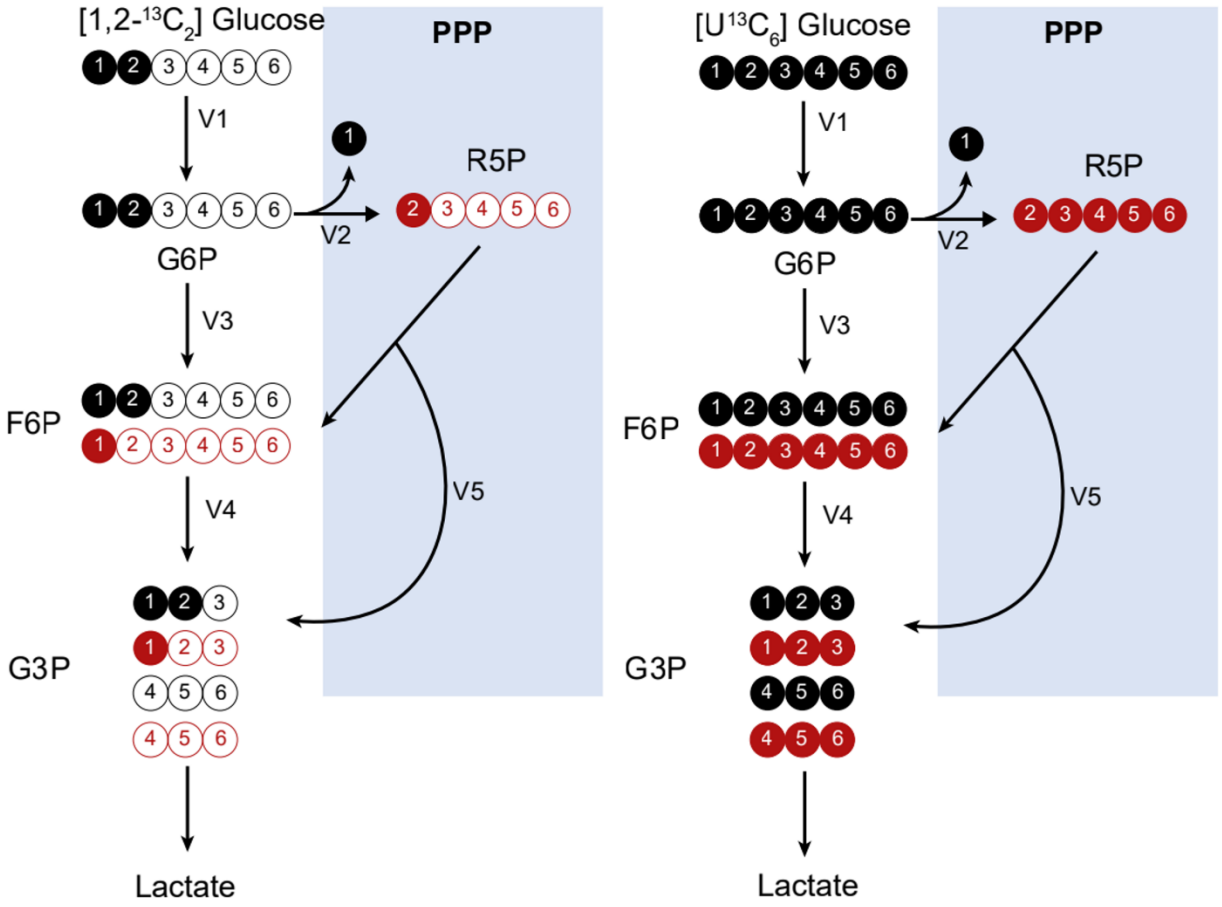

Figure 1.4. Tracers should be selected carefully to optimize information for pathways of interest. [1,2-$^{13}C_2$] glucose generates an M + 1 isotopomer after entering the PPP as R5P that is eventually metabolized into M + 1 F6P and G3P, whereas glucose that is directly metabolized into F6P generates M + 2 isotopomers. Therefore, the ratio of M + 1 and M + 2 isotopomers in metabolites such as F6P and G3P, as well as derivatives such as lactate and pyruvate, can be compared to determine relative activity at the PPP branchpoint. Red = carbons that pass through the PPP; black = carbons that pass through the main glycolytic pathway. Abbreviations: glucose-6-phosphate (G6P), ribose-5-phosphate (R5P), fructose-6-phosphate (F6P), glyceraldehyde-3-phosphate (G3P), pentose phosphate pathway (PPP).

Mass spectrometry is highly sensitive, allowing thousands of compounds to be detected at micromolar or nanomolar concentrations [76,78]. This sensitivity reduces the sample size needed for analysis, which can be important for high throughput cell culture or when taking multiple samples from an animal model [32]. Although mass spectrometry methods can detect low metabolite concentrations, they are limited in distinguishing isotopomers from natural abundance background when isotope enrichment is low [79].

LC-MS and GC-MS are the two primary separation techniques paired with mass spectrometry. LC-MS is a highly versatile method that uses mobile solvents (such as acetonitrile, water, and methanol) to pass metabolites through a column and separate them by properties such as polarity, charge, and size. Following separation, metabolites are ionized through electrospray ionization or atmospheric pressure ionization [77]. Sample preparation is simpler in LC-MS because, in contrast to GC-MS, metabolites do not typically have to be derivatized, although they can be derivatized to improve signal or ionize compounds that are resistant to ionization [77,80]. The other primary advantage of LC-MS is that it can detect a broader range of molecules, including low-abundance phosphorylated metabolites and cofactors [78,80]. Despite its broad coverage, there is currently no single LC method that can simultaneously measure polar and nonpolar compounds. Reverse-phase chromatography separates nonpolar compounds such as fatty acids but cannot retain polar compounds, while hydrophilic-interaction chromatography separates polar compounds. Furthermore, LC-MS is prone to ion suppression effects in which high-abundance ions reduce ionization and signal of coeluting ions [75,80]. For most iMFA applications, these drawbacks are minimized by the fact most current metabolites of interests are polar, but this limitation may need to be overcome for iMFA encompassing nonpolar metabolites.

GC-MS enables efficient metabolite separation but requires chemical derivatization to increase volatility for improved detection, which complicates sample preparation. However, GC-MS allows superior detection of low-molecular weight and volatile species, improved metabolite separation, and reduced ion suppression effects [78]. GC-MS instruments are also less expensive to set up and maintain compared to LC-MS instruments, and GC-MS is preferred over LC-MS for compounds such as sterols, sugars, and very-short-chain fatty acids [75,81]. GC-MS is less laborious and requires smaller samples than LC-MS, but LC-MS can detect a larger range of metabolites [78]. Indeed, some compounds cannot be detected via GC-MS, which means that proxy metabolites or closely related intermediates must be used instead. For example, GC-MS cannot directly detect PPP intermediates (e.g., ribulose-5-phosphate) and instead relies on distal components derived from the PPP (e.g., the amino acid histidine, whose carbon backbone is derived from ribulose-5-phosphate). Despite the limited coverage of GC-MS compared to LC-MS, it provides sufficient information on the metabolites typically used in iMFA [81].

NMR requires minimal sample preparation and does not require chromatographic methods to separate metabolites since the spectra provide sufficient structural information for compound identification [76]. NMR can also detect position-specific labeling [79]. For example, NMR has been used to identify labeling in the second and third carbon positions of lactate following incubation with [2-^{13}C] glucose, allowing discrimination of PPP vs. glycolytic flux. This aspect of NMR is especially helpful to determine which atoms in a metabolite are labeled, especially when multiple tracers are used simultaneously [79]. A major disadvantage of NMR is its lack of sensitivity, which means that a larger sample is needed for detection [75–77]. For these reasons, MS is typically better suited for cell culture or animal samples in which metabolite concentrations fall in the micromolar range.

Tandem mass-spectrometry (Tandem MS) is an emerging technique with the benefits of both MS and NMR. Tandem MS uses collision energy to break precursor ions into smaller product ion fragments. This fragmentation allows position specific atom information to be derived from MS data [82]. Tandem MS has increased accuracy when compared to traditional GC-MS and LC-MS and also provides broader coverage by improving detection of low abundance isotopomers [83]. Tandem MS is challenging to use as an iMFA input because the mathematical iMFA framework must be expanded to integrate the fragmented isotopomer information. Algorithms were recently described but are not commonly implemented in existing MFA software [84]. To the best of my knowledge, eiFlux is the only MFA software that allows users to use Tandem MS data [27].

1.5.4.5. Isotope-assisted metabolic flux analysis

One approach to analyze isotope labeling data is to manually assess the MDVs, which provide qualitative insight into differential metabolic activity among experimental groups [22]. The concept is intuitive in simple metabolic systems, as increased metabolic activity will lead to increased metabolite labeling enrichment in the given pathway. However, interpreting MDV labeling patterns can become difficult in real-world metabolic networks due to factors such as natural isotope abundance, compartmentalization, reversible/cyclic reactions, and complex atom rearrangements [20,23]. For example, an isotope-labeled metabolite generates a unique set of isotopomers as it is incorporated into the first, second, and third rounds of the tricarboxylic acid (TCA) cycle. TCA MDV complexity scales with

the number of carbon atoms, since molecules with *n* carbon atoms can have 2^n MDV isotopomers. Thus, large-scale complex metabolic networks are difficult to analyze manually [15,20].

Isotope-assisted metabolic flux analysis (iMFA) is a mathematical technique based on optimization, which determines the metabolic fluxome by fitting metabolic labeling data onto a metabolic reaction network model [164,165]. iMFA was originally developed to engineer microbial strains (metabolic engineering); however, it has more recently been used to analyze a variety of eukaryotic systems. iMFA improves my ability to understand metabolic complexity, and by doing so, can advance metabolomic and fluxomic analysis beyond what is currently possible.

In isotope-assisted metabolic flux analysis (iMFA), cells are incubated with heavy carbon isotope labeled nutrients (e.g., ^{13}C-glucose). The labeled carbons are incorporated into downstream products, creating isotope-labeled forms of each downstream metabolite, which are known as isotopologues. For each metabolite, the relative abundance of every isotopologue is quantified with mass spectrometry or nuclear magnetic resonance. The iMFA model then integrates these data along with extracellular metabolic fluxes into a stoichiometric mathematical model to predict metabolic reaction flux values and confidence intervals for each flux in a given metabolic network [166].

iMFA uses the mathematical relationship between flux and isotopologue labeling patterns to estimate fluxes (Figure 1.5). It starts with an initial guess for all metabolic fluxes in the network and simulates the set of isotopologues that would result from the flux set. Simulated isotopologue labeling patterns are then compared with the experimentally derived isotopes to calculate the residual error. This process is iterated to minimize error [162] between experimental and simulated data. The best-fit fluxes are returned.

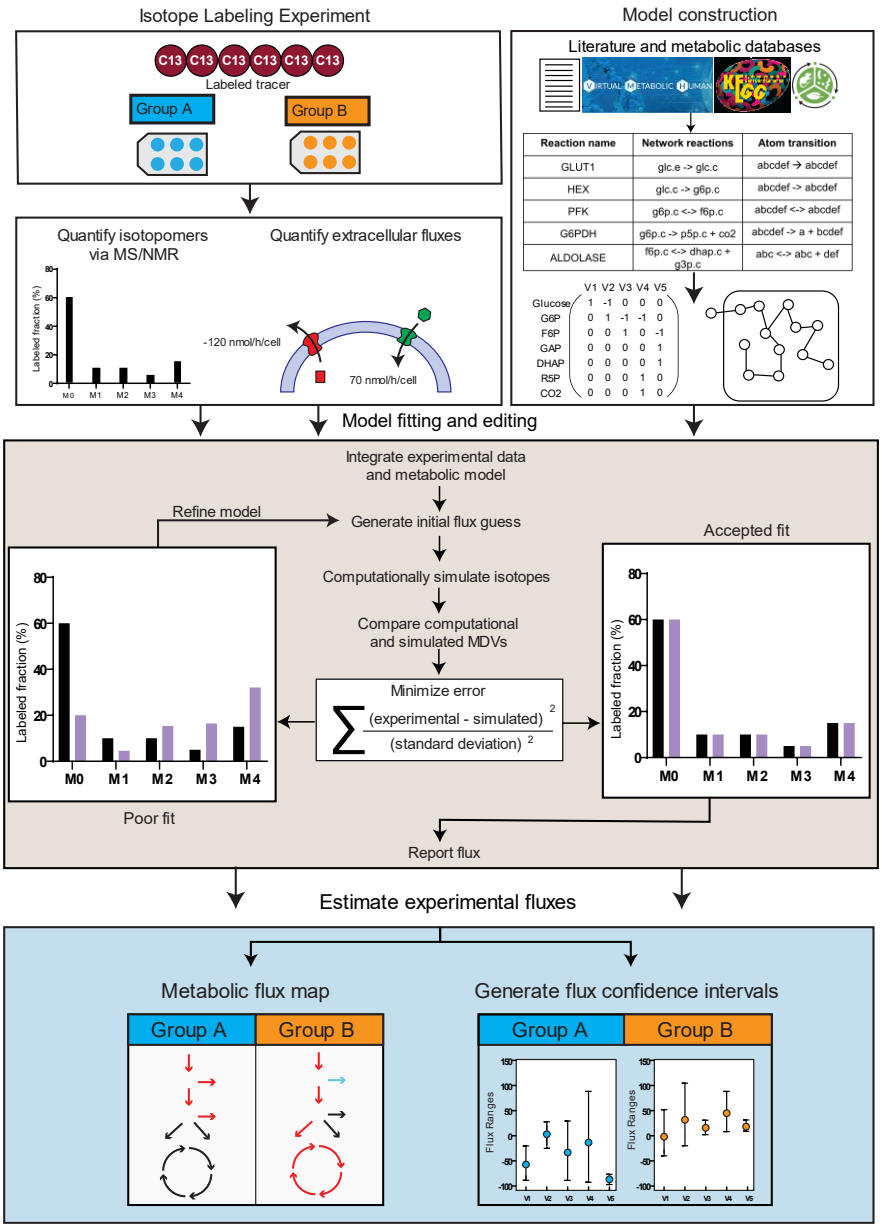

Figure 1.5. Isotope-assisted Metabolic Flux Analysis Workflow. The three major inputs for iMFA are isotope labeling experiment data, extracellular fluxes, and a metabolic model. The model can be constructed using literature and publicly available databases that delineate the metabolic reactions and atom transitions specific to the organism, tissue, or cell of interest. For most software, this network can be input as a table of reactions along with the corresponding stoichiometry and atom transitions. The table gets converted to a mathematical representation within the user-friendly software. Once the experimental data is fitted to the reaction model, the software generates an initial flux estimate and uses this to computationally simulate MDVs. The fit between simulated and experimentally derived MDVs is assessed, and the process iterates by refining the flux values until a satisfactory fit is achieved. The final flux estimates can be used to output a quantitative metabolic flux map and generate confidence intervals for each flux in the network.

iMFA can be divided into three subtypes. Steady-state iMFA is the most computationally simple version and requires that the system is at metabolic steady-state (no net accumulation or consumption of metabolites) as well as isotopic steady state (isotopologue patterns do not change). Instationary isotopic MFA (INST-MFA) is used to predict fluxes in systems that are at metabolic steady state but not isotopic steady state. This allows estimation in systems with large metabolic pools that do not achieve isotopic steady state within reasonable experimental time constraints. Finally, dynamic MFA is a relatively new and computationally intensive method that is being used to predict fluxes in systems that fail to achieve either metabolic or isotopic steady state.

A key advantage of iMFA and qualitative analysis is that it allows quantification of otherwise non-observable intracellular fluxes. Metabolic systems are inherently complex due to the presence of reversible, cyclic, and exchange fluxes, which greatly complicate labeling patterns. Furthermore, while it is typical to assume that increased metabolite labeling indicates increased absolute flux or activity in a metabolic pathway, this approach can be quickly confounded in mammalian cells, which have numerous carbon inputs. For example, the TCA cycle takes in carbons from glycolysis, fatty acids, and amino acids. In a glucose labeling experiment, the relative percentage of glucose-labeled TCA intermediates can decrease due to decreased pyruvate transport, increased influx of unlabeled amino acid derivatives, or both [167,168]. In addition, iMFA can incorporate large datasets and help highlight poor fitting data, which typically occurs either due to measurement errors or erroneous assumptions about the metabolic system.

Currently, there are no published studies of BMEC iMFA models. However, I previously developed an endothelial-specific iMFA model to examine the impact of glycolytic inhibitors on human umbilical vein endothelial cell (HUVEC) metabolism. In this study, I integrated data from glucose isotope labeling experiments with ^{13}C metabolic flux analysis (^{13}C MFA) to determine how targeted inhibition of the polyol (fidarestat), pentose phosphate (DHEA), and hexosamine biosynthetic (azaserine) pathways altered endothelial metabolism. Fidarestat and DHEA-treated HUVEC showed decreased ^{13}C enrichment of glycolytic, TCA metabolites and amino acids. Azaserine-treated HUVEC primarily showed ^{13}C enrichment differences in UDP-GlcNAc but also showed decreased labeling in some TCA cycle intermediates. Decreased labeling of TCA intermediates suggested lower activity in the TCA cycle, however, I also

observed two to three times higher glutamine uptake in fidarestat and azaserine-treated cells. To determine whether decreased labeling was due to lower glucose influx into the TCA cycle, increased influx of unlabeled glutamine and other carbon sources, or a combination of two, I used my model to quantify the exact metabolic changes. ^{13}C MFA estimated decreased pentose phosphate pathway flux and increased TCA activity with reversed malate shuttle direction in fidarestat and DHEA-treated HUVEC. In contrast, ^{13}C MFA estimated increases in both pentose phosphate pathway and TCA activity in azaserine-treated cells. These data show the potential importance of endothelial malate shuttle activity and suggest that inhibiting glycolytic side branch pathways can change the metabolic network, highlighting the need to study systemic effects following enzyme inhibition in endothelial cells [169].

1.6. Structure of Dissertation

The first chapter of this dissertation focused on the relevant background and motivations for this work, specifically detailing Niemann-Pick Disease, brain endothelial cell metabolism, blood-brian barrier physiology, as well as nanogel and drug delivery applications. Chapter 2 discusses the impact of cholesterol depletion and NPC1 inhibition on BMEC barrier integrity and tight junction phenotype. Chapter 3 investigates the metabolic changes that occur in BMECs following NPC1 inhibition and is primarily centered on changes in glucose and mitochondrial metabolism. In Chapter 4, I characterize the transport and uptake of NIPAA-m nanogels in BMECs. Finally, I summarize the key conclusions of my work and discuss future directions in Chapter 5.

.

Chapter 2 - NPC1 inhibition and cholesterol depletion increased BBB small molecule permeability

2.1. Introduction:

The blood-brain barrier (BBB) is critical for healthy neurological function, as it protects the brain from inflammatory and neurotoxic elements found in the blood [1]. The BBB is primarily formed by brain microvascular endothelial cells (BMECs) bound together by tight junction (TJ) proteins, including zonula occludens (ZO), claudin, occludin, and junctional adhesion molecules. Together, these proteins form a complex which seals adjacent cells together and minimizes paracellular gaps. The remaining gaps only permit diffusion of ions and small nonpolar molecules, while larger compounds must instead transverse through selective transcellular transport pathways to enter the brain. BBB breakdown and dysfunction secondary to altered tight junction morphology can therefore allow infiltration of toxic substances and potentially contribute to or even precipitate neurological decline. Notably, BBB dysfunction has been implicated in several neurological pathologies, including Alzheimer's disease, Parkinson's disease, stroke, and multiple sclerosis [2,3].

Our current understanding of BBB dysfunction in rare inherited disorders of cholesterol metabolism such as Niemann-Pick Disease Type C remains limited, despite the plethora of evidence that demonstrates the importance of cholesterol in tight junction function. Cholesterol is a crucial component of mammalian cell membranes, and its presence in the plasma membrane regulates many membrane proteins, including tight junction proteins. For example, cholesterol depletion with methyl-β cyclodextrin (MβCD) significantly increased barrier permeability in the Caco-2 intestinal cell line by displacing claudins from tight junction-associated lipid rafts [4,5]. Knockout of the adherens junction protein α-catenin, which

leads to cholesterol loss from the plasma membrane, as well as direct MβCD treatment led to loss of claudins from cell-cell junctions in mouse epithelial cells. Addition of exogeneous cholesterol reversed this effect [6]. MβCD has also been shown to decrease claudin-5 and increase BBB permeability in rats [7]. Computational analysis also suggests that claudins in the BBB must be palmitoylated to localize to cholesterol-rich lipid rafts [8], highlighting another important link between barrier function and cholesterol.

Together, these studies highlight a need to further examine BBB physiology and function in the context of Niemann-Pick Disease Type C as well as other inherited cholesterol disorders. An improved understanding of BBB changes can potentially inform novel therapeutic and preventative strategies in these diseases. Furthermore, there is a need to examine the effect of cholesterol depletion in human brain cells. The majority of prior studies investigating the effect of cholesterol on tight junctions were conducted in epithelial cells, which differ significantly from BMECs, while those specifically examining brain endothelial cells used computational or murine models.

To address these gaps, I examined the impact of cholesterol depletion and NPC1 inhibition in iPSC-derived BMECS (iPSC-BMECs). Although iPSC-BMECs retain some epithelial characteristics [9], these cells provide an excellent model of barrier function as exemplified by high transendothelial electrical resistance (TEER; 2000-6000 ohms) [10]. Furthermore, iPSC-BMECs are amenable to genetic editing through CRISPR-Cas9, allowing me to generate a disease-specific model. In this work, I used both pharmacological and genetic models of NPC1-deficiency as well the cholesterol depleting agent MβCD to understand how altered cholesterol impacts iPSC-BMEC barrier function. I rigorously examined changes in permeability through tight junction morphology analysis, size-selective permeability tracer assays, and western blot. Overall, this work emphasizes the potential of BBB dysfunction in NP-C and highlights brain endothelial cells as potential therapeutic targets.

2.2. Methods

2.2.1. Cell culture, differentiation, and NPC inhibition

IMR90 induced pluripotent stem cells (iPSCs; WiCell) were differentiated into BMEC-like cells (iPSC-BMECs) using previously established protocols [10,11]. iPSCs were cultured on Matrigel-coated (Corning,

354230) plates in mTeSR-Plus medium (STEMCELL Technologies, 100-0276). Upon reaching ~70% confluence, iPSCs were detached using Accutase (Thermo Fisher, A1110501), centrifuged at 1000 rpm for five minutes, resuspended in mTeSR-Plus medium containing 10 µM Y-27632 (ROCK inhibitor; Tocris, 1254), and then seeded at ~21,000 cells/cm^2 on Matrigel-coated six-well plates. The next day, the medium was changed to E6 (STEMCELL Technologies, 05946) and replaced daily for the next four days. The medium was then changed to either human endothelial serum free media (hESFM; Thermo Fisher, 11111044) or neurobasal medium (Thermo Fisher, 21103049) supplemented with 2% B27 (Thermo Fisher, 17504001), 20 ng/mL basic fibroblast growth factor (bFGF; Peprotech, 100-18B), and 10 µM retinoic acid (RA; Millipore Sigma, R2625-50MG). On day 6, the cells were detached with Accutase and then subcultured onto extracellular matrix (ECM) coated 0.4 µm pore Transwell filters (Corning, 3460), well plates, glass cover slips (confocal microscopy), or #1.5 coverglass black walled 96-well plates (high-throughput imaging). The ECM consisted of 50% pure water, 40% collagen IV (Millipore Sigma, C7521) and 10% fibronectin (Millipore Sigma, F2006).

For experiments, confluent iPSC-BMECs were treated with heSFM supplemented with 2% B27 containing U18666A (Sigma, U3633), an NPC inhibitor that blocks free cholesterol from leaving the late endosome; methyl-β-cyclodextrin (MβCD; Sigma, C4555), which transiently removes cholesterol from the plasma membrane; 2-hydroxypropyl-β-cyclodextrin (HPβCD; Roquette, 128446), which sequesters accumulated cholesterol from the lysosome into other organelles [12], or solvent control.

2.2.2. Cell Viability

Cell viability after U18666A or MβCD treatment was assessed using a Live/Dead assay (ThermoFisher Scientific, L3224) as per manufacturer's instructions. Briefly, cells were incubated with 4 µM ethidium homodimer (EtHd) and 1 µM Calcein-AM in heSFM with 2% B27 for 30 minutes. Methanol-treated cells were used as a positive control for cell death. After washing, media was replaced and cells were imaged using an Echo Revolve microscope with a 20X objective. The number of calcein-positive and Ethd-positive cells were then counted using ImageJ. Specifically, each image was background corrected, thresholded to create a binary image, and then subjected to the watershed tool to separately identify cells in close physical proximity. Each individual cell was then considered a particle and counted using the Analyze Particles tool

in ImageJ. The number of calcein-positive cells was divided by total cell count to get the percentage of live cells.

2.2.3. Cholesterol localization and quantity

Cholesterol localization and quantity were determined via filipin and Amplex Red assays, respectively. For cholesterol localization, cells were fixed with 4% paraformaldehyde for 15 minutes at room temperature, blocked with 5% goat serum containing 0.1 mg/mL filipin (Millipore Sigma, SAE0088-1M), and then incubated overnight with the lysosomal marker 1:100 rabbit anti-LAMP1 (Abcam, ab24170). Each well was then washed with phosphate buffered saline (PBS) 3 times and then stained with a secondary solution containing 0.5 mg/mL filipin, 1:200 anti-rabbit secondary (A-11012), and 1:2000 DRAQ5 (nuclei; 62254). For Perfingolysin-O (PFO) staining, cells were incubated with 2 µg/mL PFO instead of filipin. In both cases, the plate was washed 3 times and then imaged with Nikon Eclipse T2i microscope in widefield mode with a 40X water objective.

For total cholesterol quantity, an Amplex Red Cholesterol Assay Kit (ThermoFisher) was used as per manufacturer protocol. Cells were lysed with 1x Reaction Buffer and homogenized on ice for 10 seconds. Homogenized samples were added to a 96 well plate with Amplex Red working solution and incubated at 37°C for 30 minutes. Fluorescence was read using a Spark Multimode Microplate Reader at 530-590 nM excitation-emission.

2.3.4. Sterol Analysis

For sterol analysis, cells were quenched in ice-cold 80/20 methanol and extracts were shipped to the University of Colorado School of Medicine Metabolomics Core. Sample extracts were randomized and 8 µL was injected onto a Q Exactive MS by a Vanquish UHPLC (ThermoFisher, San Jose, CA, USA). Chromatography was achieved using an ACQUITY UPLC HSS T3 column (150 x 2.1 mm, 1.8 µM, Waters, Milford, MA, USA) over a 17-minute gradient in positive mode, as previously described [13]. Atmospheric pressure chemical ionization was used to introduce eluent to the MS which scanned in full MS mode (1 µscans) over the range of 150-1500 m/z. Technical mixes were injected approximately every ten samples to determine instrument stability [13].

2.3.5. RT-PCR

RNA was isolated from iPSC-BMECs using an RNEasy Mini Kit (Qiagen), quantified on a Nanodrop 2000c (Thermo Fisher), and converted to cDNA using a High-Capacity cDNA Reverse Transcription kit (Thermo Fisher) and a ProFlex Thermal Cycler (ThermoFisher). qPCR was performed using a QuantStudio 7 Flex qPCR System (ThermoFisher), with primers for SREBF2 (Hs01081784_m1), HMGCR (Hs00168352_m1), CLDN5 (Hs00533949_s1). RPLP0, a ribosomal protein, was used as the housekeeper gene (Hs00420895_gH; all from ThermoFisher). RT-PCR data were analyzed using the comparative CT method.

2.3.6. Transendothelial Resistance (TEER) and Permeability Assays

Transendothelial resistance (TEER) was measured in iPSC-BMECs on 0.4 µm pore Transwell inserts in triplicate using STX4-Plus electrodes and the Epithelial Volt/Ohm Meter 3 (EVOM3; World Precision Instruments). Resistance values were corrected by subtracting the resistance of a cell-free Transwell insert. TEER values are reported as Ohms x cm^2, for which the resistance value was multiplied by the Transwell insert area (1.12 cm^2 for 12-well; 0.33 cm^2 for 24-well).

For permeability experiments, iPSC-BMEC media was replaced with fresh heSFM with 2% B27 and either 10 µM sodium fluorescein (Sigma-Aldrich, F6377); 10 µM cadaverine (ThermoFisher Scientific, A30679); 200 µg/mL 4 kDa (Sigma-Aldrich, 46944), 10 kDa (Thermofisher Scientific, D1863), or 70 kDa dextran (Sigma-Aldrich, 53471); or 220 µg/mL Evans Blue (Sigma-Aldrich, E2129). Every 15 minutes, 50 µL of basolateral media was removed, placed in a black bottom 96-well plate, and replaced with 50 µL fresh media. After one hour, 5 µL apical media was collected, placed in a black bottom 96-well plate, and diluted 1:10 with 45 µL heSFM + 2% B27 media. Fluorescence values were then quantified with a Tecan Spark Multimode Plate Reader, using the appropriate excitation and emission settings. Intensity values were corrected for background and signal loss. Apical media fluorescence intensities were multiplied by 10 to account for dilution.

Clearance volume and permeability coefficient values were calculated as previously described [14]. Briefly, the basolateral fluorescence intensity values were corrected for the volume removed at each time

point. Clearance volume (μL) was then calculated by multiplying the corrected fluorescence intensity values by the total basolateral media volume (μL) and normalizing to apical media fluorescence intensity as:

$$Clearance\ volume\ = \frac{Basolateral\ volume * Basolateral\ fluorescence\ intensity}{Apical\ fluorescence\ intensity}$$

The clearance rate C_r, defined as the change in clearance volume over time ($\frac{dC}{dT}$), was normalized to the clearance volume of a cell-free sample and used to calculate the inverse permeability coefficient ($\frac{1}{P_{coeff}}$) as:

$$Inverse\ permeability\ \left(\frac{1}{P_{coeff}}\right) = \frac{1}{C_{r,sample}} - \frac{1}{C_{r,cell-free}}$$

The permeability coefficient was then normalized to the Transwell insert area.

2.3.7. Cell-cell junction visualization and quantification

To visualize tight junctions, iPSC-BMECs were fixed in either ice-cold methanol or 4% paraformaldehyde, depending on manufacturer's recommendations (Table 2), for 20 minutes and then blocked immediately with 5% donkey serum (Sigma Aldrich, S30-100mL) in PBS (ThermoFisher, 70011069) for one hour. For paraformaldehyde-fixed cells, the blocking solution was supplemented with 0.2% Triton X-100 (Alfa Aesar, A16046) to permeabilize cells. Cells were then incubated with primary antibodies (Table 2) overnight at 4°C. After thorough washing, cells were labeled with the appropriate secondary antibodies (Table 2) as well as DAPI (nuclei; ThermoFisher, 62248) for one hour at room temperature. Samples were imaged on a Nikon 2Ti Eclipse microscope with a 20X (for perimeter analysis) or 60X oil (for tight junction morphology analysis) objective in confocal mode.

Perimeter analysis was performed on the NIS-Elements software. First, a maximum intensity projection of each image was created using both rolling pixel and subtract constant background correction function modules. Each image was then thresholded to select only tight junctions by minimizing fluorescence that was not localized to the cell border using the "Tight Borders" segmentation tool. The NIS elements total perimeter function module was used to calculate total tight junction perimeter for each image. This was then divided by the total nuclei count to get the total perimeter per image.

Tight junctions were analyzed using the Junction Analyzer Program (JAnaP; https://github.com/StrokaLab/JAnaP) [15]. Briefly, I delineated the perimeters of randomly selected cells by

first defining points on the cell edges (waypoints). JAnaP then connected the waypoints by creating a path between them that followed the maximum fluorescence intensity. The paths were then automatically stitched together to create the full cell perimeter. Each pixel along the cell perimeter was then characterized as having a junction or no junction based on an intensity threshold (set at 15 across all data). Each junction was then categorized as continuous or discontinuous based on the path length adjacent to the junction. In my case, a continuous junction was defined as longer than 15 pixels (1.335 µM for an image in which 1 pixel = 0.089 µM). At least 5 cells were randomly selected and traced per image to collect a minimum of 90 cells per group from each independent experiment.

Continuity at multicellular junctions was quantified manually by a blinded observer. A multicellular junction was defined as a junction formed with three or more cells. Each multicellular junction was categorized as continuous (defined as having no holes or gaps in the junction), discontinuous (defined as having holes or gaps in the junction), or unknown (if a clear classification could not be made). Multicellular continuity percentage was calculated as the number of total continuous multicellular junctions divided by the total number of multicellular junctions.

2.3.8. Western Blot

To analyze intracellular proteins, cells were lysed in RIPA buffer (ThermoFisher Scientific, 89901) supplemented with Halt Protease and Phosphatase Inhibitor (ThermoFisher Scientific, PI78440). Protein concentration was quantified via BCA assay (ThermoFisher Scientific, 23225). Normalized protein samples, sample buffer (ThermoFisher Scientific, NP0008) and reducing agent (ThermoFisher Scientific, NP0009) were combined, boiled at 70°C for 5 minutes, and then separated using 4-12% Bis-Tris gels (ThermoFisher Scientific, NP0323). Proteins were transferred to PVDF (ThermoFisher Scientific, IB24001) or nitrocellulose membranes (ThermoFisher Scientific, IB23001) using an iBlot2 (ThermoFisher Scientific, IBL21001). Membranes were then blocked for 1 hour in 5% bovine serum albumin in PBS containing 0.5% Tween 20 (ThermoFisher Scientific, 85113) to reduce non-specific binding. Membranes were incubated in primary antibodies overnight (Table 2), followed by 2 hours in the respective horseradish peroxidase conjugated-secondary antibody (Table 2). Protein bands were imaged using an Alpha Innotech Fluorchem Imager (Protein Simple). Band intensities were analyzed using AlphaView software.

Table 2.1:

Target	Company, Product #	Immunofluorescence: Membrane, dilution, secondary	Western blot: Membrane, dilution, secondary
Claudin5	ThermoFisher Scientific, 4C3C2	Methanol, 1:50 Donkey-anti Mouse 488 (Thermo Fisher, A-21202)	PVDF, 1:1000 Anti-Mouse (Promega, W4021)
ZO1	Cell Signaling, 13663S	Methanol, 1:50 Donkey-Anti Rabbit 488 (Thermo Fisher, A-21206)	Nitrocellulose, 1:500 Anti-Rabbit IgG (Promega, W4011)
Occludin	Cell Signaling, 13663S	Methanol, 1:50 Donkey-Anti Rabbit 488 (Thermo Fisher, A-21206)	PVDF, 1:1000 Anti-Rabbit IgG (Promega, W4011)
Occludin	Thermo Fisher, 33-1500	Methanol, 1:50 Donkey-Anti Mouse 594 (Thermo Fisher, A-21203)	N/A
VE-Cadherin	R&D Systems, AF938	N/A	PVDF, 1:1000 Anti-Goat IgG (ThermoFisher Scientific R-21459)
p-VE Cadherin	Sigma Aldrich, ABT1760	N/A	PVDF, 1:1000 (Promega, W4021)
LAMP1	Abcam, ab24170	Paraformaldehyde, 1:200 Donkey anti-Rabbit (Thermo Fisher, A-21207)	PVDF, 1:1000 Anti-Rabbit IgG (Promega, W4011)
NPC1	Novus Biologicals, NB400-148	N/A	PVDF 1:1000 Anti-Rabbit IgG (Promega, W4011)

2.3.9. CRISPR-Cas9 NPC1 knock out

To generate NPC1 knockout (NPC-KO) iPSCs, I targeted exon 6 of the NPC1 gene using a guide sequence strand ACGCCAUGUAUGUCAUCAUG (Synthego), as described previously [16]. I first confirmed presence of the target in IMR90 iPSCs by isolating iPSC DNA using the Quick-DNA Miniprep Plus kit (Zymo) as per manufacturer's instructions. I then quantified DNA content with a Nanodrop 2000c and amplified a 531-base pair region containing the target sequence with custom primers (ThermoFisher Scientific, Table 1) using the Amplitaq Gold 360 Master Mix kit. Bands were examined via gel electrophoresis to confirm presence of the target sequence.

Table 2.2 : Primer Sequences for Guide Strands

Primer	Sequence
Forward	5'-CCCTACGCGCAAGTTTATTG-3'
Reverse	5'-CATGCAATGGTATTCATGGAG-3'

NPC1 knockout in IMR90 iPSCs was performed with the Neon Transfection system (ThermoFisher Scientific). iPSCs were detached with Accutase and resuspended in 100 µL R buffer at 1.35 x 10^6 cells/mL with 30 µM guide strand and Cas9 reagent. Cells were then electroporated for two pulses at 1100 V, 30 millisecond pulse width. Transfected cells were then pipetted onto Matrigel coated plates in MTESR-plus media with 10 µM Y-27632 and cultured until 70% confluent.

iPSCs were then dissociated into a single cell suspension with Accutase and seeded sparsely onto a six well plate. Single colonies were picked off with a sterile pipette, transferred into 24-well plates, and cultured until confluent. Each clonal colony was then split into three wells for cryogenic preservation in Cryostore freezing media (StemCell), DNA analysis by Sanger sequencing (GeneWiz), protein validation by Western blot. Sanger sequencing (scored with ICE software) and Western blot were used to confirm knockouts, and phenotypic validation was performed with a filipin immunofluorescence assay. The knockout line used for this study had a 100% knockout score by Sanger sequencing, did not show an NPC1 band on Western blot, and colocalized filipin with lysotracker by immunofluorescence. The transfected wild-

type control had a 6% knockout score, showed an NPC1 band on Western blot, and localized most filipin to the cell membrane.

2.3.10. Statistical Analysis

Statistics were analyzed in GraphPad Prism. Non-parametric Mann-Whitney tests were used to compare two unpaired datasets, except for JAnaP data, which was analyzed with a Kolmogorov-Smirnov test. One-way Kruskal-Willis non-parametric test was used to compare multiple groups, followed by *post hoc* Dunn's multiple comparison test. Data were considered statistically significant if $p < 0.05$.

2.4. Results:

2.4.1. U18666A treatment depleted membrane cholesterol and induced an NPC1-like phenotype in iPSC-BMECs

To determine if U18666A could induce an NPC1-like phenotype in iPSC-BMECs, I treated iPSC-BMECS with 0, 1, 5, or 10 μM U18666A for 48 hours and examined cholesterol distribution with filipin. Cholesterol distribution changed from broadly distributed across the entire cell membrane in untreated samples to a punctate, perinuclear localization in treated samples (representative images in Figure 2.1A). The U18666A effect increased with treatment concentration. I confirmed that cholesterol was depleted in U18666A-treated iPSC-BMECs via Amplex Red. Cells treated with 10 μM U18666A had ~25% less cholesterol ($p = 0.0059$) than untreated cells (Figure 2.1B).

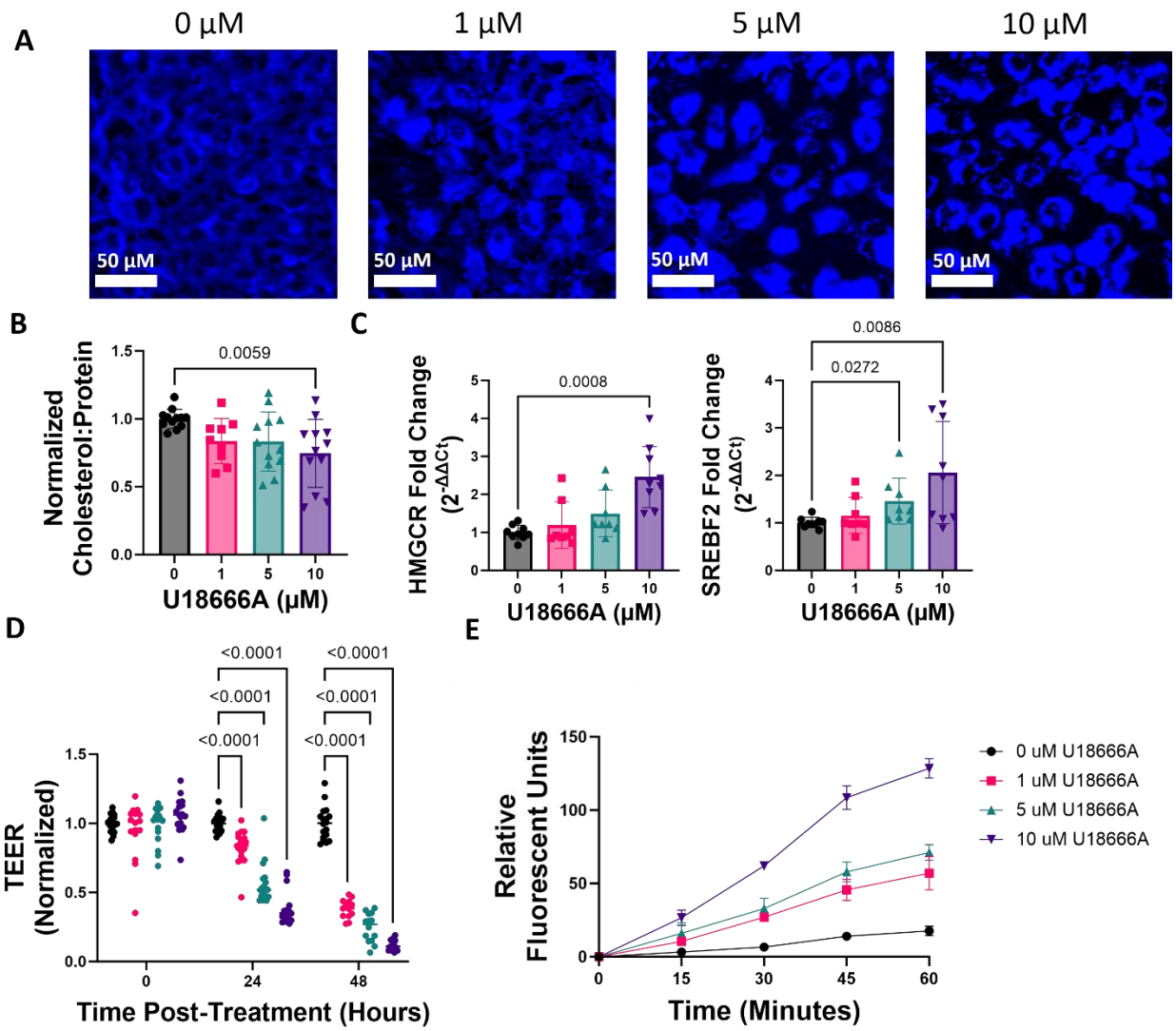

Figure 2.1. U18666A inhibition of NPC1 altered iPSC-BMEC cholesterol distribution and barrier integrity. (A) Representative fluorescent microscopy images of iPSC-BMECs treated with 0, 1, 5, and 10 µM U18666A for 48 hours and stained with filipin (blue) to visualize cholesterol localization. Representative images from three independent experiments (B) Cholesterol content from U18666A-treated iPSC-BMECs analyzed with Amplex Red. (C) *HMGCR* and *SREBF2* expression after 48 hours of U18666A treatment, analyzed by RT-PCR. All fold changes normalized to untreated control. n = 8-9 from 3 independent experiments. (D) Transendothelial electrical resistance (TEER) and (E) representative sodium fluorescein permeability of iPSC-BMECs treated with U18666A for 48 hours. For TEER, n = 13-21 from 6 independent experiments. Kruskal-Willis non-parametric test with Dunn's multiple comparison test was used to determine significance for figures 1B-1C. 2-way ANOVA parametric test with Šídák's multiple comparisons test was used to determine significance for 1D. Data shown are mean +/- SD.

NPC1 deficient cells have been shown to upregulate cholesterol biosynthetic genes such as the rate limiting enzyme of cholesterol synthesis, HMG-CoA reductase (HMGCR), as well as the key cholesterol

synthesis regulator, sterol element binding protein (SREBP2) [17,18] To further validate that U18666A induced an NPC1-like phenotype, I quantified HMGCR and SREBP2 expression in untreated and U18666A treated iPSC-BMECs. I observed increased HMGCR (2.46-fold, p = 0.0008) and SREBP2 (2.06 fold, p = 0.0086) expression with 10 µM U18666A, which corroborated an NPC1-like phenotype (Figure 2.1C). I further confirmed that the higher U18666A concentrations did not cause cell death (via Live/Dead assay; Figures 2.2A, 2.2B; phase contrast; Figure 2.2C).

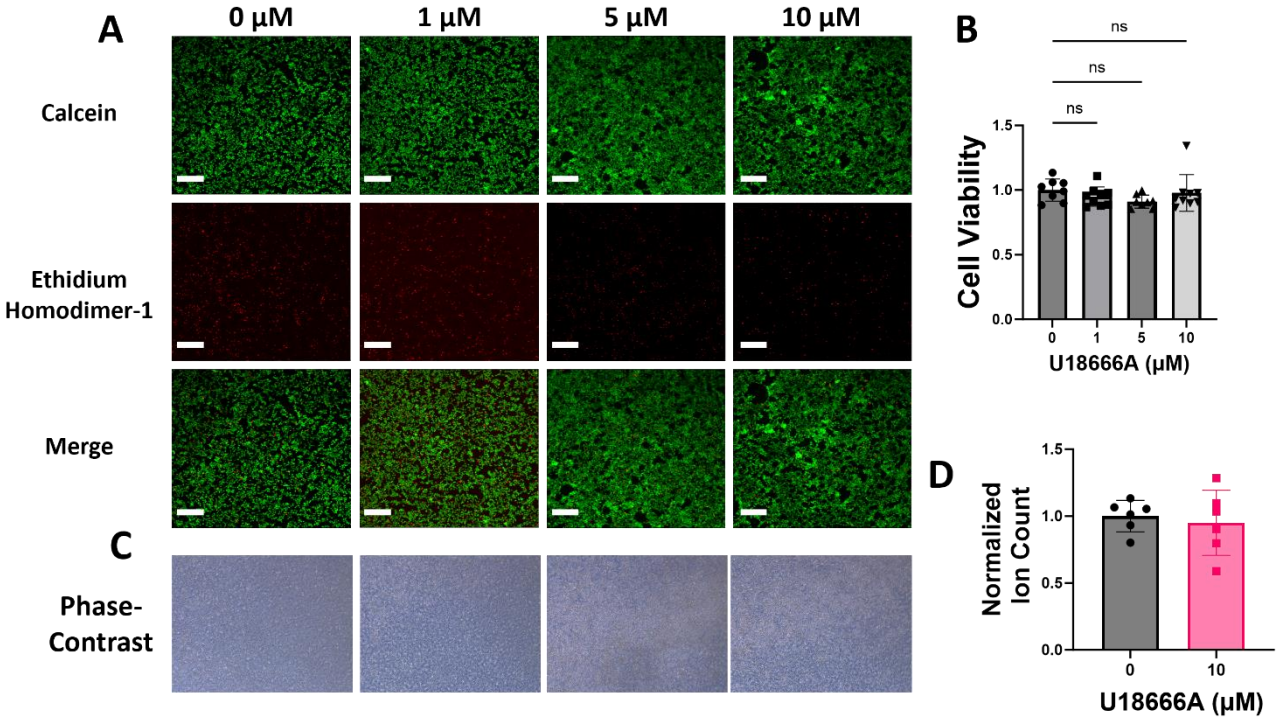

Figure 2.2. U18666A did not decrease iPSC-BMEC viability or inhibit cholesterol synthesis. (A) Representative images and (B) quantification of a Live/Dead assay on iPSC-BMEC treated with 0, 1, 5, or 10 µM U18666A for 24 hours. Calcein (green) indicates live cells, with ethidium homodimer-1 (red) indicates dead cells. Statistical significance determined with Kruskal-Willis non-parametric test followed by *post-hoc* Dunn's multiple comparison test. N = 9 from 3 independent experiments (C) Phase contrast imaging of iPSC-BMEC monolayer on transwells after 48 hours of treatment. (D) Ion count of desmosterol (n=6). Analyzed with Mann-Whitney test for statistical significance.

High U18666A concentration can inhibit 3β-hydroxysterol Δ-24-reductase (DHCR24) and lead to increased cholesterol biosynthesis; however, I did not observe an increase in levels of desmosterol, a

cholesterol synthesis intermediate, via mass spectrometry (Figures 2.2D) [19].These data show that iPSC-BMECs treated with 10 μM U18666A demonstrate an NPC-1 like phenotype.

2.4.2. NPC1 inhibition impaired iPSC-BMEC barrier integrity

We then assessed the impact of U18666A on iPSC-BMEC barrier integrity. TEER decreased with increasing U18666A (Figure 2.1D). With 10 μM U18666A, TEER decreased by 62% at 24 hours ($p < 0.0001$) and 88% at 48 hours ($p < 0.0001$). Statistically significant decreases were also observed with 1 μM and 5 μM U18666A; however, the magnitude of change was lower (62% and 75%, respectively, at 48 hours).

U18666A also increased iPSC-BMEC permeability to sodium fluorescein, a small molecule tracer (MW ~ 376 Da) often used in permeability studies (Figure 2.1E). As with TEER, 10 μM U18666A induced the largest effect on iPSC-BMEC permeability to sodium fluorescein. At this concentration, the basolateral fluorescent signal was more than 7 times higher in the 10 μM U18666A-treated iPSC-BMECs compared to untreated cells. 5 μM and 1 μM U18666A treatment increased basolateral fluorescence by 4 times and 3.2 times, respectively.

To confirm that U18666A reduced iPSC-BMEC barrier integrity via altered membrane cholesterol, I treated cells with 3 mM MβCD, which transiently depleted cholesterol from the cell membrane without compromising cell viability (Figure 2.3A-D, F). MβCD decreased iPSC-BMEC TEER by 87% within 3 hours of treatment (Figure 2.3E).

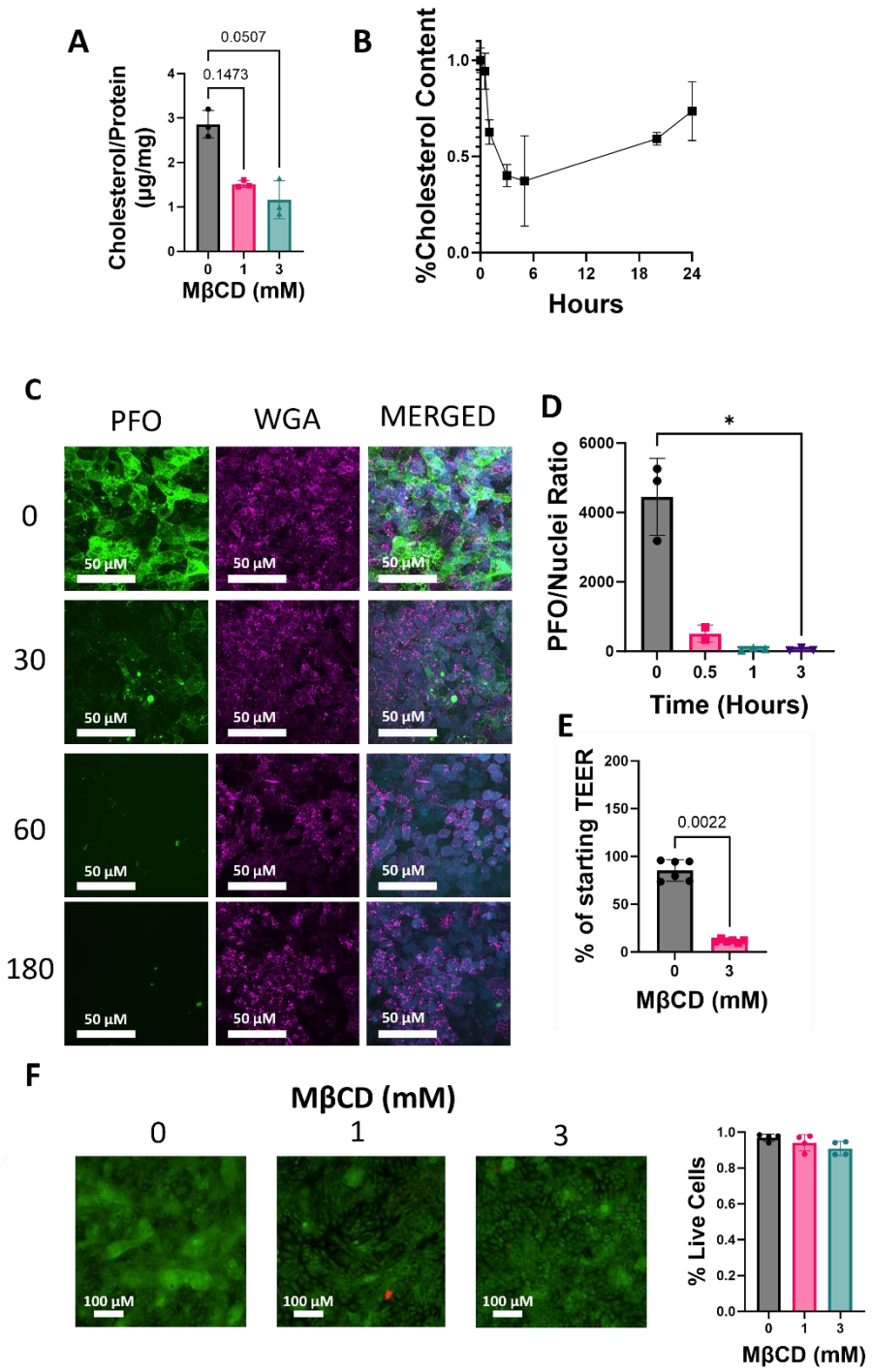

Figure 2.3. MβCD transiently depleted iPSC-BMECs membrane cholesterol and reduced TEER. Cholesterol levels were measured by an Amplex red cholesterol assay at (A) 3 hours and (B) 0 to 24 hours (Relative to starting concentration). (C) Representative images and (D) quantification of iPSC-BMECs treated with 3 mM MβCD for 3 hours and then labeled with PFO-GFP4 (green) and WGA (purple) to visualize membrane cholesterol. (E) TEER of iPSC-BMECs treated with 0 or 3 mM MβCD for 3 hours. (F) Representative images and quantification of a Live/Dead assay for iPSCs treated with 1 or 3 mM MβCD for 3 hours. Calcein (green) indicates live cells, with Ethidium (red) indicates dead cells.

2.4.3. iPSC-BMEC cholesterol depletion increased permeability to small molecules

To determine if the observed reductions in barrier function with U18666A and MβCD were size-selective, I performed permeability assays with different sized molecular weight tracers. The sodium fluorescein permeability coefficient was approximately 9-fold higher in U18666A-treated ($p < 0.0001$) and nearly 20-fold higher in MβCD-treated ($p < 0.0001$) iPSC-BMECs than untreated cells (Figure 2.4A).

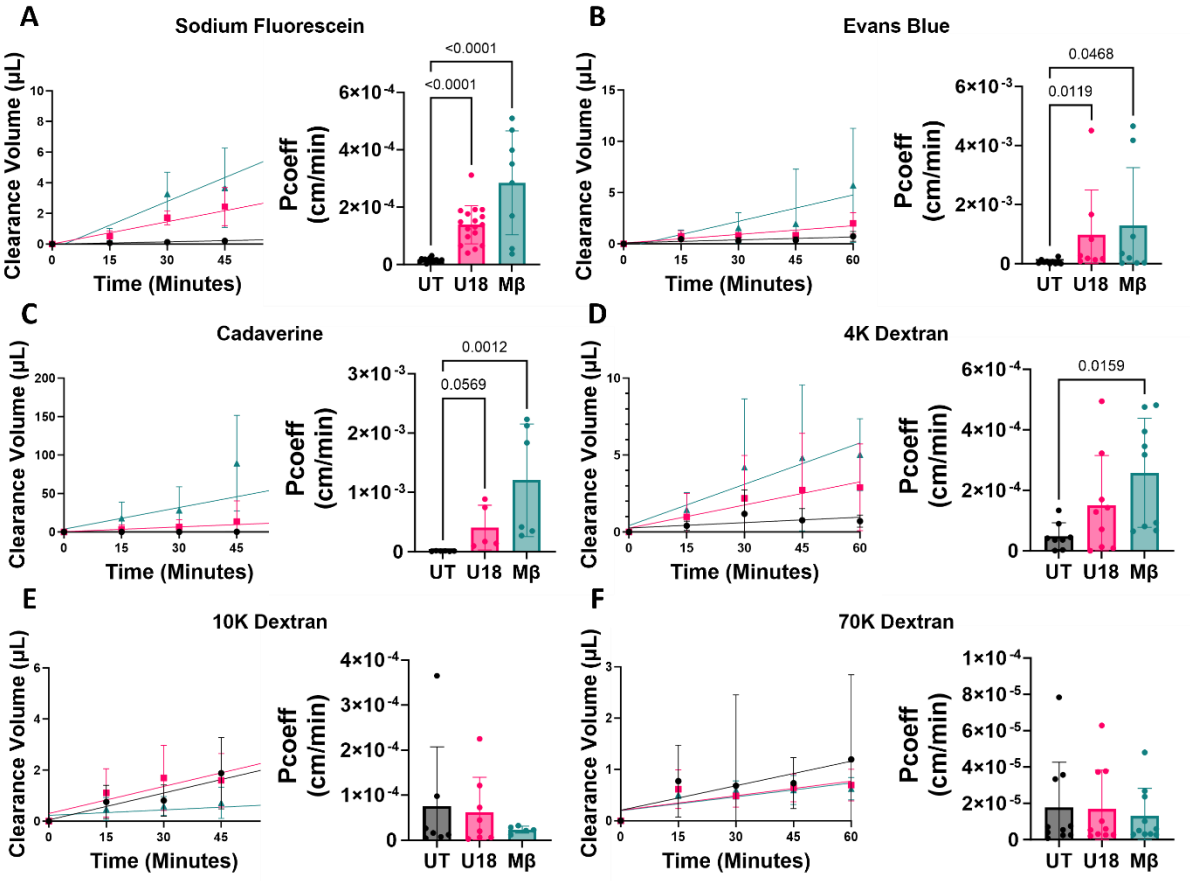

Figure 2.4. NPC1 inhibition increased iPSC-BMEC permeability to small molecules (< 10 kDa) only. iPSC-BMECs were treated with U18666A (U18), MβCD (Mβ), or solvent control (UT). Clearance volume vs. time and permeability coefficients for (A) sodium fluorescein (MW = 376.7, n = 8-18 from 4 independent experiments), (B) Evans Blue (MW = 960.8, n=8-10 from 3 independent experiments), (C) cadaverine (1 kDa, n=5-6 from 2 independent experiments) (D) 4 kDa dextran (n = 8-9, from 3 independent experiments) (E) 10 kDa dextran (n = 5-8 from 3 independent experiments) , and (F) 70 kDa dextran (n = 10 from 3 independent experiments). Statistical significance determined with Kruskal-Willis non-parametric test. Data shown are mean +/- SD

Similarly, the Evans Blue (MW ~ 960 Da) permeability coefficient was 150 times higher in U18666A-treated ($p = 0.0119$) and almost 200 times higher in MβCD-treated ($p = 0.0468$) iPSC-BMECs, while the cadaverine (MW ~ 1000 Da) permeability coefficient was 39 times higher ($p = 0.0569$) in U18666A-

treated and 115 times higher ($p = 0.0012$) in MβCD-treated iPSC-BMECs as compared to untreated cells (Figures 2.4C, 2.4D). However, I observed different effects with larger molecular weight molecules. The permeability coefficient for 4 kDa dextran trended higher in U18666A-treated cells and was only ~5 times higher in MβCD-treated iPSC-BMEC ($p = 0.0159$). There were no significant differences in the permeability coefficients for 10 kDa or 70 kDa dextran with either U18666A or MβCD (Figures 2.4E, F).

2.4.4. iPSC-BMEC cholesterol depletion altered tight junction morphology and continuity

Cholesterol depletion has been shown to delocalize tight junction proteins from the membrane [4,5]. I therefore evaluated the morphology and continuity of tight junction proteins zonula occludens 1 (ZO-1), occludin, and claudin-5 by immunofluorescence. ZO-1, which links the actin cytoskeleton to other tight junction proteins, did not appear to change with either U18666A or MβCD treatment. Both qualitative and quantitative analysis of occludin and claudin-5 showed morphological differences. Occludin continuity decreased ~13% in U18666A-treated cells ($p < 0.0001$) and ~9% in MβCD-treated ($p < 0.0001$). Upon qualitative analysis, I observed a higher frequency of cells that demonstrated a “ruffling” phenotype, where tight junctions appeared to be perpendicular to the cell border (Figure 2.5A). Finally, I observed morphological differences in claudin-5, a key tight junction protein that regulates small molecule permeability [20,21]. Claudin-5 continuity decreased approximately 8% ($p < 0.0001$) in U18666A-treated cells and approximately 11% ($p<0.0001$) MβCD-treated cells. I did not observe any morphological changes in adherens junctions proteins.

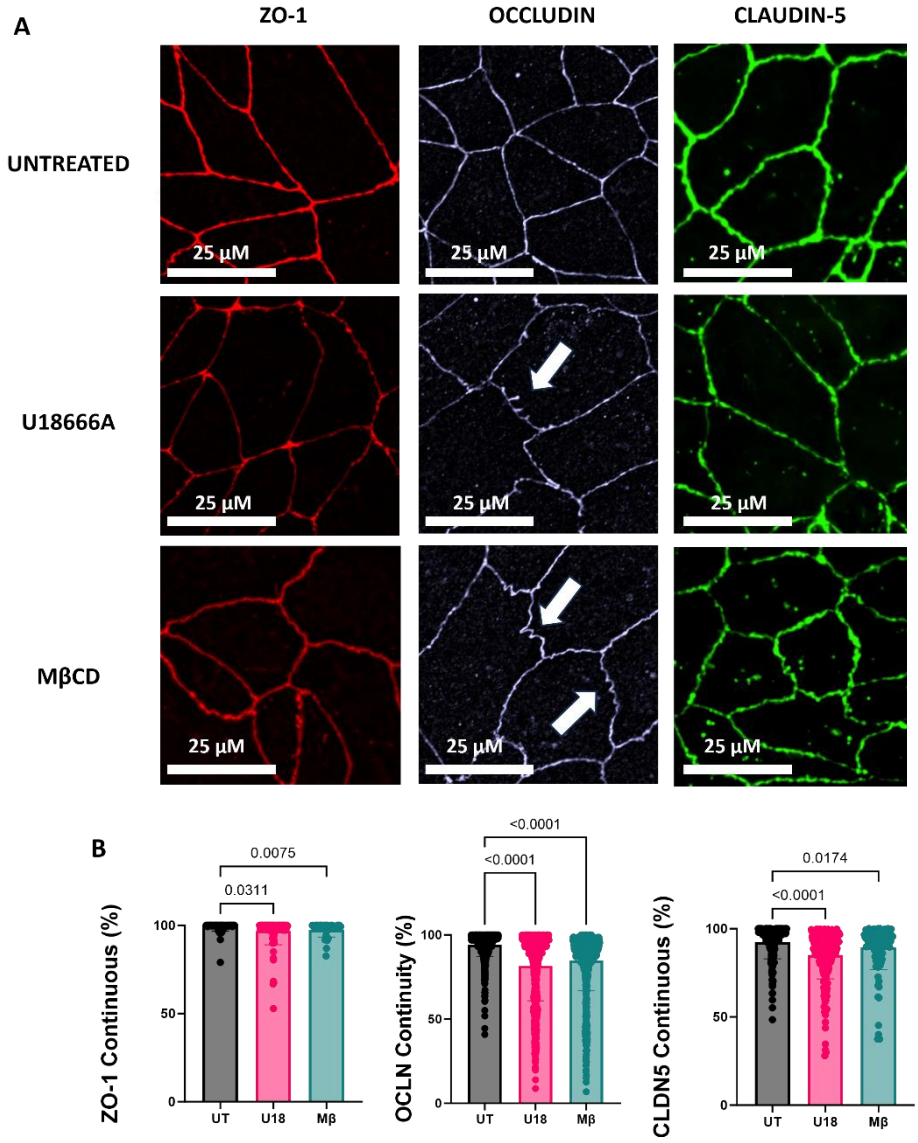

Figure 2.5. Cholesterol depletion primarily altered claudin-5 and occludin morphology with limited effect on ZO-1. iPSC-BMECs were treated with U18666A (U18), MβCD (Mβ), or solvent control (UT). (A) Representative images of ZO-1, occludin, and claudin-5. White arrows indicate perpendicular junctions (B) Percent of continuous tight junctions for ZO-1 (N = 39-98 cells), occludin (OCLN, 726-827 cells) and claudin-5 (CLDN, N=196-297 cells) as quantified by Junction Analyzer Program (JaNAP). Data from three independent experiments. Significance determined with Kruskal-Willis non-parametric test. Data shown are mean +/- SD. Scale bar = 25 µM.

2.4.5. Restoring membrane cholesterol with hydroxypropyl β cyclodextrin (HPβCD) reestablished barrier integrity

Hydroxypropyl *β* cyclodextrin (HPβCD) has been shown to reverse cholesterol accumulation, prolong animal life span, and slow human disease progression in NPC1 [12,22–24]. I therefore examined whether HPβCD could restore barrier function and tight junction protein morphology in NPC1-inhibited iPSC-BMECs. I first measured how HPβCD affected cholesterol distribution and cholesterol-related gene expression in U18666A-treated iPSC-BMECs. 1000 µM HPβCD restored membrane cholesterol

distribution (as measured via filipin, Figure 2.6A) and decreased HMGCR expression but did not significantly decrease SREBP2 expression (Figure 2.6B).

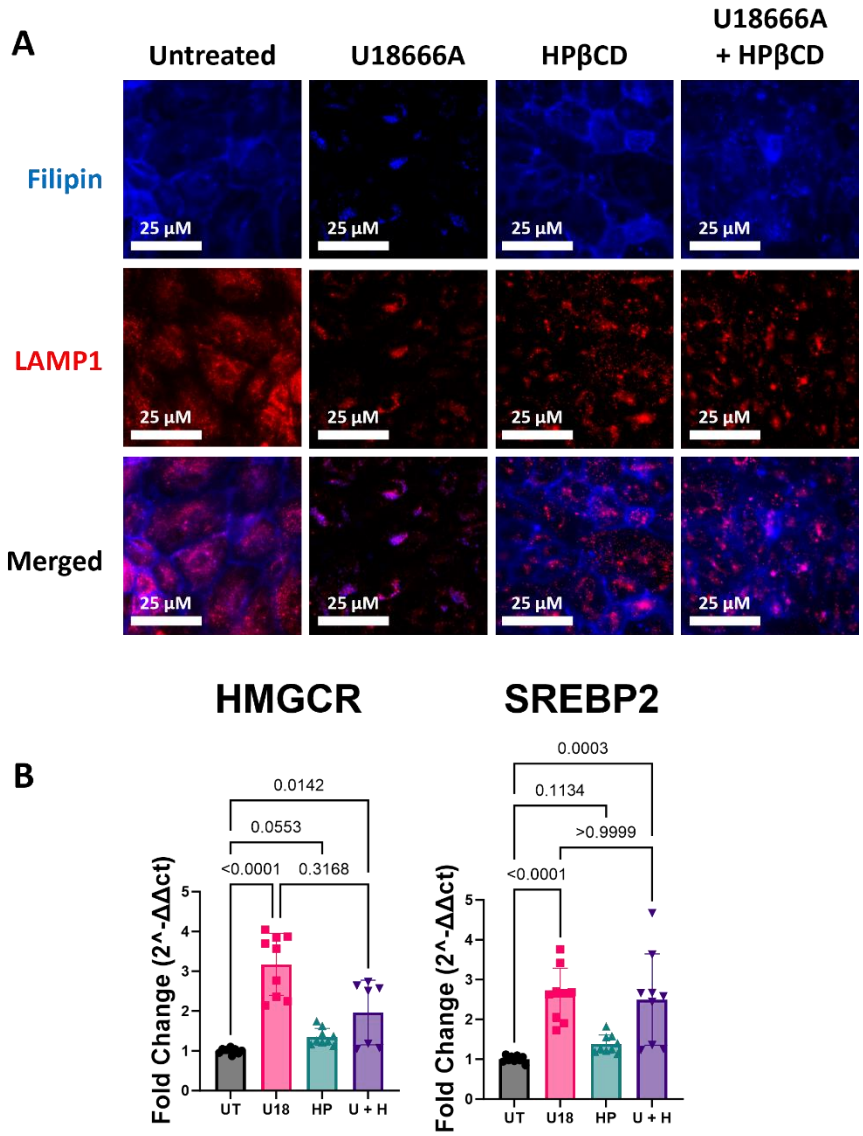

Figure 2.6. HPβCD restored cholesterol distribution in U18666A-treated iPSC-BMECs. (A) *HMGCR* and *SREBF2* expression after 48 hours of U18666A treatment with increasing concentrations of HPβCD, analyzed by RT-PCR. All fold changes normalized to untreated control. n =8-9 from three independent experiments. (B) Representative fluorescence images of filipin (cholesterol, blue) and LAMP1 (lysosomal marker, red) in iPSC-BMECS treated with U18666A and/or HPβCD.

I then examined how HPβCD impacted barrier function and claudin-5 distribution in U18666A-treated iPSC-BMECs. TEER and sodium fluorescein assays showed complete restoration of barrier function when U18666A-treated iPSC-BMECs were co-treated with HPβCD (Figure 2.7A, B). Claudin-5 perimeter

per cell was also restored with HPβCD (quantification in Figure 2.7C, representative images in Figure 2.7D).

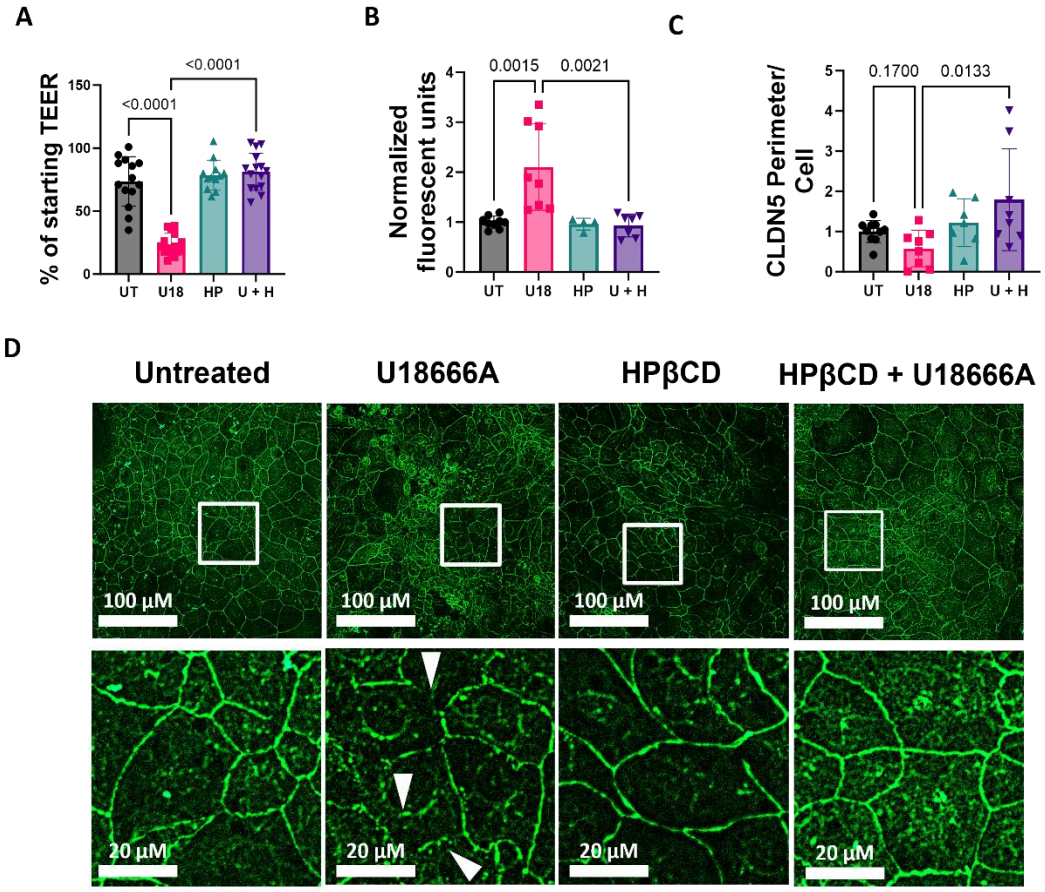

Figure 2.7. Barrier function and claudin-5 morphology were restored in U18666A-treated iPSC-BMEC with HPβCD. (A) TEER values (n = 11-17 from 4 independent experiments) and (B) sodium fluorescein signal (n-4-9 from 2 independent experiments) at the end of each permeability experiment for iPSC-BMEC treated with U18666A and HPβCD for 48 hours. (C) Quantification of claudin-5 border perimeter (n=7-10, from 3 independent experiments) and (D) representative claudin-5 (green) fluorescence microscopy images. White boxes indicate regions of interest highlighted in zoomed in images. White pointers highlight areas of complete CLDN5 disruption. Significance between multiple groups determined with Kruskal-Willis non-parametric test followed by *post-hoc* Dunn's multiple comparison test. Data shown are mean +/- SD.

2.4.6. U18666A reduced iPSC BMEC claudin-5 protein, and HPβCD restored claudin-5

To determine if changes in barrier integrity and tight junction morphology were due to changes in tight junction protein levels, I treated iPSC-BMEC with U18666A with and without HPβCD and examined tight junction proteins via Western blot. U18666A did not change ZO-1 or occludin protein levels (Figure 2.8A-

B). However, U18666A decreased iPSC-BMEC claudin-5 by more than 50% (p = 0.0235; Figure 2.8C). HPβCD nearly restored claudin-5 to baseline levels. VE-cadherin, an important adherens junction protein, increases vascular permeability when it is phosphorylated [25,26], I examined both total and phosphorylated VE-cadherin by Western blot. U18666A-treated iPSC-BMECs slightly increased both total and phosphorylated VE-cadherin, although the change was not statistically significant (Figure 2.8D, E). In addition, the ratio of phosphorylated:total VE-cadherin was unchanged with U18666A (Figure 2.8F). These data suggest that U18666A specifically affects claudin-5 via decreased protein levels but not other tight junction or adherens junction proteins. *CLDN5* mRNA levels did not decrease or change significantly from untreated cells (Figure 2.9), which may suggest that the change in protein may be due to increased degradation rather than decreased expression.

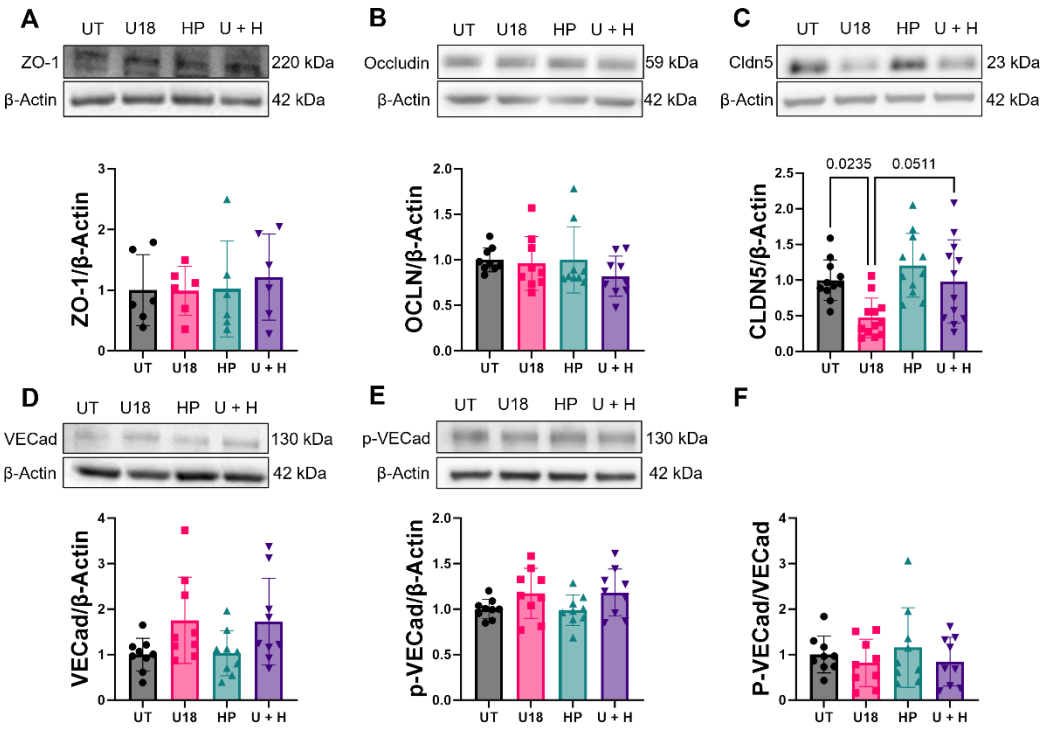

Figure 2.8. U18666A inhibition significantly reduced claudin-5, and HPβCD restored claudin-5 back to baseline. Representative and quantified western blots of iPSC-BMEC lysates treated with either 10 μM U18666A (U18), 1000 μM HPβCD (HP), both (U + H) or left untreated (UT) for 48 hours for (A) ZO-1 (n=6, from two independent experiments) (B) Occludin (n=9, 3 independent experiments) (C) claudin-5 (n=12, 4 independent experiments), (D) VE-cadherin (n=9, 3 independent experiments) (E) phosphorylated VE-cadherin (n=9, 3 independent experiments) and ratio of phosphorylated VE-cadherin to total VE-cadherin (F). Significance determined with Kruskal-Willis non-parametric test. Data shown are mean +/- SD.

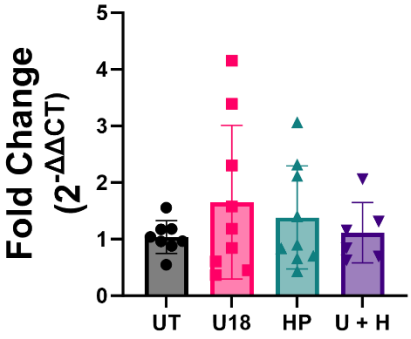

Figure 2.9. CLDN5 mRNA levels did not change with U18666A treatment. (A) iPSC-BMECs were treated with either solvent control (UT), U18666A (U18), HPβCD (HP), or U18666A and HPβCD (U+H) for 48 hours and lysed for qPCR. CLDN5 expression was normalized to the housekeeping gene RLPL0 using the comparative CT method. N = 6-9 from 3 independent experiments. Kruskal-Willis non-parametric test with Dunn's multiple comparison test was used to determine significance. Data shown are mean +/- SD.

2.4.7. NPC1 KO iPSC-BMECs also had impaired barrier integrity

Finally, I confirmed the impact of NPC1 inhibition on iPSC-BMEC barrier function using NPC1-KO iPSCs that I then differentiated into iPSC-BMECs (NPC-KO). I first validated the knockout by showing that the cells had essentially no NPC1 protein by Western blot (Figure 2.10A). NPC-KO cells also exhibited lysosomal cholesterol accumulation, as shown by filipin localization (Figure 2.10B). I then examined barrier changes in the NPC-KO iPSC-BMECs. TEER in the NPC-KO cells was approximately half the TEER of wild type cells ($p < 0.0001$, Figure 2.10C). In permeability experiments, I observed approximately 1.5-fold higher sodium fluorescein permeability coefficient ($p = 0.0559$; Figure 2.10D), which was lower than the change observed in the U18666A-treated iPSC-BMECs. While most cell edges appeared to be continuous for ZO-1, further investigation unveiled that discontinuities occurred at multicellular junctions. NPC-KO iPSC-BMEC had a ~6.5% decrease in ZO-1 continuity ($p = 0.0038$, Figure 2.11A, 2.11B). Occludin continuity also was ~9% lower in NPC-KO cells, which was similar to the change observed in U18666A-treated cells (Figure 2.11C, 2.11D). Together, these data show that NPC1 knockout also impaired iPSC-BMEC barrier integrity.

Finally, I treated NPC-KO BMECs with HPβCD to determine if this would restore cholesterol distribution and barrier function. HPβCD treatment for 48 hours partially reduced lysosomal cholesterol accumulation in NPC-KO cells (Figure 2.12). HPβCD also increased TEER in NPC-KO cells, similar to what was observed in U18666A-treated iPSC-BMEC. Thus, HPβCD may improve barrier integrity of NPC1 KO cells (Figure 2.10E).

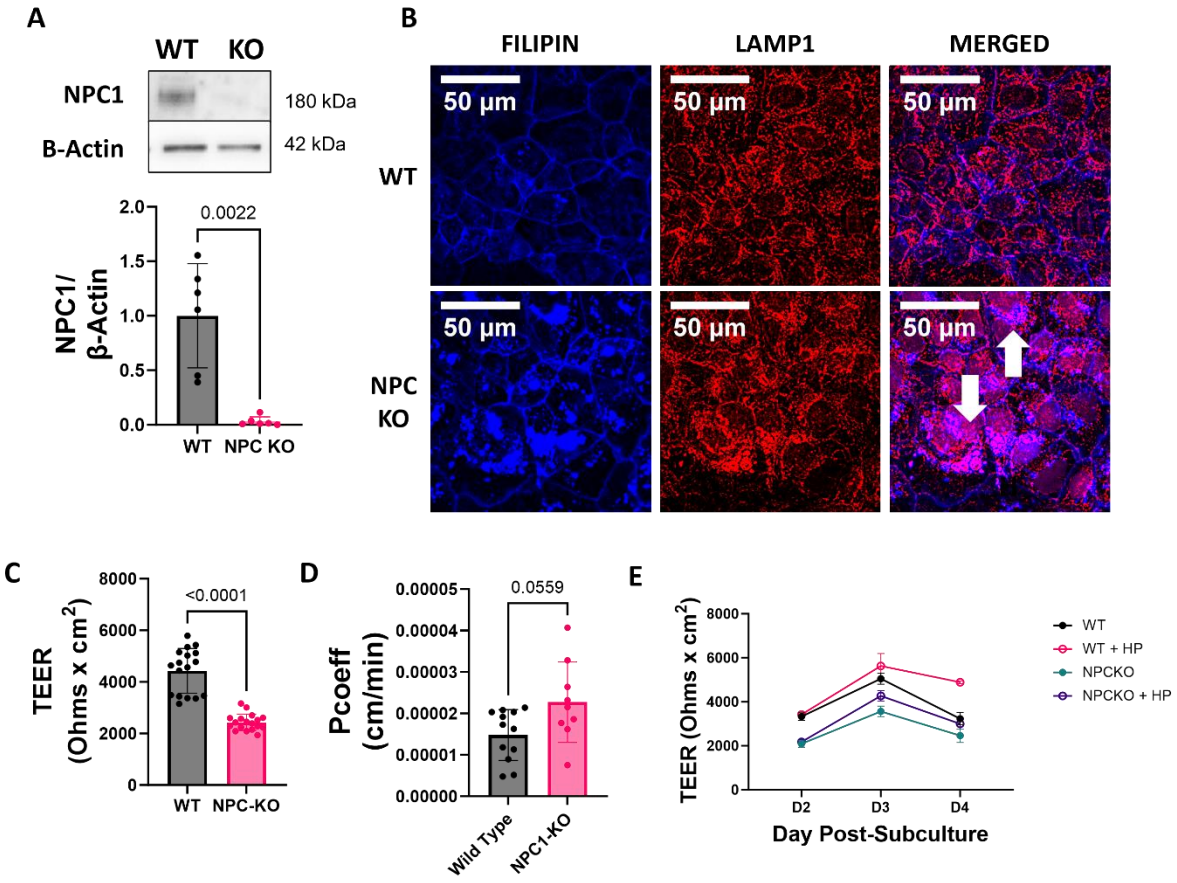

Figure 2.10. NPC-KO iPSC-BMECs showed altered cholesterol distribution and impaired barrier integrity (A) NPC1 protein level in wild-type (WT) and NPC-KO iPSC-BMECs, analyzed via western blot. (B) Representative images of WT and NPC-KO iPSC-BMECs stained with filipin (blue) or lysotracker (red). White arrows highlight areas of accumulation/overlap (purple). (C) TEER at D8 of differentiation, 2 days after subculturing on Transwell inserts (n = 17-18 samples from 3 independent differentiations). (D) Permeability coefficients of sodium fluorescein (n=9, from 3 independent differentiations). (E) Treatment with HPβCD restores barrier function.

2.5. Discussion

BBB integrity protects the brain from circulating neurotoxic factors and pathogens that contribute to neurodegeneration. Despite the importance of cholesterol in barrier integrity, the BBB remains poorly characterized in diseases of cholesterol metabolism such as NPC. I hypothesized that depleting cholesterol would diminish barrier integrity primarily by disrupting tight junction morphology. My results demonstrate that both U18666A and MβCD significantly decreased barrier integrity, increased paracellular permeability, and altered claudin-5 morphology. I found that co-treatment with the potential NPC therapeutic HPβCD restored barrier integrity following U18666A treatment. Finally, I found that

NPC1 knockout with CRISPR-Cas9 replicated trends observed in U18666A-treated iPSC-BMECs. Together, these data suggest the possibility of BBB dysfunction in NP-C and other inherited disorders of cholesterol metabolism, which may unveil new insights into the neuropathogenesis of these diseases.

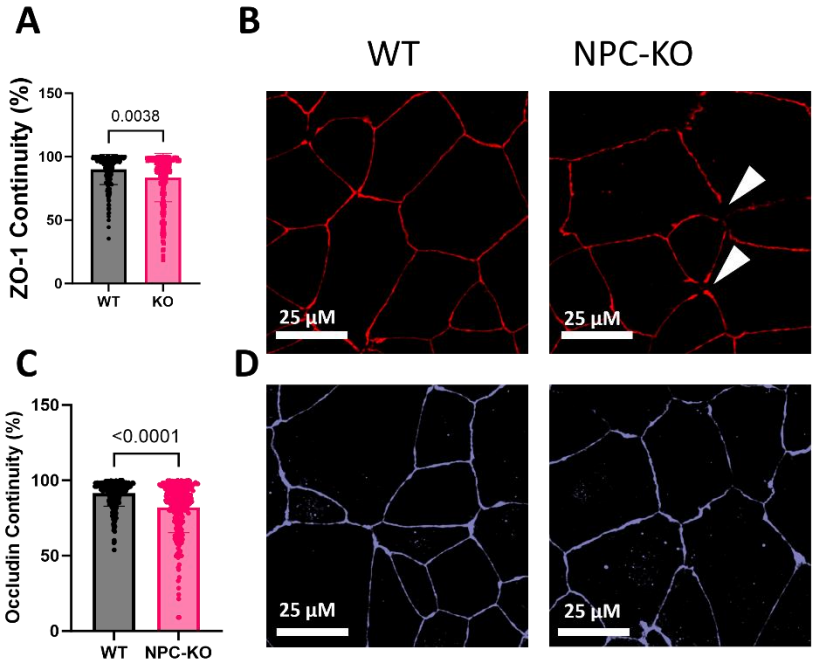

Figure 2.11. NPC-KO iPSC-BMECs showed slight changes in tight junction morphology, particularly at multicellular junctions. (A) ZO-1 continuity quantified with JanAP (N=258-272). Kolmogorov-Smirnov non-parametric test was used to calculate statistical significance. Data shown are mean +/- SD. **(B)** Representative images of WT and NPC-KO cells stained for ZO-1. Scale bars = 25 µM. **(C)** Quantification of disrupted multicellular junctions. For each well, 3 images were taken and each multicellular junction was classified as either continuous, discontinuous, or unknown by a blinded observer. The percent of continuous junctions was averaged for each well. Each data point represents the average of 3 technical replicates (9 images total, 3 per well). **(D)** Occludin continuity quantified with JanAP (N=265-275). Kolmogorov-Smirnov non-parametric test was used to calculate statistical significance. Data shown are mean +/- SD. **(E)** Representative images of occludin in WT and NPC1-KO iPSC BMECs. Scale bars = 25 µM.

Cholesterol depletion via U18666A or NPC-KO primarily affected claudin-5 and occludin. Previous work in epithelial cells demonstrated that cholesterol depletion with MβCD displaced claudins from lipid rafts [4,5] and cell-cell junctions [6]. *In vivo* evidence also showed that cholesterol depletion decreased claudin-5 and increased BBB permeability in rats [7]. Similarly, occludin has been reported to be displaced out of lipid rafts following cholesterol depletion in Caco2 epithelial cells [4,5]. The authors of these studies theorized that cholesterol was essential in maintaining functional integrity and stabilizing

interactions of TJ proteins with membrane rafts in epithelial cells [4]. A similar mechanism may also explain my results in iPSC-BMECs.

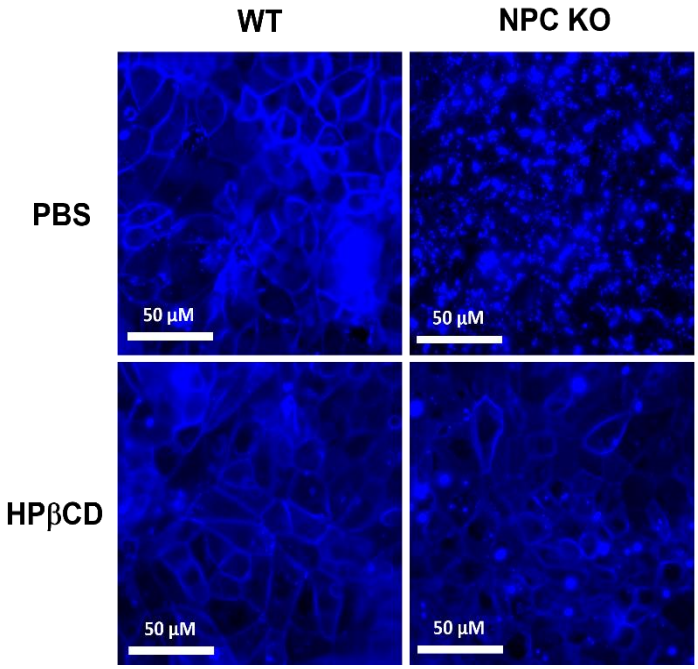

Figure 2.12. HPβCD partially restored cholesterol distribution in CRISPR-Cas9 NPC1-KO iPSC-BMECS. Representative images of iPSC-BMEC or NPC1-KO iPSC-BMECs treated with HPβCD or solvent control (PBS) for 48 hours and then stained with filipin. Scale bar = 50 μM.

I observed iPSC-BMEC permeability changes to tracers with molecular weights between 376 to 4,000 daltons. Both claudin-5 and occludin are crucial for size-selective permeability. Claudin-5 regulates small molecules (< 800 Da) permeability, as demonstrated in claudin-5 knockout mice that showed increased BBB permeability to Gd-DPTA (742 Da) and hoescht (562 Da) but not microperoxidase (1.9 kDa), 4 kDa dextran, 10 kDa dextran, or serum albumin (68 kDa) [21,27]. In a more recent study, double knockout of occludin and claudin-5 in mice increased permeability of 3 kDa but not 10 kDa permeability tracers, while single knockouts were unaffected and did not show permeability to either [28]. Size-specific changes were also noted following siRNA-knockdown of claudin-5 and occludin in mouse brain endothelial cells cultured on Transwell inserts, which showed increased permeability to a 4.3 kDa Aβ amyloid monomer but not 8.7 kDa Aβ amyloid dimer [28]. Together, these results suggest that claudin-5 and occludin are both required to restrict permeability of molecules < 4 kDa in size. Interestingly, previous work reports a lack of infiltrating peripheral immune cells or Evans blue dye (960 Da) in NPC1 mice [29]. However, it should be noted that Evans blue dye binds strongly to albumin, forming a 69 kDa tracer molecule that cannot typically cross the BBB [30]. Claudin-5 knockdown mice also do not show any evidence of

increased albumin permeability [21]. Together, these results suggest that permeability should be further evaluated in NPC1 mice with smaller tracer molecules such as sodium fluorescein, which does not bind to albumin.

U18666A treatment may have decreased claudin-5 junction continuity by decreasing claudin-5 protein level without a change in claudin-5 mRNA. Claudin-5 has been reported to undergo S-palmitoylation, a process in which the 16-carbon palmitic acid is covalently attached to the cysteine residue through a thioester bond [8]. Computational analysis suggests that palmitoylation stabilizes the interaction between claudin-5 and cholesterol, which shifts claudin-5 localization towards lipid rafts enriched in cholesterol [8]. In cholesterol-depleted cells, claudin-5 may get displaced to the cytoplasm, where it is then tagged for degradation. Thus, cholesterol depletion could induce claudin-5 degradation.

I observed decreased barrier integrity in three different models of membrane cholesterol depletion: acute cholesterol depletion (MβCD); longer-term cholesterol depletion (U18666A); and genetic cholesterol depletion (NPC1-KO). Although changes in barrier integrity were noted in all three models, the magnitude of barrier dysfunction differed with each model. MβCD reduced TEER within hours, while U18666A took 48 hours to decrease TEER to similar levels. In contrast, NPC1-KO iPSC-BMECs had TEER values that were approximately half that of their wild-type counterparts, although their TEER values remained relatively high (1938-3820 ohms/cm^2). This indicates that while genetic NPC1-deficiency leads to barrier disruption, it likely does not lead to devastating structural disruption observed in U18666A-treated iPSC-BMECs. The magnitude of barrier disruption observed in U18666A-treated iPSC-BMECs may be amplified by off-target inhibition of cholesterol synthesis or intercalation in membranes [19].

HPβCD is currently being examined for its therapeutic capabilities in treating NP-C. Mechanistically, this drug is believed to release accumulated cholesterol from the lysosome and facilitate its transport into other organelles [12,31,32]. My data support the ability of HPβCD to restore cholesterol distribution and barrier function in U18666A-treated iPSC-BMECs. However, in NPC1-KO cells, barrier function was not fully restored even though cholesterol distribution was improved. This may indicate that HPβCD is more potent as a pre-treatment preventative measure against cholesterol-depletion-induced BBB disruption rather than as a therapeutic for BMECs that with pre-existing cholesterol depletion and BBB disruption.

However, longer HPβCD treatments should be tried to fully assess its ability to restore barrier integrity in NPC1-KO iPSC-BMECs.

2.6. Limitations

While my data show that cholesterol depletion reduces BBB integrity, my studies are not without limitations. Some of the U18666A effects may arise due to potential off-target effects. U18666A intercalates in cell membranes and inhibits the cholesterol biosynthetic enzyme DHCR24 [19]. Although I did not observe an increase in desmosterol, there may still be as yet unmeasured off target U18666A effects. In addition, I examined my results in a simplified model that only included one cell type. Previous work has shown that other cell types, such as astrocytes and neurons, promote BBB integrity and elevate TEER when co-cultured with BMECs [33]. My *in vitro* model does not incorporate this communication between BMECs and other cell types that are present in the brain, which may reduce the physiological relevance of my results. In addition, I did validate my results *in vivo* to confirm that similar changes are observed in NPC1 mice. It is possible that the presence of other cell types may provide supportive cues that mitigate possible BBB dysfunction in NP-C.

2.7. Conclusions

Together, these data indicate that cholesterol depletion significantly perturbs claudin-5 and occludin, increasing barrier permeability to smaller molecules (< 4 kDa). We found that U18666A treatment diminished continuity of both claudin-5 and occludin and decreased claudin-5 protein levels. HPβCD treatment restored barrier function, claudin-5 protein, and claudin-5 morphology in U18666A-treated iPSC-BMECs. Finally, we also observed decreased barrier integrity in NPC1-KO iPSC-BMECs, although the magnitude of decrease in barrier function was smaller than that observed in U18666A-treated iPSC-BMECs. This may suggest that there are important differences between chemical and genetic ablation of NPC1 in iPSC-BMECs. Future studies examining BBB permeability in human and animal models will be necessary to confirm the extent BBB dysfunction in NP-C. If substantiated in these models, this may highlight the role of the BBB in contributing to or even precipitating neuroinflammation in NP-C and

highlight the brain endothelium as a potential therapeutic target to halt or even reverse disease progression.

Chapter 3 - NPC1 inhibition increased glycolysis and diminished mitochondrial metabolism in brain microvascular endothelial cells

3.1. Introduction

Brain microvascular endothelial cells (BMECs) dictate glucose entry into the brain by selectively taking it up from the blood and transporting it across into the brain. This process is critical for neuronal health, as the brain primarily relies on glucose to fulfill its energetic needs [57]. In addition, metabolic disturbances contribute to endothelial dysfunction, which can lead to pathological changes such as increased barrier permeability [171,172]. Both glucose hypometabolism and neurovascular dysfunction are implicated in neurological diseases such as Alzheimer's disease but are understudied in rare neurogenetic diseases such as NPC [173–176]. By understanding how altered cholesterol trafficking perturbs BMEC metabolism and transport, we can decipher how BMECs contribute to neuropathogenesis in disorders of cholesterol metabolism and potentially unveil novel interventional strategies to ameliorate disease progression.

Cholesterol is a crucial lipid in mammalian cells, and it is tightly regulated, primarily by the sterol regulatory element-binding proteins (SREBPs) [177]. Cholesterol synthesis is an energetically expensive process which requires acetyl-CoA and NADPH. Low cholesterol is sensed by the SREBPs, which then drive cholesterol synthesis. A cholesterol compensatory state may upregulate pathways that drive formation of acetyl-CoA (such as glycolysis) and NADPH (such as the pentose phosphate pathway (PPP)) to supply substrates for cholesterol biosynthesis.

These compensatory mechanisms may cause BMECs to retain more carbon for their own needs and decrease the amount they transport basolaterally. Diverted glucose may be problematic for brain health. Glucose taken up by BMECs is either metabolized or transported for basolateral delivery to other brain cells [178]. Early studies in rat BMEC suggest that ~95% of glucose is made available for transport to the brain parenchyma [179]; however, this balance may be perturbed in altered metabolic states. Interestingly, BMECs can control transcellular glucose transport by dictating apical-basolateral distribution of glucose transporters [180,181]. Studies in mouse microglia and Chinese hamster ovary (CHO) cells show that *NPC1* inhibition leads to increased oxidative stress, glycolytic gene expression, lactate secretion, and compensatory endogenous cholesterol overproduction as well as deficient decarboxylation and impaired mitochondrial transport of pyruvate [168,182,183]. When NPC1 is inhibited, BMEC glucose metabolism may increase to fuel compensatory *de novo c*holesterol biosynthesis or antioxidant production in the pentose phosphate pathway (PPP), thus limiting glucose transport to parenchymal brain cells.

In this chapter, I investigated how disrupting intracellular cholesterol trafficking with the NPC1 inhibitor U18666A altered BMEC metabolism and glucose transport. iPSC-BMECs were treated with U18666A, a potent NPC1 inhibitor. Glycolytic and mitochondrial metabolism were measured with extracellular metabolic flux measurements, heavy isotope labeling, mass spectrometry, and Seahorse flux assays. I then used instationary metabolic flux analysis (INST-MFA) to quantify changes in metabolic flux between untreated and U18666A-treated iPSC-BMECs. I further tested the impact of U18666A in human primary BMEC (hpBMEC), and finally determined how hydroxypropyl-β-cyclodextrin (HPβCD), which has shown beneficial effects in treating NP-C in animal models and early clinical trials, impacts U18666A metabolic changes and loss of barrier integrity. Collectively, our data indicates that altered cholesterol trafficking can induce metabolic dysfunction in BMECs and potentially alter metabolic homeostasis in the brain. Our results highlight a potential phenomenon through which BMEC may be implicated in altered brain metabolism and neurodegeneration in NP-C, which may unveil new therapeutic targets to attenuate BMEC effects on brain metabolism.

3.2. Materials and Methods

3.2.1. Cell Culture

iPSC-BMECs were cultured and differentiated as previously described in Chapter 2. hpBMEC (Cell Systems, ACBRI 376 V) were maintained in Endothelial Growth Medium 2-microvascular (EGM2-MV; Lonza, CC-4147) supplemented with 1% penicillin-streptomycin (Thermo Fisher, 15140163), 1% L-glutamine (Thermo Fisher, 25-030-081), and 10% fetal bovine serum (FBS; Cytiva, SH30088.03) and used through passage 9. For experiments, iPSC-BMECs and hpBMECs were switched to neurobasal media (Thermo Fisher; A2477501) containing 8.5 mM glucose, 4.5 mM glutamine, and 2% B27. Cells were then treated with media containing U18666A (Sigma-Aldrich, U3633), 2-hydroxypropyl-β-cyclodextrin (HPβCD; Roquette, 128446), dichloroacetate (DCA; Sigma-Aldrich, 347795), 2-deoxy-D-glucose (2-DG; Thermo Fisher Scientific, 111980050) or solvent control. As demonstrated in Ch 2, U18666A treatment altered cholesterol localization with no changes in cell viability.

3.2.2. Extracellular measurements

A YSI 2950 Bioanalyzer (Yellow Springs Instruments, 527690) was used to measure extracellular glucose, lactate, glutamine, and glutamate concentrations. 200 µL media samples were collected at the start of the experiment and at specified time points during the experiment. The metabolite uptake or secretion was calculated as the difference in extracellular metabolite concentration between the specified time point and the start of the experiment.

Integrated metabolism and transport were measured in two ways. First, iPSC-BMECs subcultured on 12-well Transwell inserts with heSFM containing 2% B27, 4.5 mM glutamine, 8.5 mM glucose, and either U18666A in the apical and basolateral compartments. Cells were treated for 24 hours and media was then collected from both the apical and basolateral compartments for analysis. Then, the cells were washed with PBS, and media was replaced with DMEM containing 2% B27 and 4.5 mM glutamine, as well as 8.5 mM glucose (apical media) or 8.5 mM mannitol (osmotic control, basolateral media). Cells were incubated in these media for another 24 hours. Media was then collected from both the apical and basolateral compartments for analysis.

3.2.3. RT-PCR

PCR was run as previously described in Chapter 2. Primers used include SREBF1 (Hs02561944_s1), LDHA (Hs01378790_g1), PFKP (Hs00737347_m1) and HK2 (Hs00606086_m1).

3.2.4. Seahorse metabolic assays

Oxygen consumption rate (OCR) and extracellular acidification rate (ECAR) were measured using the Seahorse Mito Stress Test (Agilent, 103015-100). On the day of the assay, media was changed to Seahorse DMEM (Agilent, 103680-100) supplemented with 5.5 mM glucose, 1 mM pyruvate, and 4.5 mM glutamine for 1 hour. The loading cartridge was prepared to inject oligomycin (1.5 µM), FCCP (0.5 µM), and rotenone + antimycin A (0.5 µM). Extracellular acidification rate (ECAR, glycolysis) and oxygen consumption rate (OCR, oxidative respiration) were measured using a Seahorse XF96 (Agilent) and analyzed using Seahorse analytics software. After each experiment, cells were fixed with 4% paraformaldehyde, and nuclei were stained with DAPI (1:1000). Four quadrants of each well were imaged using a Nikon Eclipse 2Ti with a 10X objective, and the nuclei numbers from each quadrant were summed to count the number of cells per well. Seahorse assay outputs were then normalized to cell number.

3.2.5. Mitochondrial membrane potential

Tetramethylrhodamine (TMRM) was used to analyze mitochondrial membrane potential. Cells were seeded into individual 35 mm glass-bottom dishes and cultured to confluence. Cells were then treated with 10 µM U18666A for 24 hours in neurobasal media supplemented with 2% B27. After 24 hours, the media was removed and replaced with neurobasal media containing TMRM (1:1000; source), Mitotracker Green FM (1:5000; Thermo Fisher Scientific, M7514), and Hoescht (1:2000, nuclei, Thermo Fisher Scientific, 33342) for 30 minutes. The labeling media was then aspirated and fresh neurobasal media + 2% B27 was added for 30 minutes prior to imaging to quench extracellular TMRM. Cells were then imaged on a Nikon Eclipse T2i using a 60X oil objective using a live cell imaging chamber at 37°C and 5% CO_2. Mitotracker was used to confirm that TMRM signal was specific for mitochondria. Following imaging, cells were treated with carbonyl cyanide m-chlorophenyl hydrazon (CCCP), which opens the mitochondrial permeability transition pore, to measure loss of TMRM signal from mitochondria and confirm that TMRM was specific for mitochondrial membrane potential.

TMRM signal was quantified using Nikon Elements software. Images were thresholded to eliminate background, and the total TMRM signal intensity was quantified. Nuclei were segmented and counted using the Bright Objects and Count Objects modules. TMRM intensity was then normalized to nuclei count to calculate the TMRM intensity per cell.

3.2.6. Isotope labeling and mass spectrometry

For isotope labeling experiments, BMECs were pretreated for 24 hours to achieve metabolic steady state. Cells were then then washed with PBS and media was replaced neurobasal media (Thermo Fisher; A2477501) supplemented with ^{13}C labeled metabolites. Labeling media contained 8.5 mM glucose, 4.5 mM glutamine, and 2% B27.

For instationary metabolic flux analysis (INST-MFA), iPSC-BMECs were labeled for 10 minutes, 1 hour, 4 hours, 12 hours, or 24 hours with [1,2-$^{13}C_2$]-glucose (Cambridge Isotope Laboratories, CLM-504-PK). For steady-state experiments in hpBMECs, cells were labeled for 24 hours with U-$^{13}C_6$-glucose (Cambridge Isotope Laboratories CLM-1396). At the end of the labeling period, cell culture media was collected. Cells were lysed with ice cold 80:20 methanol for 15 minutes at -80°C, and then scraped, vortexed, and centrifuged to pellet proteins. The protein pellets were air dried and lysed in RIPA buffer (Thermo Fisher, 89901). A bicinchoninic acid (BCA) protein assay kit (Thermo Fisher, 23225) was used to quantify protein concentration.

Metabolites from media and cells were quantified by the University of Colorado School of Medicine Metabolomics Core following previously established protocols [184]. Briefly, 8 mL of each sample was injected into a Q Exactive mass spectrometer (MS) in a randomized order by a Vanquish ultra-high performance liquid chromatograph (UHPLC; Thermo Fisher). Eluent was introduced to the MS through electrospray ionization, and the MS was set to scan in full MS mode (2 mscans) over 65-950 m/z. After every ten samples, technical mixes were injected to validate instrument stability [185]. Metabolites were manually annotated and integrated with the KEGG database and Maven [186,187]. Blanks, technical mixes, and ^{13}C natural abundance were used to determine peak quality [188], and the IsoCor Python package [189] was used to correct the isotope labeling. Metaboanalyst 5.0 was used to analyze data and

perform Partial Least Squares-Discriminant Analysis (PLS-DA), calculate VIP scores, and perform t-tests with false discovery rate correction [190]. Ion abundance was normalized to the protein concentration.

For sterol analysis, sample extracts were randomized and 8 µL was injected onto a Q Exactive MS by a Vanquish UHPLC using an ACQUITY UPLC HSS T3 column (150 x 2.1 mm, 1.8 µM, Waters) over a 17-minute gradient in positive mode, as previously described [156]. Atmospheric pressure chemical ionization was used to introduce eluent to the MS which scanned in full MS mode (1 µscans) over the range of 150-1500 m/z. Technical mixes were injected approximately every ten samples to determine instrument stability [156].

3.2.7. Nonstationary Isotope-Assisted Metabolic Flux Analysis

Nonstationary isotope assisted metabolic flux analysis (iMFA) was performed in INCA 2.0 (Rahim 2022) using a modified version of the core network I previously described (Moiz 2021). The metabolic map was expanded to include glutathione and GABA synthesis from glutamate, as well as an influx of undiluted aspartate. External metabolite flux rates for glutamate, glutamine, glucose, and lactate were converted into nmol/hr for each metabolite is shown in Equation 3.1:

$$(3.1) \qquad Flux\ Rate\ \left(\frac{nmol}{hr}\right) = 1000 * V * \frac{dC}{dT}$$

where V is the media volume in each well (mL), dC is the concentration change from 0 to 24 hours (mmol/L), and dT is the time period (hours).

For isotopically non-stationary MFA (INST-MFA), I fit the model with data from five different time points (10 minutes, 1 hour, 4 hour, 12 hours, and 24 hours). For all MFA experiments, INCA predicted fluxes using a Levenberg–Marquardt gradient descent algorithm. Simulations were repeated 100 times to improve the odds of finding the global optimum, each time beginning from a random initial point. The goodness of fit was based on the assumption that the minimized Sum of Squared Residuals (SSR) follows a chi-square distribution. The chi-square statistic can be used to determine whether the frequency of observations differs significantly from their frequencies. The chi-square function is defined in Equation 3.2 below:

$$(3.2) \qquad X^2 = \frac{\sum(O_i - E_i)^2}{E_i}$$

Where i is isotopomer, O is the observed isotopomer fraction, and E is the experimentally determined isotopomer fraction. The acceptable fit was based on the n–p degrees of freedom, where n is the number of independent measurements and p is the number of fitted parameters. The formula for the acceptable SSR range is shown in Equation 3.3:

$$\chi^2_{\alpha/2}(n - p), \chi^2_{(1-\frac{\alpha}{2})}(n - p) \tag{3.3}$$

All metabolites were set to a minimum error of 1% as recommended for LC-MS data [139]. To adequately fit the model and prevent either over- or underfitting, I examined residual errors for each isotopomer after each analysis. Any gross outliers that skewed the distribution were rescaled to ensure a relatively normal distribution of residual error. This adjustment process was repeated until the distribution of residuals appeared to be relatively normal.

Metabolites that produced large model errors (SSR > 150) or showed labeling states that could not be explained by biochemically feasible reactions were designated as erroneous and removed from the model. The final ^{13}C INST-MFA model consisted of 91 reactions with 539 degrees of freedom. A full metabolic model description is provided in the appendix. Confidence intervals were generated using parameter continuation.

3.2.8. Barrier permeability

iPSC-BMECs were seeded on 24 well Transwell inserts (300,000 cells/well) and treated with neurobasal media supplemented with 2% B27 containing the specified reagents for 48 hours. TEER and permeability measurements were collected and calculated as previously described in Chapter 2.

3.2.9. Statistical Analysis

Statistics were analyzed in GraphPad Prism. Non-parametric Mann-Whitney tests were used to compare two unpaired datasets. One-way Kruskal-Willis non-parametric test was used to compare multiple groups, followed by *post hoc* Dunn's multiple comparison test. Data were considered statistically significant if $p < 0.05$. For metabolomics data sets, significance was determined by using multiple t-tests followed by 2-way ANOVA followed by two-stage linear step-up procedure of Benjamini, Krieger, and Yekutieli to correct for multiple comparisons.

3.3. Results

3.3.1. U18666A increased iPSC-BMEC glycolytic metabolism

Previous work indicates that NPC1 deficiency increases glycolytic activity in microglia and CHO cells [182,191]. I therefore first examined how U18666A treatment impacted iPSC-BMEC glycolytic metabolism. Both glucose uptake and lactate secretion increased in a dose dependent manner with U18666A (Figure 3.1A). At 10 μM U18666A, glucose uptake increased by ~39% ($p < 0.0001$) and lactate secretion by ~45% ($p < 0.0001$). However, the lactate:glucose ratio did not change, indicating that glucose carbons were not being significantly diverted to fuel alternative pathways such as cholesterol biosynthesis or the TCA cycle.

I then determined how cholesterol depletion with U18666A would impact integrated iPSC-BMEC glucose metabolism and transport using iPSC-BMECs on Transwell inserts. I first measured the change in glucose and lactate concentration in Transwell inserts in which both the apical and basolateral compartments contained media with equal glucose concentrations. After 24 hours, I observed decreased glucose in both the apical (24% decrease, $p =0.0167$) and basolateral (23% decrease, $p = 0.0434$) compartments in cells treated with U18666A (Figure 3.1D), indicating that glucose uptake increased from both compartments. Similarly, lactate concentration was higher in both compartments, indicating that lactate secretion increased with U18666A (Figure 3.1D). When glucose was instead added to the apical compartment only, the glucose transported to the basolateral compartment decreased by 13-15% at 5 μM and 10 μM U18666A ($p < 0.05$) (Figure 3.1E).

I then quantified gene expression by RT-PCR to determine if the observed increase in glycolysis with U18666A was related to changes in rate-limiting glycolytic enzymes such as phosphofructose kinase (PFKP), hexokinase 2 (HK2), and lactate dehydrogenase (LDHA) (Figure 3.1F). HK2, which catalyzes glucose phosphorylation to glucose-6-phosphate, increased by approximately two-fold at all U18666A concentrations, with significant changes at 5 µM (p=0.0395) and 10 µM (p=0.0018). PFKP, which

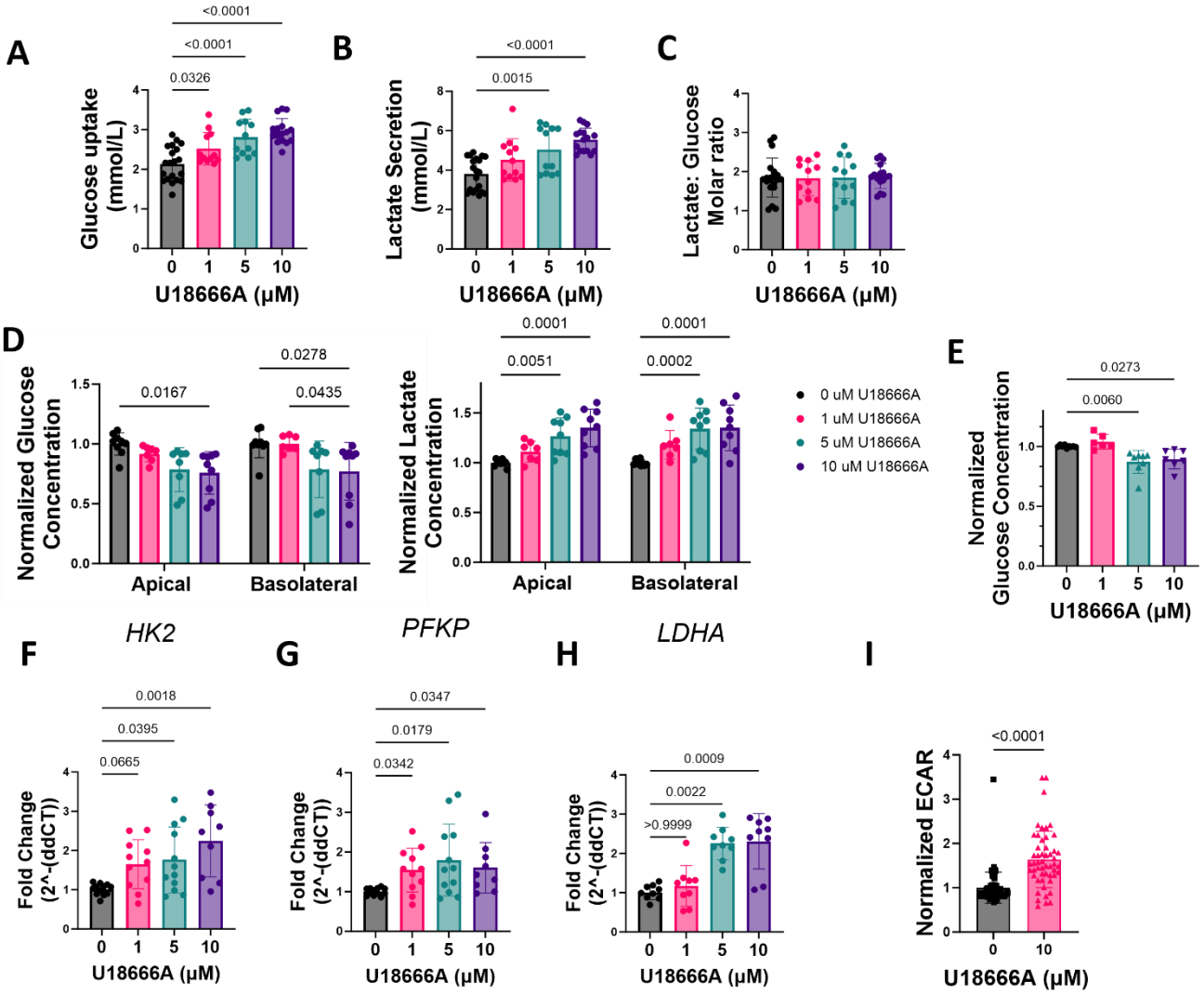

Figure 3.1. U18666A treatment significantly upregulated glucose uptake and glycolytic metabolism in iPSC-BMECs. (A) Glucose uptake, (B) lactate secretion, and (C) lactate:glucose ratio following treatment with 0, 1, 5, or 10 µM U18666A, measured with a YSI bioanalyzer. Apical and basolateral (D) glucose and (E) lactate concentrations after 24 hours in experiments where initial glucose concentration was equal in both apical and basolateral compartments. Data was normalized to mean of untreated group (E) Basolateral glucose concentration after 24 hours when only apical side contained glucose (5.5 mmol/L). Data normalized to mean of untreated group. (F-H) Gene expression and fold change calculation following RT-PCR for the rate-limiting glycolytic genes Hexokinase 2 (*HK2)*, phosphofructose kinase (*PFK),* and lactate dehydrogenase (LDHA) (n=9). (I) extracellular acidification rate (ECAR) for iPSC-BMECs treated with 10 µM U18666A for 24 hours, measured using a Seahorse metabolic flux assay. Data was pooled from four independent experiments (n=63-73). All data are shown with mean +/- standard deviation. One-way non-parametric Kruskal-Willis followed by Dunn's MCT used for multiple groups. The Mann-Whitney test was used when comparing two groups.

catalyzes fructose-6-phosphate phosphorylation into fructose-1-6-biphosphate, increased 1.75-fold at 5 µM and 10 µM U18666A ($p = 0.0179$ and $p = 0.0347$, respectively) (Figure 3.1G). LDHA also increased by nearly 2.5-fold with 5 µM and 10 µM U18666A ($p = 0.0022$ and $p = 0.0009$) and 10 µM (Figure 3.1H).

To confirm changes in glycolytic flux, I quantified extracellular acidification rate (ECAR; glycolysis) in iPSC-BMECs treated with U18666A using a Seahorse Mito Stress test. At 10 µM U18666A, ECAR increased by more than 60% ($p < 0.0001$) (Figure 3.1I). Together, these data confirm that U18666A induced an increasingly glycolytic phenotype in iPSC-BMECs.

3.3.2. Isotope labeling indicates that U18666A-treated iPSC BMECs deviate at glucose flux at key glycolytic side branch pathways

To further understand glycolytic changes in U18666A-treated iPSC-BMECs, I labeled U18666A-treated iPSC-BMECs with [1,2-$^{13}C_2$] glucose. [1,2-$^{13}C_2$] glucose determines fluxes at glycolytic branch points, particularly into the pentose phosphate pathway.

I used partial least squares discriminant analysis (PLS-DA) and variable importance projection (VIP) scores to identify metabolites with robust differences across all time points (n=3 samples per timepoint and treatment). Samples separated by time point for untreated cells across component 1 (PC1 = 44.4%, Figure 3.2A) and across component 2 for U18666A cells (PC2 = 16.8%, Figure 3.2A). The metabolites with the top 15 VIP scores include isotopomers in the non-oxidative pentose phosphate pathway (non-ox PPP) such as glyceraldehyde-3-phosphate (GAP), fructose-6-phosphate/fructose-1,6-biphosphate (2/15 isotopomers) (F6P/F16BP), and ribose-5-phosphate (3/15 ranked isotopomers). Over representation of PPP-affiliated metabolites in the VIP scores plot suggests that differences in these metabolites are consistent across multiple time points, including earlier times when other metabolites have not reached isotopic steady state.

I then examined isotopomers that delineate glucose flux into glycolytic side branch pathways (Figure 3.2C). [1,2-^{13}C] glucose forms [M+2] glucose-6-phosphate (G6P), which then can enter the PPP to form [M+1] ribulose-5-phosphate (R5P). [M+1] R5P was higher in U18666A treated cells 1-hour post-labeling

and at every time point thereafter. At 12- and 24-hours post-labeling, [M+1] R5P was ~1.5-fold higher in U18666A-treated iPSC-BMECs (p = 0.005, p < 0.0001) compared to untreated cells (Figure 3.2D).

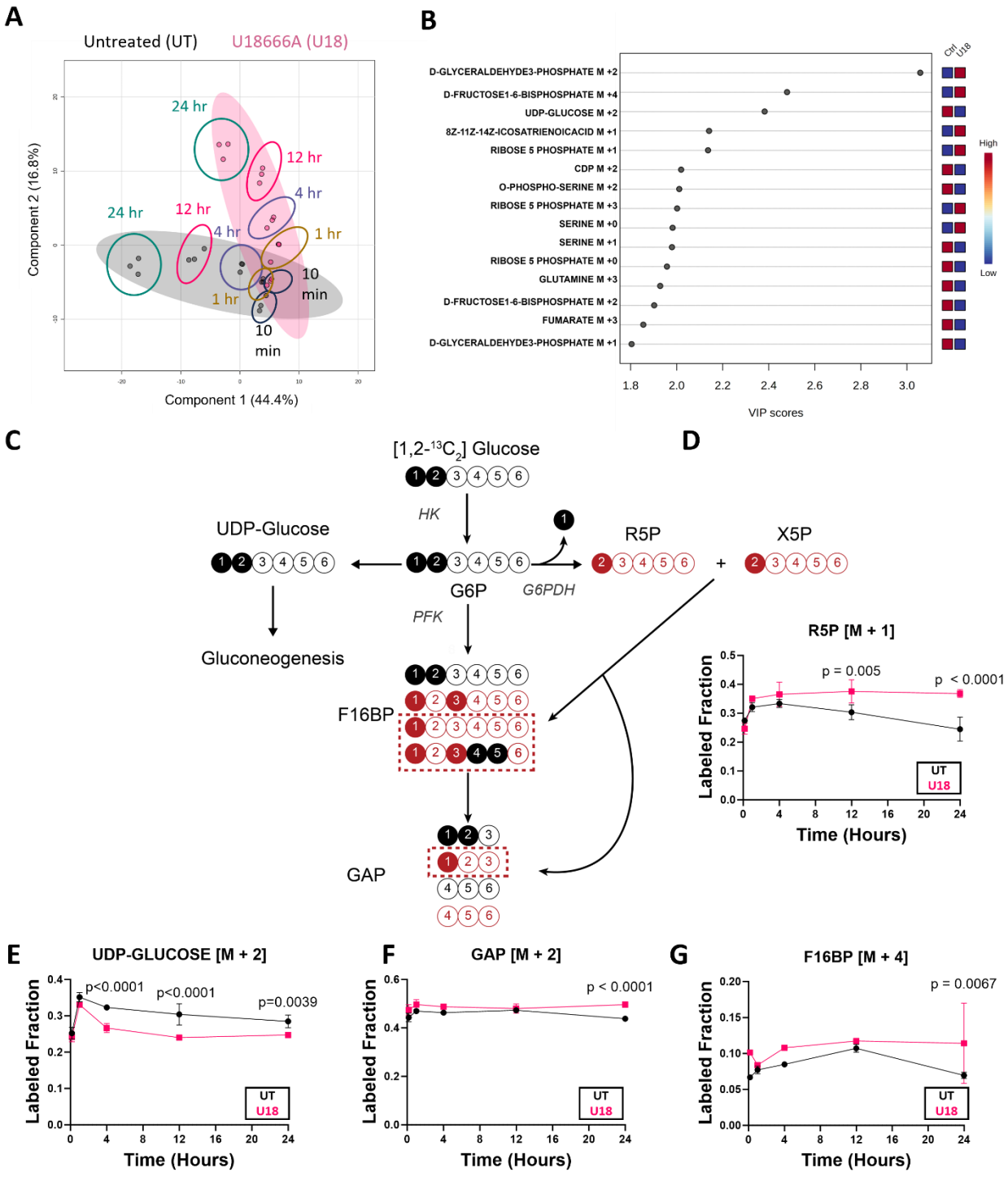

Figure 3.2. Isotope labeling experiment indicated changes in metabolic flux at key glycolytic side branch pathways. (A) Partial-least squares discriminant analysis (PLS-DA) was used to identify isotopomers that differentiate untreated and U18666A-treated iPSC BMECs across all time points. PLS-DA was created from all individual isotopomers data pooled from all time points (n = 3 per time point and treatment, n = 15 per group). Data from each time points are designated by circled outlines (B) Variable importance in project (VIP) score plots were used to identify isotopomers that consistently separated between untreated and U18666A-treated iPSC-BMECs across all time points. Plots show 15 highest ranking isotopomers (C) [$U^{13}C_{1,2}$] glucose can be used to delineate complex fluxes at key glycolytic side branch points. Glucose-6-phosphate dehydrogenase (G6PDH) catalyzes entry of G6P into the PPP. During this reaction, the first carbon of glucose-6-phosphate (G6P) is cleaved off, leaving an M + 1 six carbon sugar that eventually Is metabolized into ribose-5-phosphate (R5P) and xylulose-5-phosphate (X5P). Within the non-oxidative phase of the PPP, R5P and X5P can combine to form fructose-6-phosphate (F6P) which eventually forms fructose-1,6-biphosphate (F16BP). M +2 F16BP can be formed by either combining M + 1 X5P and M + 1 R5P or can be directly derived from M + 2 G6P that does not enter glycolytic side branches. M + 4 F16BP is uniquely formed from glycolytic derived glyceraldehyde-3-phosphate (GAP) with PPP-derived F16BP. Therefore, M + 4 and M + 1 F16BP can form only from PPP and can be used as an indication of glucose entry into the PPP, whereas the source of M + 2 F16BP remains ambiguous. GAP and F16BP isotopomers which can only be derived from the PPP are designated within the red boxes. Labeled fractions for (D) R5P M + 1 (indicative of G6P entry into the PPP), (E) UDP-Glucose (an alternative route for G6P towards glycogen synthesis), (F) M +2 GAP (which forms directly from glycolysis), and (G) M +4 F16BP (unique to PPP) are shown next to corresponding place in metabolic pathway.

[M+2] UDP-glucose, which is formed when G6P enters glycogen synthesis, was lower in U18666A treated iPSC-BMECs at nearly all time points, with a significant decrease of ~0.8-fold at 4, 12, and 24 hours (Figure 3.2E). [M+2] GAP was also higher in U18666A-treated iPSC-BMECs, particularly at 24 hours when it was ~1.14-fold higher ($p < 0.0001$; Figure 3.2F), while M+4 F16BP trended higher in U!8666A-treated iPSC-BMECs at all time points. These data indicate that U18666A treatment rewires fluxes at key glycolytic side branches, funneling glucose away from glycogen synthesis and into the PPP.

3.3.3. U18666A decreased iPSC-BMEC mitochondrial metabolism

Previous studies demonstrate diminished mitochondrial metabolism in multiple NPC1-deficient cell types, including CHO cells, mouse neurons, and patient cells [192–194]. I therefore decided to examine how U18666A affected iPSC-BMEC mitochondrial metabolism. Basal oxygen consumption rate (OCR), an indication of oxidative respiration, was nearly 40% lower ($p< 0.0001$) in U18666A-treated iPSC-BMECs (Figures 3.3A, 3.3B). Similarly, maximal respiration was ~80% lower and spare respiratory capacity was nearly 60% lower with U18666A treatment ($p < 0.0001$) (Figures 3.3C, 3.3D). Tetramethyl rhodamine ester (TMRM), which measures mitochondria membrane potential, was ~45% lower in U18666A treated cells (Figure 3.3E, 3.3F).

To determine whether changes in mitochondrial respiration were secondary to reduced influx of glucose-derived carbons into the mitochondria, I examined [1,2-$^{13}C_2$] glucose labeling patterns in

U18666A treated cells. Within 4 hours, U18666A-treated iPSC-BMECs had reduced labeling of all TCA metabolites. At 24 hours, I observed decreases of 0.88-fold in citrate ($p<0.0001$), 0.66 in α-ketoglutarate ($p<0.0001$), 0.75 fold in succinate ($p=0.0171$), 0.73 fold in fumarate ($p=0.0004$), and 0.75-fold in malate ($p<0.0001$). Aspartate labeling, which can be interpreted as an analog for oxaloacetate labeling, was decreased by 0.70-fold in U18666A treated cells (Figure 3.3G). These data suggest that U18666A reduced incorporation of glucose-derived carbons into core TCA metabolites.

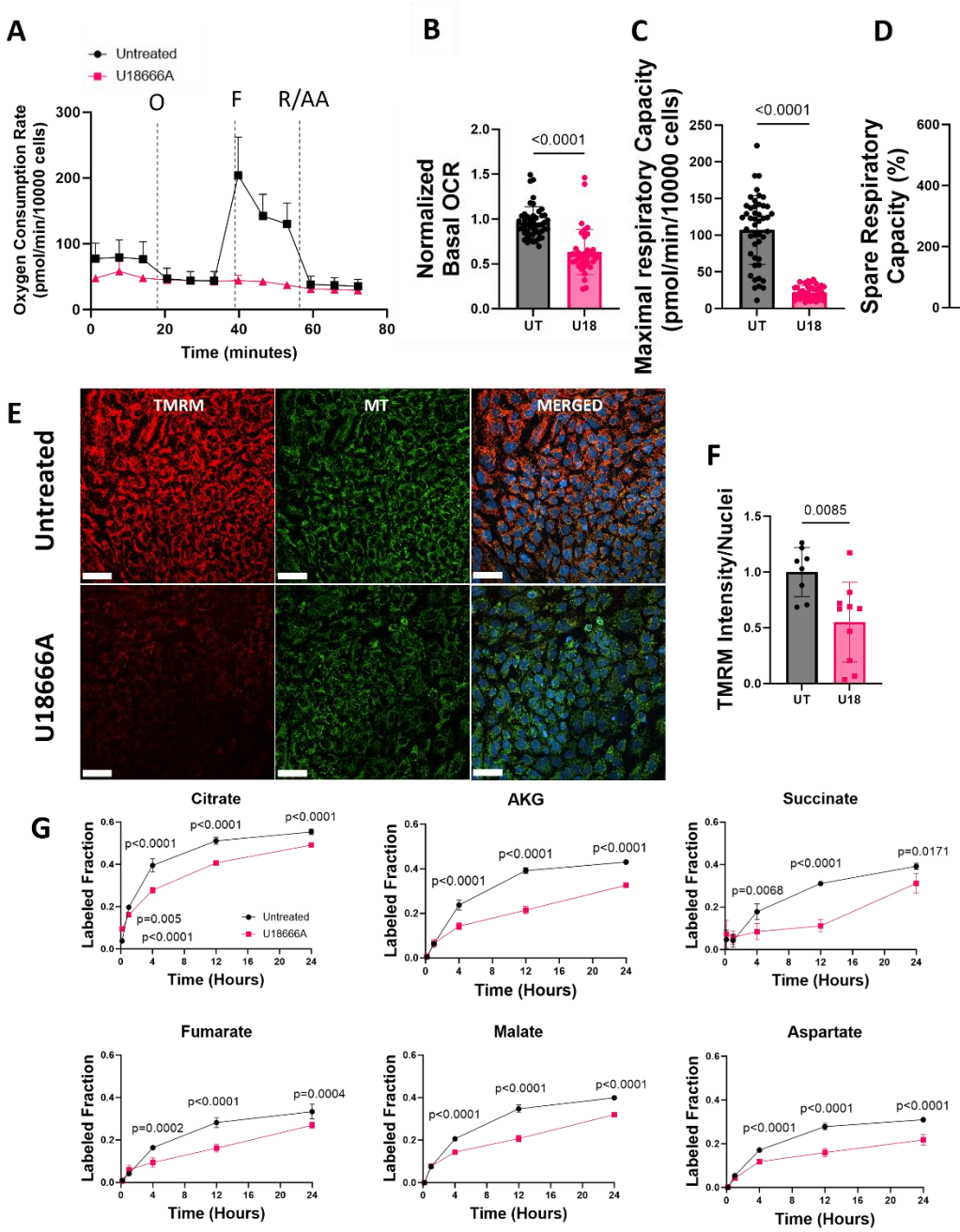

Figure 3.3. U18666A-treated iPSC-BMECs demonstrated mitochondrial dysfunction. (A) Representative figure of mitochondrial stress assay performed with Seahorse XFe96 Extracellular Flux Analyzer. Cells were injected with oligomycin (O) followed by carbonyl p-trifluoro-methoxyphenyl hydrazone (FCCP) and finally rotenone/antimycin A (R/AA) to determine basal and maximum oxygen consumption rates (OCR). Quantification of (B) basal oxygen consumption rate (OCR) and (C) spare respiratory capacity (%) pooled from 3 independent experiments (n=37-46). (D) Maximal respiration rate was pooled from 3 independent experiments (n = 37-46) (E) Tetramethylrhodamine (TMRM) staining was used to quantify mitochondrial potential in iPSC-BMECS treated with U18666A. Mitochondria imaged with Green MitoTracker. Scale bar = 20 μM. Representative images shown from 3 different experiments (n=9, 3 per experimental replicate). (F) Quantification of TMRM intensity normalized to nuclei count. Data is pooled from three independent experiments. Each data point was normalized to mean of untreated group for respective experiment (G) Labeling of citrate, alpha-ketoglutrate (AKG), succinate, fumarate, malate, and asparate over the course of 24 hours. Cells were lysed for analysis at 10 minutes, 1 hour, 4 hours, 12 hours, or 24 hours after being fed with [$U^{13}C_{1,2}$] glucose. All data are shown with mean +/- standard deviation. Mann-Whitney test was used to determine statistical significance when comparing two groups.

3.3.4. iMFA confirmed increased glycolytic side branch pathway flux and decreased mitochondrial activity

I next used isotope-assisted metabolic flux analysis (iMFA) to predict changes in intracellular metabolic fluxes throughout the metabolic network. Both isotopically stationary (iMFA) and non-stationary (INST-MFA) require the system to be at metabolic steady state [145,146]. However, steady-state iMFA requires a metabolic system to be at isotopic steady as well, which can be difficult to achieve in mammalian cells that have large intracellular pools and exchange multiple metabolites with the extracellular space. Isotopic labeling in iPSC-BMECs has never been reported prior to this study and therefore it was essential to validate steady state conditions before running iMFA.

To confirm whether the system was at metabolic steady state, I first quantified extracellular metabolite concentration over time (Figure 3.4). Both untreated and U18666A-treated iPSC-BMECs demonstrated a linear change in metabolite concentrations, showing that these cells were at metabolic steady state throughout the labeling experiment. U18666A-treated iPSC-BMECs had slightly higher glucose uptake rates (0.24 mmol/L/hr, 95% CI = 0.229-0.259 mmol/L/hr) compared to untreated iPSC-BMECS (0.20 mmol/L/hr, 95% CI = 0.174-0.229 mmol/L/hr). A similar trend was observed for lactate, which was

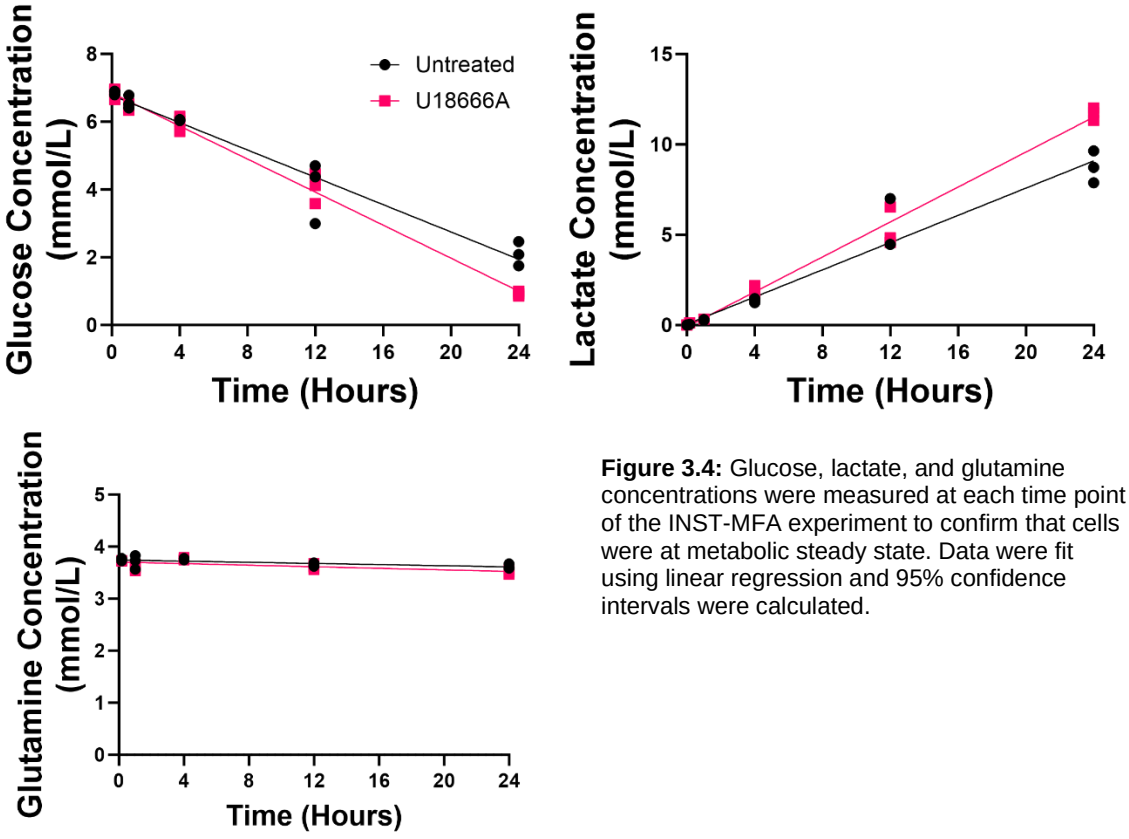

Figure 3.4: Glucose, lactate, and glutamine concentrations were measured at each time point of the INST-MFA experiment to confirm that cells were at metabolic steady state. Data were fit using linear regression and 95% confidence intervals were calculated.

secreted at a rate of 0.484 mmol/L/hr (95% CI = 0.458-0.510 mmol/L/hr) in U18666A-treated iPSC-BMECs while at a rate of 0.377 mmol/L/hr (95% CI = 0.336-0.418 mmol/L/hr) in untreated iPSC-BMECs. In contrast, glutamine uptake was not significantly different between the treatment conditions (0.007 mmol/L/hr in U18666A-treated iPSC-BMECs vs. 0.005 in untreated iPSC-BMECs).

Examination of isotope labeling patterns confirmed that iPSC-BMECs reached isotopic steady state by about 12 hours. Most of the glycolytic, PPP, and TCA cycle metabolites did not significantly change labeling patterns after 12 hours (Figure 3.5). Together, these data show that our experimental conditions are sufficient to perform both iMFA and INST-MFA in iPSC-BMECs. In addition to being exempt from isotopic steady state requirements, INST-MFA provides additional precision, particularly for reversible and cyclic fluxes, which sometimes cannot be accurately deciphered with just steady-state iMFA. For these reasons, I incorporated data from all time points for INST-MFA analysis of the [1,2-$^{13}C_2$] glucose labeled iPSC-BMECs.

INST-MFA flux output showed large changes in glucose flux into glycolytic side branch pathways and the TCA cycle (Figure 3.6). Glycolytic fluxes increased in U18666A-treated cells. Glucose to G6P flux increased by 1.12-fold, G6P to F6P flux increased by 1.08-fold, and pyruvate to lactate flux increased by 1.34-fold. PPP flux increased 1.61-fold in U18666A treated cells, while pyruvate entry into the TCA cycle decreased to 0.54-fold in U18666A treated cells. I also observed large increases in HBP pathway fluxes in U18666A treated cells, which were predicted to be near zero in the untreated cells.

All TCA cycle fluxes decreased to between 0.55-0.75-fold in U18666A-treated cells. The only exception was pyruvate carboxylation into oxaloacetate, which increased 1.15-fold with U18666A treatment. The forward isocitrate dehydrogenase (IDH) flux, which catalyzes α-ketoglutarate formation from citrate, dropped to 0.72-fold in U18666A treated cells (Appendix 1), while citrate export out of the mitochondria into the cytosol dramatically increased. In contrast, the malate shuttle, which was active in untreated iPSC-BMECs, shut down to near zero flux. Glutamine flux slightly increased, however, glutamine-derived carbons appeared to flow into glutathione and GABA synthesis primarily. There was no net flow of glutamine-derived carbons into the TCA cycle, as alpha ketoglutarate (AKG) was used to generate glutamate, which was the opposite flux direction of that observed in untreated iPSC-BMECs.

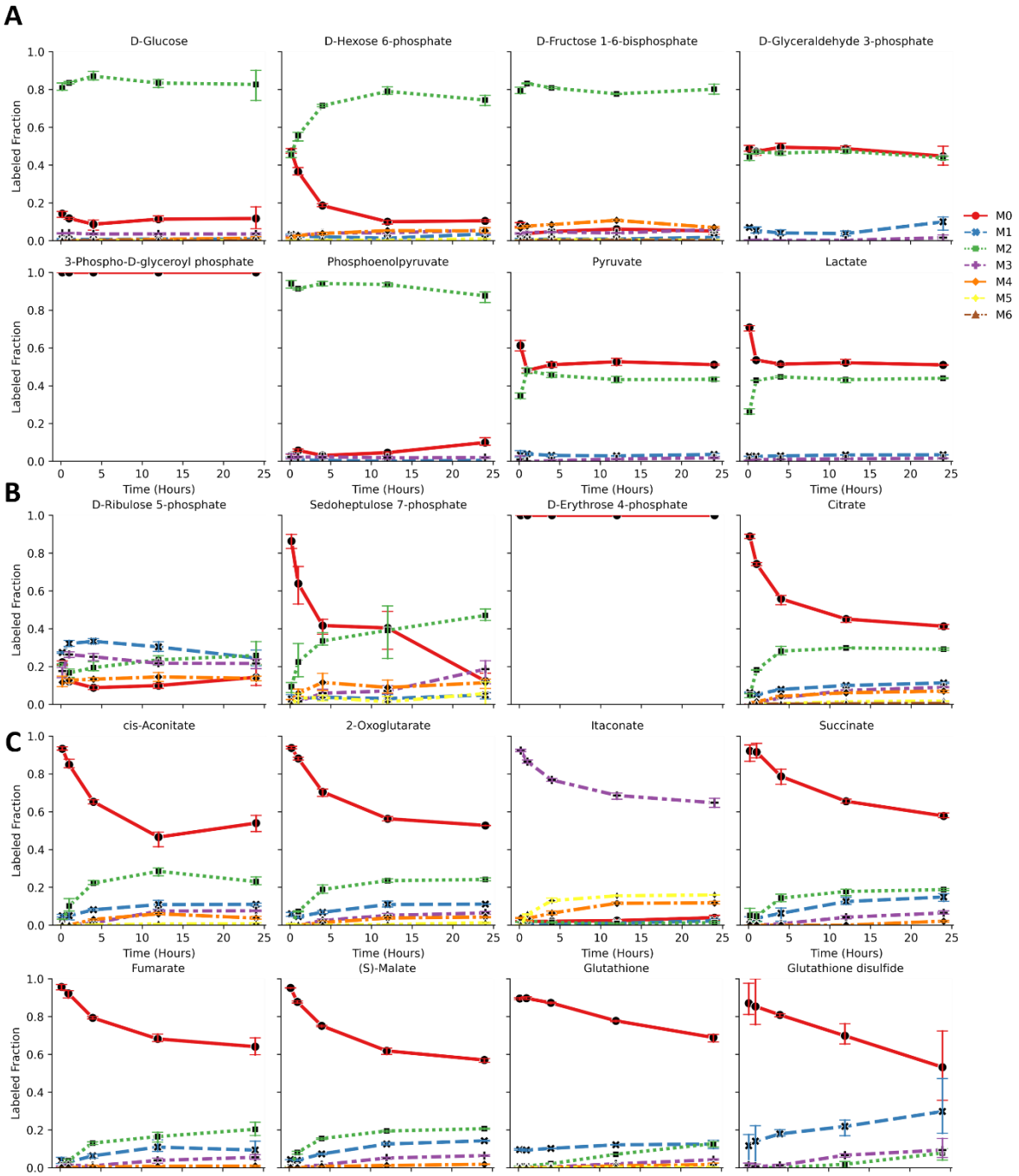

Figure 3.5. [U^{13}C$_{1,2}$]-labeled iPSC-BMECs achieved isotopic steady-state within 24 hours of labeling in core metabolic pathways. Each panel shows the labeled fraction of each isotopomer in (A) glycolytic, (B) pentose phosphate pathway (PPP), and (C) TCA pathways following labeling with [U^{13}C$_{1,2}$] glucose. Cells were lysed at 10 minutes, 1 hour, 4 hours, 12 hours, and 24 hours following labeling. Isotopomers were corrected for natural isotope abundance. All data shown represent mean +/- SD.

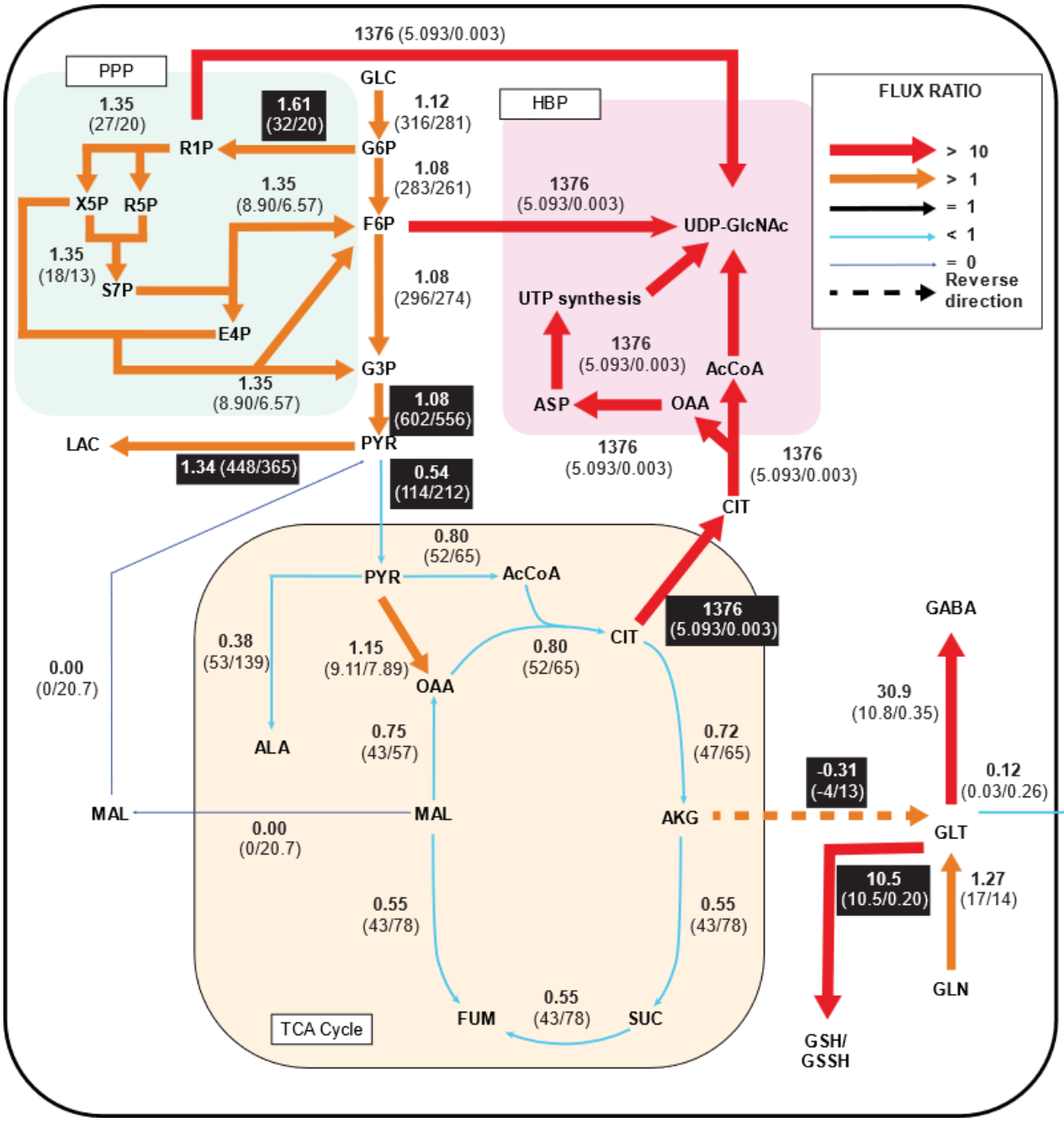

Figure 3.6. Nonstationary 13C Metabolic Flux Analysis (INST-MFA) indicated upregulated fluxes in glycolytic side branches but diminished glucose entry into mitochondria. Metabolic flux map for U18666A treated iPSC-BMECs. Arrow thickness and colors indicate relative flux ratio (defined as U18666A-iPSC BMEC flux value/untreated iPSC-BMEC flux value). Flux ratios are noted next to arrow and the flux values from U18666A-iPSC BMEC cells and untreated iPSC-BMECs are shown in parenthesis either next to or underneath the flux ratio. Blue arrows indicate reactions where U1866A-treated cells had zero or close to zero flux while untreated cells were estimated to have non-zero flux. Bright red arrows indicate reactions where there was at least a 10-fold increase in U18666A-treated cells. Dashed arrows indicate reactions in U18666A that reversed net flux direction from untreated cells. Fluxes in black boxes indicate reactions where flux intervals did not overlap between the two groups.

3.3.5. U18666A similarly decreased hpBMEC glycolysis and oxidative respiration

I then investigated whether U18666A-induced metabolic changes also occurred in human primary BMECs (hpBMECs) to determine if U18666A effects were exclusive to iPSC-BMECs. Similar to iPSC-BMECs, hpBMEC increased glycolysis, although the changes were not statistically significant. Glucose uptake increased by approximately 10% ($p = 0.0538$) and lactate secretion by 11% ($p = 0.0527$). I did not observe any changes in the lactate:glucose ratio (Figure 3.7A-C). Basal OCR decreased by nearly 60% ($p < 0.0001$) (Figures 3.7D,3.7E) and maximal respiratory and spare respiratory capacity decreased by

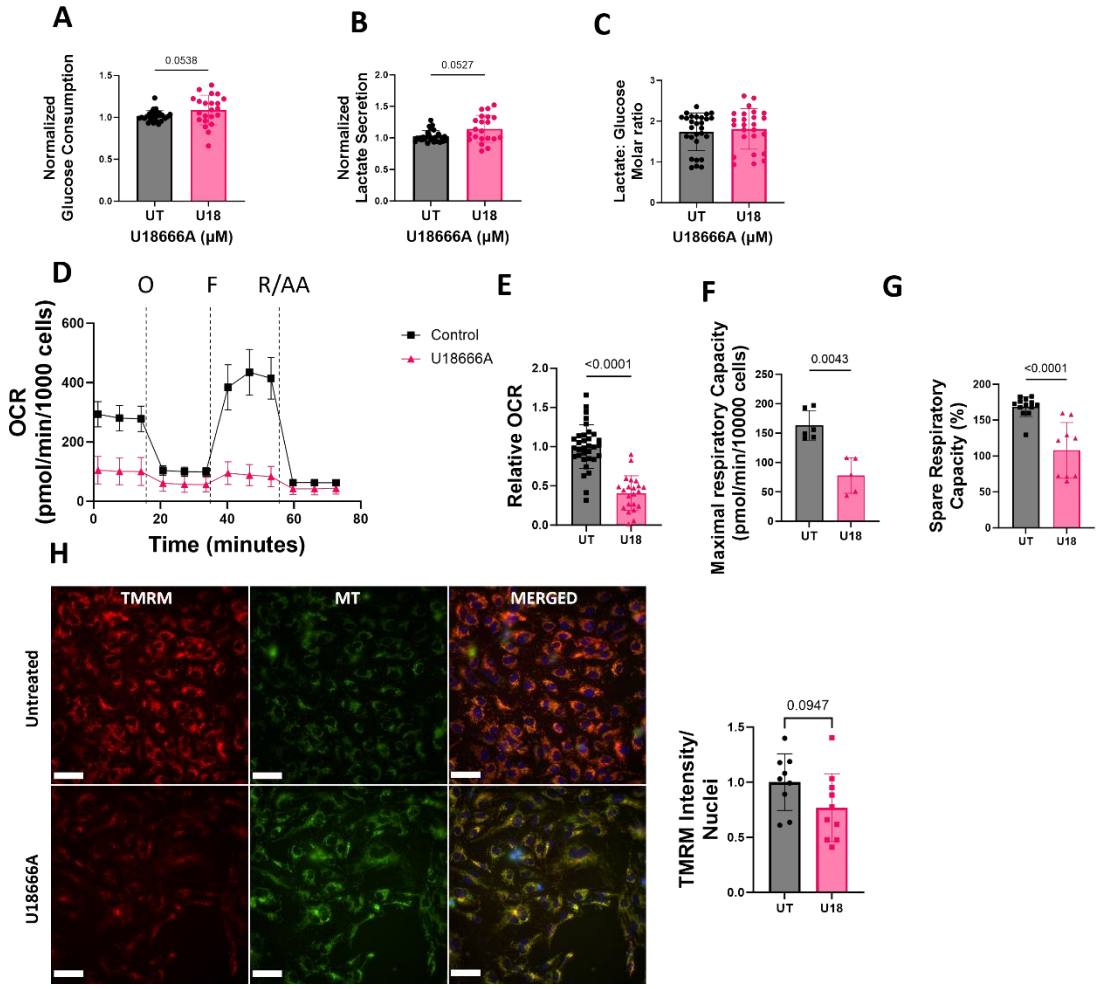

Figure 3.7. U18666A-treatment in primary hpBMECs replicated mitochondrial dysfunction. (A) Glucose uptake, (B) lactate secretion, and (C) lactate: glucose ratio in human primary BMECS (hpBMECs) following treatment with 10 μM U18666A, measured with a YSI bioanalyzer. (D) Representative OCR for hpBMECs treated with 10 μM U18666A for 24 hours, measured using a Seahorse Mito Stress assay. Quantification of (E) basal OCR, (F) respiratory capacity (n=5) (G) maximal respiration rate for hpBMECs treated with U18666A (n=13). Tetramethylrhodamine (TMRM) staining was used to quantify mitochondrial potential in iPSC-BMECS treated with U18666A. Mitochondria imaged with Green MitoTracker. Scale bar = 20 μM. Representative images and quantification shown from 3 different experiments (n=9). All data shown with mean +/- standard deviation. Mann-Whitney test used when comparing two groups.

more than 50% (Figure 3.7G). TMRM intensity per cell decreased by more than 30%, although this was not statistically significant ($p = 0.0947$) (Figure 3.7H).

To further determine how cholesterol depletion impacts glucose metabolism in hpBMECs, I labeled hpBMECs with uniformly labeled glucose (U-$^{13}C_6$-glucose) for 24 hours and analyzed the isotopomers. I selected [U-$^{13}C_6$]-glucose to improve our analysis of the HBP, which was predicted to have higher flux in the iPSC-BMEC INST-MFA. Principal component analysis showed clear separation of isotopomers across Component 1 (46.6%, Figure 3.8A).

I then examined glycolytic side branch pathway metabolites and found that the hpBMEC trends differed from those observed in iPSC-BMECs. Although I were unable to detect R5P in these samples, I did detect M+5 ribose-1-phosphate (R1P), which is readily interconverted to R5P. M+5 R1P labeled fraction decreased 0.87 fold ($p = 0.0022$), in U18666A-treated hpBMEC whereas it had increased in U18666A-treated iPSC-BMEC. Similarly, I observed decreased labeling of M+5 uridine diphosphate (UDP) (0.14-fold, $p < 0.0001$), which is derived from R5P through phosphoribosyl diphosphate. M+5 UDP-GlcNAc and M+5 UDP-Glucose, which represent incorporation of M+5 UDP, also decreased 0.18-fold ($p < 0.0001$) and 0.67-fold ($p < 0.0053$), respectively, in U18666A-treated hpBMEC (Figure 3.8E-F). Finally, M+6 UDP-GlcNAc ($p < 0.0001$), which occurs when labeled F6P enters the HBP, increased 2.12-fold and M+6 UDP-Glucose, which is sourced from fully labeled G6P that directly enters glycogen synthesis, increased 1.84-fold in U18666A-treated hpBMEC. The observation of increased UDP-Glucose labeling did not align with our observation of decreased UDP-glucose labeling in iPSC-BMECs (Figure 3.2E). Overall, labeling in glycolytic side branches shows decreased labeling of PPP and UDP-derived intermediates (which was the opposite of our observations in iPSC-BMECs) but increased labeling of HBP metabolites. There was also decreased labeling in all TCA metabolites (Figure 3.8B), which was similar to what was observed in U18666A-treated iPSC-BMEC. These data suggest that there was decreased entry of glucose-derived carbons into the TCA cycle in hpBMECs treated with U18666A.

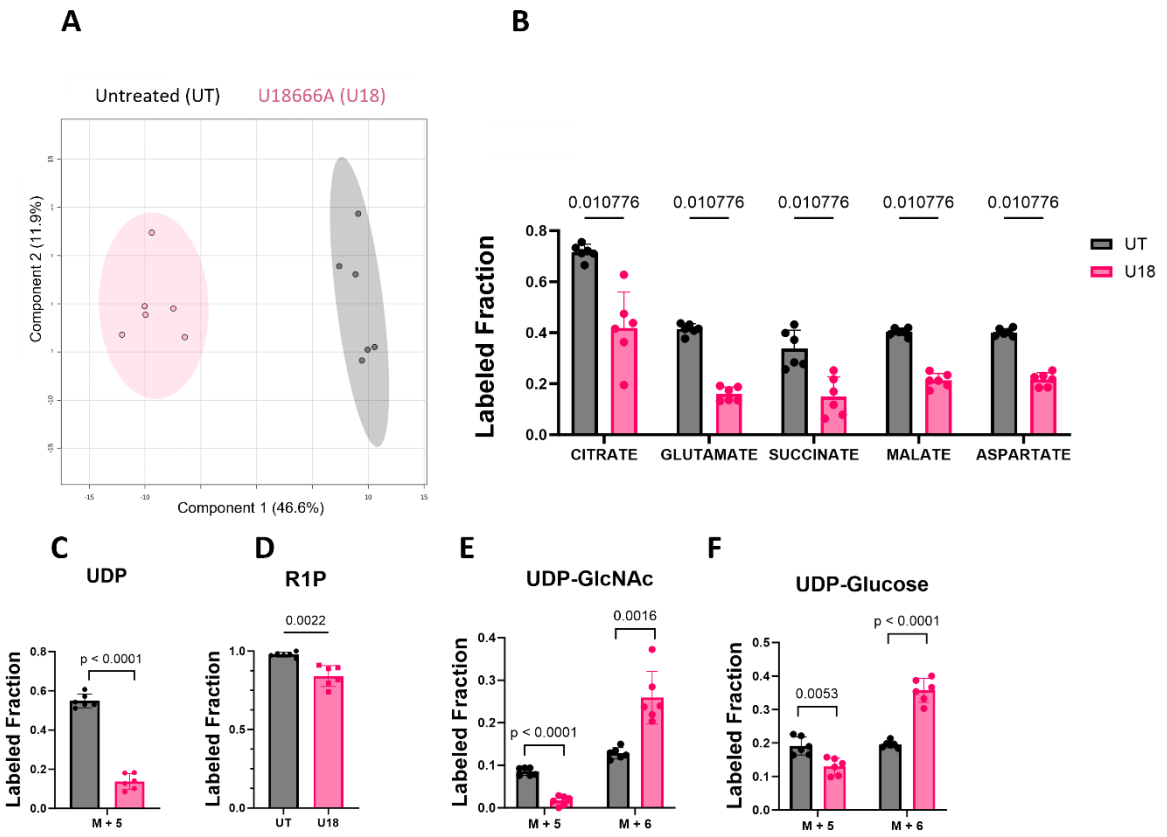

Figure 3.8. [U$^{13}C_6$] glucose labeling demonstrated that U18666A treatment in hpBMECs induced mitochondrial dysfunction but had differential flux activity in glycolytic side branches compared to U18666A-treated iPSC-BMEC. (A) Principal component analysis (PCA) score plots performed on total ion isotopomers from untreated and U18666A-treated hpBMECs as quantified by LC-MS (B) Total labeled fraction for TCA metabolites. Total labeled fraction was calculated by taking the sum of all labeled isotopomers and dividing by the sum ion count of all isotopomers. Statistical significance determined by 2-way ANOVA followed by two-stage linear step-up procedure of Benjamini, Krieger, and Yekutieli to correct for multiple comparisons (C) Labeled fraction of m + 5 isotopomers from ribose-1-phosphate (R1P). M + 5 and M + 0 were the only identified isotopomers for this metabolite. (D) Labeled fraction of M + 5, which is derived from phosphoribosyl diphosphate (PRPP), an intermediate of the pentose phosphate pathway (PPP). (E) Quantification of M + 5 UDP-N-Acetyl-Glucosamine (UDP-GlcNAc), which is indicative of M + 5 UDP combining with unlabeledN-acetylglucosamine 1-phosphate, and M + 6 UDP-GlcNAc, which is formed from direct entry of uniformly labeled glucose into the hexosamine biosynthetic pathway (HBP) via fructose-6-phosophte. (F) UDP-Glucose, a glycogen precursor, is formed from glucose-6-phosphate. M + 5 UDP-glucose indicates incorporation of labeled M + 5 UDP while M + 6 UDP-glucose indicates direct influx of G6P towards glycogenosis. Each data point was normalized to mean of untreated group for each experiment. Data shown are mean +/- SD (n=6). Statistical significance was determined by non-parametric Mann Whitney test.

3.3.6. U18666A changed intracellular abundance and exometabolomic profiles in both iPSC-BMECs and hpBMECs

I then examined the intracellular metabolomic concentrations derived from untargeted mass spectrometry of the samples from the [1,2-$^{13}C_2$] labeling experiment. Intracellular concentration data can be used to validate our INST-MFA results, which predicted decreased flux activity in TCA fluxes, while the

untargeted nature of this analysis allows us to get a more complete picture of the metabolomic changes that occur in these cells. Using PLS-DA to identify metabolites that robustly showed differences across all time points, I identified several metabolites that decreased in iPSC-BMECs treated with U18666A. I observed clear separation between the two treatments across all time points and there was no clear separation between time points within the treatments (Figure 3.9A). Using the VIP score plot, I identified three TCA metabolites (citrate, 2-oxoglutrate/alpha-ketoglutarate, and succinate) were highly ranked and all three were found to decrease in U18666A-treated iPSC-BMECs (Figure 3.9B). Citrate decreased by approximately 53% ($p<0.0001$), AKG by 39% ($p<0.0001$) and succinate by 42% ($p<0.0001$) (Figure 3.9C).

Carnitines are critical metabolites involved in fatty oxidation and mitochondrial function [31]. Interestingly, 7 of the top 20 ranked metabolites were carnitine derivates that all decreased with U18666A treatment. Specifically, L-carnitine decreased by 25% ($p = 0.0025$), propionylcarnitine (acyl-C3) decreased by 87% ($p<0.0001$), butrylcarnitine (acyl-C4) decreased by 49% ($p<0.0001$) in U18666A-treated iPSC-BMECs (Figure 3.9B, 3.9D).

Since BMECs secrete metabolites into the brain, I examined the extracellular metabolomic (exometabolomic) profile of iPSC-BMECs treated with U18666A. At 24 hours, I observed significant decreases in secretion of pyruvate (32%, $p < 0.0001$), citrate (48%, $p<0.0001$), α-ketoglutarate (31%, $p<0.0001$), and succinate (37%, $p = 0.0021$) (Figure 3.9E). Decreases were also observed for secretion of acetylcarnitine (43%, $p<0.0001$), propionylcarnitine (93%, $p<0.0001$), and butyrylcarnitine (43%, $p<0.0171$) (Figure 3.9F).

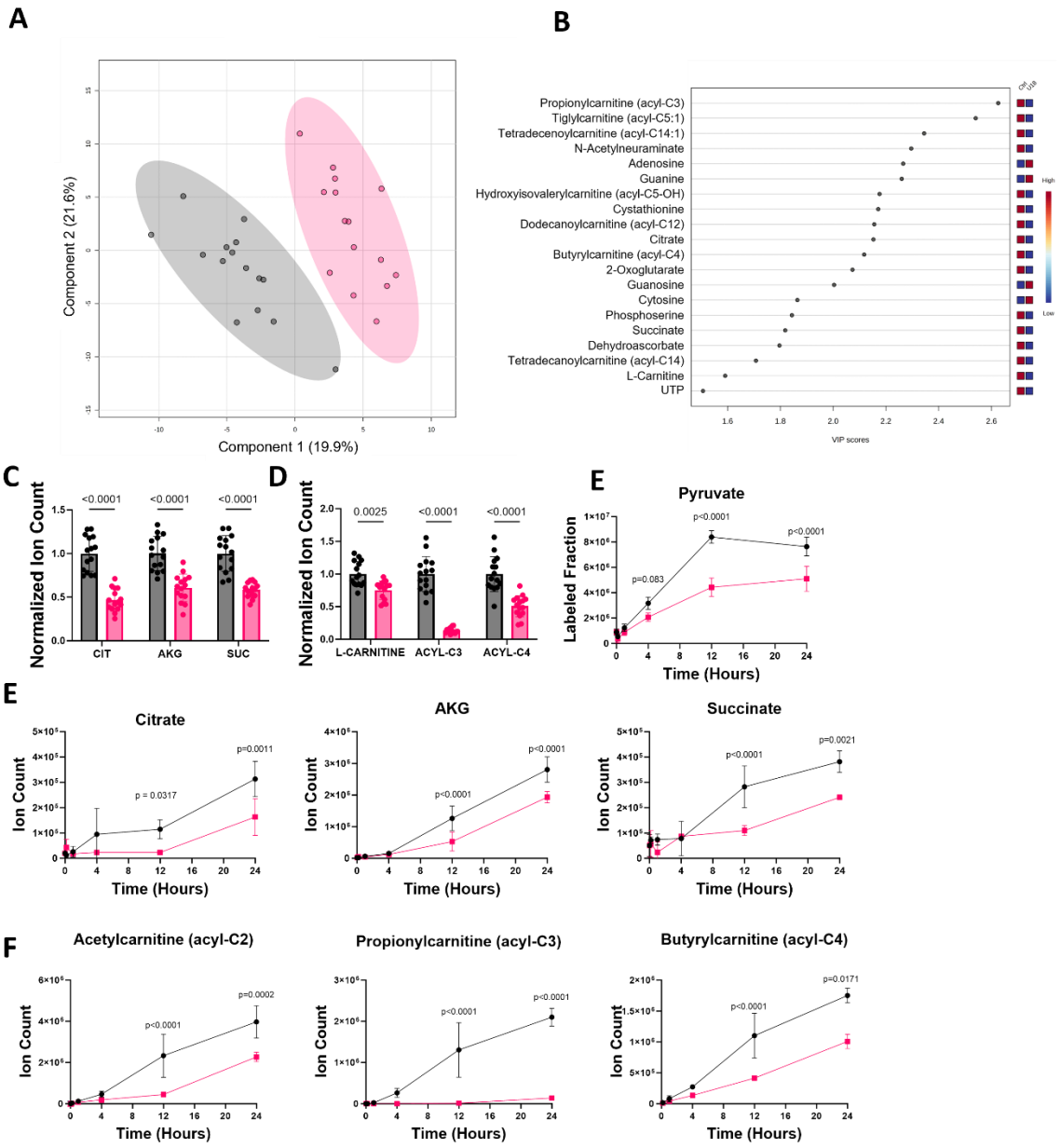

Figure 3.9. U18666A-treated iPSC-BMECs had altered intracellular and exometabolomic profile. (A) PLS-DA analysis of intracellular metabolomic profiles from iPSC-BMECs. PLS-DA was generated from intracellular metabolomic abundance data pooled from all samples and time points (n = 3 per time point and treatment, n = 15 per group). (B) Corresponding variable importance in projection (VIP) score plots highlight top 20 highest ranked metabolites and their relative differences between the two groups. (C) Normalized ion count data for intracellular pools of citrate (CIT), alpha-ketoglutarate (AKG), and succinate (SUC). Data pooled from all 5 time points and normalized to mean of respective time point. Statistical significance determined by non-parametric Mann Whitney test. (D) Normalized ion count data for intracellular pools of L-carnitine, propionylcarnitine (ACYL-C3), and butyrylcarnitine (ACYL-C4). Data pooled from all 5 time points and normalized to mean of respective time point. Statistical significance determined by non-parametric Mann Whitney test. (E) Ion count of citrate, alpha-ketoglutarate, and succinate in extracellular media. (F) Ion count of carnitines in extracellular media. For all extracellular metabolites, baseline ion count from unconditioned media was subtracted to correct for background and presence of metabolites in media. Statistical significance determined by 2-way ANOVA followed by two-stage linear step-up procedure of Benjamini, Krieger, and Yekutieli to correct for multiple comparisons. All data shown are mean +/- SD.

3.3.7. HPβCD partially restored metabolic phenotype in U18666A-treated iPSC-BMECs

I then tested whether co-treating U18666A-treated iPSC-BMECs with HPβCD, which releases cholesterol from the lysosome [16,21,22], reversed the altered extracellular and intracellular metabolic phenotypes HPβCD reduced glucose consumption and lactate secretion in U18666A-treated iPSC-BMEC by approximately 13% (p = 0.0056) and 15% (p = 0.1071), respectively (Figure 3.10A, B). Although

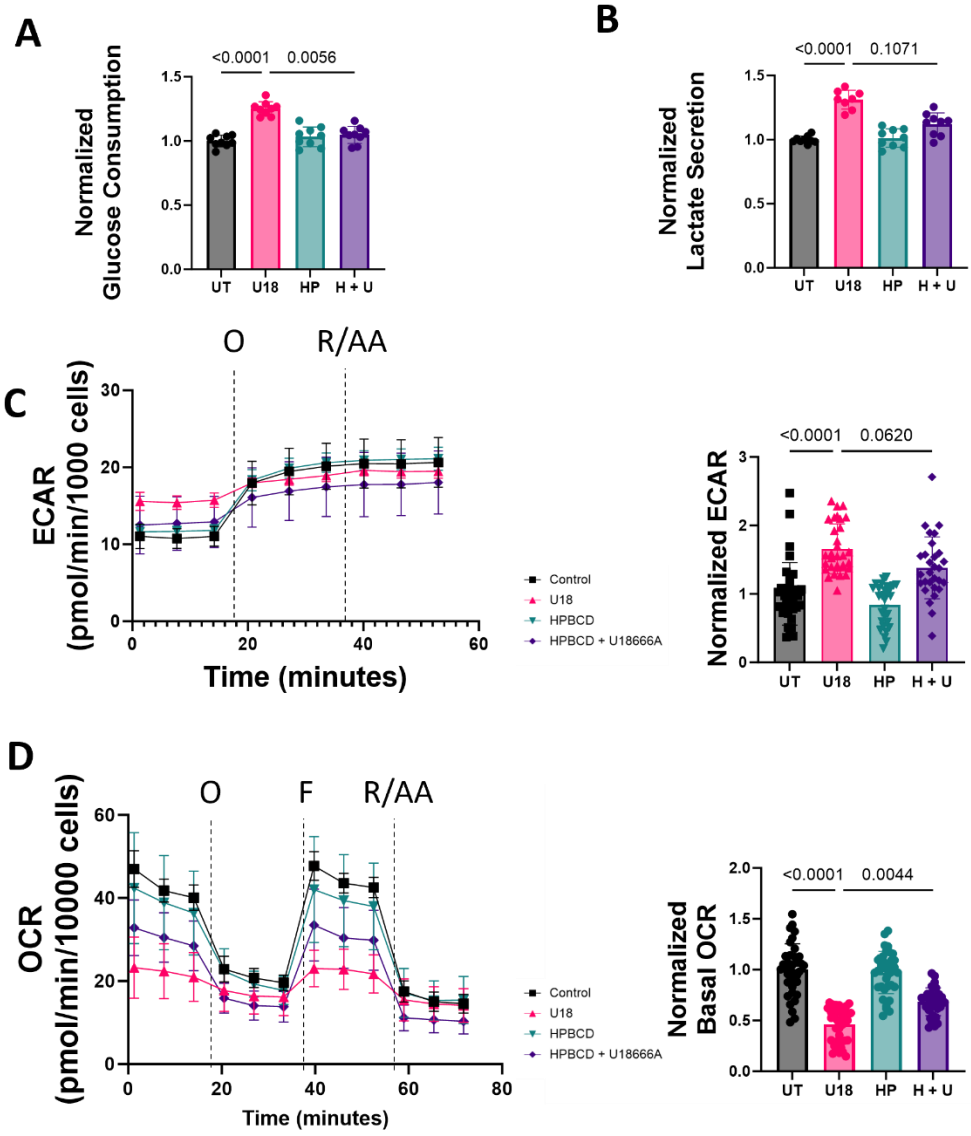

Figure 3.10. HPBCD partially restored metabolic fluxes in U18666A-treated iPSC-BMECs. YSI measurements of (A) glucose and (B) lactate (n= 9). (C) Extracellular acidification rate (ECAR) as quantified by Seahorse ATP Rate assay. Cells were injected with oligomycin and rotenone/antimycin A at specified time intervals. Quantification of basal ECAR from three independent experiments (n=31-33). (D) Oxygen consumption rate (OCR) as quantified by Seahorse Mito Stress Test. One representative experiment shown (n=6 per group). Oligomycin (O), FCCP (F), and Rotenone/Antimycin A (R/AA) were injected at specified time intervals. Quantification of basal normalized OCR pooled from four independent experiments (n= 31-36). Statistical significance was determined by Kruskal-Willis non-parametric test.

HPβCD decreased glucose uptake and lactate secretion (Figures 3.10A, 3.10B), it did not have a significant effect on ECAR (Figure 3.10C). HPβCD partially restored OCR, raising values to approximately 68% of the untreated cell levels ($p < 0.005$; Figure 3.10D).

I then examined changes in intracellular metabolism to determine whether HPβCD restored intracellular metabolites. PLS-DA demonstrated that HPβCD treatment appeared to partially restore the

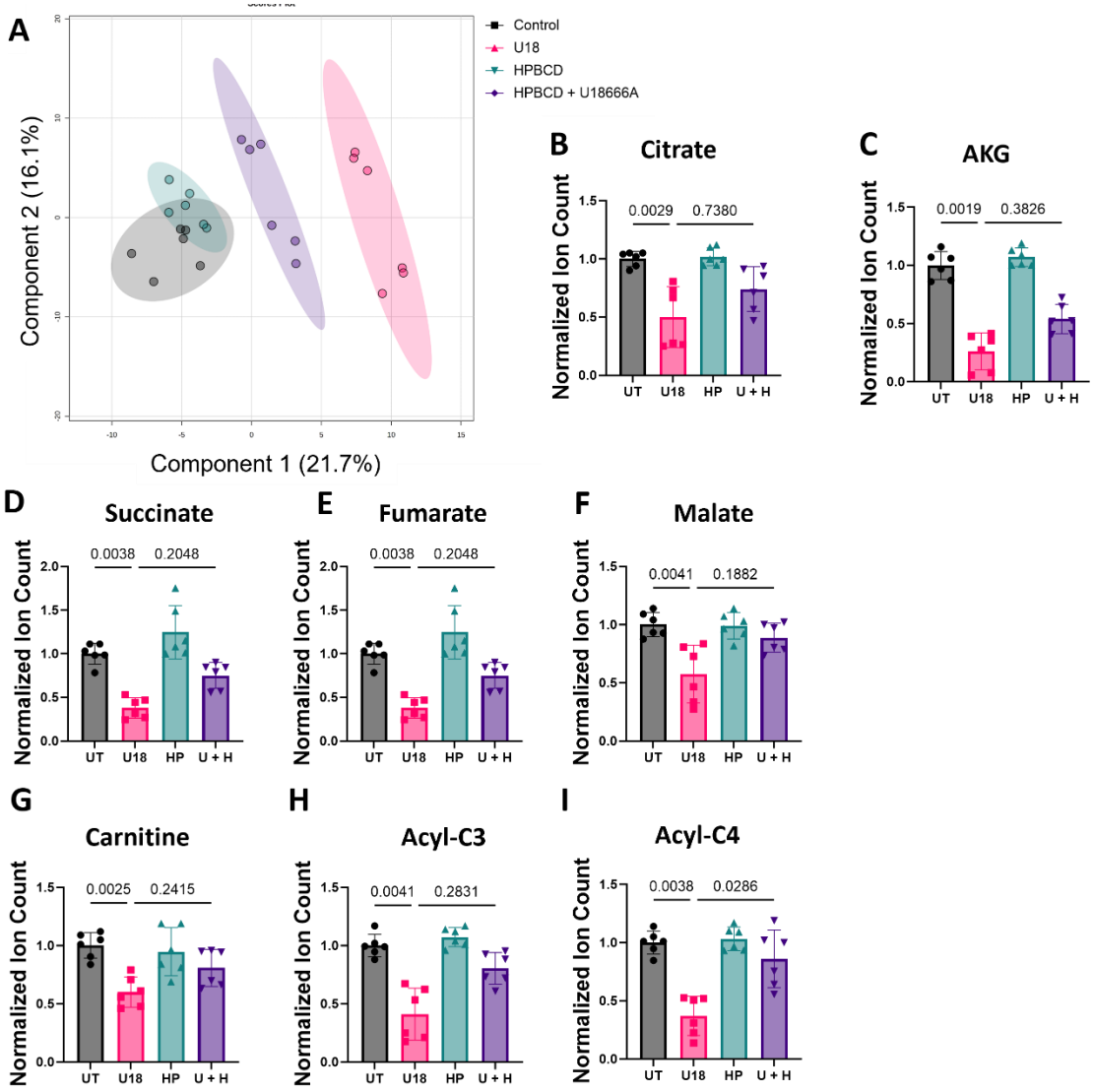

Figure 3.11. HPBCD partially restored intracellular metabolic phenotype in U18666A-treated iPSC-BMECs. (A) Principal component analysis (PCA) score plots performed on total ion abundance data for metabolite and sample quantified by LC-MS. Data shown is from two independent experiments (n=6) Normalized ion count for tricarboxylic acid (TCA) metabolites (D) citrate (E) alpha-ketoglutarate (AKG) (F) succinate (G) fumarate and (H) malate. Normalized ion counts for (I) L-carnitine (J) propionylcarnitine (acyl-C3) and (K) butyrylcarnitine (Acyl-C4) All data pooled from two independent experiments (n=6). One-way non-parametric Kruskal-Willis followed by Dunn's MCT was used to compare multiple groups. All data shown as mean +/- SD. All data shown are mean +/- SD. Each data point was normalized to mean of untreated group for each experiment.

metabolomic profile of U18666A treated BMECS closer to that of untreated BMECs (PC1 = 21.7%, Figure 3.11A). HPβCD partially restored intracellular TCA metabolite abundances, although this was not statistically significant (Figures 3.11B-3.11F). A similar trend was observed with L-carnitine (Figure 3.11G) and propionylcarnitine (Figure 3.11H), while I did observe significant increase and restoration of butyrylcarnitine levels with HPβCD treatment (Figure 3.11I).

Co-treatment with HPβCD also restored the sterol profile to untreated levels (Figure 3.12). Pregnenelone, which is generated from cholesterol in the inner mitochondrial membrane, increased approximately 18-fold ($p < 0.005$) in U18666A-treated cells but decreased to 1.8-fold of untreated cells when iPSC-BMEC were co-treated with HPβCD ($p < 0.01$). Similar patterns were observed for the lumisterol and androsterone.

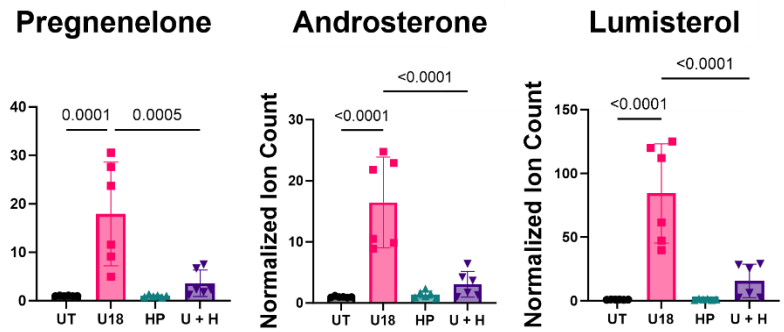

Figure 3.12. HPβCD attenuated U18666a-induced steroid accumulation in iPSC-BMECs. Normalized ion counts for sterols as quantified by LC-MS. One-way non-parametric Kruskal-Willis followed by Dunn's MCT was used to compare multiple groups. All data are shown as mean +/- SD.

PLS-DA of the exometabolome profiles demonstrated that co-treatment with HPβCD partially shifted the exometabolomic profiles of U18666A-treated iPSC-BMECs towards the untreated phenotype (Figure 3.13A). HPβCD elevated secreted propionylcarnitine by 3-fold ($p = 0.0862$) while it increased butyrylcarnitine by 1.9-fold ($p = 0.0744$) (Figure 3.13B, 3.13C). AKG increased ~2-fold with HPβCD treated, although this change was not significant ($p=0.31$) with HPβCD treatment (Figure 3.13D). Choline, an important substrate for the neurotransmitter acetylcholine [195], increased by 53% ($p=0.0023$) with U18666A treatment but was partially decreased with HPβCD (Figure 3.13E). Dopamine, another neurotransmitter, also increased 35% with U18666A treatment ($p=0.0286$) but was reduced to untreated levels with HPβCD (Figure 3.13F).

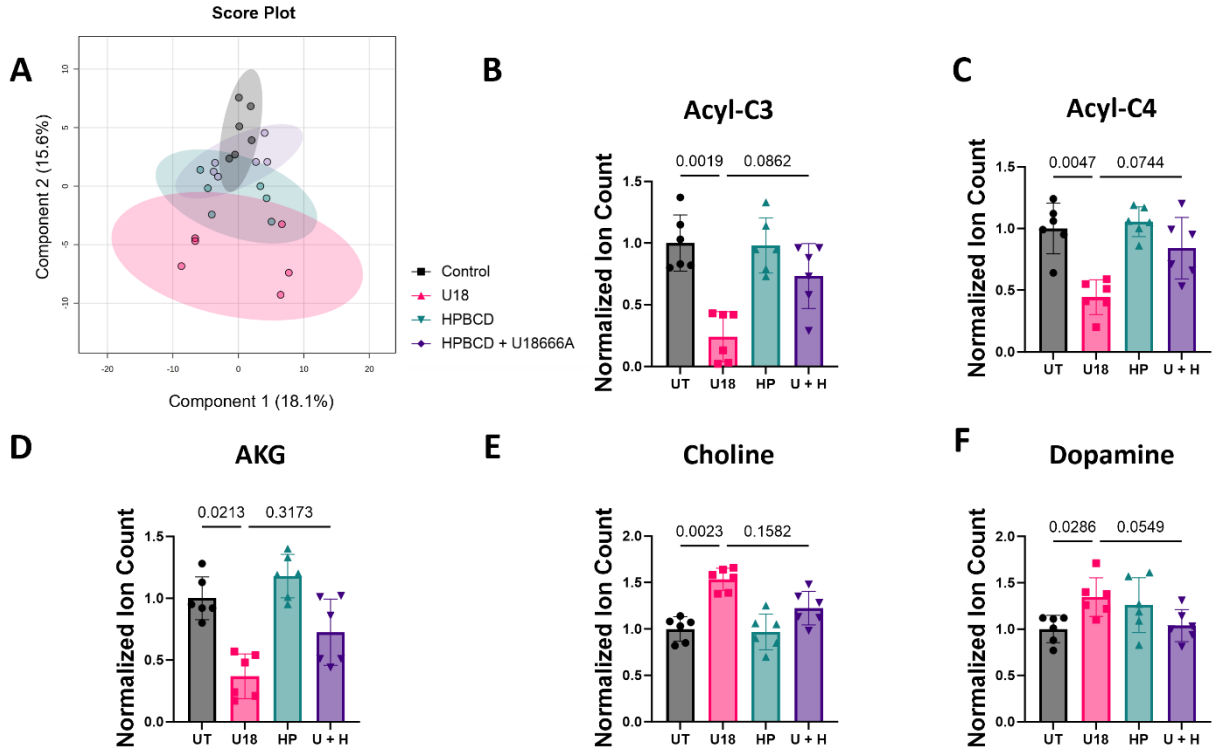

Figure 3.13. HPβCD partially restored metabolic fluxes in U18666A-treated iPSC-BMECs. (A) PCA of exometabolomic data from all groups (n=6). (D) Ion abundance in media for (D) propionylcarnitine (acyl-C3) (E) butyrylcarnitine (Acyl-C4), (F) AKG, (G) choline, and (H) dopamine. (n=6 samples from two independent experiments). One-way non-parametric Kruskal-Willis followed by Dunn's MCT was used to compare multiple groups. All data shown are mean +/- SD. Each data point was normalized to mean of untreated group for each experiment.

3.3.8. Inhibiting glycolysis attenuated U18666A-induced changes in barrier integrity

I previously showed that U18666A induced BMEC barrier dysfunction (Chapter 2). I therefore tested whether preventing U18666A-induced changes in glycolysis would prevent altered iPSC-BMEC barrier function. U18666A-treated iPSC-BMECs were co-treated with 50 mM 2-deoxy-D-glucose for 48 hours, and barrier integrity was quantified with both transendothelial electrical resistance (TEER) and sodium fluorescein permeability. iPSC-BMECs treated with U18666A had 85% lower TEER, 1.9-fold higher clearance volume, and 3.3-fold higher permeability coefficient than untreated cells. When I inhibited glycolysis in U18666A treated cells with 50 mM 2-deoxyglucose (2-DG), a glucose analog that competitively inhibits phosphoglucose isomerase [196], TEER increased by 4.51-fold, clearance volume decreased to that in untreated cells, and permeability coefficient decreased by 5-fold (Figure 3.14A-D).

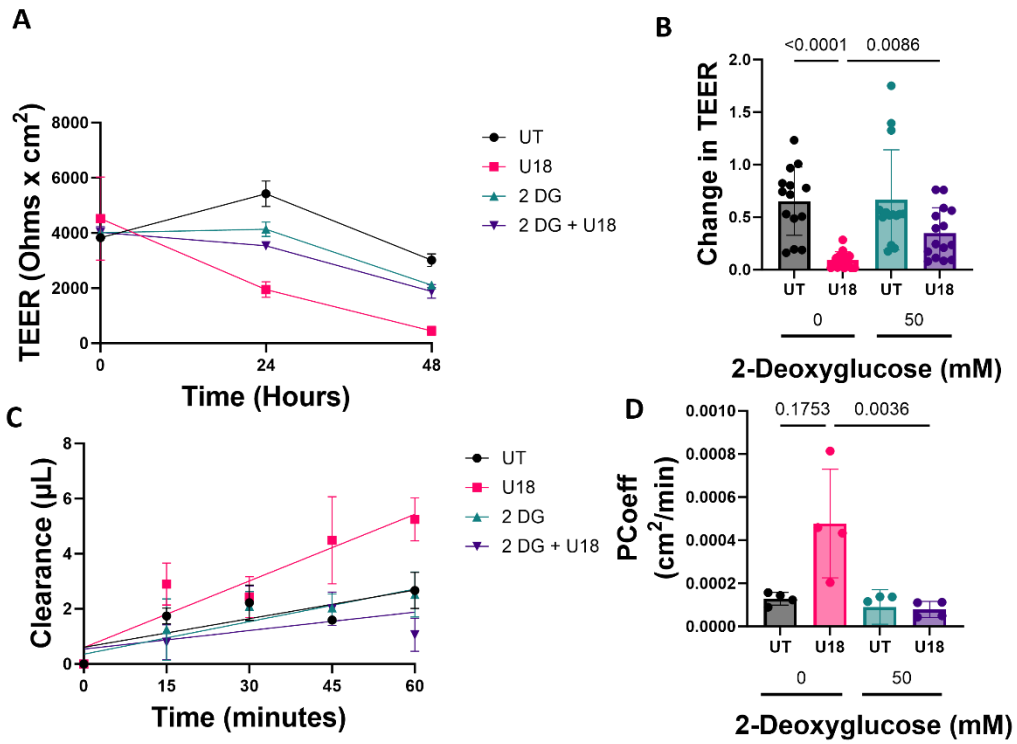

Figure 3.14. HPBCD partially restored intracellular metabolic phenotype in U18666A-treated iPSC-BMECs. (A) Principal component analysis (PCA) score plots performed on total ion abundance data for metabolite and sample quantified by LC-MS. Data shown is from two independent experiments (n=6). Normalized ion counts for tricarboxylic acid (TCA) metabolites (D) citrate (E) alpha-ketoglutarate (AKG) (F) succinate (G) fumarate and (H) malate. Normalized ion counts for (I) L-carnitine (J) propionylcarnitine (acyl-C3) and (K) butyrylcarnitine (Acyl-C4). All data pooled from two independent experiments (n=6). One-way non-parametric Kruskal-Willis followed by Dunn's MCT used to compare multiple groups. All data shown as mean +/- SD. Each data point was normalized to mean of untreated group for each experiment.

3.4. Discussion

BMECs play a crucial role in maintaining metabolic homeostasis in the brain by dictating both influx and efflux of nutrients and other macromolecules in the brain. For this reason, it is crucial to evaluate their metabolic phenotypes in neurodegenerative diseases such as NP-C and other inherited cholesterol disorders. In this study, I examined how BMEC metabolism was altered following treatment with the NPC1 inhibitor U18666A. Through isotope labeling experiments, I observed that NPC1 inhibition increased glycolysis and flux into glycolytic branch pathways. I also observed disruption of mitochondrial respiration and membrane potential, which suggested significant mitochondrial dysfunction. U18666A treatment also abolished acyl-carnitine levels and altered the exometabolomic profile of iPSC-BMECs.

Finally, I found that HPβCD treatment appeared to partially restore metabolic phenotype in iPSC-BMECs while treating with glycolytic inhibitor 2-DG partially restored barrier function. Together, these data suggest that increased glycolytic metabolism can induce barrier dysfunction in U18666A-treated iPSC-BMECs and highlight a potential target to restore barrier function in NP-C.

NPC1 inhibition increased glycolytic flux in iPSC-BMECs, which aligns with reports of increased glycolysis following NPC1 inhibition in other cell types and animal models [182,191]. Metabolomic analysis of NPC1-null mice cerebellar tissue at presymptomatic (3 weeks old), early symptomatic (5 weeks old), and late stage (7 weeks old) phases of the disease course showed evidence for major differences in glycolysis. NPC1-null mice across all ages showed elevated lactate and decreased acetyl-CoA, which in brain tissue is primarily source by pyruvate decarboxylation in the mitochondria. In 5-week-old mice, gene expression of PDH (which catalyzes mitochondrial decarboxylation of pyruvate into acetyl-CoA) decreased; while PFK1, LDHA, PDH kinase (which inhibits PDH) and pyruvate carboxylase (which converts pyruvate to oxaloacetate in the mitochondria) increased. Two forms of malic enzyme (which shuttles malate from the mitochondria for conversion into pyruvate) also decreased in 3-week-old mice [182]. Microglia from NPC1-KO mice also show an increasingly glycolytic phenotype, as evidenced by increased ECAR and expression of glycolytic genes such as glyceraldehyde-3-phosphate dehydrogenase (GAPDH) [168]. Similarly, inhibition of NPC1 in CHO cells was also found to increase lactate secretion [191]. Our data show remarkable similarities with these previous reports of glycolytic phenotypes in NPC1-deficient cells. I also observed increased lactate secretion, glycolytic gene expression and ECAR in iPSC-BMECs. Interestingly, our INST-MFA model predicted decreased PDH and malate shuttle activity but increased pyruvate carboxylase flux, which align well with gene expression observed in NPC-1 null mice [182].

Both qualitative analysis of isotopomers and quantitative analysis with INST-MFA suggest increased PPP flux in U18666A-treated iPSC-BMECs. Increased [M+1] R5P strongly indicates increased PPP flux at the G6PDH branchpoint. Further evidence for increased PPP is provided from analysis of UDP-glucose, a key substrate for glycogen synthesis which competes with the PPP for G6P substrate. Specifically, I observed a decrease in UDP-glucose labeling, which is primarily formed from G6P entering glycogen synthesis. An alternative source of [M+2] UDP-glucose can be derived from [M+2] labeled UDP;

however, I did not observe any changes in [M+2] labeled UDP between the U18666A-treated and untreated iPSC-BMECs (data not shown). This decreased flux in glycogen synthesis further suggests that G6P is being diverted towards a competitive pathway such as the PPP. Increased [M+2] labeling in GAP often indicates decreased flux into the PPP branchpoint and initially appeared to contradict the labeling observed for R5P and UDP-Glucose. Inconsistent labeling can be resolved through INST-MFA. Although I did not fit GAP into the INST-MFA model, I did also observe increased [M+2] in lactate and pyruvate and fit these into the INST-MFA model. The model output high PPP and glycolytic fluxes in U18666A-treated BMECs, which suggested that the increased GAP, lactate and pyruvate [M+2] labeling may stem from increased glycolysis rather than decreased PPP activity. Furthermore, the PPP contains several cyclic and reversible steps that can lead to alternate carbon rearrangements that significantly complicate flux analysis. INST-MFA resolved these patterns and estimated net forward flux through the PPP network. Interestingly, genes involved in PPP are upregulated in microglia from NPC1-null mice [168].

Increased glycolytic and PPP flux may occur for several reasons in NPC1-deficient cells. NPC1 deficiency increases expression of cholesterol biosynthetic enzymes, including HMG-CoA reductase (*HMGCR)*, SREBF1, and SREBF2. Increased SREBF1 expression has been shown to increase expression of glycolytic genes such as hexokinase II and may therefore play a direct role in upregulating glycolysis [177,197]. Additionally, cholesterol is an energetically expensive molecule that requires several moles of ATP, NADPH, and acetyl-CoA for its synthesis. The PPP is the primary driver of NADPH production, and studies in cancer cells show that increased cholesterol biosynthesis depletes NAPDH, which then increases PPP flux [198]. The PPP may also be upregulated to combat oxidative stress, which also has been shown to increase with NPC1-deficient mouse brain tissue [14], CHO cells [25], patient-derived neurons [39], and mouse microglia [13]. Oxidative stress reduces NADPH levels, which can then induce increase PPP flux and even lead to increased glycolysis to fuel the PPP [40].

Increased glycolysis and PPP flux could alternatively be triggered by disrupted mitochondrial metabolism following U18666A treatment. Seahorse assays indicated large changes in mitochondrial respiration, and isotope labeling further showed reduced incorporation of labeled glucose into critical TCA metabolites such as citrate, α-ketoglutarate, succinate, and malate. The change in mitochondrial respiration capacity, defined as the mitochondrial capacity to meet emergent energetic needs during acute stress or

large energetic loads [41], was particularly dramatic. Although endothelial cells are highly glycolytic and generate most of their ATP from glycolysis [2], changes in mitochondrial function can still be devastating due to its role in endothelial cell signaling, angiogenesis, autophagy, and redox balance [42]. Dysfunctional mitochondria have been implicated in vascular pathologies such as atherosclerosis, particularly due to their role in increasing reactive oxygen species [43]. Notably, spare respiratory capacity is important in responding to oxidative stress in ECs, and decreased capacity may make ECs more vulnerable to ROS stress [44].

Our model also predicts increased citrate transport from the mitochondria into the cytosol, which is notable as cytosolic citrate is the primary source of acetyl-CoA for cholesterol and lipid synthesis [199]. In fact, approximately 10% of the pyruvate-derived acetyl-CoA exits the mitochondria as cytosolic citrate. Our model does predict that all cytosolic acetyl-CoA is consumed in the HBP; however, this is a limitation of the model design as UDP-GlcNAc is the only destination for cytosolic citrate in the network. Realistically, acetyl-CoA can enter multiple metabolic pathways, and it is therefore plausible that citrate-derived acetyl-CoA may instead be used to source cholesterol synthesis. At first glance, the lactate:glucose ratio does not seem to support this idea as it remains the same as untreated cells. This would typically suggest that any additional glucose is simply secreted as lactate; however, a more nuanced picture is unveiled by the INST-MFA results. While U18666A-treated iPSC-BMECs divert glucose towards intracellular metabolic pathways, they also reduce pyruvate influx into the mitochondria. As a result, U18666A-treated iPSC-BMECs present a similar lactate-to-glucose ratio to untreated cells while still diverting glucose towards intracellular pathway sinks.

Several factors could lead to the decreased mitochondrial respiration and membrane potential observed in U18666A-treated BMECs. Reduced TCA metabolite labeling indicates decreased influx of glucose-derived pyruvate into the mitochondria, increased influx of tertiary and anaplerotic sources to fuel the TCA cycle, or a combination of both. INST-MFA suggests a significant decrease in carbon supply is at fault, as pyruvate transport to the mitochondria decreased by 46% while alpha-ketoglutarate and citrate are both transported out of the mitochondria.

To test if decreased mitochondrial flux was caused by PDH inhibition, I treated U18666A-treated iPSC-BMECs with dichloroacetate (DCA), a PDH activator, but did not notice significant changes in OCR. This aligns with a previous study in NPC1-deficient CHO cells, in which minimal mitochondrial restoration was observed with DCA treatment. Mitochondrial restoration was only observed once cholesterol transport to the mitochondria was blocked by inhibiting endosomal metastatic lymph node protein 64 (MLN64), which shuttles endosomal cholesterol to the mitochondria [46]. MLN64 expression has been found to increase in *Npc1*-null mice liver tissue and NPC1-deficient CHO cells. Treatment of NPC1-deficient CHO cells with MLN64-siRNA reduced mitochondrial cholesterol and restored mitochondrial membrane potential and superoxide levels [194,206]. I attempted to examine mitochondrial cholesterol in U18666A-treated iPSC-BMECs but was unable to isolate pure mitochondria without lysosomal contaminants. However, LC-MS analysis showed high pregnenolone in U18666A-treated iPSC-BMECs. Pregnenolone is synthesized from cholesterol that accumulates in the mitochondria; therefore, increased pregnenolone in U18666A-treated cells could indicate cholesterol accumulation in the mitochondria. Increases in pregnenolone were accompanied by increases of androsterone and lumisterol as well, suggesting a steroidogenic phenotype in U18666A-treated BMECs. This suggests a potential link between the steroidogenic phenotype and metabolic disruption should be explored further.

When I inhibited NPC1 in hpBMECs, I observed similar although smaller decreases in glycolysis, similar changes in mitochondrial respiration, and similar increased HBP flux. However, glucose flux into the PPP and glycogen synthesis were opposite in iPSC-BMECs and hpBMECs. I recently showed that while hpBMECs are similar to hiBMECs in terms of glucose metabolism [114], there are significant differences in other metabolic pathways, particularly glutamate metabolism, as well as mitochondrial morphology. It is possible that hpBMECs may have a higher capacity to increase NAPDH through other mitochondrial-based pathways, such as malic enzyme or isocitrate dehydrogenase, that lower or prevent their dependence on the PPP and glycolysis.

I also unexpectedly observed significant differences in both intracellular and extracellular levels of acyl-carnitines. Carnitines play essential roles in fatty acid metabolism, which is upregulated in quiescent endothelial cells [75]. Specifically, carnitines are formed when acyl-CoAs derived from fatty acids are bound to free carnitine to import them into the mitochondria. Disruption of quiescence may in turn also disrupt fatty

acid oxidation and subsequently carnitine metabolism. Carnitines are also synthesized from lysine and methionine; however, I did not observe any significant differences in these amino acids in U18666A-treated iPSCs. High levels of acyl carnitines are typically associated with mitochondrial dysfunction while deficiencies are not as well characterized [207]. A similar metabolic phenotype was previously observed in pulmonary microvascular endothelial cells with mutations in bone morphogenetic protein receptor 2 (BMPR2) [208]. These cells also showed an increase in glycolysis, decrease in carnitines, and decrease in TCA cycle intermediates [208]. Loss of BMPR2 has been shown to led to mitochondrial dysfunction [209]. Interestingly, NPC1 has been shown to be essential for BMPR2-mediated insulin signaling by acting as a scaffold to recruit BMPR2 to insulin receptor [210]. It is therefore plausible that disruption of this scaffolding interaction may perturb mitochondrial and carnitine metabolism in BMECs through a BMPR2-mediated mechanism.

My data show that HPβCD partially rescued the intracellular metabolome, including OCR, TCA metabolites, and carnitines. However, HPβCD did not significantly change ECAR. This may suggest that HPβCD can remove mitochondrial cholesterol but does not sufficiently decrease cholesterol synthetic factors such as SREBF1, which promote a glycolytic effect. There is evidence for this as HPβCD treatment reduced lumisterol, pregnenolone, and androsterone levels to that of untreated cells; however, my previous work in Chapter 2 (Figure 2.6B) only showed partial restoration of SREBF2 and HMGCR, suggesting that cholesterol biosynthetic factors are still active.

HPβCD partially restored the exometabolomic profile, specifically by decreasing glucose uptake and lactate secretion; increasing secreted propionylcarnitine, butyrylcarnitine, and AKG; and decreasing choline and dopamine secretion. Choline is an essential building block for the neurotransmitter acetylcholine, which plays vital roles in learning, memory, and neuromuscular control. NP-C patients have been characterized with significant cholinergic defects [211]. Dopamine is another critical neurotransmitter with important roles in cognition but with toxic effects through induction of oxidative stress and neuroinflammation in certain *in vitro* conditions. The altered levels of these two neurotransmitters may suggest that NPC1 can alter neurotransmitter balance in the brain, which can be partially restored with HPβCD treatment. Together,

these results show that HPβCD may exert a therapeutic effect without crossing the blood-brain barrier by attenuating disrupted BMEC metabolism.

I further found that NPC-1 inhibition decreased glucose transport across the brain endothelium. Interestingly, glucose hypometabolism has been recently observed in NP-C patients, predominantly in the posterior cingulate gyrus, and was found to correlate with clinical severity [174]. Glucose hypometabolism is typically associated with dysfunctional BBB glucose transport, typically due to decreased glucose transport levels and function. However, I observed increased glucose uptake in U18666A-treated iPSC-BMECs. While BMECS take up more glucose in NP-C, they may still contribute to brain glucose hypometabolism. NPC1 inhibition may decrease BMEC glucose transport due to increased BMEC glycolysis, as BMECs may consume more glucose for their own metabolic needs. Further investigation is needed to confirm whether decreased glucose transport is due to increased glucose consumption and delineate whether this may be a causal factor in glucose hypometabolism in NP-C patients. Glucose hypometabolism often precedes cognitive decline in other neurodegenerative disease, suggesting its potential as a target in diseases such as AD [67]. A similar pattern may exist in NP-C, and targeting decrease glucose transport with metabolic interventions may prevent glucose hypometabolism.

Finally, reducing U18666A-treated iPSC-BMEC glycolysis partially restored barrier integrity, a critical function of BMECs. Multiple studies have shown a link between high glucose, ROS accumulation, and BMEC barrier decline. A study in hpBMECs showed that high glucose impaired barrier function by increasing tight junction protein degradation through NADPH oxidase-derived superoxide anions [212]. High glucose is believed to increase levels of methylglyoxal, a reactive carbonyl byproduct of glycolysis, which has been shown to decrease tight junction proteins and increase permeability [213,214]. Both elevated glucose and direct treatment with methylglyoxal decreased barrier integrity in mouse BMECs *in vitro* through HIF-1α-mediated mechanisms [214,215]. This may therefore imply that decreased barrier function in NPC1-deficient BMECs is related to increased glycolytic metabolism and can therefore be targeted to restore barrier function.

3.5. Limitations

Although my study provides new insights into how metabolism is altered in BMECS afflicted by NP-C, it has several limitations. First, BMECs are closely integrated in the neurovascular unit, where they dynamically interact with and respond to cues from other brain cells. My *in vitro* models were highly simplified to focus on only one cell type. Second, I performed the majority of our experiments on BMECs cultured on impermeable well plates instead of permeable Transwell inserts, which are not as relevant in replicating barrier physiology. Third, my labeling schemes were not comprehensive as I only used glucose labels that provide a limited subset of information. Typically, glutamine labels are more informative to analyze flux in the TCA cycle. For a fully comprehensive overlook of metabolism, I would need to label metabolites using a parallel labeling scheme to target both glycolysis and other metabolic pathways to fully understand changes in the metabolic landscape [216,217]. Fourth, although the model helped unveil the changes in U18666A-treated iPSC-BMECs, its ability to fully decipher the metabolic network was restricted by both experimental and modeling limitations. Experimental constraints prevented me from measuring isotopomers of cholesterol and its precursors, which would have allowed me to explicitly quantify cholesterol synthesis. My model network was also limited to specific metabolites. This led to some unrealistic assumptions, such as that all cytosolic acetyl-CoA can only be used to generate UDP-GlcNAc. This limitation prevented me from calculating flux of acetyl-CoA into other intracellular sinks. Finally, I used U18666A to induce a pharmacological NPC model. While straightforward, this pharmacological model has limitations as U18666A can lead to off-target effects such as inhibition of the cholesterol biosynthetic enzyme 3β-hydroxysteroid-Δ24 Reductase (DHCR24) and therefore may not accurately represent the disease phenotype [121].

3.6. Conclusions

NPC1 inhibition of BMECs via U18666A treatment significantly perturbed metabolism by increasing glycolytic activity while leading to mitochondrial dysfunction. BMECs also demonstrated changes in intracellular and secreted acyl carnitines and TCA metabolites. These changes were partially attenuated by HPβCD. Together, our results show a potentially pathogenic role for BMEC metabolism in NP-C

pathogenesis, as altered BMEC metabolism may lead to vascular dysfunction, decrease glucose transport to the brain, and alter the brain's metabolic environment.

Chapter 4 - NIPAA-m nanogel uptake and transport in brain endothelial cells for treatment of Niemann-Pick Disease Type C

4.1. Introduction

The blood-brain barrier (BBB) is a tight, impermeable layer that prevents 98% of small molecule drugs and nearly all large molecule therapeutics from reaching the brain parenchyma. The BBB remains an obstacle for treating neurological diseases, including NP-C. Current NP-C treatments include miglustat, a BBB-permeable compound that can slow but not halt disease progression, and hydroxypropyl-β-cyclodextrin (HPβCD), which shows promise in halting disease in both animal and clinical trials [1]. However, HPβCD cannot penetrate the BBB due to its large size. Alternate strategies are needed to efficiently, non-invasively deliver HPβCD into the brain.

Many techniques are being explored to overcome the challenge of BBB drug delivery, including alternate delivery routes (e.g., intranasal, intrathecal), nanoscale delivery vehicles (e.g., exosomes, nanoparticles), and BBB disruption (e.g., focused ultrasound, osmotic permeabilizers [2]. A promising strategy focuses on designing pharmaceutical agents that hijack existing, specific transport systems in the brain endothelium, such as transferrin uptake, to deliver therapeutic cargo [3]. By exploiting the brain endothelium's native clathrin-mediated endocytic pathways, therapeutics can stealthily enter the brain [2]. This strategy has shown promise in animal models and early clinical trials [4,5].

Nanoparticles in particular have been extensively looked at due to their high tunability and capability to target these transport pathways [2]. NPs have modifiable features such as shape, size, functional groups, and charge that can be finely tuned to optimize transport into specific cells and tissues. Despite extensive research that shows promising results in preclinical models, little success has been obtained with nanoparticles in clinical trials. This necessitates further examination of the

factors that may hinder their uptake and transport in clinically relevant scenarios, especially in diseases states [6].

Investigating nanoparticle uptake in a disease context is crucial as pathways may become dysfunctional in disease. Cellular uptake and transport mechanisms may be altered in lipid disorders such as NP-C due to the role of cholesterol and lipid rafts in mediating these transport mechanisms. Lipid rafts are defined as microdomains in the plasma membrane that are especially rich in lipids such as cholesterol and sphingoliipids. These rafts are important sites for some internal membrane proteins, such as caveolin. Cholesterol-rich lipid rafts have particularly been noted for its importance in caveolin-mediated uptake, particularly in the formation and maintenance of caveolin in mammalian cells. Depletion of cholesterol with MβCD can abolish caveolin uptake [7–9]. Clathrin endocytosis is also dependent on cholesterol. Electron microscopy previously demonstrated that cholesterol depletion with MβCD flattens clathrin-coated pits, hindering their internalization [10].

The impact of lipids in endocytic pathways has been shown in disease models. For example, acid sphingomyelinase deficiency alters the initial uptake, basolateral reuptake, and lysosomal transport of transferrin receptor, intracellular adhesion molecule-1, and plasmalemma vesicle-associated protein-1 in BMECs [11]. NPC1-deficient fibroblasts showed decreased uptake of the clathrin endocytic marker transferrin, but interestingly, showed increased uptake of 10 kDa dextran, a marker of macropinocytosis increased [12]. Internalization of poly(β-amino ester) cationic polymers, which use clathrin- and caveolin-mediated endocytic pathways, was also reduced in NPC1-deficient Chinese hamster ovarian cells [13]. It is therefore crucial to evaluate and specifically design drug delivery strategies for the disease-specific context when designing therapeutics for NP-C.

Nanogels (NGs) synthesized with N-isopropylacrylamide (NIPAAm) and dextran-lactate-2-hydroxyethyl methacrylate (DexlactateHEMA) could potentially help treat NP-C. NGs are transported across the BBB *in vivo* and *in vitro* [14–16]. Furthermore, these NGs exhibit low cytotoxicity *in vivo* and *in vitro* and are also amenable to protein or peptide loading, allowing them to carry cargo between 5kDa to 500 kDA in size [16]. This is sufficient to encapsulate therapeutic payloads such as HPβCD for potential therapeutic delivery. To my knowledge, NG uptake has not been studied following cholesterol depletion or in NPC1deficient BMECs.

In this chapter, I examined the therapeutic potential of NG across two *in vitro* BMEC models: iPSC-BMECS and hpBMECs. Each model offers a complementary perspective. hpBMECs have a more endothelial metabolic signature and express key endothelial markers not observed in iPSC-BMECs. In contrast, iPSC-BMECs possess superior barrier function even though they retain an epithelial-like phenotype [17]. By using both models, I determined how NG uptake and transport changed across these different parameters, as substrate uptake and transport can be perturbed by both metabolism (via energy dependent uptake pathways) and barrier integrity. Different NG concentrations and formulations were evaluated for uptake, transport, and viability in both healthy and diseased BMEC models. I then measured the uptake, transport, and therapeutic potential of HPβCD-loaded nanogels in U18666A-treated neuronlike cells. My data highlights the therapeutic potential of nanogels for treatment of NP-C and other disorders of cholesterol metabolism.

4.2. Methods

4.2.1. Cell Culture

iPSC-BMECs and hpBMECs were cultured as described in Chapter 2 and Chapter 3. To model neurons, I used the neuron-like immortalized SH-SY5Y cultures, which are frequently used to model neuronal phenotypes *in vitro*. For SH-SY5Y cell (Sigma-Aldrich, 94030304-1VL) culture, cells were first expanded in DMEM/F12 media (Thermo Scientific, 11320082) containing 2 mM glutamine, 1% nonessential amino acids (Thermo Scientific,11140050), 1% penicillin-streptomycin, and 15% heat inactivated fetal bovine serum (FBS). 48 hours after seeding, media was replaced with differentiation media (neurobasal media containing 10 µM retinoic acid, 2% B27, 8.5 mM glucose, and 4 mM glutamine) to induce a more mature neuron-like phenotype. Differentiation was confirmed by staining SH-SY5Y for beta-tubulin III (Sigma-Aldrich, T8660) using the immunofluorescent staining protocol as described previously in Chapter 2. NPC1-KO CRISPR iPSC-BMECs were generated as described previously.

4.2.2. Nanogel synthesis

Nanogels composed of thermoresponsive poly(N-isopropylacrylamide) (pNIPAAm), biodegradable dextran-poly(lactate-2-hydroxyethyl-methacrylate) macromer, and acrylic acid (at designated mol %

with respect to pNIPAAm) were synthesized by Dr. Tao Lowe's group. A UV emulsion polymerization method is used to synthesize nanogels composed of thermoresponsive poly(N-isopropylacrylamide) (pNIPAAm), biodegradable dextran-poly(lactate-2-hydroxyethyl-methacrylate) macromer, and 2 mol% acrylic acid with respect to pNIPAAm. Nanogels are loaded with and without 15 wt% Kleptose in aqueous solution. The synthesized nanogels are purified by dialysis and dried by lyophilization. For all nanogel uptake studies, nanogels are additionally stained with a fluorescent (5-(4,6-Dichlorotriazinyl) Aminofluorescein) dye (DTAF).

4.2.3. Nanogel treatment

Nanogels were re-suspended in cold serum-free human endothelial serum free media (heSFM; Thermo Scientific, 11111044) and centrifuged at 1000 rpm for 5 minutes. The nanogel suspension was then sterile filtered through a 0.45 µM Titan3 PVDF filter (44504-PV). Nanogels were then diluted to the final concentration in heSFM containing 2% B27 (Thermo Scientific 17504001). For nanogel uptake and viability assays, cells were treated with heSFM with different nanogel concentrations for 24 hours. For cholesterol disruption assays, cells were first treated with 10 µM U18666A for 24 hours or 3 mM methyl-β cyclodextrin (MβCD; Sigma-Aldrich C4555-1G) for 3 hours, after which cells were treated with 1 mg/mL 2% acrylic acid nanogels for 24 hours.

Disruption of cholesterol distribution with U18666A treatment was imaged via filipin and lysosomal colocalization assays, as described in Chapter 2.

4.2.4. Live Dead Assay

Cell viability after nanogel treatment was assessed using a Live/Dead assay (ThermoFisher Scientific, L3224) as per manufacturer instructions. The number of live and dead cells was either quantified using a microplate reader for BMECs seeded on clear-bottom 96-well plates (Thermo Fisher, M33089; dose response) or as described previously in Chapter 2 (acrylic acid percentage).

4.2.5. Nanogel uptake

BMEC nanogel uptake was characterized by confocal microscopy or flow cytometry. For microscopy assays, cells were seeded onto either glass cover slips or 96-well clear bottom plates (Fisher Scientific, 12-566-70). After nanogel incubation, cells fixed with 4% paraformaldehyde (PFA; Millipore Sigma, P6148) for 20 minutes and then washed with 0.1% Trypan Blue (Thermo Scientific, 15250061) to quench extracellular DTAF. Cells were then incubated with 1:2000 DAPI (Thermo Scientific, 62248) for 10 minutes to label nuclei.

To image nanogels localized to lysosomes, cells were then blocked in 5% goat serum (Millipore Sigma, S26) in PBS (Thermo Fisher, 70011069) with 0.3% TritonX-100 (Alfa Aesar, A16046) (Millipore Sigma, SAE0088) for 1 hour at room temperature. Cells were then incubated with 1:200 LAMP1 (Abcam, ab24170) overnight. Cells were then washed three times in PBS, after which a fluorescent secondary antibody (1:200; Thermo Scientific, A-11012) and DAPI (1:2000; Thermo Scientific, 62248) were added. Samples on glass coverslips were imaged using an Eclipse Ti2 spinning disk confocal microscope (Nikon) with a 60x oil objective. Samples in 96 well plates were imaged with a 20X objective.
To quantify nanogel uptake, images were first processed with a rolling ball module to eliminate background. Small particles as well as large aggregate clumps were excluded through size and intensity thresholds. Total DTAF signal intensity was then quantified and normalized to the total nuclei count to determine intensity per cell. Nanogel-lysosome colocalization was quantified using the Cell Profiler colocalization module and Mander's coefficient.

For flow cytometry, cells were detached using either Accutase (iPSC-BMECs) or trypsin (hpBMECs). After adding media to neutralize the detachment reagent, cells were collected into microcentrifuge tubes and centrifuged at 500 rpm for 1 minute. The supernatant was removed, cells were washed with 0.01% trypan blue to quench extracellular DTAF signal and resuspended in 100 µL PBS with 1% BSA. Flow cytometry was performed with a BD FACS Celesta, and all data were analyzed using ggcyto package in R studio [249].

4.2.6. TEER and permeability assays

Paracellular nanogel transport was measured using a similar protocol to the permeability assays described in Chapter 2. Briefly, DTAF-nanogels were added to the apical compartment of BMECs seeded on 0.4 µm Transwell inserts. Media samples were then collected from the basolateral compartment after 5, 15, 30, 45, 60, 90, 120, 150, and 180 minutes. The amount of DTAF-nanogels in the media samples was determined using a microplate reader at 485/535 nm excitation/emission. The permeability coefficient was calculated as described previously. TEER measurements were taken and calculated as described previously in chapter 2.

4.2.7. Nanogel paracellular transport

Paracellular nanogel transport was measured using a similar protocol to the permeability assays described in Chapter 2. Briefly, DTAF-nanogels were added to the apical compartment of BMECs seeded on 0.4 µm Transwell inserts. Media samples were then collected from the basolateral compartment after 5, 15, 30, 45, 60, 90, 120, 150, and 180 minutes. The amount of DTAF-nanogels in the media samples was determined using a microplate reader at 485/535 nm excitation/emission. The permeability coefficient was calculated as described previously. TEER measurements were taken and calculated as described below.

4.2.8. Transcellular transport

To examine nanogel uptake and transcellular transport, BMECs on 0.4 µm Transwell inserts were incubated with DTAF-nanogels in the apical compartment for 24 hours. BMECs were washed three times with cold PBS to remove extracellular nanogels and slow transport processes. Cells were then moved to new plates with nanogel- and phenol red-free DMEM containing 2% B27, 8.5 mM D-glucose, and 4 mM glutamine. After 24 hours, media was sampled from both sides of the Transwell inserts, and fluorescence was quantified with a plate reader.

4.2.9. Statistical Analysis

Statistical analysis was performed as described previously in chapter 2.

4.3. Results

Although HPβCD shows promise in treating neurological manifestations of NP-C, it has poor BBB penetrance and causes pulmonary damage when delivered systemically. HPβCD therefore must be delivered through an invasive intrathecal route to reach the CNS. There is a need for tunable drug carriers that can be specifically targeted to the BBB to maximize the effectiveness and safety profile of this drug. Nanogels are tunable drug carriers with an excellent safety profile and drug loading capabilities. For this reason, I decided to examine their uptake and transport capabilities in BMEC to assess their potential to ferry HPβCD into the brain.

4.3.1. hpBMECs increased PNIPAAm-DEX-PLA-HEMA nanogel uptake up to 1 mg/mL without cytotoxic effects

I first examined NG uptake after 24 hours by confocal microscopy. To specifically quantify nanogels that were taken up and located intracellularly and exclude nanogels bound to cell membrane or aggregated in the extracellular space, I quenched extracellular nanogel signal by washing cells with trypan blue prior to analysis. Through this analysis, I did not observe intracellular NGs (DTAF fluorescence) until the NG concentration reached 0.5 mg/mL. At 1 mg/mL, the DTAF fluorescent intensity was 85% higher than untreated cells ($p = 0.0007$) (Figure 4.1A). hpBMEC viability actually increased slightly with NG exposure, and there was no significant decrease in cell viability at the highest NG concentration (1 mg/ml) (Figure 4.1B). Since 1 mg/ml NG showed high viability and uptake, I used 1 mg/mL NG for subsequent experiments.

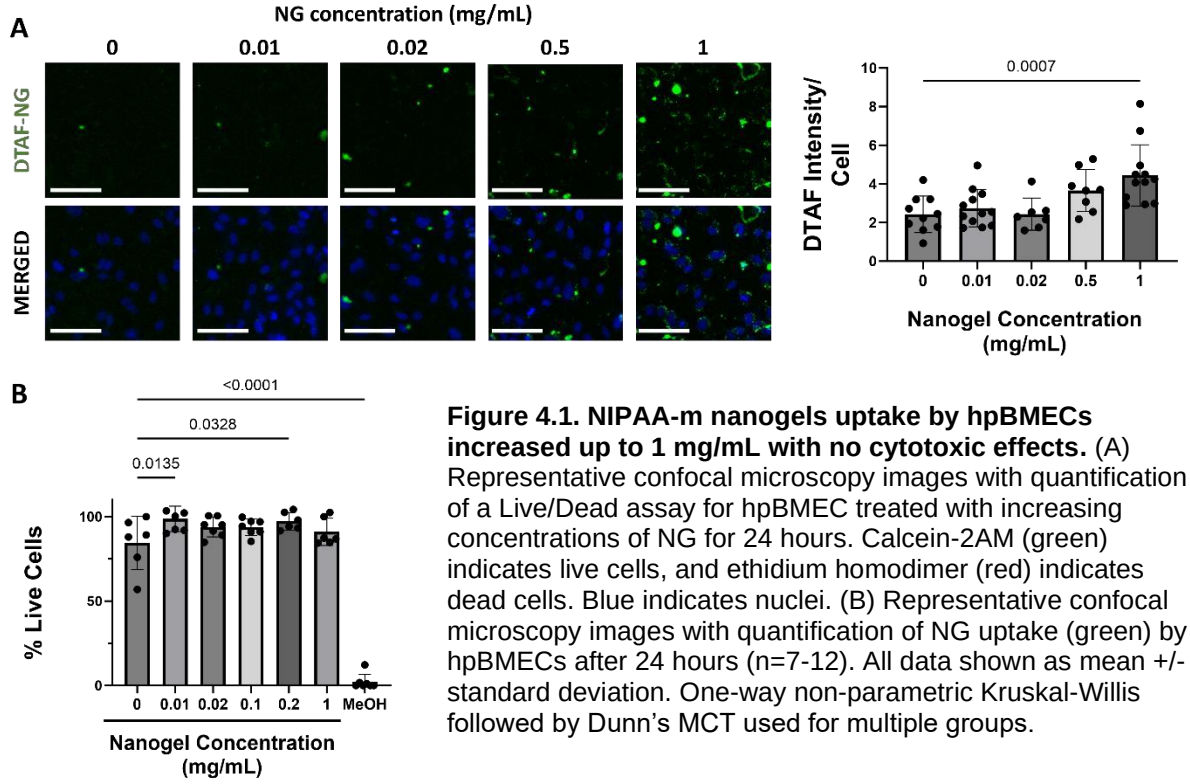

Figure 4.1. NIPAA-m nanogels uptake by hpBMECs increased up to 1 mg/mL with no cytotoxic effects. (A) Representative confocal microscopy images with quantification of a Live/Dead assay for hpBMEC treated with increasing concentrations of NG for 24 hours. Calcein-2AM (green) indicates live cells, and ethidium homodimer (red) indicates dead cells. Blue indicates nuclei. (B) Representative confocal microscopy images with quantification of NG uptake (green) by hpBMECs after 24 hours (n=7-12). All data shown as mean +/- standard deviation. One-way non-parametric Kruskal-Willis followed by Dunn's MCT used for multiple groups.

4.3.2. NGs with 2% acrylic acid had increased hpBMEC uptake and transport

Acrylic acid can be incorporated into NGs to improve their cellular uptake, stability, and release kinetics; however, high acrylic acid concentration can reduce cell viability [21]. I therefore tested 0%, 2%, and 5% acrylic acid (AA) NGs to determine if acrylic acid could improve hpBMEC NG uptake and transport while maintaining cell viability. Cell viability was statistically similar across all AA-NG formulations (Figure 4.2A, B).

I then examined how AA composition impacted cellular uptake. After 24 hours, hpBMEC took up more of both 2% and 5% AA-NG (1 mg/ml) as compared to 0% AA-NG, although neither was statistically significant (Figure 2C, 2D). BMECs must also transport NGs across the BBB for a therapeutic to reach the brain. To determine how AA impacted NG transcellular transport, I incubated hpBMEC seeded on Transwell inserts with 1 mg/ml NG for 24 hours, followed by 24 hours in fresh NG-free media. The percentage of DTAF-positive cells was approximately 2-fold higher in BMECs treated with 2% AA NGs,

although this change was not statistically significant ($p = 0.1147$, Figure 4.2E). Furthermore, hpBMECs treated with all AA-NG formulations released nanogels, as indicated by DTAF-signal in the media (Figure 4.2F). DTAF signal in the basolateral Transwell insert compartment was 2.5 fold higher ($p = 0.0142$) in 2% AA-NG treated hpBMECs compared to 0% AA-NG treated hpBMECs (Figure 2G). These data suggest that 2% AA-NG had the highest cellular uptake and transport compared to the other AA formulations. I therefore used 2% AA-NGs for subsequent experiments.

4.3.3. Disrupted cell cholesterol increased hpBMEC NG uptake and transport

Next, I examined how NG uptake and transport change when intracellular cholesterol is disrupted, as would occur in NP-C. I therefore treated hpBMECs with U18666A for 24 hours or 3 mM MβCD, which depletes membrane cholesterol, for 3 hours to test for the specific effects of cholesterol depletion. In addition, MβCD inhibits caveolin-mediated endocytosis and diminishes clathrin-mediated endocytosis [10,12]. Thus, MβCD treatments provide insight on how these pathways are involved in NG uptake and transport. NG uptake increased by 60% in U18666A-treated hpBMECs, as indicated by increased DTAF intensity/cell (Figure 4.3A, B). This was corroborated by flow cytometry, which showed an approximately 2-fold increase ($p = 0.0251$) in the percentage of DTAF-positive cells in U18666A-treated hpBMECs. Similarly, mean fluorescent intensity (MFI) increased approximately 43% in U18666A-treated hpBMECs ($p = 0.0006$; Figure 4.3D, 4.3E), as measured by flow cytometry.

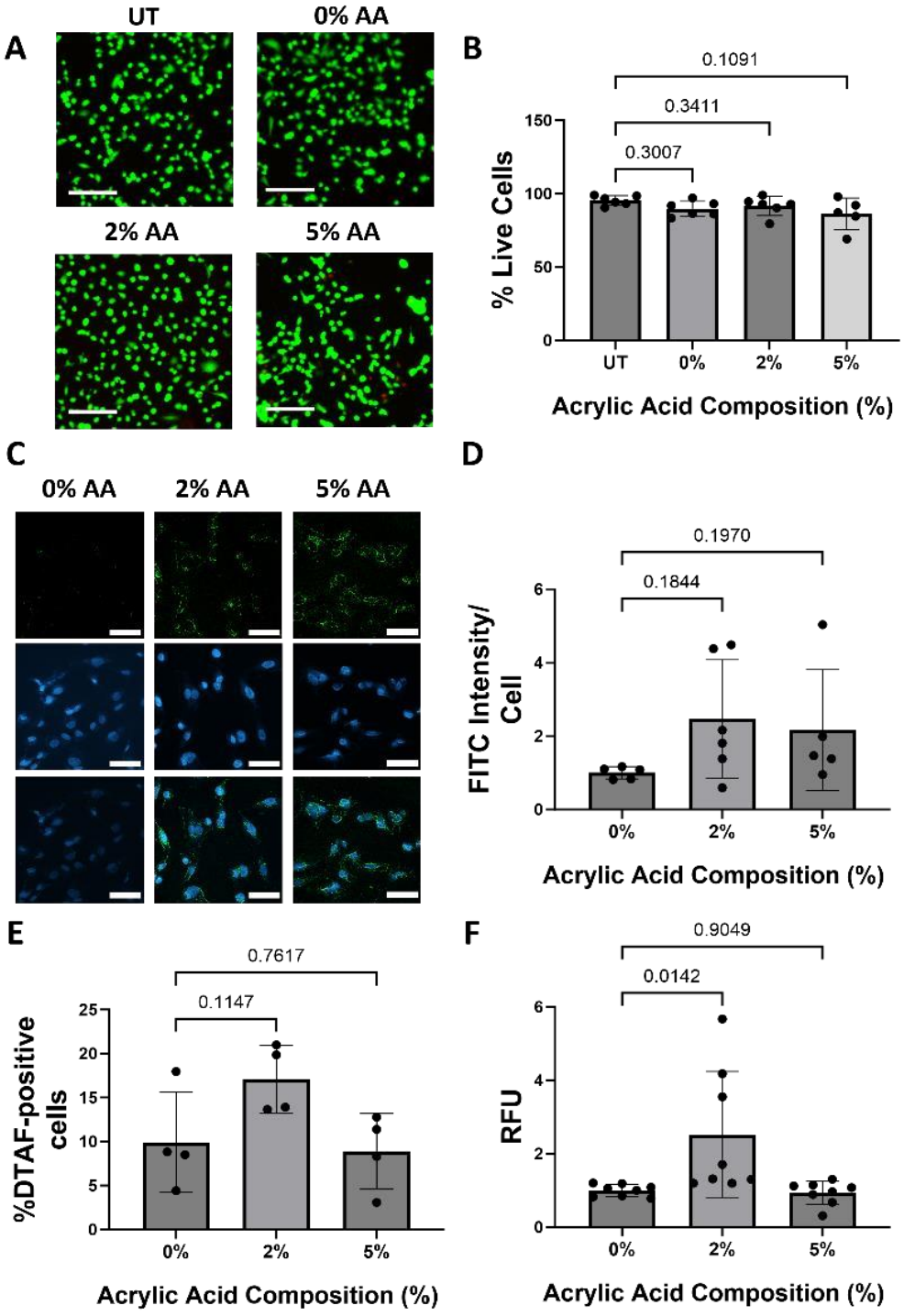

Figure 4.2. 2% acrylic acid NGs showed the highest hpBMEC uptake and transport without a change in viability. (A) Representative images and with (B) quantification of a Live/Dead assay for hpBMEC treated with 1 mg/ml NG with 0, 2, or 5% acrylic acid (AA) for 24 hours. Calcein-2AM (green) indicates live cells, and ethidium homodimer (red) indicates dead cells. Scale bar = 25 µM (C) Representative confocal microscopy images. Scale bars = 25 µM. (D) Quantification of hpBMEC uptake of NGs 0, 2, or 5% acrylic acid (AA) (n=5-6 from two independent experiments). (E) Flow cytometry quantification DTAF-positive cells following completion of transcytosis assay (n=4). (F) hpBMECs NG release, quantified as the fluorescent signal from basolateral media added to hpBMEC previously cultured with 1 mg/ml NG with 0, 2, or 5% acrylic acid (AA) for 24 hours. All data points normalized to mean of 0% AA-NG group (n=8 from two independent experiments). All data shown with mean +/- standard deviation. One-way nonparametric Kruskal-Willis followed by Dunn's MCT used for multiple groups.

NG transport also increased in MβCD-treated hpBMECs but not U18666A-treated hpBMECs. Specifically, the NG permeability coefficient increased by 42% in MβCD-treated cells ($p = 0.0101$) but only 22% in U18666A-treated cells ($p = 0.1069$), as compared to untreated cells (Figure 4.3F,G). To determine how the change in transport related to paracellular permeability, I measured TEER in U18666A- and MβCD-treated hpBMECs. U18666A-treatment reduced TEER by more than 40% ($p = 0.0573$), while MβCD decreased TEER by ~60% ($p=0.0018$; Figure 4.3H).

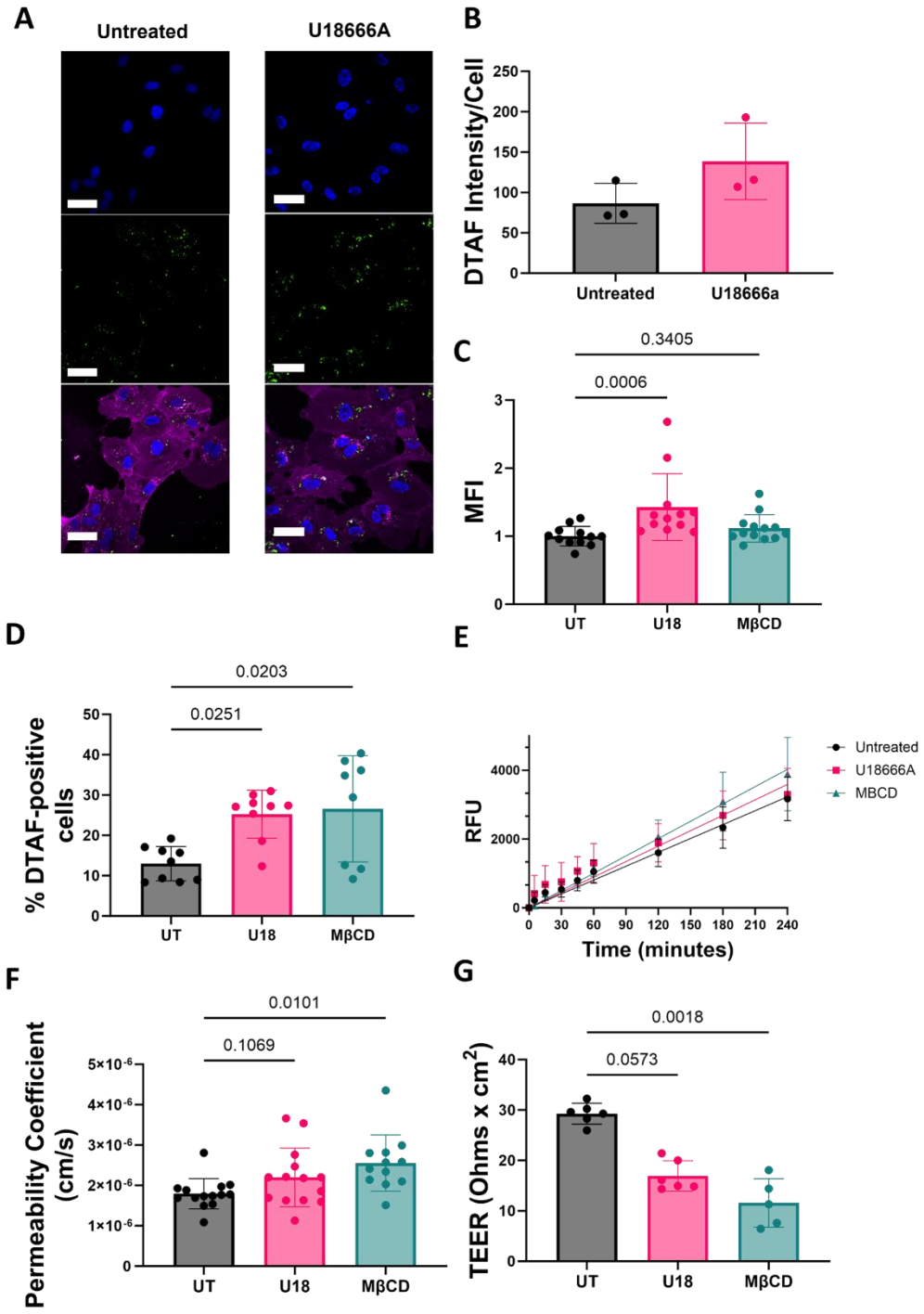

Figure 4.3. Altered cholesterol increased hpBMEC NG uptake and transport. (A) Representative confocal microscopy images of hpBMEC treated with 10 μM U18666A (1 mg/ml for 24 hours) or MβCD (3 mM for 3 hours) and then co-labeled with DAPI for nuclei and LAMP1-antibody for lysosomes. Scale bar = 50 μM. Quantification of (B) NG fluorescence per cell and (C) Mean fluorescent intensity (MFI) and (D) The percentage of DTAF-positive cells were quantified by flow cytometry in hpBMECs collected from Transwells following transcellular transport experiment. (E) Representative basolateral fluorescent time-course and (G) permeability coefficient quantification in hpBMECs treated with U18666A or MβCD (n=12, three independent experiments). (H) TEER for hpBMECs treated with U18666A or MβCD (n=6 samples). All data shown with mean +/- standard deviation. One-way non-parametric Kruskal-Willis followed by Dunn's MCT used for multiple groups.

4.3.4. U18666A-treated iPSC-BMECs also increased NG uptake

I then examined NG uptake in iPSC-BMECs, which provide an improved barrier model closer to the barrier integrity observed *in vivo* [22]. iPSC-BMECs also enable me to use NP-C knockout cells,

in addition to U18666A treated cells. Similar to hpBMEC, iPSC-BMEC calcein signal increased with NG treatment, which resulted in 5-25% higher values for cell viability (Figure 4.4A). iPSC-BMEC took up NG quickly. DTAF fluorescence per cell was statistically significant at 8 hours (19.7%, $p = 0.0011$), at 24 hours (40.0%, $p<0.0001$), and at 72 hours (93.1%, $p<0.0001$; Figure 4.4B, 4.4C). These data suggest that iPSC-BMEC continue to take up NG over time without a loss in cell viability.

Since iPSC-BMEC form a tight barrier, I next quantified BMEC monolayer barrier integrity for different NG concentrations and AA compositions. After 24 hours, there was no change in barrier integrity for iPSC-BMEC incubated with 1 mg/ml NG (Figure 4D). Addition of AA to the NG also had no effect on TEER values (Figure 4E). Finally, I examined iPSC-BMEC NG uptake with altered cholesterol trafficking (via U18666A) or cholesterol depletion (via MβCD). U18666A-treated iPSC-BMECs showed a similar pattern to U18666A-treated hpBMECs, with 4.5-fold higher NG uptake ($p = 0.0017$). However, MβCD-treated iPSC-BMECs did not show a significant change in NG uptake (Figure 4.4F).

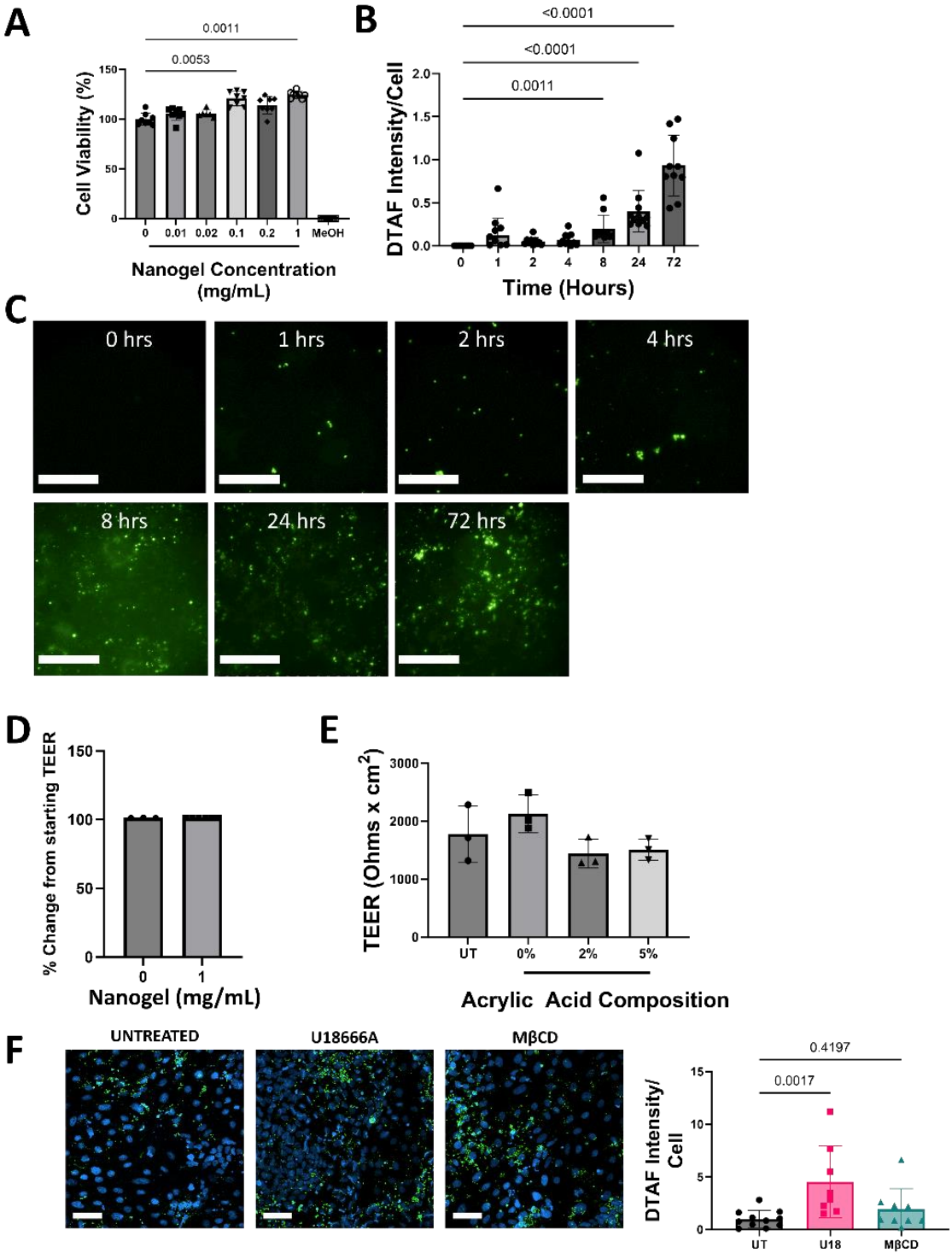

Figure 4.4. iPSC-BMEC similarly took up NG without a change in viability or barrier function, and U18666A treatment increased NG uptake. (A) Representative confocal microscopy images with quantification of a Live/Dead assay for iPSC-BMEC treated with increasing concentrations of 2% AA NGs for 72 hours. Calcein-2AM (green) indicates live cells, and ethidium homodimer (red) indicates dead cells. (B) Quantification and (C) representative confocal microscopy images of DTAF 2% AA NG uptake by iPSC-BMECs from 0 to 72 hours. Scale bar = 100 μM. Uptake was compared to 0 hour time point. (D) Change from starting TEER and (E) TEER for iPSC-BMECs treated with different NG concentrations and %AA formulations for 24 hours. (F) Representative images and quantification of 2% NG uptake in iPSC-BMECs treated with 10 μm U18666A (24 hours) or 3 mM MβCD (3 hours) (n=8-11). Green = NG, blue = nuclei. Scale bar = 25 μM. All data shown with mean +/- standard deviation. One-way non-parametric Kruskal-Willis followed by Dunn's MCT used for multiple groups.

Cholesterol distribution in U18666A-treated SH-SY5Y cells

Finally, I determined if HPβCD-loaded NG could restore function in NP-C cells. Wild-type (WT) and NPC1-KO iPSC-BMECs (KO) on Transwell inserts were cultured with either DTAF-NGs, DTAF-NGs loaded with HPβCD (HP-NG), or 4K dextran in the apical compartment. 4K Dextran was used as a permeability control since it is known to cross the BBB *in vivo* due to its small size [23]. There were no differences in NG permeability coefficient between WT and KO iPSC-BMEC. However, KO iPSC-BMEC had an 8.9 fold higher permeability coefficient for HP-NGs as compared to unloaded NGs ($p = 0.0314$). These data suggest that HPβCD-loaded nanogels can cross the BBB (Figure 4.5A).

I then examined whether HP-NGs restored cholesterol distribution in U18666A-treated cells. U18666A increased SH-SY5Y cholesterol localization to the lysosomes by nearly 4-fold compared to the untreated group ($p=0.0121$). When U18666A-treated SH-SY5Y cells were also treated with NGs, HP-NGs, or unencapsulated HPβCD for 48 hours, both HP-NG and HPβCD reduced lysosomal cholesterol accumulation by 60% ($p=0.0099$) and 75% respectively ($p = 0.0006$). However, neither treatment fully restored the cholesterol distribution to that of the untreated (UT) cells (Figure 4.5B).

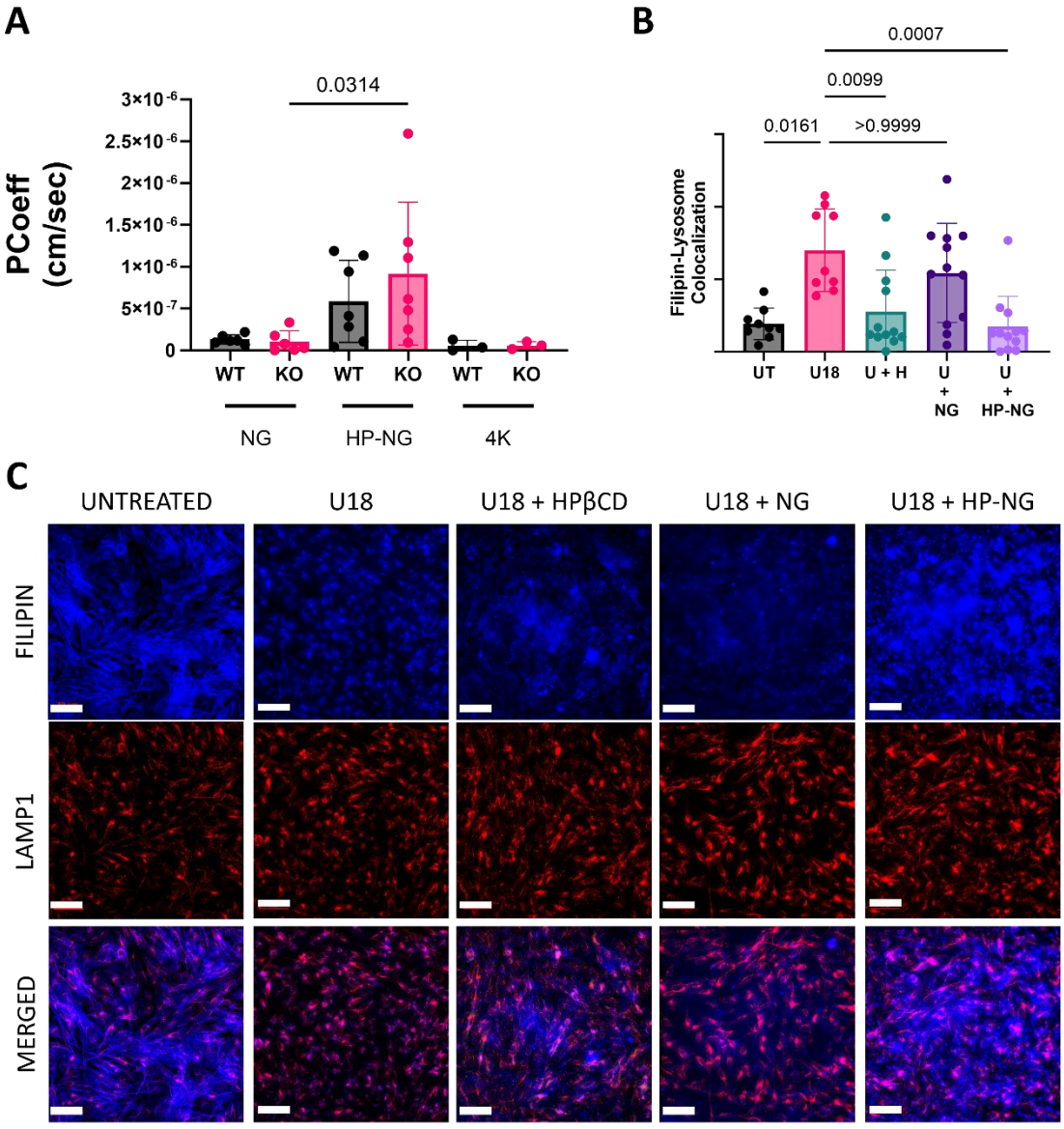

Figure 4.5. HPβCD-loaded NG were transported across iPSC-BMEC and decreased cholesterol accumulation in neuron-like cells. (A) Permeability coefficients calculated in WT and NPC-KO iPSC-BMECs with NG (NG), HPβCD- NG (HP-NG), and 4k dextran (4K). n=6 samples from two independent experiments. (B) Quantification as calculated by Mander's coefficient and (C) Representative confocal microscopy images of filipin-lysosome colocalization in SH-SY5Y neuron-like cells treated with solvent control (UT), U18666A (U18), U18666A with 1000 μM unencapsulated HPβCD (U+H), U18666A with 1 mg/mL unloaded NG (U + NG) or HPβCD-loaded NGs (U + HP-NG) for 48 hours. (n =9-12 samples). Scale bars = 50 μM. All data shown with mean +/- standard deviation. One-way non-parametric Kruskal-Willis followed by Dunn's MCT used for multiple groups.

4.4. Discussion

The BBB is a highly specialized endothelial cell layer that protects the brain from harmful neurotoxins and inflammation. However, this same barrier poses a challenging hurdle for therapeutic compounds. In this chapter, I therefore examined the uptake and transport of PNIPAAm-DEX-PLA-HEMA nanogels into both hpBMECs and iPSC-BMECs in healthy and diseased conditions. I found that nanogels were readily taken up by and transported by both BMEC cell types. Furthermore, I observed increased NG uptake in both cell types after U18666A-treatment. Finally, I found that HPβCD-loaded NGs readily crossed NPC1-KO iPSC-BMEC barriers, suggesting that they have robust transport capabilities even in the disease context. This work therefore suggests a potential application for NGs to be used in the treatment of NP-C

My uptake studies showed that nanogels were readily taken up by both hpBMECs and iPSC-BMECs and did not decrease cell viability. This aligned with previous results showing that nanogels exhibit low cytotoxicity [24]. Interestingly, cell viability increased in both hpBMECs and hiBMECs treated with nanogels as quantified by calcein-based live dead assay. In this assay, calcein-2AM emits green fluorescence when it is activated upon cleavage by intracellular esterases, which indicates metabolism in live cells. Although this indicates cell viability, the results may be confounded by other factors that impact cell metabolism or oxidative stress. For example, nanogels may increase intracellular esterase activity in these cells, which shows up as increased viability. In addition, the nanogels are formulated with DEX-PLA-HEMA, which are composed of lactate monomers. These monomers could potentially impact BMEC metabolism when they are degraded inside the cell. Therefore, the increased viability I observed with NG treatment could relate to lactate-induced changes in BMEC metabolism.

Another possibility is that nanogels disrupt endosomal function and subsequentially increase calcein signal. A previous study with poly(2(diethylamino)ethyl methacrylate) (PDEAEMA) nanoparticles noted increased calcein fluorescence in nanoparticle-treated mouse fibroblasts. Calcein does not fluoresce in the endosome, but upon reaching the cytosol, it emits a bright signal. In this study, bright signal was detected in a diffuse manner throughout the cytosol in nanoparticle-treated

cells, compare to a more punctate distribution in untreated cells, suggesting that nanoparticles disrupt endosomal engulfment of calcein [25].

Interestingly, this may show an additional beneficial aspect of nanogel usage in BMECs. In the previously mentioned study, the authors found that that while nanoparticles promote calcein endosomal escape, the nanoparticles remain trapped. This suggested the nanogels induce partial endosomal membrane disruption instead of full rupture [25]. Notably, endosomal escape is a desirable property in nanogels, as it ensures that they are able escape trafficking to the lysosome, where they can be degraded.

Recently, it has become more apparent that many drug delivery strategies to overcome the BBB must be evaluated within a disease context, as disease pathologies can perturb cell endocytic pathways and uptake mechanisms [11,26]. Endocytosis has been diminished in several neurological diseases. For example, caveolin and clathrin uptake may increase in Alzheimer's disease, which may lead to increased uptake and accumulation of amyloid beta plaque [27]. Altered endocytic uptake has been observed in the context of other diseases, such as acid sphingomyelinase A and NP-C [11,28]. In NP-C models, changes such as decreased clathrin- and caveolin uptake have been observed in Chinese hamster ovarian cells [13] and NPC1-deficient fibroblasts [12,28]. I therefore sought to examine how nanogel uptake and transport was altered in BMEC in an NP-C disease relevant state. By improving our knowledge of uptake and transport in disease states, we can better determine their potential efficacy and further optimize uptake of particles in disease specific states.

In this study, MβCD was used to specifically model the cholesterol-deplete feature of NP-C pathology as changes in uptake could be caused by either lysosomal dysfunction or cholesterol depletion. I initially hypothesized that disruption of cholesterol distribution via U18666A treatment and decreased plasma membrane cholesterol via MβCD treatment would decrease NG uptake. However, MβCD did not decrease NG uptake. This was surprising, as MβCD has been used to inhibit caveolin- and clathrin-mediated endocytosis to reduce nanoparticle uptake in other studies [9]. Cholesterol is critical for caveolae formation and cholesterol depletion through MβCD results in caveolin loss.[7]. Studies of clathrin-dependent endocytosis also show that MβCD abolished invagination of clathrin-coated pits and coated vesicle formation but did not impact receptor binding [10]. My data suggest that NGs are taken up

through a clathrin- and caveolin-independent pathway that is not affected by cholesterol depletion. NG uptake is driven by macropinocytic uptake rather than caveolin- or clathrin-mediated endocytosis.

Surprisingly, U18666A treatment increased NG uptake in both iPSC-BMEC and hpBMECs. One possible route is macropinocytosis, which has been shown to increase in NPC1-deficient fibroblasts [12]. This is further supported by my observation of increased NG uptake in U18666A treated BMECs. An alternative explanation is that my quantification of cellular uptake was not specific for uptake and also quantified nanogel retention. Uptake was quantified by measuring nanogel intensity particles per cell intensity and therefore does not discriminate between uptake and retention of these particles. Lysosomal dysfunction caused by cholesterol accumulation in NP-C has previously been theorized to hinder endocytic pathway, which may therefore trap NGs in the [12]. The relationship between lysosomal dysfunction and nanoparticle retention has actually been studied in previous work to improve efficacy of nanoparticles by promoting their cellular retention and giving them additional time to reach the cytosol prior to lysosomal clearance [29]. [22]

HPβCD-loaded NGs outperformed unloaded NGs in crossing the BBB. This result was observed in both WT and NPC-KO iPSC-BMECs; however, the effect was more pronounced in NPC-KO BMECs. Interestingly, cyclodextrins have been previously complexed to poly(lactic-co-glycolyic acid) (PLGA) particles to enhance their bioavailability [30]. Cyclodextrin can enhance permeability by interacting with cholesterol and altering membrane fluidity. It is possible that we see a similar effect in HPβCD-loaded NGs. Another possibility is that HPβCD, which is a highly hydrophobic molecule [31], may increase the overall hydrophobicity of the NG complex and therefore increase its cell penetrance. Increased hydrophobicity has been noted to increase permeability of other compounds, such as statins, across the BBB by allowing them to more easily pass through the plasma membrane [32].

Finally, both HPβCD and HPβCD-loaded NGs reduced cholesterol accumulation in the lysosome but did not restore membrane cholesterol. The effective HPβCD dose must be carefully determined, as low concentrations fail to restore cholesterol distribution while high concentration induce lysosomal exocytosis and cholesterol depletion. The optimal dosage can vary based on cell type. These results suggest that while HPβCD may be released from HPβCD-loaded NGs, the concentration may be relatively high and lead to cholesterol depletion in SH-SY5Y cells. NP-C pathology is caused by both

lysosomal dysfunction and membrane cholesterol depletion, so it still is possible that these HPβCD loaded NGs can exert a therapeutic effect. However, further evaluation is needed to optimize HPβCD concentrations and determine whether HPβCD-loaded NGs can provide clinically relevant benefits.

4.5. Limitations

Although my study provides insight into BMEC NG uptake in the context of altered cholesterol, it has several limitations. All experiments were done on a relatively short time scale (24-72 hours), whereas NG release therapeutics across weeks or even months. Thus, the HPβCD may not be fully released from the NG or match the unencapsulated HPβCD concentration in my studies. Second, while I used MβCD as an inhibitor of caveolin- and clathrin-mediated endocytosis, I did not fully evaluate NG uptake mechanisms with other endocytic inhibitors. Further work needs to be done before I can conclude that the NG uptake pathway is truly cholesterol independent.

4.6. Conclusions

PNIPAAm-DEX-PLA-HEMA nanogels demonstrated uptake and transport in BMECs with no disruption to cell viability or barrier integrity. NG also appear to be taken up in both NPC1-like and cholesterol-deplete phenotypes, even seemingly increasing cellular uptake following U18666A-treatment. Loading NG with HPβCD increased BBB permeability while still reducing cholesterol accumulation in neuron-like cells. These results therefore suggest the therapeutic potential of HPβCD-loaded NG to treat NP-C and other cholesterol metabolic disorders.

Chapter 5 – Conclusions and Future Outlook

5.1. Thesis Summary

NP-C is a progressive neurodegenerative disease with few treatment options and no known cure. To develop new therapies, it is imperative to improve our understanding of the underlying pathophysiology, especially as it pertains to the BBB. While BBB metabolic and barrier dysfunction have been characterized in neurological pathologies such as AD, Parkinson's disease, Huntington's disease, stroke, TBI, and glioma [44], currently there is little known about the state of the BBB in NP-C and other rare inherited disorders of cholesterol metabolism. This gap is particularly notable considering the importance of cholesterol in mediating the proteins that provide BMEC with their unique phenotype, such as tight junction proteins and selective uptake pathways. The goal of this thesis was to understand the impact of reduced cholesterol on the BBB to create new preventative and therapeutic strategies to slow or even reverse NP-C disease progression.

In Chapter 2, I demonstrated barrier dysfunction in iPSC-BMECs with NP-C like and altered cholesterol phenotypes. I hypothesized that BMEC cholesterol depletion would disrupt tight junction protein localization and increase barrier permeability. Indeed, I observed BMEC barrier dysfunction caused by disruption to claudin-5 and occludin morphology and junction continuity in U18666A-treated cells. Similar changes were observed when cells were treated with the cholesterol depleting agent MβCD, which suggests that barrier dysfunction may be partially attributable to the cholesterol-deplete phenotype incurred by NPC1 inhibition. Interestingly, loss of barrier integrity and claudin-5 protein was prevented by co-treatment of U18666A-treated BMEC with HPβCD. I further showed similar results in NPC1 KO iPSC BMEC, which provide a more disease relevant model. Barrier disruption correlated with the degree of cholesterol perturbation. The NPC1 knockout cells had the mildest barrier dysfunction, followed by U18666A-treated cells, and finally MβCD-treated cells. Together, these data suggest the possibility of barrier dysfunction in NP-C and other disorders of cholesterol metabolism.

In Chapter 3, I investigated how NPC1 inhibition in both iPSC-BMECs and hpBMECs impacted the metabolic network. I hypothesized that glucose uptake would decrease with U18666A treatment as membrane cholesterol is believed to be crucial for GLUT1 function [268]. Both cell types increased glycolysis, and net glucose transport across the BMEC decreased in U18666A-treated iPSC-BMECs.

Both cell types also showed diminished mitochondrial metabolism, as evidence by isotope labeling experiments, Seahorse assays, and TMRM staining. Secreted and intracellular metabolomic profiles highlighted significant depletion of acyl-carnitines and TCA metabolites. Co-treatment with HPβCD partially restored exometabolomic and intracellular metabolic profiles as well as mitochondrial respiration in U18666A-treated cells, suggesting that HPβCD may ameliorate BMEC metabolic function in NP-C. My data therefore demonstrate evidence for metabolic dysfunction in NPC1-inhibited BMECs and its potential impact to altering brain metabolic homeostasis in NP-C.

In Chapter 4, I investigated how NIPAA-m DEX-PLA-HEMA NGs could be used to carry HPβCD across the BMEC layer. I found that NG concentrations up to 1 mg/ml had little effect on cell viability, NG uptake increased up to 72 hours, and 2% acrylic acid NG had the highest uptake by BMEC. I then examined NG uptake and transport in U18666A- and MβCD-treated BMECs. Surprisingly, I found that MβCD did not inhibit NG transport and that U18666A treatment actually increased NG uptake. These data suggest that NG uptake is resistant to or even promoted the NP-C cholesterol depleted disease state.

Finally, I investigated the transport and therapeutic potential of HPβCD-loaded NG. I found that the HPβCD-loaded NG decreased cholesterol accumulation in U18666A-treated SH-SY5Y neuron-like cells.

5.2. Clinical relevance and significance to the field

Together, these studies highlight that NPC1 may impact both BMEC barrier and metabolic function. While these studies should be validated in animal models and human patients, the current findings have important implications for NP-C pathogenesis, and consequently, disease management. Barrier dysfunction can increase entry of neurotoxic and inflammatory compounds into the brain. The difference in phenotype observed with the degree of cholesterol depletion may cause

some of the heterogeneity in NP-C severity [6]. For example, patients with genetic and environmental factors that worsen cholesterol depletion may have increased barrier permeability, causing them to accumulate more neurotoxins in a shorter period time and present with earlier disease onset or more severe neurological manifestations.

In terms of metabolism, my research suggests that altered cholesterol trafficking in BMECs can potentially increase glycolytic metabolism and disrupt mitochondrial metabolism. The increased BMEC glycolytic metabolism may contribute to decreased glucose transport, as BMECs consume glucose fated for the brain parenchyma to fulfill their own metabolic needs. This could lead to hypometabolism in parenchymal brain cells, which could directly damage these cells. Alternatively, higher BMEC lactate secretion could be toxic to neurons [269]. Once again, this may situate BMECs as a potential target in NP-C and other cholesterol disorders. Targeting BMEC metabolic defects may promote BMEC glucose transport into the brain while reducing brain cell damage incurred by altered BMEC metabolite secretions.

My nanogel studies highlight their potential use as delivery agents in NP-C. Nanogels successfully crossed the BMEC monolayer in both human primary BMEC and iPSC-BMECs, which have high barrier integrity. The nanogels also crossed the BMEC monolayer with NPC1 knockout. Since these nanogels can be loaded with HPβCD, they could be used to enable this large molecule to cross the BBB and restore cholesterol distribution in peripheral brain cells in diseases involving cholesterol depletion or altered cholesterol trafficking.

5.3. Innovation

This project produced new knowledge related to cholesterol, barrier integrity, metabolism, and drug delivery in BMEC. This is the first characterization of how cholesterol affects BMEC tight junction proteins. By comparing phenotypes between U18666A and CRISPR-Cas9 NPC1-KO, I also showed how the magnitude of cholesterol depletion varies depending on whether the phenotype is induced by a pharmacological or genetic model. The differences between the two disease models highlight the importance of model design when using BMECs *in vitro* to study rare diseases. I also present the first example of INST-MFA in iPSC-BMECs and the first study of how NPC1 phenotype changes the metabolism of any endothelial cell, whether cerebral or peripheral. Finally, this study is the first to

characterize nanogel transport in iPSC-BMEC, as previous work was conducted in bovine, murine, or human primary BMECs that have lower barrier integrity. In addition, this is the first examination of nanoparticle uptake in NP-C or cholesterol-deplete BMEC models.

Overall, my data suggest that the BBB itself could become a therapeutic target in slowing NP-C disease progression. Therapies must consider that in earlier stages of disease treatment, the BBB may be more permeable, but later in the treatment, the BBB may heal and make future therapeutic delivery more difficult.

5.4. Future Directions

My research motivates and highlights the importance of future work characterizing barrier function, metabolism, and transport in NP-C BMECs. Specifically, future directions include:

5.4.1. BBB permeability changes in animal models and human patients

While I found strong evidence for size-selective changes in BBB permeability, these findings should be validated *in vivo* to confirm their translational relevance. BBB permeability in NPC1 mice was previously examined with Evan's Blue dye [205]; however, this experiment may not be able to distinguish changes in small molecule permeability as Evan's blue readily binds to albumin *in vivo* to form a 69 kDa tracer molecule. *In vivo* permeability studies should be repeated with small tracers, such as sodium fluorescein and low molecular weight dextrans, to determine whether size selective changes in BBB permeability are present in animal models.

It would also be interesting to see if there are BBB changes prior to symptomatic NP-C presentation in animal models. Analysis of BBB changes at different time points in NPC1-null mice would help us understand whether there are preclinical changes in BBB function that precede neurodegeneration or cognitive impairment, similar to what has been observed in AD [68,270] .

BMEC-specific NP-C knockout animal models could clarify the role of NPC1 depletion specifically in the BBB. BMECS can be targeted with BMEC-specific AAV vectors [271] to knockout NPC1. Alternatively, vectors could be used to restore NPC1 in the BMEC of global NPC1 knockout mice.

Together, these two models could provide a complementary perspective of how BMECs contribute to NP-C pathogenesis.

5.4.2. Mechanism(s) driving reduced claudin-5 protein in U18666A treated BMECS

I observed decreased claudin-5 protein but was not able to determine the mechanism by which claudin-5 decreases. I did not observe decreased claudin-5 mRNA expression, which suggests that decreased protein may be due to increased degradation. Claudin-5 may be delocalized from cholesterol-deplete lipid rafts and targeted for degradation. While it has been shown that palmitoylation drives claudin-5 localization to cholesterol-rich lipid rafts, there are currently no studies examining the fate of claudin-5 following disruption of lipid rafts. Decreased claudin-5 may occur due to disrupted synthesis, as this requires multiple sorting steps. Additional studies are needed to clarify why BMEC claudin-5 decreases with U18666A treatment.

5.4.3. Metabolic changes in more relevant disease models

U18666A can act in a pleiotropic manner and could disrupt cholesterol synthesis and embed into cell membranes. For this reason, it is crucial to re-examine my findings from Chapter 2 with a more specific model, such as the NPC1-KO iPSC-BMECs to determine if these results relate to cholesterol depletion via NPC-1 inhibition or other U18666A effects.

5.4.4. Mechanism(s) for altered metabolism in U18666A-treated BMECs

Cholesterol metabolism is tightly regulated and disturbances can drive a compensatory phenotype through activation of the SREBP1/2 transcription factors. I initially hypothesized that SREBP1/2 drove the observed metabolic changes in U18666A-treated cells. Both SREBP1 and SREBP2 must cleaved from their inactive precursor forms by SREBP cleavage activating protein (SCAP) to become active transcription factors. I therefore used betulin, which directly binds to and inhibits SCAP, to inhibit SREBP 1/2 activation in U18666A-treated cells. Unfortunately, betulin had no effect on U18666A-treated BMEC metabolism. I also tested whether SREBP1 or SREBP2 siRNA knockdown could prevent U18666A-induced metabolic changes. However, I was not able to successfully knock these proteins down. Thus, the mechanism by which U18666A alters BMEC metabolism still needs to be explained.

5.4.5. Mechanism(s) of BMEC nanogel uptake

I found robust nanogel uptake in both hpBMECs and iPSC-BMECs. However, further work is needed to identify the endocytic pathways that BMEC use to take up nanogels. This knowledge will help us contextualize disease-related changes and improve the particles to increase uptake in disease conditions. Although MβCD has shown evidence of inhibiting clathrin-mediated endocytosis, it is not widely used to inhibit clathrin-mediated endocytosis as it targets other pathways as well. For future investigations, siRNA knockdown of endocytotic genes could helpp determine the pathways involved in nanogel uptake.

5.4.6. HPβCD-nanogel transport and release kinetics

While I observed that HPβCD-nanogels were transport across iPSC-BMECs, I did not quantify the amount of HPβCD that was delivered due to limitations in mass spectrometry. HPβCD delivery is an important parameter to characterize for two reasons. First, it will help improve nanogel timing and dosing so that the nanogels release a therapeutic HPβCD dose over time. Second, it will be crucial to determining whether HPβCD-nanogels improve HPβCD delivery and therapeutic effect compared to unencapsulated HPβCD.

5.4.7. HPβCD-nanogel uptake, transport, and efficacy in animal models

While my study demonstrates promising results for HPβCD-nanogel uptake and transport, these results must be further examined *in vivo* to determine how nanogels cross the BBB and impact neurodegeneration in the more complex physiological environment.

Appendix

Appendix A. INST-MFA output.

The table below lists all metabolic reactions in the INST-MFA network, as well as the best fit flux value, standard error, lower bound (LB), and upper bound (UB) for each reaction in the network.

Reaction Information		Untreated iPSC-BMECs				U18666A-treated iPSC BMEC			
RxnID	Metabolic Rection	Value	StdErr	LB	UB	Value	StdErr	LB	UB
GLUT1	glc.e -> glc.c	281.383	14.0573	252.191	310.749	315.673	2.9496	309.541	321.447
R2	glc.c -> g6p.c	281.383	14.0573	252.191	310.749	315.673	2.9496	309.541	321.447
R3	g6p.c -> f6p.c	261.655	13.2675	233.888	288.678	283.852	4.874	276.854	291.675
R4 net	f6p.c <-> dhap.c + g3p.c	274.802	13.6681	246.403	303.246	296.578	3.8683	289.661	303.262
R5 net	dhap.c <-> g3p.c	274.802	13.6681	91.5393	303.036	296.578	3.8683	277.344	302.849
R6	dhap.c -> glyc3p.c	1.80E-06	1.81E-13	0	168.732	2.76E-06	8.55E-12	0	16.28
R7 net	g3p.c <-> pep.c	556.179	27.6959	499.146	613.209	602.065	8.1187	588.769	614.934
R8 net	pep.c <-> pyr.c	556.179	27.6959	499.146	613.209	602.065	8.1187	588.769	614.934
R9 net	pyr.c <-> lac.c	364.848	35.4078	292.997	436.309	488.122	13.3545	458.972	515.53
LACT	lac.c -> lac.e	364.848	35.4078	292.997	436.309	488.122	13.3545	458.972	515.53
R11	pyr.c -> pyr.m	212.086	43.9803	119.356	304.647	113.943	15.1652	NaN	NaN
R12	pyr.m -> accoa.m + co2	64.8821	6.8282	29.543	237.698	52.0922	4.7904	26.2088	117.784
R13	pyr.m + co2.d -> oaa.m	7.8965	1.1098	3.6511	28.5726	9.111	3.2557	3.7545	22.094
R14	accoa.m + oaa.m -> cit.m	64.8821	6.8282	29.543	237.698	52.0922	4.7904	26.2088	117.784
R15	cit.m -> akg.m + co2	124.82	14.4167	59.6522	478.015	218.261	45.0932	NaN	665.383
R16	akg.m + co2.d -> cit.m	59.9417	8.699	29.2609	205.08	171.262	41.5084	91.2782	527.438
R17	akg.m -> suc.m + co2	289.401	48.3609	126.899	1.19E+03	515.22	171.892	160.615	NaN
R18	suc.m + co2.d -> akg.m	211.662	43.4331	82.5792	985.607	472.239	170.246	136.917	NaN
R19 net	suc.m <-> fum.m	77.7389	7.3933	41.339	248.322	42.9813	6.3343	22.7115	98.0971
R20 net	fum.m <-> mal.m	77.7389	7.3933	41.339	248.322	42.9813	6.3343	22.7115	98.0971
R21 net	mal.m <-> oaa.m	56.9843	6.3459	25.3015	220.72	42.9813	6.3343	19.7536	94.8521
GLN_UPTAKE	gln.e -> gln.c	13.6825	1.7295	9.8855	17.3779	17.4246	1.8147	13.8806	20.9475
R23	gln.c -> glt.c	13.6825	1.7295	9.8855	17.3779	17.4246	1.8147	13.8806	20.9475
R25 net	glt.c <-> akg.m	12.8605	1.8302	9.0601	16.6016	-4.0181	3.2943	-6.3848	5.2787
R26	6pg.c -> p5p.c + co2	19.7283	4.0259	13.9273	27.6713	31.8206	4.1646	28.0969	37.0947
R27 net	p5p.c + p5p.c <-> s7p.c + g3p.c	6.5753	1.342	3.4794	9.2435	8.9092	1.6369	6.3014	11.2043

R28 net	s7p.c + g3p.c <-> f6p.c + e4p.c	6.5753	1.342	3.4794	9.2435	8.9092	1.6369	6.3014	11.2043
R29 net	p5p.c + e4p.c <-> f6p.c + g3p.c	6.5753	1.342	3.4794	9.2435	8.9092	1.6369	6.3014	11.2043
MALT net	mal.m <-> mal.c	20.7545	2.0514	-1.07E-14	41.4663	2.76E-06	1.04E-11	-5.33E-15	9.7382
PK1	mal.c -> pyr.c + co2	20.7545	2.0514	0	41.4663	2.76E-06	1.04E-11	0	9.7382

suc c	0*suc.c -> suc.p	11.3748	2.5761	5.7664	17.0786	18.0053	3.2225	8.4427	25.8191
suc m	0*suc.m -> suc.p	88.6252	2.5761	82.9214	94.2336	81.9947	3.2225	74.1809	91.5573
suc p	suc.p -> sink	100	0	100	100	100	0	100	100
cit c	0*cit.c -> cit.p	99.9979	725.516	7.11E-15	100	100	0	68.2983	100
cit m	0*cit.m -> cit.p	0.0021	725.516	0	100	1.00E-07	0	0	31.7017
cit p	cit.p -> sink	100	0	100	100	100	0	100	100
cit trans net	cit.m <-> cit.c	0.0037	0.009	7.78E-06	22.63	5.0929	1.69	3.1619	NaN
idh1-cyto net	cit.c <-> accoa.c + oaa.c	0.0037	0.009	7.78E-06	22.63	5.0929	1.69	3.1619	NaN
glut-efflux	glt.c -> glt.e	0.2696	0.2195	0	0.717	0.0331	0.0176	0	0.0704
gaba	glt.c -> gaba.c + co2	0.3516	0.7024	8.89E-07	24.0967	10.8868	51.7387	3.32E-05	NaN
oaa to asp m net	oaa.m <-> asp.m	-0.0013	0.0032	NaN	3.10E-11	0	0	0	0
oaa to asp c net	oaa.c <-> asp.c	0.0037	0.009	7.78E-06	22.63	5.0929	1.69	3.1619	NaN
asp t net	asp.m <-> asp.c	-0.0013	0.0032	NaN	6.62E-11	0	0	0	0
asp c	0*asp.c -> asp.p	95.362	696.403	85.746	100	100	0	-7.11E-15	100
asp m	0*asp.m -> asp.p	4.638	696.403	0	14.254	1.67E-06	0	0	100
asp sink	asp.p -> sink	100	0	100	100	100	0	100	100
6pg	g6p.c -> 6pg.c	19.7283	4.0259	13.9273	27.6713	31.8206	4.1646	28.0969	37.0947
asp net	asp.c + carbamoylp.c <-> orotate.c	0.0024	0.0058	4.14E-07	8.9359	5.0929	1.69	3.1619	NaN
oro net	orotate.c + 5pr1d.c <-> o5p.c	0.0024	0.0058	4.15E-07	8.9359	5.0929	1.69	3.1619	NaN
o5p	o5p.c -> co2 + utp.c	0.0024	0.0058	4.15E-07	8.9359	5.0929	1.69	3.1619	NaN
p5p net	p5p.c <-> 5pr1d.c	0.0024	0.0058	4.15E-07	8.9359	5.0929	1.69	3.1619	NaN
carbs	carbamoylp.d -> carbamoylp.c	0.0024	0.0058	4.15E-07	8.9359	5.0929	1.69	3.1619	NaN
hbp1 net	f6p.c <-> ga6p.c	0.0037	0.009	7.78E-06	22.63	5.0929	1.69	3.1619	NaN

hbp2 net	ga6p.c + accoa.c <-> naga6p.c	0.0037	0.009	7.78E-06	22.63	5.0929	1.69	3.1619	NaN
hbp3 net	naga6p.c + utp.c <-> udpnaga6p.c	0.0037	0.009	7.78E-06	22.63	5.0929	1.69	3.1619	NaN
hbp4	udpnaga6p.c -> sink	0.0037	0.009	7.78E-06	22.63	5.0929	1.69	3.1619	NaN
p5p sink	p5p.c -> sink	1.80E-06	3.10E-14	0	9.9966	2.76E-06	2.05E-12	0	6.7204
gshA	glt.c + cys.c -> gshA.c	0.2009	0.3719	1.15E-05	23.0356	10.5227	51.5992	0.7463	28.5155
gluthathione	gshA.c + glycine.c -> glutathione.c	0.2009	0.3719	1.15E-05	23.0356	10.5227	51.5992	0.7463	28.5155
gssh	glutathione.c + glutathione.c -> gssh.c	0.1004	0.1859	5.77E-06	11.5178	5.2614	25.7996	0.3732	14.2577
ala-m	pyr.m -> ala.m	139.307	44.8173	3.19E-07	244.009	52.7395	16.1617	NaN	100.151
ala-d	ala.d -> ala.m	36.9413	13.9131	0	73.5716	40.0636	30.5101	NaN	140.691
utp -d	utp.d -> upt.c	0.0013	0.0032	0	NaN	0.1161	7.06E+04	0	Inf
akg c	0*akg.m -> akg.p	1.21E-06	715.685	-7.11E-15	100	1.67E-06	7.21E+04	1.42E-14	100
akg m	0*akg.c -> akg.p	100	715.685	0	100	100	7.21E+04	[]	[]
akg p	akg.p -> sink	100	0	100	100	100	0	[]	[]
gssh-d	gssh.d -> gssh.c	0.0186	0.0462	0	6.4121	0.3361	2.1251	[]	[]

References

1. Lamri, A.; Pigeyre, M.; Garver, W.S.; Meyre, D. The Extending Spectrum of NPC1-Related Human Disorders: From Niemann-Pick C1 Disease to Obesity. *Endocr Rev* 2018, *39*, 192–220.

2. Wassif, C.A.; Cross, J.L.; Iben, J.; Sanchez-Pulido, L.; Cougnoux, A.; Platt, F.M.; Ory, D.S.; Ponting, C.P.; Bailey-Wilson, J.E.; Biesecker, L.G.; et al. High Incidence of Unrecognized Visceral/Neurological Late-Onset Niemann-Pick Disease, Type C1, Predicted by Analysis of Massively Parallel Sequencing Data Sets. *Genetics in Medicine* 2016, *18*, 41–48.

3. Vanier, M.T. Niemann-Pick Disease Type C. *Orphanet J Rare Dis* 2010, *5*, 16.

4. Chandler, R.J.; Williams, I.M.; Gibson, A.L.; Davidson, C.D.; Incao, A.A.; Hubbard, B.T.; Porter, F.D.; Pavan, W.J.; Venditti, C.P. Systemic AAV9 Gene Therapy Improves the Lifespan of Mice with Niemann-Pick Disease, Type C1. *Hum Mol Genet* 2017, *26*, 52–64.

5. Piroth, T.; Boelmans, K.; Amtage, F.; Rijntjes, M.; Wierciochin, A.; Musacchio, T.; Weiller, C.; Volkmann, J.; Klebe, S. Adult-Onset Niemann-Pick Disease Type C: Rapid Treatment Initiation Advised but Early Diagnosis Remains Difficult. *Front Neurol* 2017, *8*, 108.

6. Las Heras, M.; Szenfeld, B.; Ballout, R.A.; Buratti, E.; Zanlungo, S.; Dardis, A.; Klein, A.D. Understanding the Phenotypic Variability in Niemann-Pick Disease Type C (NPC): A Need for Precision Medicine. *npj Genomic Medicine 2023 8:1* 2023, *8*, 1–13.

7. Walterfang, M.; Chien, Y.H.; Imrie, J.; Rushton, D.; Schubiger, D.; Patterson, M.C. Dysphagia as a Risk Factor for Mortality in Niemann-Pick Disease Type C: Systematic Literature Review and Evidence from Studies with Miglustat. *Orphanet J Rare Dis* 2012, *7*, 1–17.

8. Garver, W.S.; Krishnan, K.; Gallagos, J.R.; Michikawa, M.; Francis, G.A.; Heidenreich, R.A. Niemann-Pick C1 Protein Regulates Cholesterol Transport to the Trans-Golgi Network and Plasma Membrane Caveolae. *J Lipid Res* 2002, *43*, 579–589.

9. Yu, X.-H.H.; Jiang, N.; Yao, P.-B.B.; Zheng, X.-L.L.; Cayabyab, F.S.; Tang, C.-K.K. NPC1, Intracellular Cholesterol Trafficking and Atherosclerosis. *Clin Chim Acta* 2014, *429*, 69–75.

10. Kresojević, N.; Dobričić, V.; Svetel, M.; Kostić, V. Mutations in Niemann Pick Type C Gene Are Risk Factor for Alzheimer's Disease. *Med Hypotheses* 2014, *83*, 559–562.

11. Martín, M.G.; Pfrieger, F.; Dotti, C.G. Cholesterol in Brain Disease: Sometimes Determinant and Frequently Implicated. *EMBO Rep* 2014, *15*, 1036–1052.

12. Cruz, J.C.; Chang, T.Y. Fate of Endogenously Synthesized Cholesterol in Niemann-Pick Type C1 Cells. *J Biol Chem* 2000, *275*, 41309–41316.

13. Garver, W.S.; Krishnan, K.; Gallagos, J.R.; Michikawa, M.; Francis, G.A.; Heidenreich, R.A. Niemann-Pick C1 Protein Regulates Cholesterol Transport to the Trans-Golgi Network and Plasma Membrane Caveolae. *J Lipid Res* 2002, *43*, 579–589.

14. Lamri, A.; Pigeyre, M.; Garver, W.S.; Meyre, D. The Extending Spectrum of NPC1-Related Human Disorders: From Niemann-Pick C1 Disease to Obesity. *Endocr Rev* 2018, *39*, 192–220.

15. Thelen, A.M.; Zoncu, R. Emerging Roles for the Lysosome in Lipid Metabolism HHS Public Access. *Trends Cell Biol* 2017, *27*, 833–850.

16. Hammond, N.; Munkacsi, A.B.; Sturley, S.L. The Complexity of a Monogenic Neurodegenerative Disease: More than Two Decades of Therapeutic Driven Research into Niemann-Pick Type C Disease. *Biochimica et Biophysica Acta (BBA) - Molecular and Cell Biology of Lipids* 2019, *1864*, 1109–1123.

17. Pineda M, Walterfang M, Patterson MC. Miglustat in Niemann-Pick disease type C patients: a review. *Orphanet J Rare Dis* 2018 Aug 15;13(1):140.

18. Patterson, M.C.; Garver, W.S.; Giugliani, R.; Imrie, J.; Jahnova, H.; Meaney, F.J.; Nadjar, Y.; Vanier, M.T.; Moneuse, P.; Morand, O.; et al. Long-Term Survival Outcomes of Patients with Niemann-Pick Disease Type C Receiving Miglustat Treatment: A Large Retrospective Observational Study. *J Inherit Metab Dis* 2020, *43*, 1060–1069.

19. Belmatoug, N.; Burlina, A.; Giraldo, P.; Hendriksz, C.J.; Kuter, D.J.; Mengel, E.; Pastores, G.M. Gastrointestinal Disturbances and Their Management in Miglustat-Treated Patients. *J Inherit Metab Dis* 2011, *34*, 991–1001.

20. Alam, M.S.; Getz, M.; Haldar, K. Chronic Administration of an HDAC Inhibitor Treats Both Neurological and Systemic Niemann-Pick Type C Disease in a Mouse Model. *Sci Transl Med* 2016, *8*, 1–12.

21. Abi-Mosleh, L.; Infante, R.E.; Radhakrishnan, A.; Goldstein, J.L.; Brown, M.S. Cyclodextrin Overcomes Deficient Lysosome-to-Endoplasmic Reticulum Transport of Cholesterol in Niemann-Pick Type C Cells. *Proc Natl Acad Sci U S A* 2009, *106*, 19316–19321.

22. Liu, B.; Turley, S.D.; Burns, D.K.; Miller, A.M.; Repa, J.J.; Dietschy, J.M. Reversal of Defective Lysosomal Transport in NPC Disease Ameliorates Liver Dysfunction and Neurodegeneration in the Npc1-/- Mouse. *Proc Natl Acad Sci U S A* 2009, *106*, 2377–2382.

23. Ory, D.S.; Ottinger, E.A.; Farhat, N.Y.; King, K.A.; Jiang, X.; Weissfeld, L.; Berry-Kravis, E.; Davidson, C.D.; Bianconi, S.; Keener, L.A.; et al. Intrathecal 2-Hydroxypropyl-β-Cyclodextrin Decreases Neurological Disease Progression in Niemann-Pick Disease, Type C1: A Non-Randomised, Open-Label, Phase 1-2 Trial. *Lancet* 2017, *390*, 1758–1768.

24. Ottinger, E.; Kao, M.; Carrillo-Carrasco, N.; Yanjanin, N.; Shankar, R.; Janssen, M.; Brewster, M.; Scott, I.; Xu, X.; Cradock, J.; et al. Collaborative Development of 2-Hydroxypropyl-β-Cyclodextrin for the Treatment of Niemann-Pick Type C1 Disease. *Curr Top Med Chem* 2014, *14*, 330–339.

25. Banks, W.A.; Engelke, K.; Hansen, K.M.; Bullock, K.M.; Calias, P. Modest Blood-Brain Barrier Permeability of the Cyclodextrin Kleptose: Modification by Efflux and Luminal Surface Binding. *Journal of Pharmacology and Experimental Therapeutics* 2019, *371*, 121–129.

26. Hastings C, Liu B, Hurst B, Cox GF, Hrynkow S. Intravenous 2-hydroxypropyl-β-cyclodextrin (Trappsol® Cyclo™) demonstrates biological activity and impacts cholesterol metabolism in the central nervous system and peripheral tissues in adult subjects with Niemann-Pick Disease Type C1: Results of a phase 1 trial. *Mol Genet Metab* 2022 Dec;137(4):309-319.

27. Rodriguez-Rodriguez, E.; Vázquez-Higuera, J.L.; Sánchez-Juan, P.; Mateo, I.; Pozueta, A.; Martínez-García, A.; Frank, A.; Valdivieso, F.; Berciano, J.; Bullido, M.J.; et al. Epistasis between Intracellular Cholesterol Trafficking-Related Genes (NPC1 and ABCA1) and Alzheimer's Disease Risk. *Journal of Alzheimer's Disease* 2010, *21*, 619–625.

28. Platt, F.M.; Wassif, C.; Colaco, A.; Dardis, A.; Lloyd-Evans, E.; Bembi, B.; Porter, F.D. Disorders of Cholesterol Metabolism and Their Unanticipated Convergent Mechanisms of Disease. *Annu Rev Genomics Hum Genet* 2014, *15*, 173–194.

29. Jelinek, D.; Millward, V.; Birdi, A.; Trouard, T.P.; Heidenreich, R.A.; Garver, W.S. Npc1 Haploinsufficiency Promotes Weight Gain and Metabolic Features Associated with Insulin Resistance. *Hum Mol Genet* 2011, *20*, 312–321.

30. Kresojević, N.; Dobričić, V.; Svetel, M.; Kostić, V. Mutations in Niemann Pick Type C Gene Are Risk Factor for Alzheimer's Disease. *Med Hypotheses* 2014, *83*, 559–562.

31. Kaplan, L.; Chow, B.W.; Gu, C. Neuronal Regulation of the Blood–Brain Barrier and Neurovascular Coupling. *Nat Rev Neurosci* 2020, *21*, 416–432.

32. Hashimoto, Y.; Greene, C.; Munnich, A.; Campbell, M. The CLDN5 Gene at the Blood-Brain Barrier in Health and Disease. *Fluids and Barriers of the CNS 2023 20:1* 2023, *20*, 1–22.

33. Haseloff, R.F.; Dithmer, S.; Winkler, L.; Wolburg, H.; Blasig, I.E. Transmembrane Proteins of the Tight Junctions at the Blood-Brain Barrier: Structural and Functional Aspects. *Semin Cell Dev Biol* 2015, *38*, 16–25.

34. Nitta, T.; Hata, M.; Gotoh, S.; Seo, Y.; Sasaki, H.; Hashimoto, N.; Furuse, M.; Tsukita, S. Size-Selective Loosening of the Blood-Brain Barrier in Claudin-5-Deficient Mice. *J Cell Biol* 2003, *161*, 653–660.

35. Rajagopal, N.; Irudayanathan, F.J.; Nangia, S. Palmitoylation of Claudin-5 Proteins Influences Their Lipid Domain Affinity and Tight Junction Assembly at the Blood-Brain Barrier Interface. *Journal of Physical Chemistry B* 2019, *123*, 983–993.

36. Keaney, J.; Walsh, D.M.; O'Malley, T.; Hudson, N.; Crosbie, D.E.; Loftus, T.; Sheehan, F.; McDaid, J.; Humphries, M.M.; Callanan, J.J.; et al. Autoregulated Paracellular Clearance of Amyloid-β across the Blood-Brain Barrier. *Sci Adv* 2015, *1*.

37. Saitou, M.; Furuse, M.; Sasaki, H.; Schulzke, J.R.-D.; Fromm, M.; Takano, H.; Noda, T.; Tsukita, S. Complex Phenotype of Mice Lacking Occludin, a Component of Tight Junction Strands. *Mol Biol Cell* 2000, *11*, 4131–4142.

38. Cummins, P.M. Occludin: One Protein, Many Forms. *Mol Cell Biol* 2012, *32*, 242.

39. Sugiyama S, Sasaki T, Tanaka H, Yan H, Ikegami T, Kanki H, Nishiyama K, Beck G, Gon Y, Okazaki S, Todo K, Tamura A, Tsukita S, Mochizuki H. The tight junction protein occludin modulates blood-brain barrier integrity and neurological function after ischemic stroke in mice. *Sci Rep* 2023 Feb 18;13(1):2892.

40. Itoh, M.; Furuse, M.; Morita, K.; Kubota, K.; Saitou, M.; Tsukita, S. Direct Binding of Three Tight Junction-Associated Maguks, Zo-1, Zo-2, and Zo-3, with the Cooh Termini of Claudins. *J Cell Biol* 1999, *147*, 1351.

41. Luissint, A.C.; Artus, C.; Glacial, F.; Ganeshamoorthy, K.; Couraud, P.O. Tight Junctions at the Blood Brain Barrier: Physiological Architecture and Disease-Associated Dysregulation. *Fluids Barriers CNS* 2012, *9*.

42. Sakakibara, A.; Furuse, M.; Saitou, M.; Ando-Akatsuka, Y.; Tsukita, S. Possible Involvement of Phosphorylation of Occludin in Tight Junction Formation. *J Cell Biol* 1997, *137*, 1393–1401.

43. Katsuno, T.; Umeda, K.; Matsui, T.; Hata, M.; Tamura, A.; Itoh, M.; Takeuchi, K.; Fujimori, T.; Nabeshima, Y.-I.; Noda, T.; et al. Deficiency of Zonula Occludens-1 Causes Embryonic Lethal Phenotype Associated with Defected Yolk Sac Angiogenesis and Apoptosis of Embryonic Cells. *Mol Biol Cell* 2008, *19*, 2465–2475.

44. Nelson, A.R.; Sweeney, M.D.; Sagare, A.P.; Zlokovic, B. V. Neurovascular Dysfunction and Neurodegeneration in Dementia and Alzheimer's Disease. *Biochim Biophys Acta* 2016, *1862*, 887–900.

45. Sweeney, M.D.; Kisler, K.; Montagne, A.; Toga, A.W.; Zlokovic, B. V. The Role of Brain Vasculature in Neurodegenerative Disorders. *Nat Neurosci* 2018, *21*, 1318–1331.

46. Sweeney, M.D.; Zhao, Z.; Montagne, A.; Nelson, A.R.; Zlokovic, B. V From Physiology to Disease and Back. *Physiol Rev* 2019, *99*, 21–78.

47. Greene C, Hanley N, Campbell M. Blood-brain barrier associated tight junction disruption is a hallmark feature of major psychiatric disorders. *Transl Psychiatry* 2020 Nov 2;10(1):373.

48. Kalayci, R.; Kaya, M.; Uzun, H.; Bilgic, B.; Ahishali, B.; Arican, N.; Elmas, I.; Küçük, M. Influence of Hypercholesterolemia and Hypertension on the Integrity of the Blood-Brain Barrier in Rats. *Int J Neurosci* 2009, *119*, 1881–1904.

49. Czuba, E.; Steliga, A.; Lietzau, G.; Kowiański, P. Cholesterol as a Modifying Agent of the Neurovascular Unit Structure and Function under Physiological and Pathological Conditions. *Metab Brain Dis* 2017, *32*, 935–948.

50. Kalayci, R.; Kaya, M.; Uzun, H.; Bilgic, B.; Ahishali, B.; Arican, N.; Elmas, I.; Küçük, M. Influence of Hypercholesterolemia and Hypertension on the Integrity of the Blood-Brain Barrier in Rats. *Int J Neurosci* 2009, *119*, 1881–1904.

51. de Oliveira, J.; Engel, D.F.; de Paula, G.C.; Dos Santos, D.B.; Lopes, J.B.; Farina, M.; Moreira, E.L.G.; de Bem, A.F. High Cholesterol Diet Exacerbates Blood-Brain Barrier Disruption in LDLr-/- Mice: Impact on Cognitive Function. *J Alzheimers Dis* 2020, *78*, 97–115.

52. Dias, H.K.I.; Brown, C.L.R.; Polidori, M.C.; Lip, G.Y.H.; Griffiths, H.R. LDL-Lipids from Patients with Hypercholesterolaemia and Alzheimer's Disease Are Inflammatory to Microvascular Endothelial Cells: Mitigation by Statin Intervention. *Clin Sci (Lond)* 2015, *129*, 1195–1206..

53. Dias IH, Polidori MC, Griffiths HR. Hypercholesterolaemia-induced oxidative stress at the blood-brain barrier. *Biochem Soc Trans* 2014 Aug;42(4):1001-1005.

54. Hinzey, A.H.; Kline, M.A.; Kotha, S.R.; Sliman, S.M.; Butler, E.S.O.; Shelton, A.B.; Gurney, T.R.; Parinandi, N.L. Choice of Cyclodextrin for Cellular Cholesterol Depletion for Vascular Endothelial Cell Lipid Raft Studies: Cell Membrane Alterations, Cytoskeletal Reorganization and Cytotoxicity. *Indian J Biochem Biophys* 2012, *49*, 329–341.

55. Veszelka S, Mészáros M, Porkoláb G, Rusznyák Á, Réti-Nagy KS, Deli MA, Vecsernyés M, Bácskay I, Váradi J, Fenyvesi F. Effects of Hydroxypropyl-Beta-Cyclodextrin on Cultured Brain Endothelial Cells. *Molecules* 2022 Nov 10;27(22):7738.

56. Atış M; Akcan U; Uğur Yılmaz C; Orhan N; Düzgün P; Deniz Ceylan U; Arıcan N; Karahüseyinoğlu S; Nur Şahin G; Ahıshalı B; et al. Effects of Methyl-Beta-Cyclodextrin on Blood-Brain Barrier Permeability in Angiotensin II-Induced Hypertensive Rats. *Brain Res* 2019, *1715*, 148–155.

57. Mergenthaler, P.; Lindauer, U.; Dienel, G.A.; Meisel, A. Sugar for the Brain: The Role of Glucose in Physiological and Pathological Brain Function. *Trends Neurosci* 2013, *36*, 587–597.

58. Barros, L.F.; San Martín, A.; Ruminot, I.; Sandoval, P.Y.; Fernández-Moncada, I.; Baeza-Lehnert, F.; Arce-Molina, R.; Contreras-Baeza, Y.; Cortés-Molina, F.; Galaz, A.; et al. Near-Critical GLUT1 and Neurodegeneration. *J Neurosci Res* 2017, *95*, 2267–2274.

59. Winkler, E.A.; Nishida, Y.; Sagare, A.P.; Rege, S. V; Bell, R.D.; Perlmutter, D.; Sengillo, J.D.; Hillman, S.; Kong, P.; Nelson, A.R.; et al. GLUT1 Reductions Exacerbate Alzheimer's Disease Vasculo-Neuronal Dysfunction and Degeneration. *Nat Neurosci* 2015, *18*, 521–530.

60. Leen, W.G.; Klepper, J.; Verbeek, M.M.; Leferink, M.; Hofste, T.; Van Engelen, B.G.; Wevers, R.A.; Arthur, T.; Bahi-Buisson, N.; Ballhausen, D.; et al. Glucose Transporter-1 Deficiency Syndrome: The Expanding Clinical and Genetic Spectrum of a Treatable Disorder. *Brain* 2010, *133*, 655–670.

61. Farrell CL, Pardridge WM. Blood-brain barrier glucose transporter is asymmetrically distributed on brain capillary endothelial lumenal and ablumenal membranes: an electron microscopic immunogold study. *Proc Natl Acad Sci U S A.* 1991 Jul 1;88(13):5779-83.

62. Al-Ahmad, A.J. Cell and Molecular Physiology of the Blood-Brain Barrier and Choroid Plexus: Comparative Study of Expression and Activity of Glucose Transporters between Stem Cell-Derived Brain Microvascular Endothelial Cells and HCMEC/D3 Cells. *Am J Physiol Cell Physiol* 2017, *313*, C421.

63. Stuart, C.A.; Ross, I.R.; Howell, M.E.A.; McCurry, M.P.; Wood, T.G.; Ceci, J.D.; Kennel, S.J.; Wall, J. Brain Glucose Transporter (Glut3) Haploinsufficiency Does Not Impair Mouse Brain Glucose Uptake. *Brain Res* 2011, *1384*, 15–22.

64. Koepsell, H.; De, H. Glucose Transporters in Brain in Health and Disease. *Pflügers Archiv-European Journal of Physiology* 2020, *472*, 1299–1343.

65. Régina, A.; Morchoisne, S.; Borson, N.D.; McCall, A.L.; Drewes, L.R.; Roux, F. Factor(s) Released by Glucose-Deprived Astrocytes Enhance Glucose Transporter Expression and Activity in Rat Brain Endothelial Cells. *Biochim Biophys Acta Mol Cell Res* 2001, *1540*, 233–242.

66. Huang, Y.; Lei, L.; Liu, D.; Jovin, I.; Russell, R.; Johnson, R.S.; Di Lorenzo, A.; Giordano, F.J. Normal Glucose Uptake in the Brain and Heart Requires an Endothelial Cell-Specific HIF-1 -Dependent Function. *Proceedings of the National Academy of Sciences* 2012, *109*, 17478–17483.

67. Daulatzai, M.A. Cerebral Hypoperfusion and Glucose Hypometabolism: Key Pathophysiological Modulators Promote Neurodegeneration, Cognitive Impairment, and Alzheimer's Disease. *J Neurosci Res* 2017, *95*, 943–972.

68. Mosconi L, Pupi A, De Leon MJ. Brain glucose hypometabolism and oxidative stress in preclinical Alzheimer's disease. *Ann N Y Acad Sci* 2008 Dec;1147:180-95.

69. Tang, M.; Park, S.H.; Petri, S.; Yu, H.; Rueda, C.B.; Dale Abel, E.; Kim, C.Y.; Hillman, E.M.C.; Li, F.; Lee, Y.; et al. An Early Endothelial Cell-Specific Requirement for Glut1 Is Revealed in Glut1 Deficiency Syndrome Model Mice. *JCI Insight* 2021, *6*.

70. Veys, K.; Fan, Z.; Ghobrial, M.; Bouché, A.; García-Caballero, M.; Vriens, K.; Conchinha, N.V.; Seuwen, A.; Schlegel, F.; Gorski, T.; et al. Role of the GLUT1 Glucose Transporter in Postnatal CNS Angiogenesis and Blood-Brain Barrier Integrity. *Circ Res* 2020, *127*, 466–482.

71. Pervaiz, I.; Zahra, F.T.; Mikelis, C.M.; Al-Ahmad, A.J. An in Vitro Model of Glucose Transporter 1 Deficiency Syndrome at the Blood–Brain Barrier Using Induced Pluripotent Stem Cells. *J Neurochem* 2022, *162*, 483–500.

72. Pervaiz, I.; Mehta, Y.; Sherill, K.; Patel, D.; Al-Ahmad, A.J. Ketone Bodies Supplementation Restores the Barrier Function, Induces a Metabolic Switch, and Elicits Beta-Hydroxybutyrate Diffusion across a Monolayer of IPSC-Derived Brain Microvascular Endothelial Cells. *Microvasc Res* 2023, *150*, 104585.

73. Zheng, P.P.; Romme, E.; Van Der Spek, P.J.; Dirven, C.M.F.; Willemsen, R.; Kros, J.M. Glut1/SLC2A1 Is Crucial for the Development of the Blood-Brain Barrier in Vivo. *Ann Neurol* 2010, *68*, 835–844.

74. Lee, H.; Xu, Y.; Zhu, X.; Jang, C.; Choi, W.; Bae, H.; Wang, W.; He, L.; Jin, S.; Arany, Z.; et al. Endothelium-derived Lactate Is Required for Pericyte Function and Blood–Brain Barrier Maintenance. *EMBO J* 2022, *41*.

75. Liu, C.; Wu, J.; Zou, M.H. Activation of AMP-Activated Protein Kinase Alleviates High-Glucose-Induced Dysfunction of Brain Microvascular Endothelial Cell Tight-Junction Dynamics. *Free Radic Biol Med* 2012, *53*, 1213–1221.

76. Yan, J.; Zhang, Z.; Shi, H. HIF-1 Is Involved in High Glucose-Induced Paracellular Permeability of Brain Endothelial Cells. *Cellular and Molecular Life Sciences* 2012, *69*, 115–128.

77. Li, W.; Maloney, R.E.; Aw, T.Y. High Glucose, Glucose Fluctuation and Carbonyl Stress Enhance Brain Microvascular Endothelial Barrier Dysfunction: Implications for Diabetic Cerebral Microvasculature. *Redox Biol* 2015, *5*, 80–90.

78. De Bock, K.; Georgiadou, M.; Carmeliet, P. Role of Endothelial Cell Metabolism in Vessel Sprouting. *Cell Metab* 2013, *18*, 634–647.

79. De Bock, K.; Georgiadou, M.; Schoors, S.; Kuchnio, A.; Wong, B.W.; Cantelmo, A.R.; Quaegebeur, A.; Ghesquière, B.; Cauwenberghs, S.; Eelen, G.; et al. Role of PFKFB3-Driven Glycolysis in Vessel Sprouting. *Cell* 2013, *154*, 651–663.

80. Veys, K.; Fan, Z.; Ghobrial, M.; Bouché, A.; García-Caballero, M.; Vriens, K.; Conchinha, N.V.; Seuwen, A.; Schlegel, F.; Gorski, T.; et al. Role of the GLUT1 Glucose Transporter in Postnatal CNS Angiogenesis and Blood-Brain Barrier Integrity. *Circ Res* 2020, *127*, 466–482.

81. Hawkins, R.A. The Blood-Brain Barrier and Glutamate. *Am J Clin Nutr* 2009, *90*, 867S-874S.

82. Kim, K.-S.; Jeon, M.T.; Kim, E.S.; Lee, C.H.; Kim, D.-G. Activation of NMDA Receptors in Brain Endothelial Cells Increases Transcellular Permeability. *Fluids Barriers CNS* 2022, *19*, 70.

83. Sharp, C.D.; Hines, I.; Houghton, J.; Warren, A.; Jackson, T.H.; Jawahar, A.; Nanda, A.; Elrod, J.W.; Long, A.; Chi, A.; et al. Glutamate Causes a Loss in Human Cerebral Endothelial Barrier Integrity through Activation of NMDA Receptor. *American Journal of Physiology-Heart and Circulatory Physiology* 2003, *285*, H2592–H2598.

84. Beard, R.S.; Reynolds, J.J.; Bearden, S.E. Metabotropic Glutamate Receptor 5 Mediates Phosphorylation of Vascular Endothelial Cadherin and Nuclear Localization of β-Catenin in Response to Homocysteine. *Vascul Pharmacol* 2012, *56*, 159–167.

85. Negri, S.; Faris, P.; Maniezzi, C.; Pellavio, G.; Spaiardi, P.; Botta, L.; Laforenza, U.; Biella, G.; Moccia, Dr.F. NMDA Receptors Elicit Flux-Independent Intracellular Ca2+ Signals via Metabotropic Glutamate Receptors and Flux-Dependent Nitric Oxide Release in Human Brain Microvascular Endothelial Cells. *Cell Calcium* 2021, *99*, 102454.

86. Widlansky, M.E.; Gutterman, D.D. Regulation of Endothelial Function by Mitochondrial Reactive Oxygen Species. *Antioxid Redox Signal* 2011, *15*, 1517–1530, doi:10.1089/ars.2010.3642.

87. Lee, K.E.; Kang, Y.S. L-Citrulline Restores Nitric Oxide Level and Cellular Uptake at the Brain Capillary Endothelial Cell Line (TR-BBB Cells) with Glutamate Cytotoxicity. *Microvasc Res* 2018, *120*, 29–35.

88. Kumari, S.; Mehta, S.L.; Li, P.A. Glutamate Induces Mitochondrial Dynamic Imbalance and Autophagy Activation: Preventive Effects of Selenium. *PLoS One* 2012, *7*, 39382..

89. Zuccolo, E.; Kheder, D.A.; Lim, D.; Perna, A.; Nezza, F. Di; Botta, L.; Scarpellino, G.; Negri, S.; Martinotti, S.; Soda, T.; et al. Glutamate Triggers Intracellular Ca 2+ Oscillations and Nitric Oxide Release by Inducing NAADP- and InsP 3 -Dependent Ca 2+ Release in Mouse Brain Endothelial Cells. *J Cell Physiol* 2019, *234*, 3538–3554.

90. Vazana, U.; Veksler, R.; Pell, G.S.; Prager, O.; Fassler, M.; Chassidim, Y.; Roth, Y.; Shahar, H.; Zangen, A.; Raccah, R.; et al. Glutamate-Mediated Blood–Brain Barrier Opening: Implications for Neuroprotection and Drug Delivery. *Journal of Neuroscience* 2016, *36*, 7727–7739.

91. Estes, R.E.; Lin, B.; Khera, A.; Davis, M.Y. Lipid Metabolism Influence on Neurodegenerative Disease Progression: Is the Vehicle as Important as the Cargo? *Front Mol Neurosci* 2021, *14*.

92. Vesga-Jiménez, D.J.; Martin, C.; Barreto, G.E.; Aristizábal-Pachón, A.F.; Pinzón, A.; González, J. Fatty Acids: An Insight into the Pathogenesis of Neurodegenerative Diseases and Therapeutic Potential. *Int J Mol Sci* 2022, *23*, 2577.

93. Mallick, R.; Duttaroy, A.K. Modulation of Endothelium Function by Fatty Acids. *Mol Cell Biochem* 2022, *477*, 15–38.

94. Wanders, R.J.A. Metabolic Functions of Peroxisomes in Health and Disease. *Biochimie* 2014, *98*, 36–44.

95. Liu, B.; Dai, Z. Fatty Acid Metabolism in Endothelial Cell. *Genes (Basel)* 2022, *13*.

96. Patella, F.; Schug, Z.T.; Persi, E.; Neilson, L.J.; Erami, Z.; Avanzato, D.; Maione, F.; Hernandez-Fernaud, J.R.; Mackay, G.; Zheng, L.; et al. Proteomics-Based Metabolic Modeling Reveals That Fatty Acid Oxidation (FAO) Controls Endothelial Cell (EC) Permeability. *Molecular & Cellular Proteomics* 2015, *14*, 621–634.

97. Kalucka, J.; Bierhansl, L.; Conchinha, N.V.; Missiaen, R.; Elia, I.; Brüning, U.; Scheinok, S.; Treps, L.; Cantelmo, A.R.; Dubois, C.; et al. Quiescent Endothelial Cells Upregulate Fatty Acid β-Oxidation for Vasculoprotection via Redox Homeostasis. *Cell Metab* 2018, *28*, 881-894.

98. Rajagopal, N.; Irudayanathan, F.J.; Nangia, S. Computational Nanoscopy of Tight Junctions at the Blood–Brain Barrier Interface. *Int J Mol Sci* 2019, *20*.

99. Aung, H.H.; Altman, R.; Nyunt, T.; Kim, J.; Nuthikattu, S.; Budamagunta, M.; Voss, J.C.; Wilson, D.; Rutledge, J.C.; Villablanca, A.C. Lipotoxic Brain Microvascular Injury Is Mediated by Activating Transcription Factor 3-Dependent Inflammatory and Oxidative Stress Pathways. *J Lipid Res* 2016, *57*, 955–968.

100. Nyunt, T.; Britton, M.; Wanichthanarak, K.; Budamagunta, M.; Voss, J.C.; Wilson, D.W.; Rutledge, J.C.; Aung, H.H. Mitochondrial Oxidative Stress-Induced Transcript Variants of ATF3 Mediate Lipotoxic Brain Microvascular Injury. *Free Radic Biol Med* 2019, *143*, 25–46.

101. Sim, T.M.; Tarini, D.; Dheen, S.T.; Bay, B.H.; Srinivasan, D.K. Nanoparticle-Based Technology Approaches to the Management of Neurological Disorders. *Int J Mol Sci* 2020, *21*, 1–32

102. Pandit, R.; Chen, L.; Götz, J. The Blood-Brain Barrier: Physiology and Strategies for Drug Delivery. *Adv Drug Deliv Rev* 2020, *165–166*, 1–14.

103. Dong, X. Current Strategies for Brain Drug Delivery. *Theranostics* 2018, *8*, 1481–1493.

104. Manthe RL, Loeck M, Bhowmick T, Solomon M, Muro S. Intertwined mechanisms define transport of anti-ICAM nanocarriers across the endothelium and brain delivery of a therapeutic enzyme. *J Control Release* 2020 Aug 10;324:181-193.

105. Arora, S.; Sharma, D.; Singh, J. GLUT-1: An Effective Target To Deliver Brain-Derived Neurotrophic Factor Gene Across the Blood Brain Barrier. *ACS Chem Neurosci* 2020, *11*, 1620–1633.

106. Lei, T.; Yang, Z.; Jiang, C.; Wang, X.; Yang, W.; Yang, X.; Xie, R.; Tong, F.; Xia, X.; Huang, Q.; et al. Mannose-Integrated Nanoparticle Hitchhike Glucose Transporter 1 Recycling to Overcome Various Barriers of Oral Delivery for Alzheimer's Disease Therapy. *ACS Nano* 2023, *18*, 3250.

107. Jiang, X.; Xin, H.; Ren, Q.; Gu, J.; Zhu, L.; Du, F.; Feng, C.; Xie, Y.; Sha, X.; Fang, X. Nanoparticles of 2-Deoxy-d-Glucose Functionalized Poly(Ethylene Glycol)-Co-Poly(Trimethylene Carbonate) for Dual-Targeted Drug Delivery in Glioma Treatment. *Biomaterials* 2014, *35*, 518–529.

108. Villaseñor, R.; Lampe, J.; Schwaninger, M.; Collin, L. Intracellular Transport and Regulation of Transcytosis across the Blood–Brain Barrier. *Cellular and Molecular Life Sciences* 2019, *76*, 1081–1092.

109. Pulgar, V.M. Transcytosis to Cross the Blood Brain Barrier, New Advancements and Challenges. *Front Neurosci* 2019, *13*, 1–9.

110. Fuentealba, R.A.; Liu, Q.; Zhang, J.; Kanekiyo, T.; Hu, X.; Lee, J.M.; Ladu, M.J.; Bu, G. Low-Density Lipoprotein Receptor-Related Protein 1 (LRP1) Mediates Neuronal Aβ42 Uptake and Lysosomal Trafficking. *PLoS One* 2010, *5*.

111. Parkar, N.S.; Akpa, B.S.; Nitsche, L.C.; Wedgewood, L.E.; Place, A.T.; Sverdlov, M.S.; Chaga, O.; Minshall, R.D. Vesicle Formation and Endocytosis: Function, Machinery, Mechanisms, and Modeling. *Antioxid Redox Signal* 2009, *11*, 1301–1312.

112. Barar, J.; Rafi, M.A.; Pourseif, M.M.; Omidi, Y. Blood-Brain Barrier Transport Machineries and Targeted Therapy of Brain Diseases. *BioImpacts* 2016, *6*, 225–248.

113. Bien-Ly, N.; Yu, Y.J.; Bumbaca, D.; Elstrott, J.; Boswell, C.A.; Zhang, Y.; Luk, W.; Lu, Y.; Dennis, M.S.; Weimer, R.M.; et al. Transferrin Receptor (TfR) Trafficking Determines Brain Uptake of TfR Antibody Affinity Variants. *Journal of Experimental Medicine* 2014, *211*, 233–244.

114. Piantino, M.; Louis, F.; Shigemoto-Mogami, Y.; Kitamura, K.; Sato, K.; Yamaguchi, T.; Kawabata, K.; Yamamoto, S.; Iwasaki, S.; Hirabayashi, H.; et al. Brain Microvascular Endothelial Cells Derived from Human Induced Pluripotent Stem Cells as in Vitro Model for Assessing Blood-Brain Barrier Transferrin Receptor-Mediated Transcytosis. *Mater Today Bio* 2022, *14*, 100232.

115. Pinzõn-Daza, M.L.; Garzõn, R.; Couraud, P.O.; Romero, I.; Weksler, B.; Ghigo, D.; Bosia, A.; Riganti, C. The Association of Statins plus LDL Receptor-Targeted Liposome-Encapsulated Doxorubicin Increases in Vitro Drug Delivery across Blood–Brain Barrier Cells. *Br J Pharmacol* 2012, *167*, 1431.

116. Wagner, S.; Zensi, A.; Wien, S.L.; Tschickardt, S.E.; Maier, W.; Vogel, T.; Worek, F.; Pietrzik, C.U.; Kreuter, J.; von Briesen, H. Uptake Mechanism of ApoE-Modified Nanoparticles on Brain Capillary Endothelial Cells as a Blood-Brain Barrier Model. *PLoS One* 2012, *7*.

117. Re, F.; Cambianica, I.; Zona, C.; Sesana, S.; Gregori, M.; Rigolio, R.; La Ferla, B.; Nicotra, F.; Forloni, G.; Cagnotto, A.; et al. Functionalization of Liposomes with ApoE-Derived Peptides at Different Density Affects Cellular Uptake and Drug Transport across a Blood-Brain Barrier Model. *Nanomedicine* 2011, *7*, 551–559.

118. Andreone, B.J.; Chow, B.W.; Tata, A.; Lacoste, B.; Ben-Zvi, A.; Bullock, K.; Deik, A.A.; Ginty, D.D.; Clish, C.B.; Gu, C. Blood-Brain Barrier Permeability Is Regulated by Lipid Transport-Dependent Suppression of Caveolae-Mediated Transcytosis. *Neuron* 2017, *94*, 581-594.

119. Lanser, D.M.; Bennett, A.B.; Vu, K.; Gelli, A. Macropinocytosis as a Potential Mechanism Driving Neurotropism of Cryptococcus Neoformans. *Front Cell Infect Microbiol* 2023, *13*, 1331429.

120. Seo, J.; Oh, D.B. Mannose-6-Phosphate Glycan for Lysosomal Targeting: Various Applications from Enzyme Replacement Therapy to Lysosome-Targeting Chimeras. *Anim Cells Syst (Seoul)* 2022, *26*, 84–91.

121. Dhami, R.; Schuchman, E.H. Mannose 6-Phosphate Receptor-Mediated Uptake Is Defective in Acid Sphingomyelinase-Deficient Macrophages: Implications for Niemann-Pick Disease Enzyme Replacement Therapy. *J Biol Chem* 2004, *279*, 1526–1532.

122. Rappaport, J.; Manthe, R.L.; Solomon, M.; Garnacho, C.; Muro, S. A Comparative Study on the Alterations of Endocytic Pathways in Multiple Lysosomal Storage Disorders. *Mol Pharm* 2016, *13*, 357–368.

123. Zadka, Ł.; Sochocka, M.; Hachiya, N.; Chojdak-Łukasiewicz, J.; Dzięgiel, P.; Piasecki, E.; Leszek, J. Endocytosis and Alzheimer's Disease. *Geroscience* 2024, *46*, 71.

124. Leite, D.M.; Seifi, M.; Ruiz-Perez, L.; Nguemo, F.; Plomann, M.; Swinny, J.D.; Battaglia, G. Syndapin-2 Mediated Transcytosis of Amyloid-β across the Blood–Brain Barrier. *Brain Commun* 2022, *4*.

125. Zhang, Y.; Zou, Z.; Liu, S.; Miao, S.; Liu, H. Nanogels as Novel Nanocarrier Systems for Efficient Delivery of CNS Therapeutics. *Front Bioeng Biotechnol* 2022, *0*, 1208.

126. Pinelli, F.; Perale, G.; Rossi, F. Coating and Functionalization Strategies for Nanogels and Nanoparticles for Selective Drug Delivery. *Gels* 2020, *6*.

127. Huang, X.; Misra, G.P.; Vaish, A.; Flanagan, J.M.; Sutermaster, B.; Lowe, T.L. Novel Nanogels with Both Thermoresponsive and Hydrolytically Degradable Properties. *Macromolecules* 2008, *41*, 8339–8345.

128. Ballauff, M.; Lu, Y. "Smart" Nanoparticles: Preparation, Characterization and Applications. *Polymer (Guildf)* 2007, *48*, 1815–1823.

129. Ghaeini-Hesaroeiye, S.; Bagtash, H.R.; Boddohi, S.; Vasheghani-Farahani, E.; Jabbari, E. Thermoresponsive Nanogels Based on Different Polymeric Moieties for Biomedical Applications. *Gels* 2020, *6*, 1–32.

130. Lippmann, E.S.; Al-Ahmad, A.; Azarin, S.M.; Palecek, S.P.; Shusta, E. V. A Retinoic Acid-Enhanced, Multicellular Human Blood-Brain Barrier Model Derived from Stem Cell Sources. *Sci Rep* 2014, *4*.

131. Lippmann, E.S.; Azarin, S.M.; Kay, J.E.; Nessler, R.A.; Wilson, H.K.; Al-Ahmad, A.; Palecek, S.P.; Shusta, E. V Human Blood-Brain Barrier Endothelial Cells Derived from Pluripotent Stem Cells. *Nat Biotechnol* 2012, *30*, 2014.

132. Neal, E.H.; Marinelli, N.A.; Shi, Y.; McClatchey, P.M.; Balotin, K.M.; Gullett, D.R.; Hagerla, K.A.; Bowman, A.B.; Ess, K.C.; Wikswo, J.P.; et al. A Simplified, Fully Defined Differentiation Scheme for Producing Blood-Brain Barrier Endothelial Cells from Human IPSCs. *Stem Cell Reports* 2019, *12*, 1380–1388, doi:10.1016/j.stemcr.2019.05.008.

133. Linville, R.M.; Nerenberg, R.F.; Grifno, G.; Arevalo, D.; Guo, Z.; Searson, P.C. Brain Microvascular Endothelial Cell Dysfunction in an Isogenic Juvenile IPSC Model of Huntington's Disease. *Fluids Barriers CNS* 2022, *19*, 54.

134. Lu, T.M.; Houghton, S.; Magdeldin, T.; Durán, J.G.B.; Minotti, A.P.; Snead, A.; Sproul, A.; Nguyen, D.H.T.; Xiang, J.; Fine, H.A.; et al. Pluripotent Stem Cell-Derived Epithelium Misidentified as Brain Microvascular Endothelium Requires ETS Factors to Acquire Vascular Fate. *Proc Natl Acad Sci U S A* 2021, *118*.

135. Lippmann, E.S.; Azarin, S.M.; Palecek, S.P.; Shusta, E. V. Commentary on Human Pluripotent Stem Cell-Based Blood–Brain Barrier Models. *Fluids Barriers CNS* 2020, *17*, 64.

136. Weber, C.M.; Moiz, B.; Zic, S.M.; Alpízar Vargas, V.; Li, A.; Clyne, A.M. Induced Pluripotent Stem Cell-Derived Cells Model Brain Microvascular Endothelial Cell Glucose Metabolism. *Fluids Barriers CNS* 2022, *19*, 1–15.

137. Haq, S.; Grondin, J.A.; Khan, W.I. Tryptophan-derived Serotonin-kynurenine Balance in Immune Activation and Intestinal Inflammation. *The FASEB Journal* 2021, *35*.

138. Piantino M, Louis F, Shigemoto-Mogami Y, Kitamura K, Sato K, Yamaguchi T, Kawabata K, Yamamoto S, Iwasaki S, Hirabayashi H, Matsusaki M. Brain microvascular endothelial cells derived from human induced pluripotent stem cells as *in vitro* model for assessing blood-brain barrier transferrin receptor-mediated transcytosis. *Mater Today Bio* 2022 Mar 10;14.

139. Coisne, C.; Tilloy, S.; Monflier, E.; Wils, D.; Fenart, L.; Gosselet, F. Cyclodextrins as Emerging Therapeutic Tools in the Treatment of Cholesterol-Associated Vascular and Neurodegenerative Diseases. *Molecules* 2016, *21*, 1–22.

140. Mahammad, S.; Parmryd, I. Cholesterol Depletion Using Methyl-β-Cyclodextrin. *Methods Mol Biol* 2015, *1232*, 91–102.

141. Chen, F.W.; Li, C.; Ioannou, Y.A. Cyclodextrin Induces Calcium-Dependent Lysosomal Exocytosis. *PLoS One* 2010, *5*, 15054.

142. Alboni, S.; Secco, V.; Papotti, B.; Vilella, A.; Adorni, M.P.; Zimetti, F.; Schaeffer, L.; Tascedda, F.; Zoli, M.; Leblanc, P.; et al. Hydroxypropyl-β-Cyclodextrin Depletes Membrane Cholesterol and Inhibits SARS-CoV-2 Entry into HEK293T-ACEhi Cells. *Pathogens* 2023, *12*.

143. Cenedella, R.J. Cholesterol Synthesis Inhibitor U18666A and the Role of Sterol Metabolism and Trafficking in Numerous Pathophysiological Processes. *Lipids* 2009, *44*, 477–487.

144. Cenedella, R.J.; Jacob, R.; Borchman, D.; Tang, D.; Neely, A.R.; Samadi, A.; Mason, R.P.; Sexton, P. Direct Perturbation of Lens Membrane Structure May Contribute to Cataracts Caused by U18666A, an Oxidosqualene Cyclase Inhibitor. *J Lipid Res* 2004, *45*, 1232–1241.

145. Du, X.; Parent, J.M. Using Patient-Derived Induced Pluripotent Stem Cells to Model and Treat Epilepsies. *Curr Neurol Neurosci Rep* 2015, *15*, 71.

146. Paik, D.T.; Chandy, M.; Wu, J.C. Patient and Disease–Specific Induced Pluripotent Stem Cells for Discovery of Personalized Cardiovascular Drugs and Therapeutics. *Pharmacol Rev* 2020, *72*, 320.

147. McTague, A.; Rossignoli, G.; Ferrini, A.; Barral, S.; Kurian, M.A. Genome Editing in IPSC-Based Neural Systems: From Disease Models to Future Therapeutic Strategies. *Front Genome Ed* 2021, *3*, 630600.

148. Peter, F.; Rost, S.; Rolfs, A.; Frech, M.J. Activation of PKC Triggers Rescue of NPC1 Patient Specific IPSC Derived Glial Cells from Gliosis. *Orphanet J Rare Dis* 2017, *12.*.

149. Prabhu, A. V.; Kang, I.; De Pace, R.; Wassif, C.A.; Fujiwara, H.; Kell, P.; Jiang, X.; Ory, D.S.; Bonifacino, J.S.; Ward, M.E.; et al. A Human IPSC-Derived Inducible Neuronal Model of Niemann-Pick Disease, Type C1. *BMC Biol* 2021, *19*, 1–12.

150. Cho, C.F.; Wolfe, J.M.; Fadzen, C.M.; Calligaris, D.; Hornburg, K.; Chiocca, E.A.; Agar, N.Y.R.; Pentelute, B.L.; Lawler, S.E. Blood-Brain-Barrier Spheroids as an in Vitro Screening Platform for Brain-Penetrating Agents. *Nature Communications 2017 8:1* 2017, *8*, 1–14.

151. Weber, C.M.; Clyne, A.M. Sex Differences in the Blood-Brain Barrier and Neurodegenerative Diseases. *APL Bioeng* 2021, *5*.

152. Jiang, L.; Li, S.; Zheng, J.; Li, Y.; Huang, H. Recent Progress in Microfluidic Models of the Blood-Brain Barrier. *Micromachines (Basel)* 2019, *10*.

153. Henstridge, C.M.; Spires-Jones, T.L. Modeling Alzheimer's Disease Brains in Vitro. *Nat Neurosci* 2018, *21*, 899–900.

154. Rosas-Hernandez, H.; Cuevas, E.; Lantz, S.M.; Paule, M.G.; Ali, S.F. Isolation and Culture of Brain Microvascular Endothelial Cells for In Vitro Blood-Brain Barrier Studies. *Methods Mol Biol* 2018, *1727*, 315–331.

155. Elbrecht, D.H.; Long, C.J.; Hickman, J.J. Transepithelial/Endothelial Electrical Resistance (TEER) Theory and Applications for Microfluidic Body-on-a-Chip Devices. *J Rare Dis Res Treat* 2016, *1*, 46–52.

156. Srinivasan, B.; Kolli, A.R.; Esch, M.B.; Abaci, H.E.; Shuler, M.L.; Hickman, J.J. TEER Measurement Techniques for in Vitro Barrier Model Systems. *J Lab Autom* 2015, *20*, 107–126.

157. Jang, C.; Chen, L.; Rabinowitz, J.D. Metabolomics and Isotope Tracing. *Cell* 2018, *173*, 822–837.

158. Suthers, P.F.; Burgard, A.P.; Dasika, M.S.; Nowroozi, F.; Van Dien, S.; Keasling, J.D.; Maranas, C.D. Metabolic Flux Elucidation for Large-Scale Models Using 13C Labeled Isotopes. *Metab Eng* 2007, *9*, 387–405.

159. Nielsen, J. It Is All about Metabolic Fluxes. *J Bacteriol* 2003, *185*, 7031.

160. Buescher, J.M.; Antoniewicz, M.R.; Boros, L.G.; Burgess, S.C.; Brunengraber, H.; Clish, C.B.; DeBerardinis, R.J.; Feron, O.; Frezza, C.; Ghesquiere, B.; et al. A Roadmap for Interpreting (13)C Metabolite Labeling Patterns from Cells. *Curr Opin Biotechnol* 2015, *34*, 189–201.

161. Antoniewicz, M.R. A Guide to (13)C Metabolic Flux Analysis for the Cancer Biologist. *Exp Mol Med* 2018, *50*, 19.

162. Rahim, M.; Ragavan, M.; Deja, S.; Merritt, M.E.; Burgess, S.C.; Young, J.D. INCA 2.0: A Tool for Integrated, Dynamic Modeling of NMR- and MS-Based Isotopomer Measurements and Rigorous Metabolic Flux Analysis. *Metab Eng* 2022, *69*, 275–285..

163. Liu, X.; Olszewski, K.; Zhang, Y.; Lim, E.W.; Shi, J.; Zhang, X.; Zhang, J.; Lee, H.; Koppula, P.; Lei, G.; et al. Cystine Transporter Regulation of Pentose Phosphate Pathway Dependency and Disulfide Stress Exposes a Targetable Metabolic Vulnerability in Cancer. *Nat Cell Biol* 2020, *22*, 476–486.

164. Antoniewicz, M.R. Methods and Advances in Metabolic Flux Analysis: A Mini-Review. *J Ind Microbiol Biotechnol* 2015, *42*, 317–325.

165. Dai, Z.; Locasale, J.W. Understanding Metabolism with Flux Analysis: From Theory to Application. *Metab Eng* 2017, *43*, 94–102.

166. Moiz, B.; Garcia, J.; Basehore, S.; Sun, A.; Li, A.; Padmanabhan, S.; Albus, K.; Jang, C.; Sriram, G.; Clyne, A.M. (13)C Metabolic Flux Analysis Indicates Endothelial Cells Attenuate Metabolic Perturbations by Modulating TCA Activity. *Metabolites* 2021, *11*.

167. Moiz, B.; Li, A.; Padmanabhan, S.; Sriram, G.; Clyne, A.M. Isotope-Assisted Metabolic Flux Analysis: A Powerful Technique to Gain New Insights into the Human Metabolome in Health and Disease. *Metabolites* 2022, *12*, 1066.

168. Moiz, B.; Sriram, G.; Clyne, A.M. Interpreting Metabolic Complexity via Isotope-Assisted Metabolic Flux Analysis. *Trends Biochem Sci* 2023, *48*, 553–567.

169. Moiz, B.; Garcia, J.; Basehore, S.; Sun, A.; Li, A.; Padmanabhan, S.; Albus, K.; Jang, C.; Sriram, G.; Clyne, A.M. 13 C Metabolic Flux Analysis Indicates Endothelial Cells Attenuate Metabolic Perturbations by Modulating TCA Activity. *Metabolites* 2021, *11*.

170. Kadry, H.; Noorani, B.; Cucullo, L. A Blood-Brain Barrier Overview on Structure, Function, Impairment, and Biomarkers of Integrity. *Fluids Barriers CNS* 2020, *17*.

171. Abdullahi, W.; Tripathi, D.; Ronaldson, P.T. Blood-Brain Barrier Dysfunction in Ischemic Stroke: Targeting Tight Junctions and Transporters for Vascular Protection. *Am J Physiol Cell Physiol* 2018, *315*, C343–C356.

172. Lambert, D.; O'Neill, C.A.; Padfield, P.J. Depletion of Caco-2 Cell Cholesterol Disrupts Barrier Function by Altering the Detergent Solubility and Distribution of Specific Tight-Junction Proteins. *Biochemical Journal* 2005, *387*, 553–560.

173. Lambert, D.; O'Neill, C.A.; Padfield, P.J. Methyl-Beta-Cyclodextrin Increases Permeability of Caco-2 Cell Monolayers by Displacing Specific Claudins from Cholesterol Rich Domains Associated with Tight Junctions. *Cell Physiol Biochem* 2007, *20*, 495–506.

174. Shigetomi, K.; Ono, Y.; Inai, T.; Ikenouchi, J. Adherens Junctions Influence Tight Junction Formation via Changes in Membrane Lipid Composition. *Journal of Cell Biology* 2018, *217*, 2373–2381.

175. Lu, T.M.; Houghton, S.; Magdeldin, T.; Durán, J.G.B.; Minotti, A.P.; Snead, A.; Sproul, A.; Nguyen, D.-H.T.; Xiang, J.; Fine, H.A.; et al. Pluripotent Stem Cell-Derived Epithelium Misidentified as Brain Microvascular Endothelium Requires ETS Factors to Acquire Vascular Fate. *Proceedings of the National Academy of Sciences* 2021, *118*.

176. Neal, E.H.; Marinelli, N.A.; Shi, Y.; McClatchey, P.M.; Balotin, K.M.; Gullett, D.R.; Hagerla, K.A.; Bowman, A.B.; Ess, K.C.; Wikswo, J.P.; et al. A Simplified, Fully Defined Differentiation Scheme for Producing Blood-Brain Barrier Endothelial Cells from Human IPSCs. *Stem Cell Reports* 2019, *12*, 1380–1388.

177. Neal, E.H.; Katdare, K.A.; Shi, Y.; Marinelli, N.A.; Hagerla, K.A.; Lippmann, E.S. Influence of Basal Media Composition on Barrier Fidelity within Human Pluripotent Stem Cell-Derived Blood-Brain Barrier Models. *J Neurochem* 2021, *159*, 980–991.

178. Reisz, J.A.; Zheng, C.; D'Alessandro, A.; Nemkov, T. Untargeted and Semi-Targeted Lipid Analysis of Biological Samples Using Mass Spectrometry-Based Metabolomics. In *High-Throughput Metabolomics: Methods and Protocols*; D'Alessandro, A., Ed.; Springer New York: New York, NY, 2019; pp. 121–135

179. Stebbins, M.J.; Wilson, H.K.; Canfield, S.G.; Qian, T.; Palecek, S.P.; Shusta, E. V. Differentiation and Characterization of Human Pluripotent Stem Cell-Derived Brain Microvascular Endothelial Cells. *Methods* 2016, *101*, 93–102.

180. Gray, K.M.; Katz, D.B.; Brown, E.G.; Stroka, K.M. Quantitative Phenotyping of Cell–Cell Junctions to Evaluate ZO-1 Presentation in Brain Endothelial Cells. *Ann Biomed Eng* 2019, *47*, 1675–1687.

181. Jia, Z.; Yang, M.; Zhao, Y.; Li, X.; Yang, C.; Qiao, L.; Li, H.; Du, J.; Lin, J.; Guan, L. CRISPR-Cas9-Mediated NPC1 Gene Deletion Enhances HEK 293 T Cell Adhesion by Regulating E-Cadherin. *Mol Biotechnol* 2023, *65*, 252–262.

182. Han, S.; Wang, Q.; Song, Y.; Pang, M.; Ren, C.; Wang, J.; Guan, D.; Xu, W.; Li, F.; Wang, F.; et al. Lithium Ameliorates Niemann-Pick C1 Disease Phenotypes by Impeding STING/SREBP2 Activation. *iScience* 2023, *26*.

183. Pugach, E.K.; Feltes, M.; Kaufman, R.J.; Ory, D.S.; Bang, A.G. High-Content Screen for Modifiers of Niemann-Pick Type C Disease in Patient Cells. *Hum Mol Genet* 2018, *27*, 2102–2112.

184. Greene, C.; Hanley, N.; Campbell, M. Claudin-5: Gatekeeper of Neurological Function. *Fluids Barriers CNS* 2019, *16*.

185. Ramirez, C.M.; Taylor, A.M.; Lopez, A.M.; Repa, J.J.; Turley, S.D. Delineation of Metabolic Responses of Npc1−/−nih Mice Lacking the Cholesterol-Esterifying Enzyme SOAT2 to Acute Treatment with 2-Hydroxypropyl-β-Cyclodextrin. *Steroids* 2020, *164*, 108725.

186. Calias, P. 2-Hydroxypropyl-β-Cyclodextrins and the Blood-Brain Barrier: Considerations for Niemann-Pick Disease Type C1. *Curr Pharm Des* 2017, *23*, 6231.

187. Li, W.; Chen, Z.; Chin, I.; Chen, Z.; Dai, H. The Role of VE-Cadherin in Blood-Brain Barrier Integrity under Central Nervous System Pathological Conditions. *Curr Neuropharmacol* 2018, *16*, 1375–1384.

188. Lugano, R.; Vemuri, K.; Barbera, S.; Orlandini, M.; Dejana, E.; Claesson-Welsh, L.; Dimberg, A. CD93 Maintains Endothelial Barrier Function by Limiting the Phosphorylation and Turnover of VE-Cadherin. *The FASEB Journal* 2023, *37*.

189. Campbell, M.; Kiang, A.S.; Kenna, P.F.; Kerskens, C.; Blau, C.; O'Dwyer, L.; Tivnan, A.; Kelly, J.A.; Brankin, B.; Farrar, G.J.; et al. RNAi-Mediated Reversible Opening of the Blood-Brain Barrier. *Journal of Gene Medicine* 2008, *10*, 930–947, doi:10.1002/JGM.1211.

190. Cougnoux, A.; Drummond, R.A.; Collar, A.L.; Iben, J.R.; Salman, A.; Westgarth, H.; Wassif, C.A.; Cawley, N.X.; Farhat, N.Y.; Ozato, K.; et al. Microglia Activation in Niemann-Pick Disease, Type C1 Is Amendable to Therapeutic Intervention. *Hum Mol Genet* 2018, *27*, 2076–2089.

191. Yao L, Xue X, Yu P, Ni Y, Chen F. Evans Blue Dye: A Revisit of Its Applications in Biomedicine. Contrast *Media Mol Imaging* 2018 Apr 22;2018:7628037. .

192. Canfield, S.G.; Stebbins, M.J.; Morales, B.S.; Asai, S.W.; Vatine, G.D.; Svendsen, C.N.; Palecek, S.P.; Shusta, E. V. An Isogenic Blood–Brain Barrier Model Comprising Brain Endothelial Cells, Astrocytes, and Neurons Derived from Human Induced Pluripotent Stem Cells. *J Neurochem* 2017, *140*, 874–888.

193. Li, X.; Sun, X.; Carmeliet, P. Hallmarks of Endothelial Cell Metabolism in Health and Disease. *Cell Metab* 2019, *30*, 414–433.

194. Goveia, J.; Stapor, P.; Carmeliet, P. Principles of Targeting Endothelial Cell Metabolism to Treat Angiogenesis and Endothelial Cell Dysfunction in Disease. *EMBO Mol Med* 2014, *6*, 1105–1120.

195. Liguori, C.; Chiaravalloti, A.; Sancesario, G.; Stefani, A.; Sancesario, G.M.; Mercuri, N.B.; Schillaci, O.; Pierantozzi, M. Cerebrospinal Fluid Lactate Levels and Brain [18F]FDG PET Hypometabolism within the Default Mode Network in Alzheimer's Disease. *Eur J Nucl Med Mol Imaging* 2016, *43*, 2040–2049.

196. Kao, Y.H.; Cheng, M.; Velakoulis, D.; Walterfang, M.; Sivaratnam, D. Brain Hypometabolism in Rare Genetic Neurodegenerative Disease: Niemann-Pick Disease Type C, Spinocerebellar Ataxia and Huntington Disease Assessed by FDG PET. *Asia Ocean J Nucl Med Biol* 2021, *9*, 167–172.

197. Zilberter, Y.; Zilberter, M. The Vicious Circle of Hypometabolism in Neurodegenerative Diseases: Ways and Mechanisms of Metabolic Correction. *J Neurosci Res* 2017, *95*, 2217–2235.

198. Daulatzai, M.A. Cerebral Hypoperfusion and Glucose Hypometabolism: Key Pathophysiological Modulators Promote Neurodegeneration, Cognitive Impairment, and Alzheimer's Disease. *J Neurosci Res* 2017, *95*, 943–972.

199. Horton, J.D.; Goldstein, J.L.; Brown, M.S. SREBPs: Activators of the Complete Program of Cholesterol and Fatty Acid Synthesis in the Liver. *J Clin Invest* 2002, *109*, 1125.

200. Yazdani, S.; Jaldin-Fincati, J.R.; Pereira, R.V.S.; Klip, A. Endothelial Cell Barriers: Transport of Molecules between Blood and Tissues. *Traffic* 2019, *20*, 390–403.

201. Goldstein, G.W.; Csjtey, J.; Diamond, I. CARRIER MEDIATED GLUCOSE TRANSPORT IN CAPILLARIES ISOLATED FROM RAT BRAIN1. *J Neurochem* 1977, *28*, 725–728.

202. Worzfeld, T.; Schwaninger, M. Apicobasal Polarity of Brain Endothelial Cells. *Journal of Cerebral Blood Flow & Metabolism* 2016, *36*, 340.

203. Betz, A.L.; Firth, J.A.; Goldstein, G.W. Polarity of the Blood-Brain Barrier: Distribution of Enzymes between the Luminal and Antiluminal Membranes of Brain Capillary Endothelial Cells. *Brain Res* 1980, *192*, 17–28.

204. Kennedy, B.E.; LeBlanc, V.G.; Mailman, T.M.; Fice, D.; Burton, I.; Karakach, T.K.; Karten, B. Pre-Symptomatic Activation of Antioxidant Responses and Alterations in Glucose and Pyruvate Metabolism in Niemann-Pick Type C1-Deficient Murine Brain. *PLoS One* 2013, *8*, e82685.

205. Beltroy, E.P.; Richardson, J.A.; Horton, J.D.; Turley, S.D.; Dietschy, J.M. Cholesterol Accumulation and Liver Cell Death in Mice with Niemann-Pick Type C Disease. *Hepatology* 2005, *42*, 886–893.

206. Nemkov, T.; Hansen, K.C.; D'Alessandro, A. A Three-Minute Method for High-Throughput Quantitative Metabolomics and Quantitative Tracing Experiments of Central Carbon and Nitrogen Pathways. *Rapid Communications in Mass Spectrometry* 2017, *31*, 663–673.

207. Nemkov T, Reisz JA, Gehrke S, Hansen KC, D'Alessandro A. High-Throughput Metabolomics: Isocratic and Gradient Mass Spectrometry-Based Methods. *Methods Mol Biol* 2019;1978:13-26.

208. Clasquin MF, Melamud E, Rabinowitz JD. LC-MS data processing with MAVEN: a metabolomic analysis and visualization engine. *Curr Protoc Bioinformatics*. 2012 Mar;Chapter 14:Unit14.11.

209. Melamud, E.; Vastag, L.; Rabinowitz, J.D. Metabolomic Analysis and Visualization Engine for LC-MS Data HHS Public Access. *Anal Chem* 2010, *82*, 9818–9826.

210. Nemkov, T.; D'Alessandro, A.; Hansen, K.C. Three-Minute Method for Amino Acid Analysis by UHPLC and High-Resolution Quadrupole Orbitrap Mass Spectrometry. *Amino Acids* 2015, *47*, 2345–2357.

211. Millard, P.; Delépine, B.; Guionnet, M.; Heuillet, M.; Bellvert, F.; Létisse, F. IsoCor: Isotope Correction for High-Resolution MS Labeling Experiments. *Bioinformatics* 2019, *35*, 4484–4487.

212. Pang, Z.; Zhou, G.; Ewald, J.; Chang, L.; Hacariz, O.; Basu, N.; Xia, J. Using MetaboAnalyst 5.0 for LC–HRMS Spectra Processing, Multi-Omics Integration and Covariate Adjustment of Global Metabolomics Data. *Nat Protoc* 2022, *17*, 1735–1761.

213. Kennedy, B.E.; Madreiter, C.T.; Vishnu, N.; Malli, R.; Graier, W.F.; Karten, B. Adaptations of Energy Metabolism Associated with Increased Levels of Mitochondrial Cholesterol in Niemann-Pick Type C1-Deficient Cells. *J Biol Chem* 2014, *289*, 16278.

214. Chen, F.W.; Davies, J.P.; Calvo, R.; Chaudhari, J.; Dolios, G.; Taylor, M.K.; Patnaik, S.; Dehdashti, J.; Mull, R.; Dranchack, P.; et al. Activation of Mitochondrial TRAP1 Stimulates Mitochondria-Lysosome Crosstalk and Correction of Lysosomal Dysfunction. *iScience* 2022, *25*, 104941.

215. Yu, W.; Gong, J.S.; Ko, M.; Garver, W.S.; Yanagisawa, K.; Michikawa, M. Altered Cholesterol Metabolism in Niemann-Pick Type C1 Mouse Brains Affects Mitochondrial Function. *J Biol Chem* 2005, *280*, 11731–11739.

216. Balboa, E.; Castro, J.; Pinochet, M.J.; Cancino, G.I.; Matías, N.; José Sáez, P.; Martínez, A.; Álvarez, A.R.; Garcia-Ruiz, C.; Fernandez-Checa, J.C.; et al. MLN64 Induces Mitochondrial Dysfunction Associated with Increased Mitochondrial Cholesterol Content. *Redox Biol* 2017, *12*, 274–284.

217. Flanagan, J.L.; Simmons, P.A.; Vehige, J.; Willcox, M.D.P.; Garrett, Q. Role of Carnitine in Disease. *Nutr Metab (Lond)* 2010, *7*, 30.

218. Bertrand, D.; Wallace, T.L. A Review of the Cholinergic System and Therapeutic Approaches to Treat Brain Disorders. *Curr Top Behav Neurosci* 2020, *45*, 1–28.

219. Ralser, M.; Wamelink, M.M.; Struys, E.A.; Joppich, C.; Krobitsch, S.; Jakobs, C.; Lehrach, H. A Catabolic Block Does Not Sufficiently Explain How 2-Deoxy-d-Glucose Inhibits Cell Growth. *Proc Natl Acad Sci U S A* 2008, *105*, 17807.

220. Gosmain, Y.; Dif, N.; Berbe, V.; Loizon, E.; Rieusset, J.; Vidal, H.; Lefai, E.; Berbe, V.; Loizon, E.; Rieusset, J.; et al. Regulation of SREBP-1 Expression and Transcriptional Action on HKII and FAS Genes during Fasting and Refeeding in Rat Tissues. *J Lipid Res* 2005, *46*.

221. Hu, J.; Liu, N.; Song, D.; Steer, C.J.; Zheng, G.; Song, G. A Positive Feedback between Cholesterol Synthesis and the Pentose Phosphate Pathway Rather than Glycolysis Promotes Hepatocellular Carcinoma. *Oncogene 2023 42:39* 2023, *42*, 2892–2904.

222. Jürs, A. V.; Völkner, C.; Liedtke, M.; Huth, K.; Lukas, J.; Hermann, A.; Frech, M.J. Oxidative Stress and Alterations in the Antioxidative Defense System in Neuronal Cells Derived from NPC1 Patient-Specific Induced Pluripotent Stem Cells. *International Journal of Molecular Sciences 2020, Vol. 21, Page 7667* 2020, *21*, 7667.

223. Moon, S.J.; Dong, W.; Stephanopoulos, G.N.; Sikes, H.D. Oxidative Pentose Phosphate Pathway and Glucose Anaplerosis Support Maintenance of Mitochondrial NADPH Pool under Mitochondrial Oxidative Stress. *Bioeng Transl Med* 2020, *5*.

224. Marchetti, P.; Fovez, Q.; Germain, N.; Khamari, R.; Kluza, J. Mitochondrial Spare Respiratory Capacity: Mechanisms, Regulation, and Significance in Non-Transformed and Cancer Cells. *FASEB Journal* 2020, *34*, 13106–13124.

225. Kluge MA, Fetterman JL, Vita JA. Mitochondria and endothelial function. *Circ Res.* 2013 Apr 12;112(8):1171-88.

226. Ciccarelli, G.; Conte, S.; Cimmino, G.; Maiorano, P.; Morrione, A.; Giordano, A. Mitochondrial Dysfunction: The Hidden Player in the Pathogenesis of Atherosclerosis? *Int J Mol Sci* 2023, *24*.

227. Dranka, B.P.; Hill, B.G.; Darley-Usmar, V.M. Mitochondrial Reserve Capacity in Endothelial Cells: The Impact of Nitric Oxide and Reactive Oxygen Species. *Free Radic Biol Med* 2010, *48*, 905.

228. Gnoni, G. V.; Priore, P.; Geelen, M.J.H.; Siculella, L. The Mitochondrial Citrate Carrier: Metabolic Role and Regulation of Its Activity and Expression. *IUBMB Life* 2009, *61*, 987–994.

229. Charman, M.; Kennedy, B.E.; Osborne, N.; Karten, B. MLN64 Mediates Egress of Cholesterol from Endosomes to Mitochondria in the Absence of Functional Niemann-Pick Type C1 Protein. *J Lipid Res* 2010, *51*, 1023–1034.

230. Kalucka, J.; Bierhansl, L.; Conchinha, N.V.; Missiaen, R.; Elia, I.; Brüning, U.; Scheinok, S.; Treps, L.; Cantelmo, A.R.; Dubois, C.; et al. Quiescent Endothelial Cells Upregulate Fatty Acid β-Oxidation for Vasculoprotection via Redox Homeostasis. *Cell Metab* 2018, *28*, 881-894.e13.

231. Fessel, J.P.; Hamid, R.; Wittmann, B.M.; Robinson, L.J.; Blackwell, T.; Tada, Y.; Tanabe, N.; Tatsumi, K.; Hemnes, A.R.; West, J.D. Metabolomic Analysis of Bone Morphogenetic Protein Receptor Type 2 Mutations in Human Pulmonary Endothelium Reveals Widespread Metabolic Reprogramming. *Pulm Circ* 2012, *2*, 201–213.

232. Diebold, I.; Hennigs, J.K.; Feldman, B.J.; Correspondence, M.R. BMPR2 Preserves Mitochondrial Function and DNA during Reoxygenation to Promote Endothelial Cell Survival and Reverse Pulmonary Hypertension. *Cell Metab* 2015, *21*, 596–608.

233. Mao H, Li L, Fan Q, Angelini A, Saha PK, Wu H, Ballantyne CM, Hartig SM, Xie L, Pi X. Loss of bone morphogenetic protein-binding endothelial regulator causes insulin resistance. *Nat Commun*ications 2021 Mar 26;12(1):1927.

234. Benussi A, Cotelli MS, Cantoni V, Bertasi V, Turla M, Dardis A, Biasizzo J, Manenti R, Cotelli M, Padovani A, Borroni B. Clinical and neurophysiological characteristics of heterozygous *NPC1* carriers. *JIMD Rep*, 2019 Jun 28;49(1):80-88.

235. Kim, D.; Kim, K.A.; Kim, J.H.; Kim, E.H.; Bae, O.N. Methylglyoxal-Induced Dysfunction in Brain Endothelial Cells via the Suppression of Akt/HIF-1α Pathway and Activation of Mitophagy Associated with Increased Reactive Oxygen Species. *Antioxidants* 2020, *9*, 1–17.

236. Crown, S.B.; Long, C.P.; Antoniewicz, M.R. Optimal Tracers for Parallel Labeling Experiments and (13)C Metabolic Flux Analysis: A New Precision and Synergy Scoring System. *Metab Eng* 2016, *38*, 10–18.

237. Woo Suk, A.; Antoniewicz, M.R. Parallel Labeling Experiments with [1,2-13C]Glucose and [U-13C]Glutamine Provide New Insights into CHO Cell Metabolism. *Metab Eng* 2013, *15*, 34–47.

238. Sim, T.M.; Tarini, D.; Dheen, S.T.; Bay, B.H.; Srinivasan, D.K. Nanoparticle-Based Technology Approaches to the Management of Neurological Disorders. *Int J Mol Sci* 2020, *21*, 1–32.

239. van Lengerich, B.; Zhan, L.; Xia, D.; Chan, D.; Joy, D.; Park, J.I.; Tatarakis, D.; Calvert, M.; Hummel, S.; Lianoglou, S.; et al. A TREM2-Activating Antibody with a Blood–Brain Barrier Transport Vehicle Enhances Microglial Metabolism in Alzheimer's Disease Models. *Nat Neurosci* 2023, *26*, 416.

240. Sanchez-Covarrubias, L.; Slosky, L.M.; Thompson, B.J.; Davis, T.P.; Ronaldson, P.T. Transporters at CNS Barrier Sites: Obstacles or Opportunities for Drug Delivery? *Curr Pharm Des* 2014, *20*, 1422–1449.

241. Saraiva, C.; Praça, C.; Ferreira, R.; Santos, T.; Ferreira, L.; Bernardino, L. Nanoparticle-Mediated Brain Drug Delivery: Overcoming Blood-Brain Barrier to Treat Neurodegenerative Diseases. *Journal of Controlled Release* 2016, *235*, 34–47.

242. Kiss, A.L.; Botos, E. Endocytosis via Caveolae: Alternative Pathway with Distinct Cellular Compartments to Avoid Lysosomal Degradation? *J Cell Mol Med* 2009, *13*, 1228.

243. Sharma, D.K.; Brown, J.C.; Choudhury, A.; Peterson, T.E.; Holicky, E.; Marks, D.L.; Simari, R.; Parton, R.G.; Pagano, R.E. Selective Stimulation of Caveolar Endocytosis by Glycosphingolipids and Cholesterol V. *Mol Biol Cell* 2004, *15*, 3114–3122.

244. Subtil, A.; Gaidarov, I.; Kobylarz, K.; Lampson, M.A.; Keen, J.H.; Mcgraw, T.E. Acute Cholesterol Depletion Inhibits Clathrin-Coated Pit Budding. *Proc Natl Acad Sci U S A* 1999, *96*, 6775–6780.

245. Rodal, S.K.; Skretting, G.; Garred, Ø.; Vilhardt, F.; Van Deurs, B.; Sandvig, K. Extraction of Cholesterol with Methyl-β-Cyclodextrin Perturbs Formation of Clathrin-Coated Endocytic Vesicles. *Mol Biol Cell* 1999, *10*, 961.

246. Loeck, M.; Placci, M.; Muro, S. Effect of Acid Sphingomyelinase Deficiency in Type A Niemann-Pick Disease on the Transport of Therapeutic Nanocarriers across the Blood–Brain Barrier. *Drug Deliv Transl Res* 2023, *13*, 3077–3093.

247. Eltoukhy, A.A.; Sahay, G.; Cunningham, J.M.; Anderson, D.G. Niemann-Pick C1 Affects the Gene Delivery Efficacy of Degradable Polymeric Nanoparticles. *ACS Nano* 2014, *8*, 7905.

248. Azadi, A.; Hamidi, M.; Khoshayand, M.R.; Amini, M.; Rouini, M.R. Preparation and Optimization of Surface-Treated Methotrexate-Loaded Nanogels Intended for Brain Delivery. *Carbohydr Polym* 2012, *90*, 462–471.

249. Phu, V.; Jiang, W.; Gottardo, R.; Finak, G. GgCyto: Next Generation Open-Source Visualization Software for Cytometry. *Bioinformatics* 2018, *34*, 3951.

250. Kim, Y.K.; Kim, E.J.; Lim, J.H.; Cho, H.K.; Hong, W.J.; Jeon, H.H.; Chung, B.G. Dual Stimuli-Triggered Nanogels in Response to Temperature and PH Changes for Controlled Drug Release. *Nanoscale Res Lett* 2019, *14*, 1–9.

251. Shi, L.; Zeng, M.; Sun, Y.; Fu, B.M. Quantification of Blood-Brain Barrier Solute Permeability and Brain Transport by Multiphoton Microscopy. *J Biomech Eng* 2014, *136*.

252. Zhang, Y.; Zou, Z.; Liu, S.; Miao, S.; Liu, H. Nanogels as Novel Nanocarrier Systems for Efficient Delivery of CNS Therapeutics. *Front Bioeng Biotechnol* 2022, *10*, 954470.

253. Wong, A.S.M.; Mann, S.K.; Czuba, E.; Sahut, A.; Liu, H.; Suekama, T.C.; Bickerton, T.; Johnston, A.P.R.; Such, G.K. Self-Assembling Dual Component Nanoparticles with Endosomal Escape Capability. *Soft Matter* 2015, *11*, 2993–3002.

254. Muro, S. Alterations in Cellular Processes Involving Vesicular Trafficking and Implications in Drug Delivery. *Biomimetics* 2018, *3*.

255. Zadka, Ł.; Sochocka, M.; Hachiya, N.; Chojdak-Łukasiewicz, J.; Dzięgiel, P.; Piasecki, E.; Leszek, J. Endocytosis and Alzheimer's Disease. *Geroscience* 2024, *46*, 71,

256. Rappaport J, Garnacho C, Muro S. Clathrin-mediated endocytosis is impaired in type A-B Niemann-Pick disease model cells and can be restored by ICAM-1-mediated enzyme replacement. *Mol Pharm*. 2014 Aug 4;11(8):2887-95

257. Patel S, Kim J, Herrera M, Mukherjee A, Kabanov AV, Sahay G. Brief update on endocytosis of nanomedicines. *Adv Drug Deliv Rev*. 2019 Apr;144:90-111.

258. Li, F.; Wen, Y.; Zhang, Y.; Zheng, K.; Ban, J.; Xie, Q.; Wen, Y.; Liu, Q.; Chen, F.; Mo, Z.; et al. Characterisation of 2-HP-β-Cyclodextrin-PLGA Nanoparticle Complexes for Potential Use as Ocular Drug Delivery Vehicles. *Artif Cells Nanomed Biotechnol* 2019, *47*, 4097–4108.

259. Wang, Z., Zhang, X., Deng, Y. *et al.* Complexation of hydrophobic drugs with hydroxypropyl-β-cyclodextrin by lyophilization using a tertiary butyl alcohol system. *J Incl Phenom Macrocycl Chem* **57**, 349–354 (2007).

260. Sodero, A.O.; Barrantes, F.J. Pleiotropic Effects of Statins on Brain Cells. *Biochimica et Biophysica Acta (BBA) - Biomembranes* 2020, 183340.